

**INTEGRATED CONCURRENT MULTI-BAND
RADIOS AND MULTIPLE-ANTENNA SYSTEMS**

Thesis by

Hossein Hashemi

In Partial Fulfillment of the Requirements

for the Degree of

Doctor of Philosophy

California Institute of Technology

Pasadena, California

2003

(Defended September 15, 2003)

© 2003

Hossein Hashemi

All Rights Reserved

Acknowledgements

In the past four years, perhaps the most important lesson I have learnt is that association with science in any form, getting a doctorate degree in my case, involves two parts. The first part, learning scientific facts and contributing to it, is something I have always enjoyed doing. Living a scientific life among an elite group of people in an exceptional place is the other part, and I did not have much of that experience before I came to Caltech. I was fortunate to enjoy the assistance, experience, support and friendship of many without whom I might not have been able finish this journey successfully. Here, I hope that I can express at least some part of my appreciation to all those who have helped my professional as well as personal life in the past few years.

First of all, I want to thank my academic advisor and my friend, Prof. Ali Hajimiri. What I learned from him goes well beyond pure academics. His high level of energy, intuition, wisdom, and efficiency, admittedly too difficult to follow for many, is a major contributor to one of the most successful groups in the field. I would like to acknowledge his personal assistance during my admission to Caltech and for helping me in adapting to the new environment. I would also like to thank him for giving me the opportunity to do the research I liked to do, and lastly for his major support for my future career. I look forward to many years of friendship and professional collaboration with him.

Prof. David Rutledge deserves a lot of credit for maintaining a wonderful environment in the third and fourth floor of Moore building. The close and friendly interaction between Caltech's High-Speed Integrated Circuits Group (Hajimiri's group) and Caltech's RF and Microwave Group (Rutledge's group) is somehow unique and has continuously benefited both groups. I am also grateful to Prof. Rutledge for his kind

personal assistance in a number of occasions including advising me about my future career.

Special thanks to my great colleagues and friends who had a substantial influence in my work at Caltech, especially Dr. Lawrence Cheung, Prof. Donhee Ham, Prof. Hui Wu, Behnam Analui and my office-mates (and *dudes*) Arun Natarajan and Xiang Guan who I'm sure will miss my loud presence in the room. The design of the multiple-antenna system in such a short time, deemed to be too risky by many of my friends, was only made possible by Xiang's enthusiastic collaboration. Jim Buckwalter and Arun read many of my paper manuscripts, proposals, and thesis and gave me valuable comments on the material.

I am also thankful to many others in Caltech for their assistance in different stages of my Ph.D., Dr. Blythe Deckman, Milan Kovacevic, Dr. Matthew Morgan, Dai Lu, Dr. Taavi Hirvonen, Prof. Jim Rosenberg, Prof. Mike Delisio, Kent Potter, Niklas Wadefalk, Ann Shen, Abbas Komijani, Ehsan Afshari, Dr. Ichiro Aoki, Dr. Scott Kee, Roberto Aparicio, Sam Mandegar, Chris White, Masoud Sharif, Amir Faraji-Dana, Florian Bohn, Rumi Chunara, Prof. Ali Jadbabaie, Naveed Near-Ansari, Dale Yee, Linda Dozsa, Carol Sosnowski, Heather Jackson, Parandeh Kia, and Jim Endrizzi.

I would like to thank the committee members in my candidacy exam. Prof. David Rutledge, Prof. Thomas McGill, Dr. Sander Weinreb, and Prof. Jehoshua Bruck gave me valuable feedback and insights during my presentation that I used in the later stages of my work.

I also want to thank my Ph.D. defense committee members, Dr. Sander Weinreb, Prof. Babak Hassibi, Prof. Yu-Chong Tai, and Prof. Oscar Painter, for their time.

I appreciate the financial assistance from the sponsors of my research. Conexant Systems (now Skyworks Inc.) assisted with the fabrication of the concurrent receiver. In particular I appreciate the help of Rahul Magoon, Frank Intveld, Ron Hlavac, Annie Wu, Terry Whistler, and Steve Lloyd. The multiple-antenna system was fabricated by IBM Corporation. I acknowledge the graduate fellowship from Intel Foundation given to me in my fourth year as a Ph.D. student and the assistance of Dr. Soumyanath Krishnamurthy

in that regard. Other sponsors for my research include The Lee Center for Advanced Networking at Caltech, Caltech Center for Neuromorphic Systems Engineering (CNSE), National Science Foundation (NSF), and Xerox Corporation. I would also like to thank the von Brimer Foundation for the Outstanding Accomplishment Award, Analog Devices for the Outstanding Student Designer Award, and the Association of Professors and Scholars of Iranian Heritage (APISH) for the Young Scholar Award.

Solving difficult electrical engineering problems has always been the easy and fun part for me as long as my personal life is going smoothly. That's why the following group of people are very special to me.

It's only fair to start with my friend of 17 years, Sam, whose devotion to his friends is always exemplary. My room-mate and very good friend, Behnam, has been almost like a family member to me in the past couple of years. Amir and Helia are probably the only people with whom I shared many of my personal ups and downs over the past year. My cousin, Nikoo, has filled the void of my family in many ways and has also helped me a lot in proofreading the thesis manuscript. Many good friends were always present to lift my spirits and have a lot of fun over the past few years: Matthieu, Lisa, Arun, Jim, Donhee, Hui, Maryam, Fati, Ehsan, Abbas, Behroo, Abdi, Roya, Alireza, Ali, Leila, Lars, Ladan, Amir, Ichiro, Scott, Yazdan, Amirhossein, Javadagha and of course my close friends and running mates Taka and Jeremy and many others.

I would not be at this stage of my life had I not come across the single most influential person in my academic life, Prof. Ali Fotowat from Sharif University of Technology. The inspiration he has given me is indescribable in such a short space, but truly acknowledged.

Finally, it's time to mention the most important people in my life, my parents, who did everything that is humanly possible, so that I could reach *any* goal I dreamed of throughout my life. My dad showed me how hard work and patience always pays off. He also let me dismantle (well, in my words *fix*) every single electrical apparatus in the house, knowing that they would be gone forever! I learned not to settle for anything but the best from my mum who has always been the pillar of strength for the whole family.

My loving sister, Nikroo, should know that I am very proud of her as a sister and as a person for what she does every day. Our new family member, Ali, is in many ways the brother I never had.

This thesis is dedicated to my family as a small appreciation of their unconditional love. Merci maman, merci baba!

Abstract

This thesis presents a unique view on radio systems that can simultaneously function at multiple frequency bands. These radios offer a higher data-rate and robustness in addition to the added functionality in the performance of wireless systems. Our treatment includes the definition of such novel radios, formulation of their singular characteristics, proposition for transceiver architectures, and invention of circuit blocks.

Various transceiver architectures for this new class of *concurrent multi-band radios* are proposed. The results for an integrated concurrent dual-band receiver operating at 2.4 GHz and 5.2 GHz frequency bands for wireless networking applications are presented. Meticulous frequency-planning results in a high level of integration and a low power design for the concurrent receiver. Several new circuit concepts including the concurrent multi-band low-noise amplifier are demonstrated in this design. A general class of these concurrent multi-band amplifiers is investigated with numerous implementations of integrated concurrent dual-band and triple-band amplifiers.

A theoretical treatment of nonlinear oscillators with multi-band resonator structures is also offered. It is shown that given certain nonlinearities these oscillators can generate multi-frequency outputs. The phase-noise of such negative-resistance oscillators with general resonator structure is addressed. By providing a link between the stored and dissipated energies of a network and its associated circuit parameters, useful interpretations of resonator quality factor are derived. With the aid of this analysis and the previously developed phase-noise models, dependencies of phase-noise on the resonator structure are derived. Based on our theoretical results, enhanced resonators with higher quality factor providing a superior oscillator phase-noise are proposed.

Finally, in order to enhance the performance of wireless systems by exploiting the spatial properties of the electromagnetic wave, multiple-antenna radios in phased-array configuration are investigated. The phased-array technology results in higher immunity to unwanted interference and therefore achieves a superior overall system capacity in a shared environment. The first fully integrated multiple-antenna receiver targeting the 24 GHz ISM band using silicon technology is presented. The phased-array radio at 24 GHz is a cheap solution for high data-rate WLAN, as well as for fixed wireless broadband access applications.

Contents

Acknowledgements	iii
Abstract	vii
List of Figures	xiv
List of Tables	xxi
Chapter 1 Introduction	1
1.1 Motivation.....	1
1.2 Organization.....	3
Chapter 2 Multi-Band/Multi-Mode Radio Systems	5
2.1 Frequency Spectrum and Narrow-Band Communications.....	5
2.2 Why Multi-Band/Multi-Mode Radio?.....	8
2.3 A Review of Existing Multi-Mode/Multi-Band Radio Architectures.....	10
2.3.1 Multi-Band Receiver Architectures.....	12
2.3.1.1 Heterodyne Architecture	13
2.3.1.2 Homodyne/Low-IF Architectures	13
2.3.1.3 Image-Reject Architectures	15
2.3.2 Multi-Band Transmitter Architectures.....	16
2.3.2.1 Multi-Step Up-Conversion	16
2.3.2.2 Direct Up-Conversion	17
2.3.2.3 Up-Conversion via Direct VCO Modulation.....	18
2.3.3 LO Generation in Multi-Band Transceivers	19
2.4 Summary.....	19

Chapter 3	Concurrent Multi-Band Radio	21
3.1	Benefits of Concurrency	21
3.2	Concurrent Receiver Architectures	22
3.2.1	Parallel Single-Band Receivers	23
3.2.2	Parallel Receivers with a Wide-Band Front-End	24
3.2.3	Parallel Receivers with a Multi-Band Front-End	25
3.2.4	Multi-Band Sub-Sampling Receiver	26
3.2.5	Direct Digitization (Digital Radio)	28
3.3	A Concurrent Dual-Band Receiver	29
3.4	Concurrent Transmitter Architectures	33
3.4.1	Scenario 1: Same Data for All Frequency Bands	34
3.4.2	Scenario 2: Different Data for Each Frequency Band	35
3.5	Adverse Effects and New Metrics in Concurrent Radios	36
3.6	Summary	39
Chapter 4	Concurrent Multi-Band Amplifiers	40
4.1	A Review of Single-Band LNA Design Issues	41
4.1.1	Technology	41
4.1.2	Topology	42
4.2	Concurrent Multi-Band Low-Noise Amplifiers	44
4.2.1	Concurrent Multi-Band LNA Design Methodology	45
4.2.1.1	General Amplifier in Common-Source Configuration	46
4.2.1.2	Input Matching	47
4.2.1.3	Noise Matching	49
4.2.1.4	Load Circuit, Output Matching and Gain	59
4.2.1.5	Practical Considerations	60
4.2.2	Concurrent LNA Design Examples and Measurement Results	64
4.2.2.1	A High-Performance Concurrent Dual-Band LNA	64
4.2.2.2	A Fully Integrated Concurrent Dual-Band Amplifier	69
4.2.2.3	Fully Integrated Concurrent Triple-Band Amplifiers	72
4.3	Multi-Band Power Amplifiers	74
4.4	Summary	75

Chapter 5	An Experimental Concurrent Dual-Band Receiver	77
5.1	Top-Level Radio Design	77
5.1.1	WLAN Standards and System Analysis	78
5.1.2	Receiver Architecture	81
5.2	Receiver Building Blocks	86
5.2.1	Concurrent Dual-Band LNA	86
5.2.2	Concurrent Dual-Band RF Mixer	88
5.2.3	IF Image-Rejection Mixers	88
5.2.4	Local Oscillator Frequency Generation	89
5.2.5	Analog Frequency Dividers	91
5.3	Experimental Results.....	97
5.4	Summary.....	102
Chapter 6	Oscillators with Multi-Band Resonators	103
6.1	Time-Domain Response of Multi-Frequency Oscillators	104
6.1.1	A Brief Overview of Second-Order Oscillators	105
6.1.2	A Brief Review of Previous Work	108
6.1.3	Problem Formulation of a Fourth-Order System	110
6.1.4	Multi-Frequency Oscillations in Fourth-Order System	115
6.1.5	A Few Potential Applications of Multi-Frequency Oscillations	122
6.2	Phase-Noise of Oscillators with a Generalized Resonator Structure	123
6.2.1	Resonator Quality Factor	125
6.2.1.1	Resonator Quality Factor without Coupling Terms	128
6.2.1.2	Resonator Quality Factor Including Coupling Terms	129
6.2.1.3	Useful Expressions for Resonator Quality Factor	131
6.2.2	Phase Noise	134
6.2.3	Circuit Examples	138
6.3	Summary.....	143
Chapter 7	A Multiple-Antenna Phased-Array Radio	144
7.1	Brief Overview of Multiple-Antenna Systems	145
7.1.1	Spatial Diversity	147

7.1.1.1	Receiver Diversity.....	147
7.1.1.2	Transmitter Diversity	148
7.1.2	Phased Array	149
7.1.2.1	Phase Shift vs. Time Delay.....	154
7.2	Phased-Array Radio Architectures.....	155
7.2.1	Phase Shifting and Signal Combining in Signal Path.....	155
7.2.2	Phase Shifting in Local-Oscillator Path.....	156
7.2.3	Digital Array Implementation	157
7.3	A 24 GHz Phased-Array Radio.....	159
7.3.1	Receiver Architecture	160
7.3.2	Receiver Building Blocks	164
7.3.2.1	RF Front-End	164
7.3.2.2	IF Circuitry ⁴⁷	165
7.3.2.3	Generating Multiple Phases of Local Oscillator.....	165
7.3.2.4	A 19 GHz Multi-Phase Voltage Controlled Oscillator	170
7.3.2.5	Phase-Selection Circuitry	172
7.3.2.6	LO Phase-Distribution Network.....	175
7.3.3	Measurement Results of the Implemented Receiver	177
7.4	Summary.....	190
Chapter 8	Conclusion	192
8.1	Summary.....	192
8.2	Recommendations for Future Work.....	193
Appendix A	General Small-Signal Expressions for a Common-Source Amplifier	195
Appendix B	Noise Source Transformations	197
Appendix C	Nonlinear Differential Equation of a Fourth-Order System with Multiple Sources of Loss	198
Appendix D	Possibility of Simultaneous Oscillations with a Fifth-Order Nonlinearity Expansion	201

Appendix E	Explicit Phase-Noise Derivation of a Fourth-Order Resonator Based on [110]	205
Bibliography		210

List of Figures

Figure 2.1: Simplified illustration of single-band radios (a) time-duplex (b) full-duplex ...	11
Figure 2.2: Illustration of cross-talk caused by the image signal in the receiver.....	12
Figure 2.3: A multi-band / multi-mode receiver based on Heterodyne architecture [6].....	13
Figure 2.4: A direct-conversion multi-band receiver for mobile-phone applications [15] ..	15
Figure 2.5: Dual-band receiver based on Weaver's image-rejection scheme [9].....	16
Figure 2.6: Dual-band transmitter using dual up-conversion for CDMA standards [10]	17
Figure 2.7: Dual-band direct-conversion transmitter for CDMA standards [14]	18
Figure 2.8: Dual-band transmitter based on direct-modulation of VCO frequency [15].....	19
Figure 3.1: Concurrent receiver implementations using multiple parallel single-band, receivers in (a) heterodyne (b) direct down-conversion architectures.....	24
Figure 3.2: Concurrent receiver implementation using a wide-band front-end in (a) heterodyne (b) direct down-conversion architectures.....	25
Figure 3.3: Concurrent receiver implementation using a multi-band front-end in (a) heterodyne (b) direct down-conversion architectures.....	26
Figure 3.4: Frequency domain representation of down-conversion using bandpass subsampling.....	27
Figure 3.5: Frequency domain representation of multi-band subsampling	28
Figure 3.6: Generic architecture of a direct digitization radio.....	29
Figure 3.7: Evolution process of two parallel receivers to a concurrent dual-band receiver	30
Figure 3.8: Concurrent dual-band receiver architecture.....	31
Figure 3.9: Operation principle of the proposed concurrent dual-band receiver in frequency domain.....	33
Figure 3.10: Proposed concurrent dual-band transmitter in scenario 1.....	34
Figure 3.11: Proposed concurrent dual-band transmitter in scenario 2.....	35
Figure 3.12: Depiction of cross-band compression.....	37

Figure 3.13: Depiction of $(n+m)$ order cross-band intermodulation	37
Figure 3.14: Illustration of reciprocal mixing caused by local oscillator phase-noise.....	38
Figure 4.1: Commonly used single-band CMOS LNAs (a) common-gate (b) common-source with inductive degeneration	43
Figure 4.2: Generic schematic of existing multi-band amplifiers.....	45
Figure 4.3: General model for a single-stage amplifier in common-source configuration. .	46
Figure 4.4: General representation of any noisy 2-port (a) and its equivalent circuit (b)....	50
Figure 4.5: (a) NF and f_i for a bipolar transistor with $\tau_F=3.67ps$ (b) Different noise contributions to the total NF from (4.16) (NF numbers for 5.8 GHz).....	56
Figure 4.6: NF of a 0.18 μm CMOS transistor at 5.8 GHz with finger width of 2 μm vs. n_f and V_{od}	57
Figure 4.7: (a) NF , f_T of a 20 x 2.5 μm / 0.18 μm CMOS transistor. (b) I_D , g_m , g_{d0} of the transistor. (c) Different noise contributions to the total NF from (4.16) (NF numbers at 5.8 GHz).....	58
Figure 4.8: Basic illustration revealing that the combination of multi-frequency signals requires a more linear amplifier design	61
Figure 4.9: Simulated return-loss of a dual-band (dotted-curve) and a triple-band (solid-curve) input matching circuitry (a) $Q_{ind}=100$ (b) $Q_{ind}=10$	62
Figure 4.10: (a) Simulated results comparing the value of triple-band (solid-curve), dual-band (bold dotted-curve) and single-band (dotted-curve) impedance functions (b) Typical curve for the quality factor of on-chip spiral inductors that is used to generate impedance function curves.....	63
Figure 4.11: Concurrent dual-band CMOS LNA (biasing circuitry not shown)	65
Figure 4.12: Voltage-gain and S_{11} in concurrent dual-band CMOS LNA of Figure 4.11....	66
Figure 4.13: Chip micrograph for the concurrent dual-band CMOS LNA in Figure 4.11..	67
Figure 4.14: Schematic and layout of an integrated dual-band CMOS amplifier.....	70
Figure 4.15: Voltage-gain and return-loss of concurrent dual-band amplifier of Figure 4.14	71
Figure 4.16: Schematic and layout of an integrated triple-band CMOS amplifier	73
Figure 4.17: Voltage-gain and return-loss of concurrent triple-band amplifiers using the topology in Figure 4.16. (a) CMOS version (b) Bipolar version	74

Figure 5.1: Complete schematic of the fully integrated concurrent dual-band receiver	82
Figure 5.2: Frequency planning of the concurrent dual-band receiver in Figure 5.1.....	84
Figure 5.3: Simplified schematic of the concurrent dual-band LNA.....	87
Figure 5.4: Simplified schematic of the dual-band RF mixer.....	88
Figure 5.5: Simplified schematic of IF one pair of image-rejection mixers.....	89
Figure 5.6: Simplified schematic of the 6.3 GHz PLL ²³	90
Figure 5.7: (a) Two-stage stagger-tuned poly-phase structure for LO quadrature generation; (b) its frequency response in complex domain.....	91
Figure 5.8: Simplified schematic of the divide-by-two ILFD in [105] and [106]	93
Figure 5.9: Simplified schematic of the proposed divide-by-three ILFD	94
Figure 5.10: Divide-by-three principle of operation under no input signal at (a) fundamental oscillation frequency (b) odd harmonics of oscillation frequency (c) even harmonics of oscillation frequency.....	94
Figure 5.11: Simulated results of the ILFD in Figure 5.9 with no injected input power and for $f_{osc}=2.1$ GHz: (a) frequency contents of current in $M_{3,4}$, (b) frequency contents of current in the LC series branch of L_s and C_s	95
Figure 5.12: Simulated locking-range of the implemented ILFD-based 6.3 GHz divide-by- three versus divider's current consumption	96
Figure 5.13: Die micrograph of the first version of concurrent receiver (off-chip LO).....	97
Figure 5.14: Die micrograph of the second version of concurrent receiver (fully integrated)	98
Figure 5.15: Test board to measure the performance of concurrent receiver	99
Figure 5.16: Typical measurement setup for the concurrent receiver.....	99
Figure 5.17: Measured gain of the concurrent receiver at two bands of interest.....	100
Figure 5.18: Large-signal gain characteristic of the receiver at the higher frequency band	100
Figure 6.1: A simple model for a second-order electrical oscillator.....	105
Figure 6.2: Cross-coupled pair oscillator with a simple second order LC resonator and the plot of resonator's impedance magnitude	107
Figure 6.3. Triode oscillator with two degrees of freedom analyzed in [121]	109
Figure 6.4: The simple model used to analyze the oscillator in Figure 6.6.....	110

Figure 6.5: Impedance magnitude of the fourth-order resonator of Figure 6.4 when ω_s is closer to: (a) ω_2 , (b) ω_1	111
Figure 6.6: Cross-coupled pair oscillator with the fourth-order dual-resonance tank depicted in Figure 6.4	115
Figure 6.7: Graphical representation of the stability of multiple solutions to (6.14) for a 3 rd order power expansion of the nonlinear voltage-current characteristic.....	119
Figure 6.8: Simulation results showing asynchronous oscillations in Figure 6.6.....	121
Figure 6.9: Dual-band Colpitts-type oscillator generating synchronous oscillations	122
Figure 6.10: A potential single-chain concurrent receiver using a multi-band oscillator ..	123
Figure 6.11: General model of a negative-resistance oscillator with a resonator.....	124
Figure 6.12: Frequency spectrum magnitude of a sixth-order and a second-order resonator (a sixth-order resonator structure is shown in Figure 6.13)	127
Figure 6.13: A sixth-order triple-band resonator	127
Figure 6.14: Two examples of resonators that use coupled inductors: (a) Quality factor increases, since coupling energy adds to total stored energy (i_1 and i_2 in-phase). (b) Quality factor decreases, since coupling energy subtracts from total stored energy (i_1 and i_2 out-of-phase).....	131
Figure 6.15: Impedance definition of a one-port network.....	132
Figure 6.16: Illustration of phase-noise definition per unit bandwidth.....	135
Figure 6.17: Cross-coupled pair oscillator with a fourth-order resonator implemented using transformers.....	139
Figure 6.18: Impedance magnitude of the higher-order resonators (solid-curves) compared to the second-order LC resonator of Figure 6.2 (dotted curves) (a) fourth-order resonator used in oscillator of Figure 6.6 (b) sixth-order resonator used in oscillator of Figure 6.13 (c) fourth-order transformer-based resonator used in oscillator of Figure 6.17 [Coupling-factor $k=0.9$ is assumed in this figure]	140
Figure 6.19: A proposed combination of three coupled inductors in a resonator structure to achieve a higher energy-based definition of quality factor that results in an enhanced phase-noise performance if inserted in an oscillator core.....	142
Figure 6.20: Simulated phase-noise of three cross-coupled oscillators at 5 GHz having a common core with different resonator structures in Figure 6.2, Figure 6.17, and Figure	

6.19. Oscillation amplitude is 0.830 V, 0.805 V and 0.795 V for these cases, respectively.....	142
Figure 7.1: Wireless communication channels (a) line-of-sight (b) multi-path fading.....	145
Figure 7.2: Narrower antenna beams using multiple-antenna elements.....	146
Figure 7.3: Characteristic of a received signal envelope in a typical fading channel (courtesy of [137]).....	147
Figure 7.4: Simplified scheme of a maximal ratio combining receiver using spatial diversity	148
Figure 7.5: Illustration of a MIMO system and space-time coding at the transmitter	149
Figure 7.6: Phased-array concept (gain control block is only necessary when controlling multiple peaks and nulls is desired).....	151
Figure 7.7: Schematic of a phased-array receiver used for <i>SNR</i> calculations	153
Figure 7.8: Phased-array receiver using signal-path (<i>RF</i> or <i>IF</i>) phase shifting.....	156
Figure 7.9: Phased-array receiver using LO phase shifting.....	157
Figure 7.10: Phased-array receiver using baseband signal processing (digital array)	158
Figure 7.11: Block-diagram schematic of the 24 GHz phased-array receiver.....	162
Figure 7.12: Relative gain of the array with 4-bit discrete phase shifting	163
Figure 7.13: Schematic of the 24 GHz front-end consisting of a 2-stage LNA and Gilbert-type mixers in each channel	164
Figure 7.14: Schematic of the 4.8 GHz <i>IF</i> stage consisting of <i>IF</i> amplifiers and double-balanced Gilbert-type mixers	165
Figure 7.15: A first-order passive all-pass filter and its phase transfer-function.....	166
Figure 7.16: Broadband phase shifting using all-pass functions	167
Figure 7.17: A generic phase-interpolator and a vector-diagram for sinusoid input signals	168
Figure 7.18: An array of coupled oscillators for multiple phase generation	169
Figure 7.19: Multi-phase oscillators in ring configuration (a) using delay elements (b) traveling wave oscillator with a transmission line	170
Figure 7.20: Schematic of the 19 GHz VCO that generates 16 phases of LO.....	171
Figure 7.21: Buffers after the oscillator core.....	172

Figure 7.22: Schematic of LO phase selection circuitry for each path (biasing not shown). (a) selecting one of 8 oscillator output pairs; (b) dummy array to maintain constant loading for all phases; (c) sign selector	174
Figure 7.23: Array response with $\pm 2.5^\circ$ of mismatch in LO phase distribution (thick line) compared to the ideal case (thin line) for 8-path receiver	175
Figure 7.24: Tree structure used for a symmetric distribution of 16 LO phases	176
Figure 7.25: Die micrograph of the 24 GHz fully integrated phased-array receiver	177
Figure 7.26: Oscillation frequency vs. varactors' control voltage	178
Figure 7.27: Oscillator output spectrum and phase-noise at 18.70 GHz	179
Figure 7.28: PFN of various oscillators	180
Figure 7.29: Measurement setup for 4-channel array characterization	181
Figure 7.30: Close-up of the measured chip mounted on a brass substrate	182
Figure 7.31: Input return-loss of the receiver	183
Figure 7.32: Receiver small-signal transfer function for the main and image signals	184
Figure 7.33: Large-signal response of the receiver at 23 GHz input frequency	184
Figure 7.34: Intermodulation test of the receiver (a) Typical output spectrum when two large-signal input tones are applied (b) Results of two-tone test	185
Figure 7.35: Received pattern measurements of the phased-array system with two operating paths	186
Figure 7.36: Simulated beam-width comparison of the 8-channel phased array with the case when only 2 paths are working	187
Figure 7.37: Received pattern measurements of the phased-array system with four operating paths compared with theory	187
Figure A.1: Equivalent small-signal model for the generic amplifier of Figure 4.3	195
Figure B.2: Illustration of noise source transformation in (a) series (b) parallel cases	197
Figure C.3: A second-order oscillator model with multiple sources of loss	198
Figure E.4: Simplified model used to calculate ISF of an oscillator with a fourth-order resonator in Figure 6.6	205
Figure E.5: Simplified model used to calculate ISF of an oscillator with a fourth-order resonator in Figure 6.6	209

List of Tables

Table 2.1: Selected portions of FCC-allocated frequency-spectra for narrow-band communications.....	7
Table 2.2: Selectivity of selected narrow-band communication receiver systems	8
Table 2.3: Today's predominant mobile-phone standards	9
Table 4.1: Comparison of V_{char} , and ω_T in different sub-micron CMOS processes.....	54
Table 4.2: Performance summary of the concurrent dual-band CMOS LNA.....	68
Table 4.3: Comparison of existing single-band CMOS LNAs and the concurrent multi-band LNA at the same frequency bands (S-band and C-band)	68
Table 5.1: Summary of a few wireless networking standards at 2.4 GHz and 5 GHz.....	80
Table 5.2: Receiver target numbers for standards in Table 5.1	81
Table 5.3: Concurrent receiver frequency planning that uses only divide-by-two.....	84
Table 5.4: Concurrent receiver frequency planning that exploits divide-by-three and divide-by-two circuit blocks	85
Table 5.5: Component values of the implemented divide-by-three ILFDs in Figure 5.9 (a) 6.3 GHz to 2.1 GHz divider (b) 2.1 GHz to 0.7 GHz divider	96
Table 5.6: Concurrent dual-band receiver performance summary	101
Table 6.1: Quality factor comparison for different resonator structures.....	141
Table 7.1: Summary of the measured performance of the 24 GHz phased-array receiver	189
Table 7.2: Comparison of recently published silicon-based receivers around 24 GHz	190

Chapter 1

Introduction

Achieving the highest possible performance of wireless devices, irrespective of cost, was the primary focus of early radio engineers. The advent of commodity wireless appliances has gradually shifted the emphasis towards the most affordable solution. With the increase in demand, and rapid improvements in the semiconductor technology, the cost of wireless devices has considerably reduced. Additionally, the complexity of operations performed on Integrated Circuits (ICs) has grown exponentially [1]. In this environment of decreasing cost and increasing complexity, acquiring *more functionality and flexibility* is the best objective for future integrated wireless devices. This thesis presents such an approach towards *increased functionality and performance* of integrated wireless systems.

1.1 Motivation

As a result of the shared medium in wireless communications, the valuable frequency-spectrum has been divided to serve a diverse range of applications. Conventionally, wireless devices operate at a frequency band allocated for a particular application. Since received signals from other wireless devices act as undesirable interference, radio transceivers are often designed for a narrow frequency bandwidth. The limited operation bandwidth of these systems makes them incapable of functioning at frequency bands other than their own.

On the other hand, wireless systems capable of operating at multiple frequency bands are useful in numerous applications. Oftentimes, within a given application space, different modes of operation demand the operability at more than one frequency band. A good

example of such a *multi-mode* system is the common household radio that has to cover, at least, the AM and FM frequency bands. Additionally, radio transceivers that can be used for more than one application are of a great interest. *Multi-band* mobile phone terminals with capability of wireless connection to the Internet are examples of the latter case.

In this thesis, we will present a unique view on multi-mode and multi-band radio systems that can simultaneously function at multiple frequency bands. These novel radios offer a higher data-rate, robustness, and improvement, in addition to the added functionality, in the performance of wireless systems. Our treatment comprises of the definition of such novel radios, formulation of their particular characteristics, proposals for potential transceiver architectures, and invention of circuit blocks. Throughout the discussions, our theoretical findings are verified with experimental implementations of the developed concepts.

The performance of wireless systems can be further enhanced by exploiting the spatial properties of the electromagnetic wave. The combination of signals extracted from (or inserted to) different physical points of a propagated wave increases the energy of the signal. Using *multiple-antenna* systems is a natural way of collecting and generating signal energy at different points in space in order to achieve higher data-rate wireless communications.

With the goal of demonstrating a significant improvement in the performance of traditional wireless devices, and in order to bridge the scientific gap between the conventional integrated-circuit designs and microwave techniques, the design and implementation of an ultra high-frequency multiple antenna radio system will be presented. Of particular interest is the integration of the complete system on a commercially available silicon technology that paves the way for a low-cost alternative for high-performance wireless communication schemes.

The contributions of our study include the development of original concepts and new theoretical findings together with practical implications in the area of integrated multi-mode, multi-band, and multiple-antenna radio systems.

1.2 Organization

After describing the traditional narrow-band radio design from a historical basis, the motivations behind advancing to multi-band and multi-mode wireless systems will be explained in Chapter 2. We will then present a brief overview of existing multi-band and multi-mode radio architectures.

Traditional multi-band transceivers that will be discussed in Chapter 2 are incapable of a simultaneous operation at multiple frequency bands. In Chapter 3 we will introduce the new concept of concurrent multi-band radios and will show their benefits in many cases. Receiver and transmitter architectures for this new class of radios will be revealed, many of which relying on the novel building blocks that will be described in detail throughout this thesis. Furthermore, upcoming challenges particular to concurrent multi-band radios, as well as new metrics for characterizing those systems, will be discussed.

Chapter 4 covers the theory, design, and implementation of concurrent multi-band amplifiers that serve as key parts in concurrent radio architectures. A general class of concurrent low-noise amplifiers that can achieve minimum noise-figure, input matching, and narrow-band gain at multiple frequency bands are introduced and analyzed comprehensively. Based on the results of our general treatment, a number of integrated concurrent dual- and triple-band amplifiers are designed and implemented. The validity of our theoretical predictions is confirmed through successful measurements of the concurrent amplifiers.

The implementation of the first experimental concurrent dual-band receiver is presented in Chapter 5. The complete cycle of system realization, starting from radio specification and receiver architecture down to the building block level design and extensive measurements is described. A meticulous frequency-planning results in a high level of integration and a low power design for the concurrent receiver. Several new circuit concepts, including current-sharing two-stage concurrent low-noise amplifiers and injection locked analog divide-by-three circuits, are demonstrated in this design. The implemented concurrent receiver can significantly increase the functionality, robustness, and bit-rate of wireless networking schemes.

In Chapter 6, we will present a theoretical treatment of multi-frequency oscillators. Nonlinear oscillators with multi-band resonator structures, under certain conditions, are capable of generating tone at distinct frequencies. A thorough analysis of one such oscillator with a dual-band resonator is carried out, providing the conditions of simultaneous multi-frequency oscillations. In the second part of this chapter, the phase-noise of negative-resistance oscillators with general resonator structures is addressed. By providing a link between the stored and dissipated energies of a network and its associated circuit parameters, useful interpretations of resonator quality factor are derived. With the aid of this analysis and the previously developed phase-noise models, dependencies of phase-noise to the resonator structure are derived. Inspired from our theoretical findings, enhanced resonators with a higher quality factor that can provide a superior oscillator phase-noise are proposed.

In Chapter 7, integrated multiple-antenna radios in phased-array configuration are investigated. A brief overview of different types of multiple-antenna systems is presented in order to demonstrate their effectiveness in high data-rate and reliable wireless communication schemes. A comparison of various architectures for such systems is followed by a practical design of an ultra high-frequency phased-array radio receiver on a conventional silicon technology. The successful implementation of this radio is achieved by a collection of innovative integrated-circuit and microwave techniques in addition to simulation, modeling, and characterization of such high-frequency designs.

The summary of the presented results as well as suggestions for future work are offered in Chapter 8.

Chapter 2

Multi-Band/Multi-Mode Radio Systems

Electromagnetic waves are used for wireless transmission of information in a variety of applications. The majority of radio transceivers are designed for a particular purpose; for example, a TV tuner converts the received electromagnetic wave into picture and sound, while a mobile phone uses these waves for wireless voice and data communications. Often, these wireless devices have different modes of operation. For instance, one can use a single radio tuner to listen to either AM or FM radio broadcast stations. The multi-standard mobile phone terminal is a more recent illustration of a *multi-mode radio*. Radio systems with different modes of operation are the subject of this chapter. After explaining the fundamental reason behind the historical application-specific radio design, motivations for evolving to multi-mode radios will be discussed. A few instances of existing multi-mode radio architectures will be followed by the discussion of the role of such systems in the future of wireless communications.

2.1 Frequency Spectrum and Narrow-Band Communications

A generic radio uses propagating electromagnetic waves in a common medium, *air*, for information transmission. Unlike copper twisted-pair wires in wireline telephony applications or a glass fiber for optical communications, air in wireless applications is not an inherently directional medium for electromagnetic waves. In other words, at any location, one could listen to all the transmitted information in all directions through the air. Without any provision, it will be virtually impossible for any radio receiver to detect its signal of interest among all the other unwanted *interfering* signals. Several users can share

the common medium for transmitting and receiving signals using any of the *multiple access* schemes such as Time-Division (TDMA), Frequency-Division (FDMA), or Code-Division (CDMA) [3].

At the same time, this common medium has to be used for numerous applications that are very dissimilar in nature. For instance, a broadcasting TV station sends a powerful signal in all directions so that the received signal quality in the entire neighborhood is sufficiently high. Meanwhile, a satellite receiver extracts its intended data of a tiny signal emitted from a distant location. Consequently, a government agency called the Federal Communications Commission, FCC, was established in 1934 and is responsible for allocating and regulating radio communications in the United States. Similar regulating agencies have been established elsewhere in the world. In order to allow different applications to coexist and function simultaneously, the frequency-spectrum has been divided into numerous narrow sectors, each allocated for a particular application. A very limited selection of FCC frequency-allocations from 1 MHz to 100 GHz is shown in Table 2.1. The distinction in the nature of these applications has resulted in various restrictions such as maximum allowable emitted power or modulation type for each of these narrow frequency bands. A number of often conflicting factors, many of them historical, economical, and political, have been considered in the frequency spectrum planning. A number of the common trade-offs considered among data rate, range, and frequency of operation are briefly described below.

Based on Shannon's theorem, the maximum data-rate of a communication channel, known as channel capacity, C , is related to the frequency bandwidth of the channel, BW , and the signal-to-noise ratio, SNR in the following manner [2]:

$$C = BW \cdot \log_2(1 + SNR) \quad (2.1)$$

As we move to higher frequencies, more bandwidth becomes available for communication. However, signal power of a propagating wave decreases rapidly with frequency [3] and lowers the overall SNR term in (2.1). Additionally, due to technological limitations, communicating at higher frequency bands has been traditionally more expensive. Even

based on the overly simplistic and limited discussion above, we can appreciate the subtlety in the planning of the frequency spectrum.

	1 MHz	1 GHz	10 GHz	100 GHz
Broadcast				
FM Radio	88-108			
Television	54-88 , 174-216 , 470-608 , 614-806			
Cellular Telephone	824-849 , 869-894			
Personal Communications				
Broadband		1.850-1.990		
Narrowband	901-902 , 930-931 , 940-941			
Unlicensed		1.910-1.930 , 2.390-2.400		
RFID (Radio ID Devices)	902-928	2.400-2.500		
Industrial, Scientific & Medical (ISM)	40.66-40.7 , 902-928	2.45-2.50 , 5.725-5.875		24-24.25 , 59-64
Unlicensed National Information Infrastructure (UNII)		5-5.35 , 5.65-5.85		
Paging and Radiotelephone Services	35 , 43 , 152 , 158 , 454-455 , 459-460 , 929-930 , 931-932			
Local Multipoint Distribution Service (LMDS)				27.5-29.5 , 31-31.3
Satellite Services				
Direct Broadcast / Direct to Home		11.7-12.2 , 12.2-12.7 , 17.3-17.7		
Digital Audio Radio Service (DARS)	2.320-2.345			
Global Positioning System (GPS)	1.215-1.240 , 1.35-1.40 , 1.559-1.610			
Vehicle Anti-Collision Radar/ Stolen Vehicle Recovery Systems	162.0125-173.2			45.5-46.9 , 76-77 , 95-100

Table 2.1: Selected portions of FCC-allocated frequency-spectra for narrow-band communications

As a result of the frequency allocation (e.g., Table 2.1), the majority of communications though air is essentially narrow-band¹ where the ratio of center frequency of the utilized band to its bandwidth is often between 100 and 10,000 (Table 2.2). In order to

communicate effectively and achieve a high performance, every radio transceiver is highly selective around a particular frequency band and rejects all the other present signals. Several radio architectures such as heterodyne, homodyne and regenerative can achieve the necessary selectivity at high frequencies. However, due to the selective nature of narrow-band communications and the distinction in specifications of various systems such as bandwidth, modulation type, power levels, etc., none of the conventional radio transceivers is capable of supporting multiple applications, simultaneously.

The issue of narrow-band radios that are able to function for multiple applications is the topic of next section.

	Channel BW (MHz)	Frequency Band (MHz)	Selectivity (f_{center} / BW)
Radio Broadcast			
AM	0.01	0.54-1.60	$\approx 54-160$
FM	0.2	88-108	≈ 500
TV Broadcast			
VHF	6	54-88 , 174-216	$\approx 10-35$
UHF	6	470-806	$\approx 80-135$
Global Positioning System			
L1 Commercial Band	2	1575	≈ 750
Cordless Phone			
DECT	0.7	1880 - 1897	≈ 2700
Mobile Phone			
PCS 1900 (GSM)	0.2	1930-1990 (Rcv)	$\approx 10,000$
IS-95 (CDMA)	1.250	1930-1990 (Rcv)	≈ 1600
Satellite Broadcast			
DirecTV	24	12,200-12,700	≈ 500

Table 2.2: Selectivity of selected narrow-band communication receiver systems

2.2 Why Multi-Band/Multi-Mode Radio?

As previously mentioned, narrow-band communication and spectrum allocation have enabled the coexistence of multiple standards and applications in an efficient fashion. Accordingly, every wireless radio is designed and optimized to operate for *a particular application* at its allocated frequency band. At the same time, oftentimes various frequency

¹ Recently, wide-band communication for low-power, short-range and high data-rate commercial applications is receiving more attention [4].

bands with distinct specifications such as modulation type and power emission ratings are allocated for *the same application*. Mobile phone communication is a common case where multiple frequency bands with a variety of specifications are used. Due to the diversity of these radio specifications at different frequency bands, a conventional mobile phone terminal can only operate under one standard at a particular frequency band. Some of today's mobile-phone standards are listed in Table 2.3, as a demonstration of this concept².

	GSM		CDMA	
	E-GSM	DCS1800 (PCS1900)	IS-95	W-CDMA
Downlink Band	925-960 MHz	1805-1880 MHz (1930-1990)	869-894 MHz (1930-1990)	2110-2170 MHz
Uplink Band	880-915 MHz	1710-1785 MHz (1850-1910)	824-849 MHz (1850-1890)	1920-1980 MHz
Channel Bandwidth	200 kHz		1.25 MHz	1.25/5/10/20 MHz
Downlink Data-Rate	22.8 kbit/s		1.2/2.4/4.8/9.6/14.4 kbit/s	2 ⁿ kbit/s (n=5..11)
Uplink Data-Rate	22.8 kbit/s		1.2/2.4/4.8/9.6/14.4 kbit/s	2 ⁿ kbit/s (n=4..10)
Modulation	GMSK		BPSK	QPSK
Multiple Access	TDMA		Direct Sequence CDMA	
Duplexing	FDD		FDD	
Maximum Output Power	30 / 33 dBm		24 dBm	23-30 dBm
GMSK: Gaussian Minimum Phase Keying		TDMA: Time Domain Multiple Access		
QPSK: Quadrature Phase Shift Keying		CDMA: Code Division Multiple Access		
BPSK: Binary Phase Shift Keying		FDD: Frequency Division Duplexing		

Table 2.3: Today's predominant mobile-phone standards

These diverse sets of standards have prompted the design and manufacturing of multi-standard mobile phone terminals. These multi-mode systems can operate at different standards in various regions of the world and eliminate the need to carry more than one phone while traveling.

² The brief description of mobile-phone standards is only to demonstrate one instance of an application with multiple designated frequency bands. These examples do not limit our general discussions and treatments of the multi-mode and multi-band wireless systems.

Perhaps the most common multi-mode system is the common household radio receiver itself, which usually receives both AM and FM broadcast signals, one at a time. In addition to radios and mobile-phones, there are other types of applications where multi-mode systems have received a lot of attention. Wireless networking is another example of numerous standards prompting the creation of multi-mode transceivers. Different aspects for wireless networking applications will be discussed in Chapter 5.

There is also an increasing interest in radio systems that support more than one application. For instance, adding wireless networking ability to the existing mobile phone terminals might be realized in the near future. Radio architectures for mobile-phones with global-positioning-system (GPS) capability have already been discussed in the literature [6]. Such multi-mode systems that *simultaneously* support various applications operating at different frequency bands are the subject of Chapter 3.

There is a subtle distinction between multi-mode and multi-band in existing publications. Multi-band systems operate for several standards occupying different frequency bands. For instance, a dual-band GSM mobile-phone usually refers to a system that can operate at 900 MHz and 1800 MHz frequency bands (refer to Table 2.3). More generally, multi-mode transceivers can function for various standards residing in the same frequency band or in disjointed ones³.

In the next section, some of the proposed and implemented transceiver architectures for multi-band systems, mostly in mobile-phone and wireless networking applications, are briefly reviewed.

2.3 A Review of Existing Multi-Mode/Multi-Band Radio Architectures

A complete radio transceiver consists of two separate paths, radio receiver and radio transmitter (Figure 2.1). In the receiver chain, the collected signal from the antenna is amplified, filtered and down-converted in frequency for reliable detection and demodulation in the following signal-processing stages. In the transmitter section, the modulated signal has to be up-converted to the appropriate radio frequency and amplified

³ A dual-mode mobile phone for DCS1800 and IS95 standards is an example of a system that supports two standards at the same frequency band (refer to Table 2.3).

before entering the antenna for proper propagation. Therefore, sections that are closer to the antenna operate at the higher frequency in the transceiver chain. In particular, the first active block in the receiver, a low-noise amplifier (LNA), increases the level of the received signal without adding a significant amount of noise. On the transmitter side, a power amplifier (PA) provides the desirable amount of signal energy to the antenna.

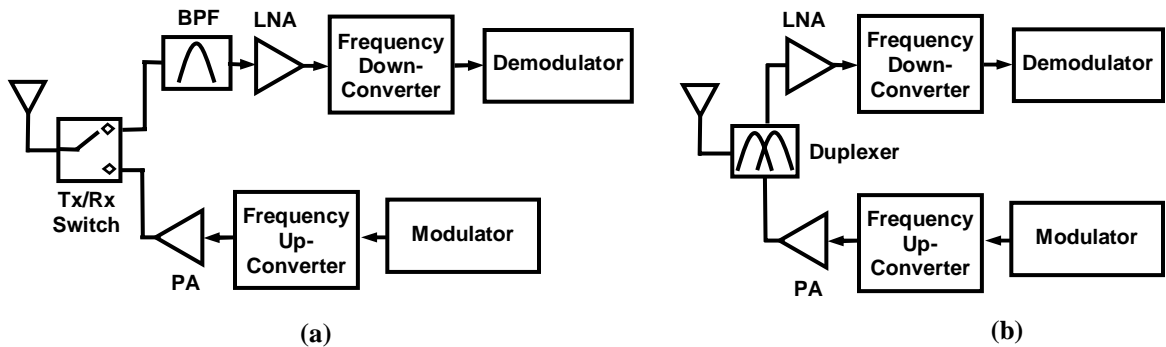


Figure 2.1: Simplified illustration of single-band radios (a) time-duplex (b) full-duplex

Regardless of the radio architecture, the connection of the transceiver's front-end to the antenna is a function of the duplexing method. Both the output of power-amplifier (PA) and the input of low-noise amplifier (LNA) have to be connected to the antenna with a high isolation between them. The isolation is required to protect the sensitive receiver front-end circuitry from the large signal levels at the PA output and to minimize the leakage of the transmitted signal energy to the receiver path. In full-duplex systems, such as CDMA standard in mobile-phones, where the receiver and transmitter are simultaneously on, bulky duplex filters that separate receive and transmit bands are usually unavoidable (Figure 2.1 b). In time-duplex schemes such as the GSM standard for mobile-phones, there is a time gap between receive and transmit frames. In these schemes, a transmit/receive (TR) switch, followed by bulky surface-acoustic-wave (SAW) filters in receiver chain in many cases, separates the antenna connection to each path (Figure 2.1 a). For multi-band systems, more duplexers, TR switches, and SAW filters are needed to accommodate all of the desired frequency bands.

2.3.1 Multi-Band Receiver Architectures

In practice, the high selectivity required in narrow-band communications (Table 2.2) can hardly be achieved with any practical filter at radio frequencies. Therefore, the desired selectivity is often achieved in multiple stages. The carrier frequency of the received signal is lowered in one or more steps allowing for filtering and demodulation at lower frequencies. In a common process known as down-conversion, the carrier frequency of a modulated signal can be reduced by multiplying (or mixing) it with a constant tone signal of a local oscillator (LO)⁴. Unfortunately, in a multiplier, the *image* of the main signal with respect to the LO frequency is down-converted along with the main signal to the same frequency causing an unwanted cross-talk (Figure 2.2). Usually, distinct receiver architectures vary in the number of down-conversion stages, the method to remove the unwanted image signal, as well as the choice of placement and value of gain and filtering stages.

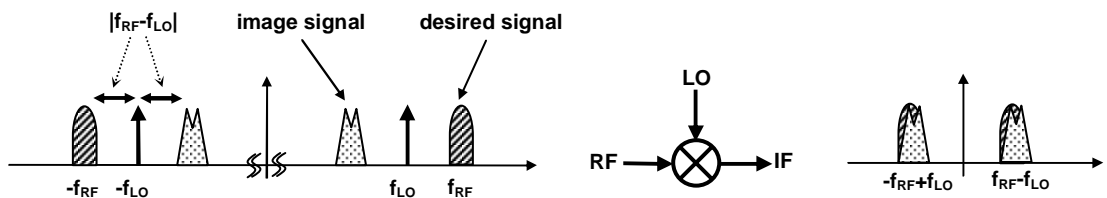


Figure 2.2: Illustration of cross-talk caused by the image signal in the receiver

Most of today's wireless receivers use any of these general architectures: heterodyne, homodyne, low-IF, and image-rejection receivers such as the ones originally proposed by Weaver [8] or Hartley [7]. Similarly, all these architectures have been employed in the multi-band receivers for various applications. In the following sections, advantages and disadvantages of each of these architectures for multi-band and multi-mode systems are briefly discussed.

⁴ Similarly, the carrier frequency can be increased in a mixing process (up-conversion).

2.3.1.1 Heterodyne Architecture

Heterodyne receivers achieve a large selectivity by down-converting the received RF signal in multiple steps (usually two), and by extensive filtering at each intermediate-frequency (IF) section before converting the analog baseband signal to a digital one for demodulation and further signal processing. Filtering at *RF* and *IF* stages is usually achieved via external SAW filters that attenuate the energy at the image frequency band for reduced cross-talk. In a multi-band heterodyne system, there will be a larger number of external image-rejection filters resulting in a larger footprint, higher power consumption, and a higher overall cost for the system. A simplified schematic of a triple-band receiver for CDMA phone standards integrated with GPS capability (quad-mode radio) that uses a heterodyne architecture is shown in Figure 2.3 ([6]).

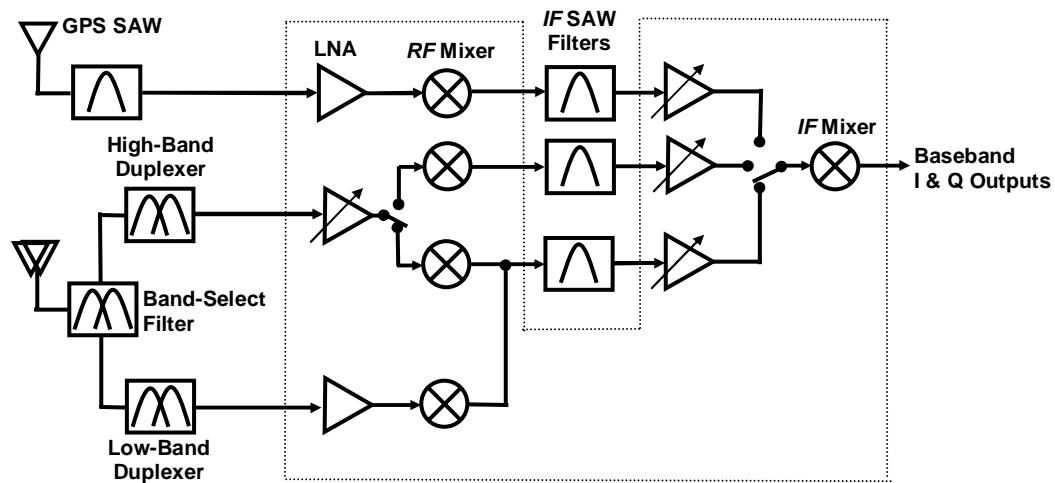


Figure 2.3: A multi-band / multi-mode receiver based on Heterodyne architecture [6]

2.3.1.2 Homodyne/Low-IF Architectures

The cross-talk caused by the image signal can also be eliminated if a pair of multipliers with in-phase and quadrature-phase LO signals are used in the down-version stage.

Homodyne (also known as zero-IF or direct-conversion) receivers perform the radio frequency down-conversion in only one step using a pair of high dynamic-range in-phase

and quadrature mixers. Image-frequency and interference rejections as well as amplitude control are performed at dc for the most part. Unfortunately, several sources of noise, including self-mixing of the LO signal due to leakage, component mismatches, and low-frequency noise of devices contribute to an undesired amount of signal energy at the zero frequency [17],[18]. A direct-conversion scheme requires extra circuitry for the removal of the so-called dc-offset signal.

The aforementioned problem of dc-offset can be eliminated in a low-IF architecture, where the received RF signal is down-converted to a very low frequency instead of zero frequency. However, low-IF architectures necessitate low-frequency building blocks such as filtering and gain stages with a higher bandwidth to further process the signal. A higher bandwidth in many of these blocks including analog-to-digital converters is usually gained at the price of larger power consumption. Final down-conversion to zero frequency that might be necessary in some of the low-IF implementations can be done at the digital domain.

Many prefer the added expense of baseband signal-processing in these systems for the benefit of reduced number of off-chip components which usually translates to a cheaper overall cost compared to heterodyne architectures. Figure 2.4 shows a simplified schematic of a quad-band mobile-phone receiver for GSM standards that uses a direct-conversion architecture [15]. Note that in-phase and quadrature-phase paths can be generated by phase shifting the *RF* signal (Figure 2.4), or more commonly, the *LO* signal [5].

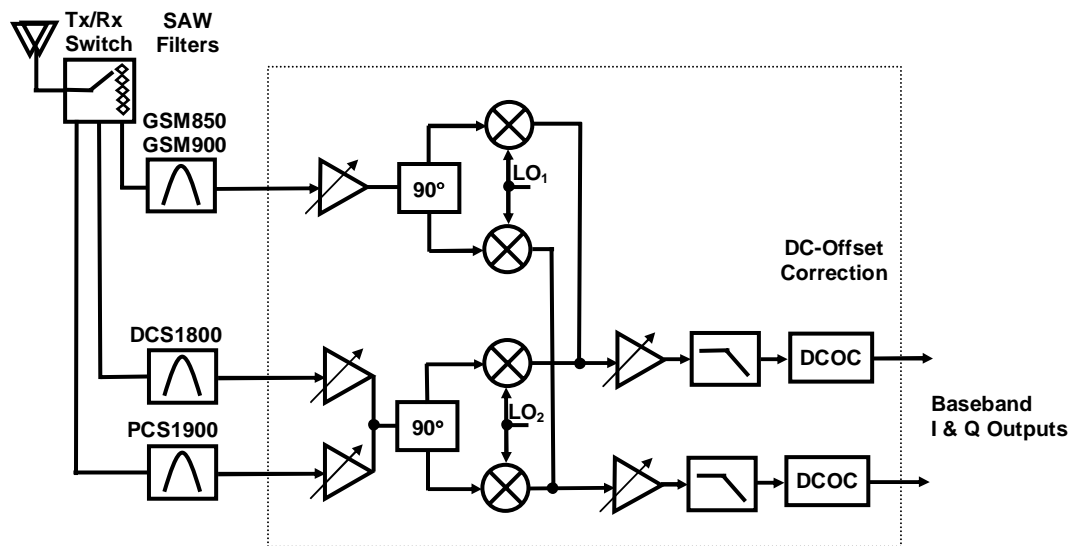


Figure 2.4: A direct-conversion multi-band receiver for mobile-phone applications [15]

2.3.1.3 Image-Reject Architectures

The required high-selectivity in most standards is achieved through bulky SAW filters in heterodyne receivers or through high dynamic-range wide-band baseband circuits in direct-conversion and low-IF architectures. Hence, architectures that select the narrow-band channel of interest while rejecting the image-frequency before baseband without the use of any *IF* SAW filters are desirable. Down-converting the *RF* signal in orthogonal phases (in-phase and quadrature) and combining the outcome constitutes the basis for image-reject architectures [7]-[8]. Usually, the image-rejection of these architectures is limited to the matching of integrated components and can be enhanced with digital calibration [16]. An example of such an image-reject receiver for a dual-band system, where clever frequency planning allows for sharing of many circuit blocks, is shown in Figure 2.5 ([9]). The propagation of the one of the desired inputs and its corresponding image signal along the receiver chain is also depicted to illustrate the image rejection principle of the Weaver down-converter.

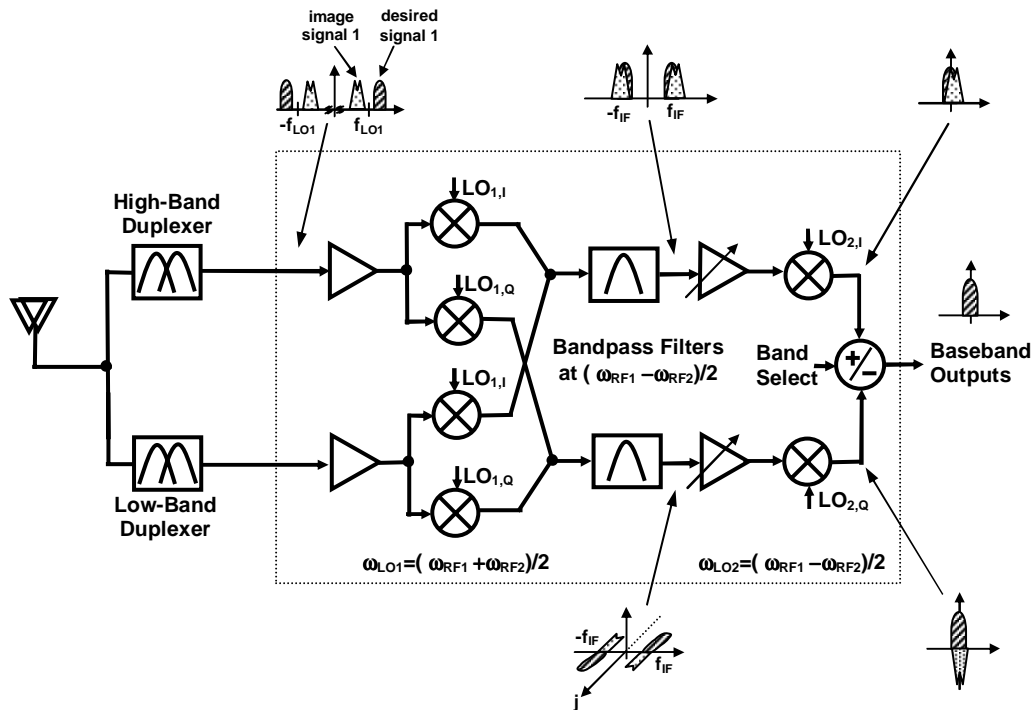


Figure 2.5: Dual-band receiver based on Weaver's image-rejection scheme [9]

2.3.2 Multi-Band Transmitter Architectures

Multi-step up-conversion (heterodyne), direct up-conversion (homodyne), and image-reject up-conversion architectures, as well as direct modulation of the transmit VCO for constant-envelope modulation signals has been used in the design of multi-band transmitters. We will briefly review these approaches in the following subsections:

2.3.2.1 Multi-Step Up-Conversion

Up-conversion of the baseband signal to an RF carrier in multiple steps allows for a more uniform distribution of gain and gain-control which, for instance, could be as large as 90dB in CDMA standards for mobile-phones, between the IF and RF stages. However, external IF filters add to the system complexity, power consumption, board area, and cost. A simplified schematic of a dual-band/tri-mode transmitter for the two CDMA standards mentioned in Table 2.3 that uses a two-step up-conversion is shown in Figure 2.6 ([10]).

Note that if different IF frequencies are chosen for each RF band as in this case, multiple off-chip filtering are used at the IF stage.

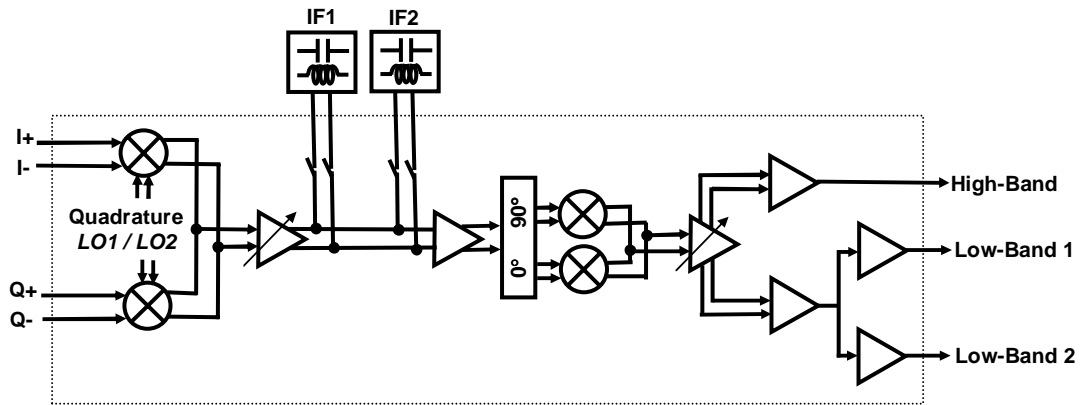


Figure 2.6: Dual-band transmitter using dual up-conversion for CDMA standards [10]

2.3.2.2 Direct Up-Conversion

Among other transmitter architectures, direct up-conversion of the baseband signal to the desired RF frequency uses the fewest number of off-chip components. Eliminating the unwanted DC-offset from up-conversion and achieving a large range of amplitude-control at RF are the design challenges in this architecture. Also if the local oscillator operates at a very close frequency to the transmitted signal band, its output frequency could be modulated or even changed (*i.e.*, frequency pulling [17]) in the presence of strong signal coming from the power amplifier output. The relatively low requirement for the gain-control in WLAN standards has led to a large number of multi-mode designs based on direct-conversion architecture [11]-[13]. The simplified schematic of a dual-band tri-mode transmitter for CDMA standards in [14] is shown in Figure 2.7.

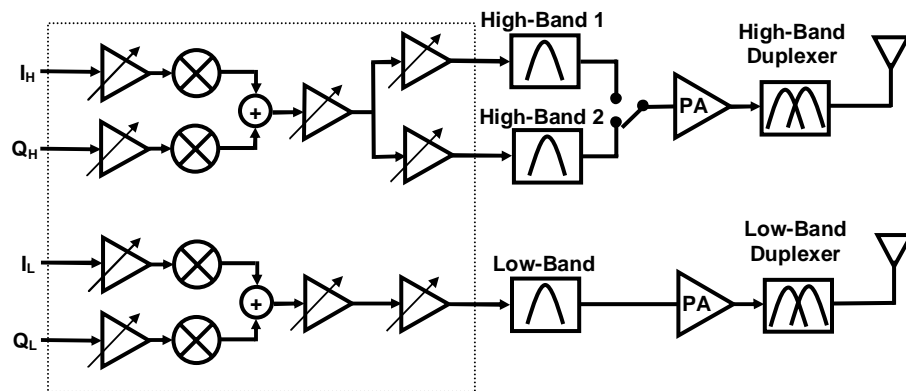


Figure 2.7: Dual-band direct-conversion transmitter for CDMA standards [14]

2.3.2.3 Up-Conversion via Direct VCO Modulation

By varying the frequency of a voltage-controlled-oscillator (VCO), we can directly up-convert the modulated baseband signal into the desired radio-frequency. The constant amplitude of the VCO output limits the use of this scheme to constant-envelope signal modulations, such as GMSK used in GSM mobile-phone standard. Moreover, due to the nonlinear control-voltage to output frequency transfer function, the baseband signal should be preconditioned prior to applying to VCO control-voltage. A feedback loop stabilizes the output frequency of VCO. A dual-band transmitter based on the direct modulation of VCO frequency in a frequency-translation loop is illustrated in Figure 2.8 ([15]).

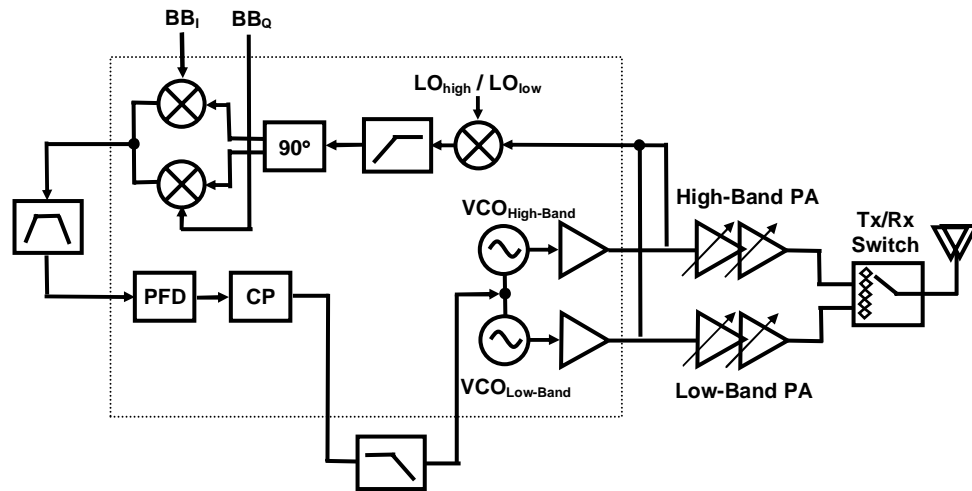


Figure 2.8: Dual-band transmitter based on direct-modulation of VCO frequency [15]

2.3.3 LO Generation in Multi-Band Transceivers

Building blocks that generate the local-oscillator (LO) signal necessary for signal up/down-conversion consume a significant portion of the overall radio area and power. Naturally, in multi-band systems a number of LO signals at different frequencies should be generated. Most multi-band architectures use a delicate frequency planning in order to share as many of the LO generation building blocks as possible.

For instance, in direct-conversion multi-band mobile-phone transceivers operating around 900 MHz and 1800 MHz frequency bands, a single oscillator in conjunction with a divide-by-two can generate both necessary LO signals [14]. Even for multi-band systems without an integer ratio of RF frequencies, a single oscillator at the proper frequency can generate all the necessary LO signals with the help of a frequency divider and multipliers [6], [15]. These added blocks eliminate the use of two separate frequency synthesizer loops that consume a substantial chip area.

2.4 Summary

Evidently, the demand for wireless terminals that can support more standards and applications is only increasing. Third generation mobile phones are due to have a multi-

band multi-mode capability that allows universal operation. Addition of other features, such as GPS, to these terminals mandates the coverage of extra frequency bands. Similarly, multiple standards and frequency bands allocated for wireless networking applications have resulted in a substantial need for multi-band multi-mode WLAN systems.

In summary, the spectrum allocation for wireless communication results in narrow-band radios optimized for a particular frequency band. Additionally, the increasing demand for terminals with more functionality requires the design of wireless systems that can operate at multiple frequency bands. Therefore, novel architectures and systems with multi-band/multi-mode features are deemed promising for high-performance communications in the future. In this chapter, we reviewed some of the existing *non-concurrent* transceiver architectures for multi-mode and multi-band systems.

Chapter 3

Concurrent Multi-Band Radio

In the previous chapter, the role of multi-band and multi-mode systems as an integral part of radio communications was demonstrated. These systems add the possibility to operate in *one* of different standards or frequency bands at any given time. In this chapter, the novel concept of concurrency is introduced for multi-band systems. Concurrent multi-band systems, by definition, are capable of *simultaneous* operation at multiple frequency bands at any given time. In this chapter we explain the benefits of such radios, followed by a few proposed transceiver architectures. Some of the novel architectures benefit from the new building blocks that will be introduced in later chapters.

3.1 Benefits of Concurrency

Simultaneous operation at multiple frequency bands in the traditional applications of *non-concurrent* multi-band radios may not appear very advantageous. After all, the mobile phone user will be using only one frequency band for his/her voice communication at any given time. However, there are numerous cases where concurrent multi-band operation is highly desirable. Some of the potential benefits of concurrent radios can be categorized as follows:

A) More Functionality

There seems to be a large demand, and in some cases mandates, to add more functionality to the existing wireless devices. One example of this is the desire to add positioning capability to the mobile phone. In fact, the FCC's wireless Enhanced 911 (E911) rules seek to improve the effectiveness of wireless 911 service by providing 911 dispatchers with a

very precise location estimation of the call, within 50 meters in most cases [19]. One method to achieve this accuracy is to integrate a Global Positioning System (GPS) capability to the mobile phones (*e.g.*, [20]). At the same time, adding an interface for connecting the device to the wireless local area networks (WLAN) for data transmission is desirable. With a concurrent radio, a person can talk on his mobile phone while data is being downloaded from the Internet to his device using the WLAN receiver and the GPS receiver maintains track of his location at any time.

B) Higher Data Rate

Simultaneous access to multiple frequency bands increases the effective bandwidth of the system and hence allows for a higher communication data rate. Imagine a concurrent receiver that supports different WLAN standards (*e.g.*, IEEE 802.11a and 802.11b). This receiver can simultaneously use channels at both frequency bands for faster communication and more flexibility⁵.

C) System Robustness

Using multiple frequency bands simultaneously not only increases the communication data-rate, but also makes the system more robust by providing additional frequency diversity. Since the wave propagation and channel fading properties at different frequency bands (*i.e.* different wavelengths) are different (*e.g.*, [3]), in case of failure at one band, an uninterrupted communication on the other band will be maintained in the concurrent radio.

D) Performance Improvement

In a few circumstances, especially in remote-sensing applications that use electromagnetic waves, more data can be collected at various wavelengths. Multi-frequency Synthetic-Aperture-Radar (SAR) and multi-band/multi-channel radiometry are examples of systems where multiple frequency bands are used to acquire more information remotely.

3.2 Concurrent Receiver Architectures

In the following sections a few potential concurrent transceiver architectures are studied. On the receiver side, desirable architectures are those with a smaller chip area and/or

⁵ It is already assumed that the environment in our hypothetical case does support both standards and channels at both frequency bands for our single user. Just recently, single wireless network access points that can simultaneously support multiple standards at 2.4GHz and 5.2GHz have been introduced to the market [40].

consume less battery power. It is worth mentioning that in the following description of various concurrent transceiver architectures, only signal-path designs are presented. As discussed in the previous chapter, a proper frequency planning can be applied to most of these architectures to reuse some of the resources (*e.g.*, frequency synthesizers) in LO-generation sections.

3.2.1 Parallel Single-Band Receivers

Probably the most trivial solution for a concurrent multi-band receiver is to have a number of single-band receivers in parallel and use each for one particular frequency band. Figure 3.1 shows examples of the aforementioned implementation where each single-band receiver is using a standard heterodyne architecture in (a), and direct down-conversion architecture in (b). More generally, different architectures for each of the parallel receivers can be conceived.

Despite the fact that this scheme is general and can be expanded to any number of frequency bands, it is not the most efficient architecture. Later, we will show architectures that share the valuable resources (*i.e.*, battery power, chip area) by introducing novel and unconventional building blocks.

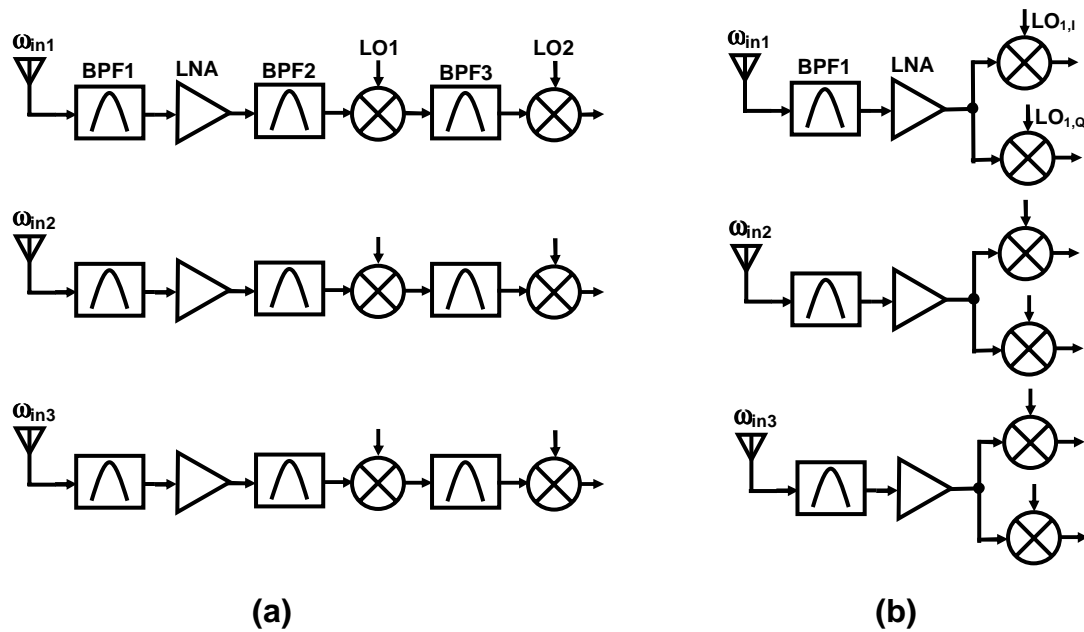


Figure 3.1: Concurrent receiver implementations using multiple parallel single-band receivers in (a) heterodyne (b) direct down-conversion architectures

3.2.2 Parallel Receivers with a Wide-Band Front-End

A receiver with a wide-band front-end consisting of an antenna and low-noise amplifier (LNA) that can collect signal power at a large range of frequencies followed by appropriate down-converters can be used to receive any number of frequency bands within that range. In Figure 3.2, a broadband front-end is followed by separate down-conversion paths for each frequency band. This scheme might have some advantage in terms of chip area and/or power consumption over the previous method, depending on the implementations of wide-band LNA⁶. The direct down-conversion architecture of Figure 3.2 (b) is fairly versatile in that by controlling the local oscillator frequency, the operation bands of the concurrent receiver can be varied.

Broadband front-end nevertheless suffers from a serious shortcoming: it not only receives the frequency bands of interest, but also all the other undesirable frequencies get amplified by it. These unwanted signals might have a large signal power and can potentially

⁶ It is also noteworthy that normally antenna size increases with its bandwidth.

limit the dynamic range of the receiver due to the nonlinearities inherent to any implementation.

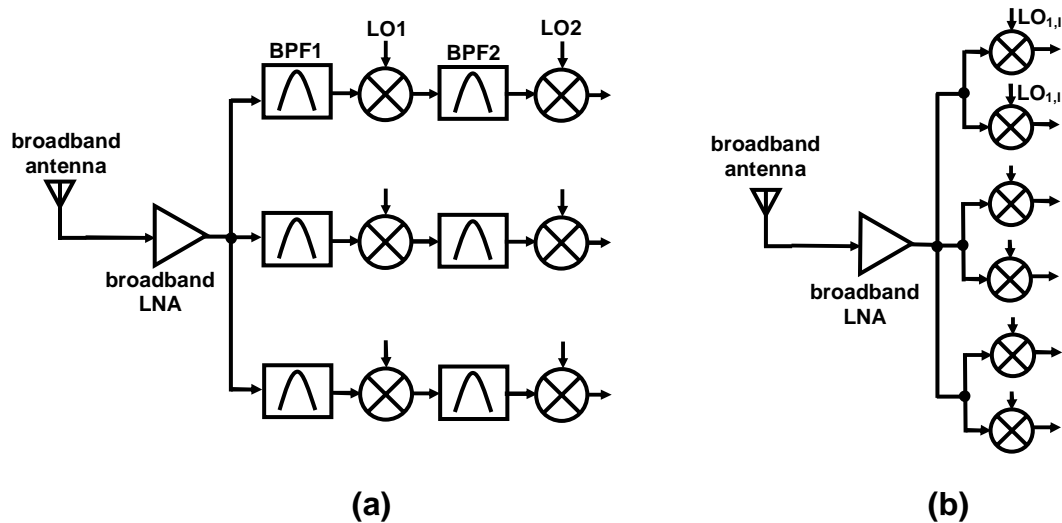


Figure 3.2: Concurrent receiver implementation using a wide-band front-end in (a) heterodyne (b) direct down-conversion architectures

3.2.3 Parallel Receivers with a Multi-Band Front-End

The shortcoming of the previous architecture can be improved by replacing the wide-band front-end with one that has a multiple narrow-band response at frequency bands of interest (Figure 3.3). This multi-band front-end consists of a multi-band antenna (*e.g.*, [28]-[30]), followed by a multi-band filter (*e.g.*, [31]) and a concurrent multi-band LNA that provides simultaneous gain and matching with a low added noise at multiple frequency bands [26]. More discussions on the design of a concurrent multi-band front-end will be provided in section 3.3.

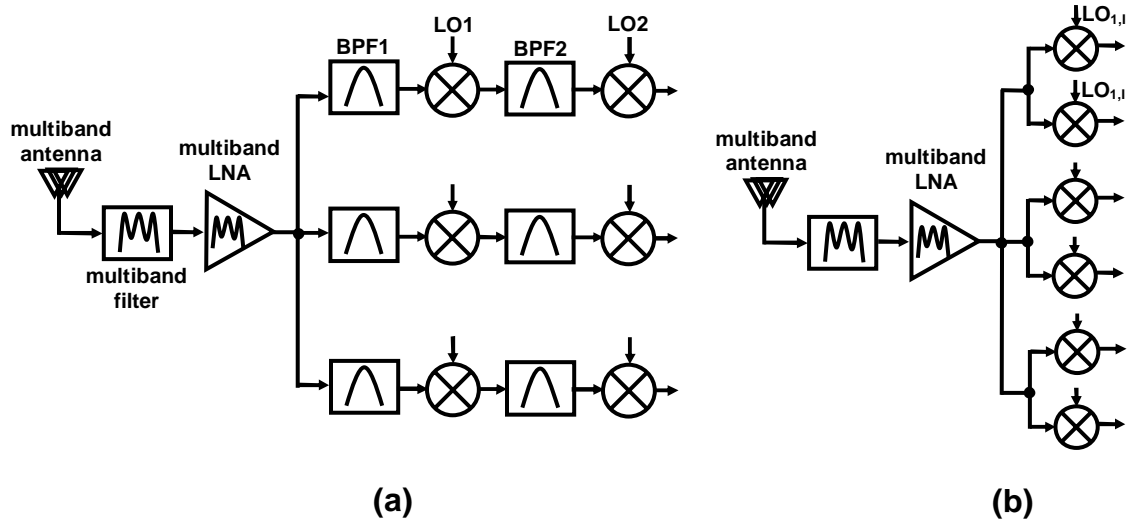


Figure 3.3: Concurrent receiver implementation using a multi-band front-end in (a) heterodyne (b) direct down-conversion architectures

3.2.4 Multi-Band Sub-Sampling Receiver

According to Shannon's original statement of sampling theorem, any signal that contains no frequencies higher than BW [Hz] can be completely determined by discrete samples of the signal spaced $(1/2 BW)$ [sec] apart [21]. Sampling of band-limited signals has been extended to bandpass signals that have energy in the frequency interval (f_L, f_U) where $BW=f_U-f_L$ [22]. The classical bandpass theorem for uniform sampling states that the signal can be reconstructed if the sampling rate is at least $f_s^{(\min)}=2f_U/n$, where n is the largest integer within f_U/BW . A graphical representation of bandpass sampling in the frequency domain can be seen in Figure 3.4. In the frequency domain, the effect of uniform sampling is equal to repeatedly shifting the signal by integer multiples of the sampling rate, f_s . If these shifted versions of the signal can not be superimposed on one another, the original signal can be recovered easily with appropriate filtering. Using this graphical representation, the aforementioned condition for permissible sampling rates can be derived. There are two important observations in the bandpass sampling scheme. First, note that the sampling rate can be much lower than the center frequency of the signal. Second, we not only can recover the signal in its original form by filtering at the correct center frequency,

but also can filter any other replica of the signal and effectively shift the center frequency of the signal without disturbing its frequency contents. This point has instigated schemes that use the so-called sub-sampling to down-convert the RF signal to a lower frequency [23],[24]. Subsampling receivers traditionally have a good linearity performance, but have the disadvantage of noise-folding and hence a lower SNR at the output. As shown in Figure 3.4, both the signal and the wide-band background noise are shifted several times, the latter resulting in an increased total in-band background noise. Filtering the bandpass signal prior to sampling can lower the noise and increase the receiver sensitivity.

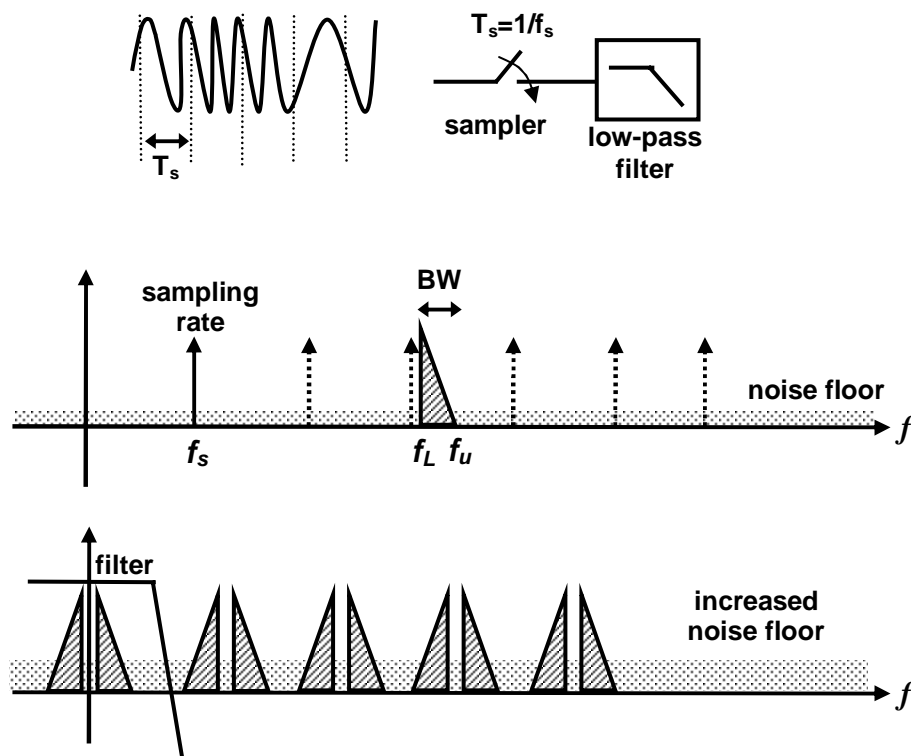


Figure 3.4: Frequency domain representation of down-conversion using bandpass subsampling

Bandpass subsampling can be further expanded to bandpass signals. Similar to the previous case, expressions for permissible sampling rates can be derived (*e.g.*, [25]). Once again, Figure 3.5 shows the essence of this concept without any mathematical details and can be used to find the allowable rates for any set of discrete signals. In practice, the frequency bands of interest might not have the same bandwidth and most likely are not equally spaced

in frequency domain. This may result in very low sampling rates which will consequently increase in-band noise due to noise-folding. Therefore, a multi-band filtering scheme is desired at the front-end to limit the effect of out-of-band noise. Additionally, using the multi-band filtering instead of a wide-band front-end is required to reduce the undesirable interferences that limit the dynamic range of the receiver as previously discussed.

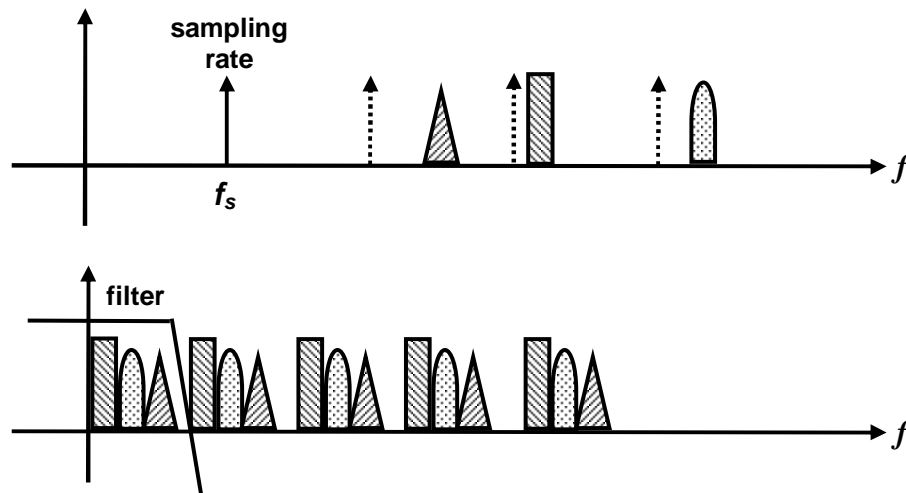


Figure 3.5: Frequency domain representation of multi-band subsampling

3.2.5 Direct Digitization (Digital Radio)

Most modern wireless radio receivers down-convert the input RF signal to a lower frequency (intermediate frequency, IF, or baseband) and then convert the low-frequency analog signal to a digital one for further processing. With the rapid improvement in device technology providing faster, smaller, and cheaper active elements, digital circuits are now capable of operating at GHz range frequencies. Hence, there is a large interest in moving the analog-to-digital conversion to higher frequencies (Figure 3.6). Versatile digital circuitry can then process the high-frequency signal (*e.g.*, filter, demodulate). Ideally, such a digital processor can be programmed to process signals at different frequency bands and standards (software defined radio), as well as multi-band signal structures. In theory, direct digitization of a radio-frequency signal is an intriguing idea, but there are extremely difficult challenges in practice with the current technologies. High resolution analog-to-

digital converters (ADC) that can operate at multiple Gsamples/sec range with the tough dynamic-range requirements of radio standards are still not on the horizon for implementation. At the same time, the dynamic-range of these ADCs usually comes at the price of increased power consumption. As power consumption of digital circuitry increases in proportion to the frequency of operation, justifying the direct digitization for low-power portable radio receivers becomes more difficult. Upon availability of the desired ADC, the clear advantages of such implementations in the future are their performance scaling with technology improvements, ideally automated and faster design cycles, programmability, and extreme versatility in architectures and applications. In the following section we introduce an alternative approach that does not suffer from these deficiencies.

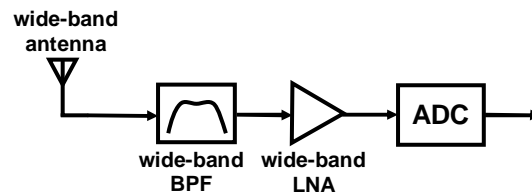


Figure 3.6: Generic architecture of a direct digitization radio

3.3 A Concurrent Dual-Band Receiver

In this section, a new concurrent dual-band receiver architecture is introduced which is capable of simultaneous operation at two-different frequencies without dissipating twice as much power or a significant increase in cost and footprint [26]. The concurrent operation is realized through an elaborate frequency conversion scheme in conjunction with a novel concurrent dual-band low noise amplifier (LNA). These new concurrent multi-band LNAs provide simultaneous narrow-band input matching and gain at multiple frequency bands, while maintaining low noise. Figure 3.7 illustrates the conceptual evolution of a dual-band receiver, starting with two totally independent heterodyne receiving paths, and leading to an efficient concurrent dual-band receiver.

The first gain stage in a concurrent dual-band receiver is its LNA. Traditional single-band LNAs use a single or cascode transistor stage to provide wide-band transconductance

and combine it with proper passive resonant circuitry at the input and output, as discussed briefly in the previous section. This approach shapes the frequency response, ensures stability, and achieves gain and matching at the single band of interest [27].

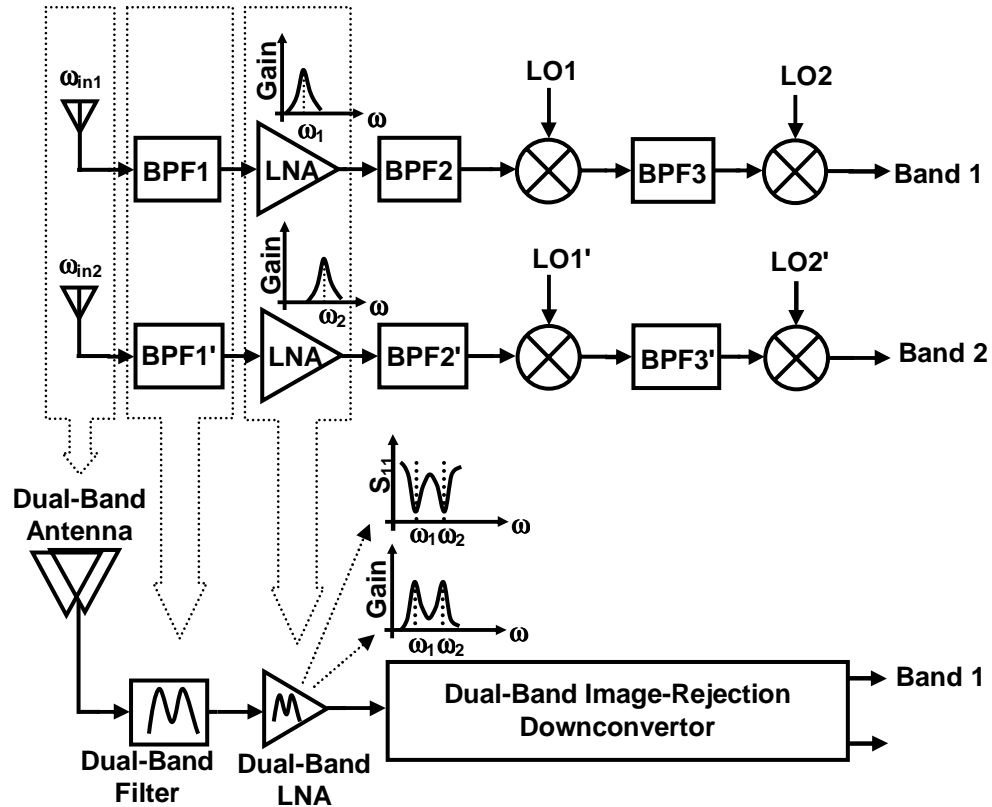


Figure 3.7: Evolution process of two parallel receivers to a concurrent dual-band receiver

A very important observation is that the transconductance of the transistor is inherently wide-band and can be used to provide small-signal gain and matching at other frequencies without any penalty in the power dissipation. This leads to a compact and efficient front-end for a concurrent dual-band receiver which consists of a dual-band antenna [28]-[30], followed by a monolithic dual-band filter [31] and a concurrent dual-band LNA that provides simultaneous gain and matching at two bands. This is illustrated in the lower part of Figure 3.7. A detailed approach to the design and analysis of such a multi-band LNA will be described in Chapter 4. It should be noted that the concurrent dual-band receiver does not use any dual-band switch [32] or diplexer [33], since simultaneous reception at both

bands is desired. A dual-band down-conversion scheme is subsequently needed to translate different information-carrying signals to baseband with as few local oscillators (LO) and external filters as possible, while maintaining isolation between the two bands. This can be achieved in numerous ways (*e.g.*, heterodyne, homodyne). Figure 3.8 shows a simplified block diagram of one such receiver that evolves from the single-band image-reject architecture proposed by Weaver [34].

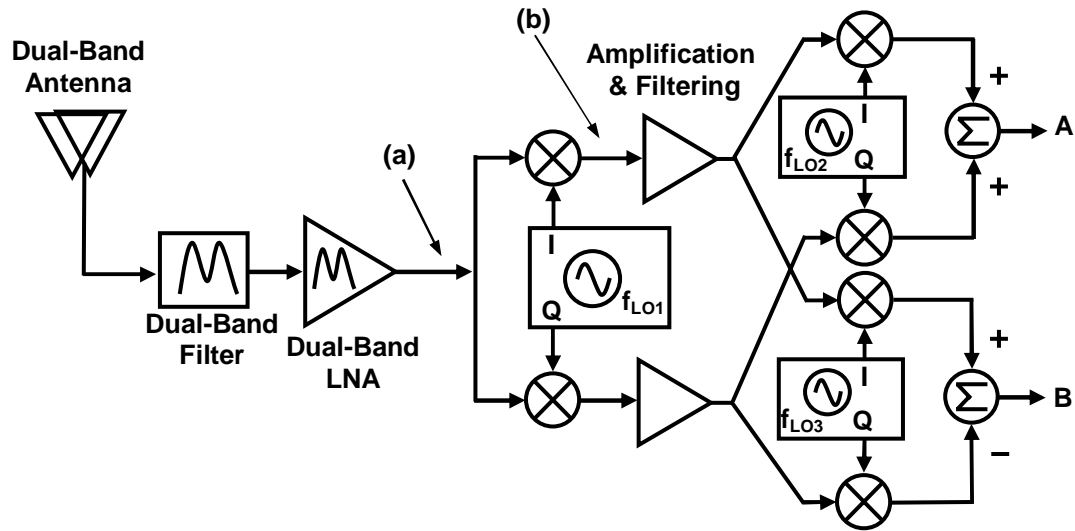


Figure 3.8: Concurrent dual-band receiver architecture

The frequency of the first local oscillator (LO) that appears after the LNA and performs the first down-conversion determines the image frequency(ies) and plays an important role in the performance of the system. For a *non-concurrent* receiver, it has been proposed to choose the first LO frequency halfway between the two frequency bands and select the band of interest by choosing the appropriate sideband produced by an image-separation mixer [9]. Although this method is sufficient for the non-concurrent approaches, it will suffer from serious shortcomings if used for a *concurrent* receiver, where the LNA amplifies the signal in both of the desired bands. This is due to the fact that one band is the image of the other and there is no attenuation of the image by either the antenna or the filter. The situation is exacerbated by the LNA gain in the image band. In this scenario, one is solely relying on the image rejection of the single sideband receiver, which is limited by

the phase and amplitude mismatch of the quadrature LOs and the signal paths [35],[36], and is usually insufficient in a concurrent receiver.

An alternative approach, which does not suffer from the above problem and in fact significantly improves the image rejection, is to use an offset LO, as shown in Figure 3.9. The LO frequency is offset from the midpoint of the two bands of interest (f_A and f_B) in such a way that the image of the first band at f_A falls at the notch of the front-end transfer function at f_{IA} . The attenuation at f_{IA} is determined by the compounded attenuation of the dual-band antenna, filter, and LNA. Similarly, the image of the second band at f_B will fall outside the pass-band of the front-end at f_{IB} and will be attenuated accordingly. Using a quadrature first LO makes the stage fit to act as the first half of any single-sideband image-reject architecture, similar to that proposed by Weaver [34]. Since the receiver has to demodulate two bands concurrently and independently, two separate paths *must* be used eventually. Each path is comprised of the second half of the image reject architecture, as shown Figure 3.8, which provides further image rejection (Figure 3.9). This architecture eliminates an extra antenna, a front-end filter, an LNA, and a pair of high-frequency mixers, which in turn results in power, footprint, and area savings. In addition, large image rejection in excess of that of the single-sideband receiver is achieved through this diligent frequency planning and proper usage of stop-band attenuation. A concurrent dual-band receiver based on this proposed architecture is implemented and will be discussed in detail in Chapter 5.

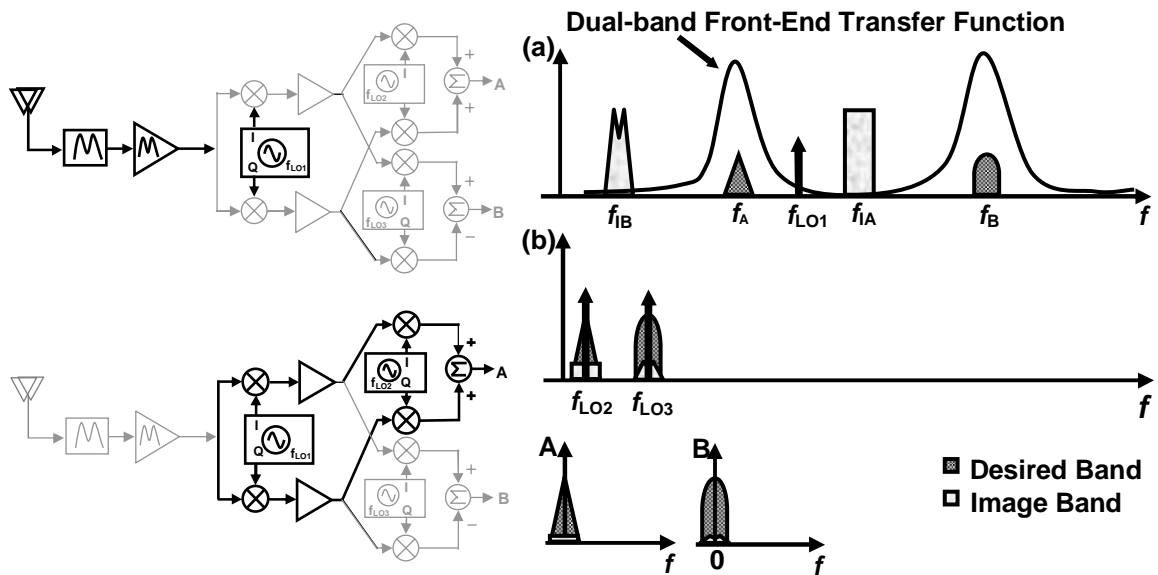


Figure 3.9: Operation principle of the proposed concurrent dual-band receiver in frequency domain

3.4 Concurrent Transmitter Architectures

Concurrent transmission at multiple frequency bands is very different from the receiver case, both in definition and in implementation. From the definition point of view, there are two possibilities. The first is to send the same signal over multiple frequency bands to achieve frequency diversity. The second scenario is to send different data over multiple frequency bands. Transmitter architectures can vary drastically depending on the aforementioned situations. It should also be noted that in the majority of standards, the overall power consumption of the transmitter is dominated by the power-amplifier (PA) efficiency and output power. In future chapters we will argue that unlike a concurrent low-noise amplifier, a concurrent multi-band power-amplifier does not offer major savings in power consumption. Hence, the most desirable feature in concurrent architectures is chip area savings and package size reduction. Additionally, concurrent multi-band transmitters face important questions concerning linearity and undesired cross-band intermodulation products. We will elaborate on these issues in Section 0 and Chapter 4.

The transmitter architecture for each of these scenarios in a dual-band case is proposed in the following sections and is subject to further investigation for future implementations.

3.4.1 Scenario 1: Same Data for All Frequency Bands

In some instances, data is transmitted simultaneously at multiple frequency bands for more reliable communication due to the added frequency diversity⁷. In such systems, the same baseband signal has to be up-converted to two higher frequency bands at the same time.

In this case, two-step up-conversion schemes are usually advantageous over homodyne solutions due to their immunity to frequency pulling and LO leakage to the output. As mentioned in Section 3.3, by placing the first LO in the middle of frequency bands, the two desired bands become the image of each other. With the second LO at the average frequency of the two bands, both baseband signals will now be up-converted to the desired location (Figure 3.10).

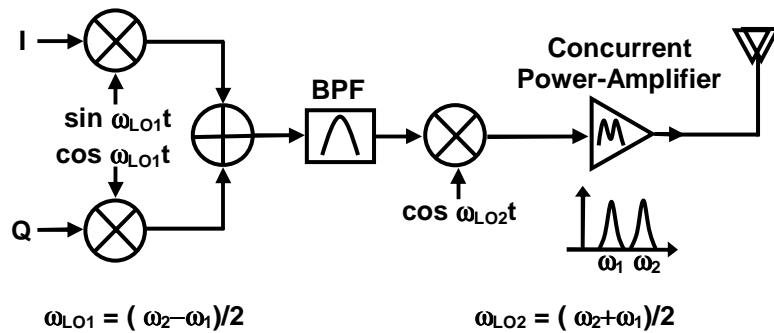


Figure 3.10: Proposed concurrent dual-band transmitter in scenario 1

At this stage, a concurrent dual-band power amplifier is required to submit the large-amplitude signal to the dual-band antenna for propagation. As will be briefly discussed in Chapter 4, the design of such a block is completely different from the design of concurrent LNA that mainly deals with signals with relatively smaller amplitude.

⁷ The added reliability gained by frequency diversity comes at the expense of precious frequency spectrum. Hence, frequency diversity is only foreseeable in rare instances such as ultra-reliable satellite or military communications [3].

3.4.2 Scenario 2: Different Data for Each Frequency Band

In most commercial cases, it is likely to have situations in which different data has to be transmitted simultaneously at different frequency bands. Transmitting voice and data at two different bands is just one example of such a case.

We can exploit the same frequency planning scheme as before in a two-step up-conversion of data to the two desired frequency bands. As before, LO generating frequency synthesizers are shared in both transmitter paths. If a concurrent dual-band power amplifier is available, signal powers at the two frequency bands can be combined and fed to a single concurrent PA (Figure 3.11).

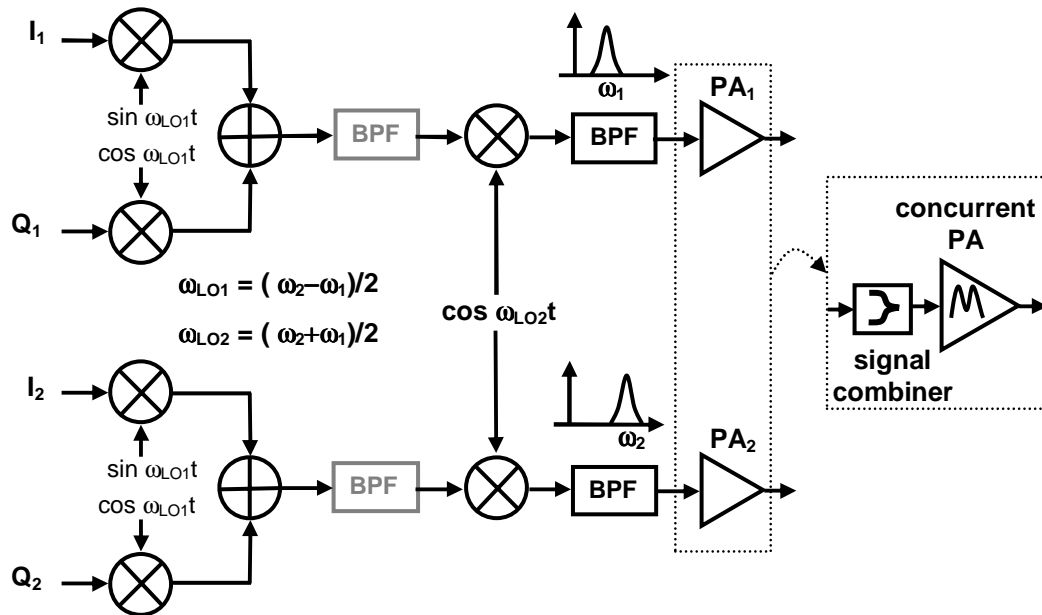


Figure 3.11: Proposed concurrent dual-band transmitter in scenario 2

The design and implementation of concurrent multi-band transmitters is an open area for future investigations. In the next section, we will discuss some of the limitations of concurrent multi-band designs and will define new metrics to quantify those adverse effects.

3.5 Adverse Effects and New Metrics in Concurrent Radios

The new concept of concurrency in multi-band radios result in additional concerns and constraints in the design of these systems. Some of these issues, such as chip area and power consumption savings are architecture dependent; however, the issues that deal with the presence of more signal tones in the radio chain are more fundamental and have to be dealt with in a systematic manner. Therefore, new metrics to characterize these issues are defined in this section.

Most of the new concerns in the design of concurrent radios trace back into linearity issues of active devices. Linearity is an important measure in the receiver as it determines the size of the largest signal that can be handled by the receiver and controls its dynamic range. At the same time, nonlinearities in the transmitter causes the generation of out-of-band signals, a phenomenon referred to as spectral regrowth. Leakage of the transmitted signal into neighboring frequencies limits the sensitivity of other receivers intending to use those frequencies and hence is strongly prohibited by the FCC.

The linearity of single-band radio blocks such as amplifiers is often described using its n^{th} order intercept point, IP_n , and 1-dB compression point, $CP1$. By definition, $CP1$ is the signal power at which the small-signal gain drops by 1dB from its small-signal value. Another adverse effect caused by nonlinearity in radio systems is the intermodulation between different frequencies. If tones at different frequencies are applied to the input of a nonlinear block, multiple tones with linear combinations of input frequencies will appear at the output. With certain nonlinearities and input tones, these unwanted intermodulation terms appear at the frequency band of interest and lower the performance of the receiver. For instance, the output of a system with a 3rd order nonlinearity given two input tones at ω_1 and ω_2 includes tones at $3\omega_1$, $3\omega_2$, $2\omega_1 \pm \omega_2$, $\omega_1 \pm 2\omega_2$. For close ω_1 and ω_2 , the latter two nonlinear terms appear very close to the input tones. By definition, a third-order intercept point, $IP3$, is the signal power at which these nonlinear terms at $2\omega_1 - \omega_2$ and $\omega_1 - 2\omega_2$ have the same magnitude as the linear terms at ω_1 and ω_2 . In a concurrent multi-band radio, the $IP3$ and $CP1$ in each band with no significant signal in the other bands are still important and will be referred to as $IP3_{inband}$ and $CP1_{inband}$, respectively. However, due to the concurrent multi-band nature of the radio, other non-linearity measures should also be

considered. A strong signal in any band can compress the gain at all frequencies. A *cross-band* compression measure can be defined as the signal power in band *A* that causes a 1 dB drop in the gain in band *B* compared to its small-signal value which will be denoted as $CP1_{A>B}$ (Figure 3.12). In addition to this cross-band compression, in-band signals from different desired bands can mix due to non-linearity and cause in-band undesired signals, as shown in Figure 3.13. We denote the input intercept point associated with this cross-band intermodulation as $IPn_{\text{crossband}}$, where n is the order of non-linearity leading to this effect. We will use these measures to characterize the concurrent LNA designs in Chapter 4.

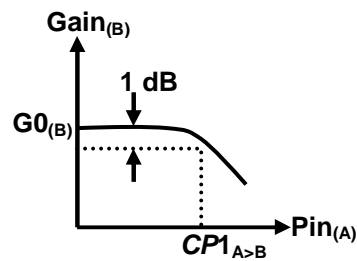


Figure 3.12: Depiction of cross-band compression

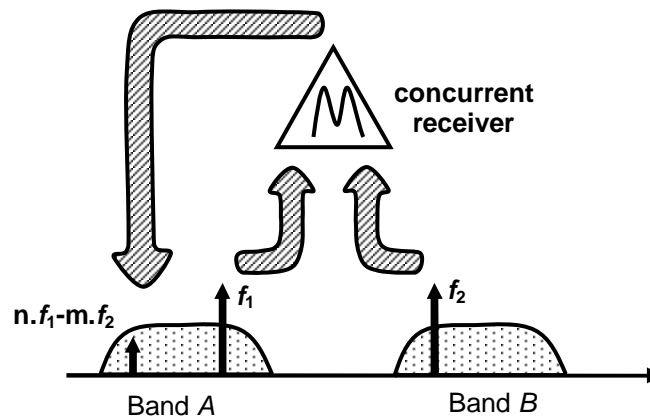


Figure 3.13: Depiction of $(n+m)$ order cross-band intermodulation

Another adverse effect in the concurrent radio is the intermodulation of desired signals with local oscillator phase-noise. An ideal oscillator is expected to generate power at only the oscillation frequency and possibly its harmonics. However, due to the presence of noise

in oscillator core, the output spectrum of any real oscillator shows signal power at frequencies around the oscillation frequency as well. As a result, the oscillator output shows noise skirts around oscillation frequency until it reaches a constant noise floor [39]. In the mixing process, the input signal is convolved with the local-oscillator signal and is down- or up-converted to a desired frequency band. More signals can be down- or up-converted to the same frequency band due to the convolution of undesired frequency bands with the non-ideal oscillator power spectrum (Figure 3.14). Blocking requirements specified by the standard usually set the spectral mask for local oscillator phase-noise performance in single-band receivers.

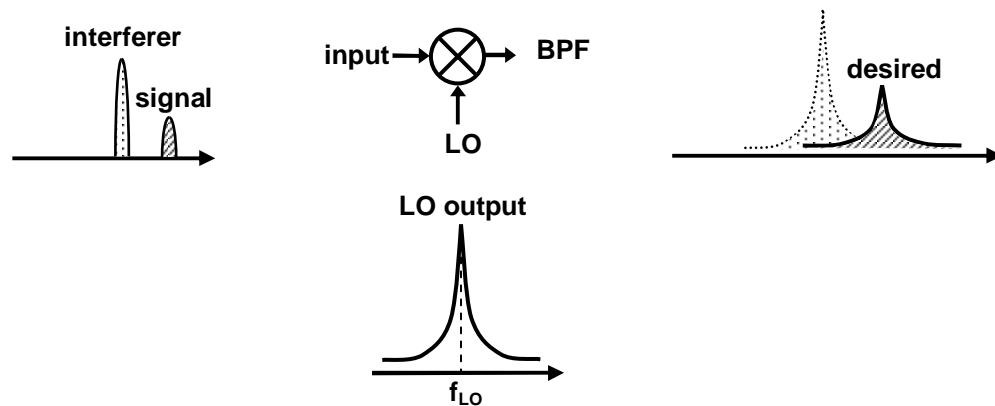


Figure 3.14: Illustration of reciprocal mixing caused by local oscillator phase-noise

In case of a multi-band signal at the mixer input, reciprocal mixing causes an unwanted leakage of all the input frequency bands to the intended down- or up-converted frequency for each of them (Figure 3.14). Hence, a large signal at one of the frequency bands can deteriorate the reception of a weak signal at another frequency band. In a concurrent dual-band receiver intended for mobile-phone and GPS applications, the mobile-phone received signal can dominate the GPS received signal by more than 110dB. A more positive point is that in almost all practical cases, frequency bands of interest are separated enough, so that reciprocal mixing is caused by noise floor of local-oscillator spectra. This noise floor should be minimized by careful design of a low-noise PLL and its subsequent LO buffers/drivers.

3.6 Summary

We introduced the novel concept of concurrent operation of multi-band radios that could constitute a significant portion of future wireless communication. In this chapter, several practical architectures for these radios, including some that use novel building blocks, were shown and their related issues were discussed.

Chapter 4

Concurrent Multi-Band Amplifiers

The diverse range of modern wireless applications necessitates communication systems with more bandwidth and flexibility. More recently, dual-band transceivers have been introduced to increase the functionality of such communication systems by switching between two different bands to receive one band at a time [9],[41]-[43]. While switching between bands improves the receiver's versatility (*e.g.*, in multi-band mobile phones), it is not sufficient in the case of a multi-functionality transceiver where more than one band needs to be received simultaneously (*e.g.*, a multi-band mobile phone with a global positioning system, GPS, receiver and a Bluetooth interface).

Radio architectures capable of simultaneous operation at multiple frequency bands were discussed in Chapter 3. It was shown that thanks to novel building blocks such as concurrent multi-band amplifiers, it is possible to design compact transceiver with minimal overhead for simultaneous operation. The concurrent multi-band low-noise amplifiers provide simultaneous narrow-band input matching and gain at multiple frequency bands, while maintaining a low noise level. Multi-band power-amplifiers can significantly reduce the active die area and hence reduce the cost. The theory and design of such concurrent multi-band amplifiers is the subject of this chapter.

Section 4.1 reviews the current advances of single-band LNAs from technological and architectural points of view. After a brief review of existing non-concurrent multi-band amplifiers, the general design methodology of concurrent multi-band LNAs with design examples and experimental implementations are described in Section 4.2. Multi-band

power-amplifiers are briefly addressed in Section 4.2.2.2 followed by the summary in the final section.

4.1 A Review of Single-Band LNA Design Issues

Being the first active element in the receiver chain, the noise figure, NF , of an LNA plays a significant role in the overall NF of the receiver, which controls its sensitivity and output signal-to-noise ratio (SNR) [46]. Before exploring the design details of concurrent multi-band LNAs, it is helpful to review some of the existing technological and topological choices for single-band LNAs.

4.1.1 Technology

The bipolar junction transistor was the first solid-state active device to provide practical gain and noise figure at microwave frequencies [47]. In the seventies, breakthroughs in the development of field-effect transistors (FET) (*e.g.*, GaAs MESFET), led to higher gain and lower NF than bipolar transistors for the frequencies in the range of several gigahertz [48]. Currently, advanced FETs and bipolar transistors still compete for lower NF and higher gain at frequencies in excess of 100 gigahertz. Examples are the high-electron-mobility-transistors (HEMT), such as Pseudomorphic-HEMT (PHEMT) [49], Metamorphic-HEMT (MHEMT) [50], as well as heterojunction-bipolar-transistors (HBT) [51] [52], built using a variety of semiconductor materials (*e.g.*, GaAs, InP, Si, and SiGe).

Traditionally, low-noise amplifiers at high frequencies have been made using transistors with high electron-mobility and high saturation velocity on high-resistivity substrates for the following principal reasons:

- 1) Higher carrier mobility and peak drift velocity result in a higher transistor transconductance and shorter carrier transit time [48] for a given current. Thus allowing for the reduction of the dc current for the same transconductance (gain) in transistors which lowers the input-referred noise and hence the NF . This gives compound semiconductors a significant advantage over silicon, as for instance, the electron mobility and the peak drift velocity are typically six and two times larger, respectively, for GaAs when compared to silicon [48].

- 2) Higher carrier mobility also results in lower parasitic drain and source series resistors. The parasitic source resistance can be a major contributor to the overall noise figure of certain low noise amplifiers, such as those used for satellite communications.
- 3) Due to mostly technological limitations, the series input resistance of silicon-based transistors is usually higher than those of compound semiconductors. In particular, the lower resistance of the metal gate of GaAs MESFETs compared to higher resistance of the poly-silicon gate in MOSFETs and thin bases in bipolar transistors, result in a lower NF for GaAs transistors.
- 4) The loss properties of on-chip passive components can have a significant effect on the noise and gain performance of the LNAs. High resistivity substrates minimize the substrate loss components. As the loss and noise are closely related through the fluctuation-dissipation theorem of statistical physics [53] [54], the energy loss reduction translates to a lower noise figure for the amplifier.

Despite the abovementioned limitations of silicon technologies, several silicon low-noise amplifiers have been reported. Meyer, *et al.*, reported one of the early low-noise amplifiers made on a low resistivity (*i.e.*, lossy) silicon substrate using bipolar junction transistors for commercial cellular applications [55], where very low NF is not needed. Recently, a large number of efforts have been reported to use the advanced digital CMOS processes for single-chip implementation of the complete radio transceiver [55] [56] [57]. Significant progress in CMOS LNA design has been made during the last several years where more recent results, such as [58] demonstrate significant improvements over the earlier works [59] [60] [61] and show that CMOS LNAs can be a worthy competitor for compound semiconductor implementations in many portable applications.

4.1.2 Topology

Although several different topologies have been proposed to implement LNAs, we will only focus on two most common single-stage⁸ LNAs in CMOS processes, namely, the common-gate topology [60] and inductively-degenerated common-source stage [62] [61] shown in Figure 4.1.

⁸ This discussion is also valid for the first stage of multi-stage LNAs.

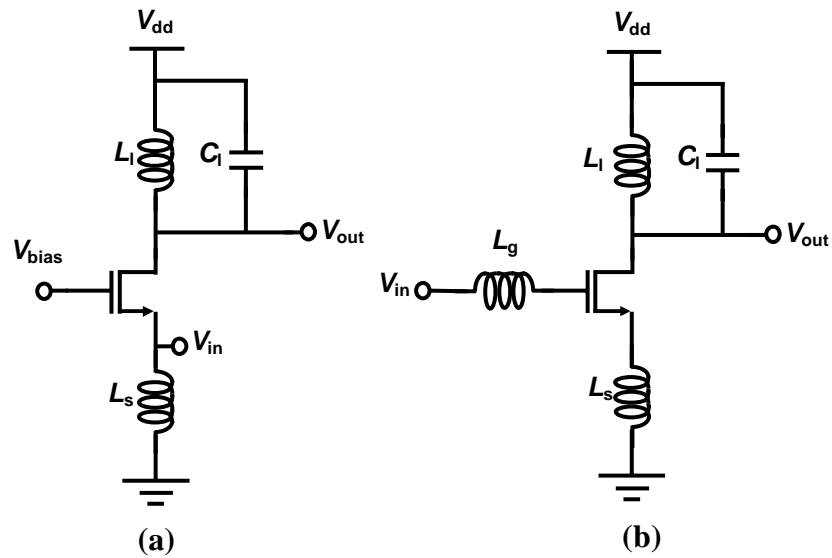


Figure 4.1: Commonly used single-band CMOS LNAs (a) common-gate (b) common-source with inductive degeneration

The common-gate configuration uses the resistive part of the impedance looking into the source of the transistor to match the input to a well-defined source impedance (*e.g.*, 50Ω). This impedance is $1/(g_m+g_{mb})$ in the case of a MOSFET, where g_m and g_{mb} are transconductances of the top-gate and back-gate transistors, respectively. However, it can be shown that the NF is lower bounded to 2.2 dB for a perfectly matched long-channel CMOS transistor [60] unless a transformer is used at the input [63].

In a common-source LNA, inductive degeneration is used to generate the real part of the input impedance needed to match the LNA input to the preceding antenna or filter. Strutt and Van der Ziel first noticed that inductive degeneration can enhance the output signal-to-noise ratio [64]. The ideal lossless inductive feedback moves the source impedance for optimum noise figure towards the optimum power match with a minor increase in the minimum noise figure [65]. Unfortunately, in silicon implementations the loss associated with inductors will degrade the NF . It should be mentioned that in these cases, cascode configuration can be used to enhance the stability and reverse-isolation of the amplifier.

While the problem of achieving the lowest noise in an amplifier has been solved for a general case through a mathematical treatment [66], this general approach still does not provide the necessary insights into the design.

An alternative approach is to use Smith-charts to find the optimum impedance for noise and power matching at the input of the amplifier for given active device [67],[68],[27]. Although, the Smith-chart is a very convenient tool for seeing how close we are to the minimum NF and the maximum gain of a given device, it does not show the effect of individual noise sources on the total NF . This is particularly important for a concurrent multi-band LNA, since different noise sources behave differently at different frequencies.

Unlike bipolar transistors whose dc current sets the transconductance and minimum noise-figure, MOSFETs offer extra degrees of freedom in choosing the device width and length. These extra degrees of freedom can be used to improve the noise figure and the gain of the amplifier. Recently, some work has been done to calculate and minimize the NF of a single-band common-source CMOS LNA with inductive degeneration using a more systematic approach [61]. In the next section, we present a general approach for the design of concurrent multi-band LNAs which are important building blocks in concurrent receivers introduced in Chapter 3.

4.2 Concurrent Multi-Band Low-Noise Amplifiers

Today's multi-band amplifiers are designed to operate at one of the multiple supported frequency bands at any given time and are therefore non-concurrent. Such amplifiers are suitable for non-concurrent multi-band receivers such as dual-band mobile phones or dual-standard WLAN receiver cards. A typical multi-band amplifier is a combination of separate amplifiers, each designed for a particular frequency band. Transistor sizing, input/output matching circuitry, and bias current for each single-band amplifier are selected independently. The input and output of these amplifiers may be combined depending on the transceiver architecture. However, switches in the bias and/or signal path guarantee that at any given time, only one amplifier is operational in the radio chain. A generic block diagram of the existing multi-band amplifiers is shown in Figure 4.2.

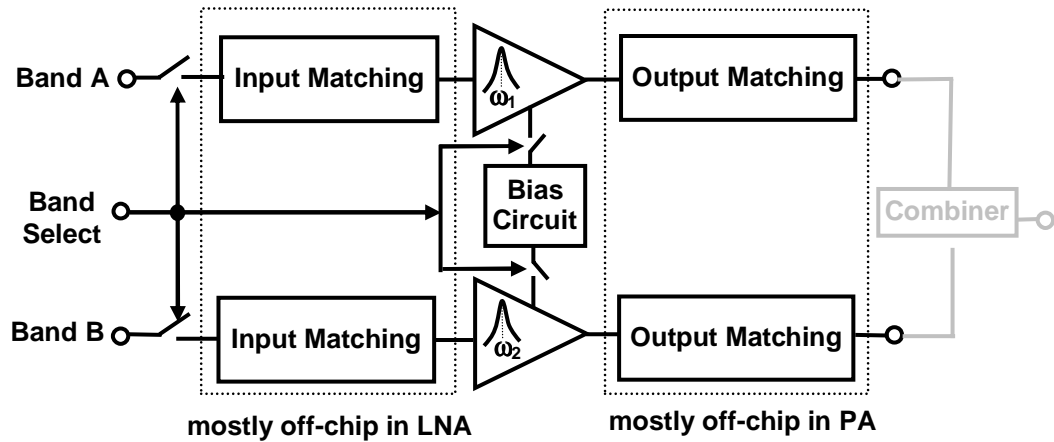


Figure 4.2: Generic schematic of existing multi-band amplifiers

If the switches are eliminated, this scheme can potentially be used as a concurrent multi-band amplifier. In the next section, concurrent amplifier topologies that are more area- and power-efficient will be introduced.

4.2.1 Concurrent Multi-Band LNA Design Methodology

In a single-band LNA, passive networks are used to shape the response of the wide-band transconductance of the active device in the frequency domain to achieve gain and matching at the frequency of interest. This concept can be generalized to multiple frequency bands noting that the intrinsic transconductance of the active device is inherently wide-band and can be used at multiple frequencies, simultaneously.

It is crucial to note the fundamental differences between the concurrent and the existing non-concurrent approaches. In conventional dual-band LNAs, either one of the two single-band LNAs is selected according to the instantaneous band of operation [70], [71], or two (three) single-band LNAs are designed to work in parallel using two (three) separate input matching circuits and two (three) separate resonant loads [9],[72]. The former approach is non-concurrent, while the latter consumes twice (three times) as much power if used in a concurrent setting. The other existing approach is to use a wide-band amplifier in the front-end [73]. Unfortunately, in a wide-band LNA, strong unwanted blockers are amplified together with the desired frequency bands and significantly degrade the receiver sensitivity.

In this section, we present an analytical approach to the design of a general class of integrated concurrent multi-band LNAs. The concurrent LNA is proposed as a solution to the aforementioned problems in a concurrent receiver.

4.2.1.1 General Amplifier in Common-Source Configuration

In this subsection, we use a general model for an amplifier in the common-source configuration to obtain an equivalent circuit for the input impedance and a general expression for the gain at multiple frequencies. This equivalent circuit will be used to achieve simultaneous power and noise matching in a concurrent multi-band LNA. Figure 4.3 shows a transistor⁹ with arbitrary gate impedance, Z_g , gate-source impedance, Z_{gs} , source impedance, Z_s , gate-drain impedance, Z_{gd} , and load impedance, Z_L . The impedances shown in Figure 4.3 also include the transistor's inherent passive components (e.g., C_{gs} , C_{gd}). General expressions for input impedance and voltage-gain of this amplifier are found in Appendix A.

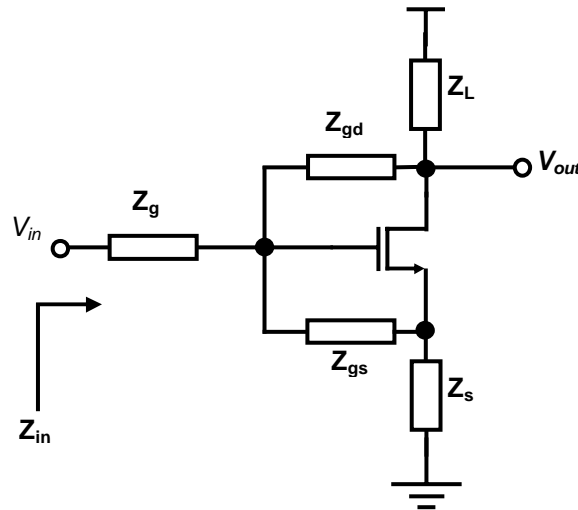


Figure 4.3: General model for a single-stage amplifier in common-source configuration.

⁹ While the general active device discussed here is a MOS transistor, a similar analysis applies to other active devices (e.g., BJT, GaAs MESFET.)

4.2.1.2 Input Matching

The input of an LNA is either fed directly by the antenna or is connected to the antenna through a band-pass filter, a diplexer/duplexer, or both. In any case, the impedance looking into the input of the LNA should be power matched (*i.e.*, in matched complex conjugate fashion¹⁰) to the impedance of the preceding stage for maximum signal power transfer. Additionally, it is essential to provide the correct impedance to the preceding stage to satisfy its nominal specifications (*e.g.*, bandpass filter characteristics, such as roll-off, etc. depend on filter loading).

The expressions in Appendix A can be further simplified if we assume that Z_{gd} is much larger than the other impedances. This assumption neglects the effect of the transistor's intrinsic C_{gd} and its associated miller-effect. Then, the input impedance expression of (A.1) simplifies to:

$$Z_{in} = Z_g + Z_{gs} + Z'_s(1 + g_m Z_{gs}) \quad (4.1)$$

In (4.1), g_m is the small-signal transconductance of the transistor and Z'_s is the overall impedance at the transistor source including the source-bulk impedance. This expression will be used in the following section to design multi-band input matching networks.

Theoretically, the input impedance of any stable amplifier with a non-zero real part can be perfectly matched to any arbitrary source impedance (with positive real part) for a single frequency using lossless passive components at the input of the amplifier [74]. Equation (4.1) can be used to generalize this *power match* concept to multiple frequencies. It can be used to generate numerous topologies to achieve simultaneous impedance matching at multiple distinct frequencies.

In an LNA, it is also necessary to achieve a *noise match* at the input for the frequency(ies) of interest to minimize the noise figure. In the following section on noise matching, we will demonstrate that one way to minimize the noise figure of the amplifier of Figure 4.3 is by designing the passive network so that it satisfies $Z_g + Z_{gs} + Z'_s = 0$ at

¹⁰ In large-signal devices, power match does not necessarily correspond to the complex conjugate matching. However, since the LNA design is based on small-signal principals, we can use two terms, synonymously.

multiple frequencies of interest. However, this can only be achieved using lossless passive components. Therefore, in practice, one should minimize $Z_g + Z_{gs} + Z'_s$, to its smallest real part, R_{\min} , at these frequencies. Having satisfied the above condition, the input impedance will be

$$Z_{in} = g_m Z_{gs} Z'_s + R_{\min} \quad (4.2)$$

Theoretically, a large number of passive topologies for Z_{gs} and Z'_s can provide input impedance matching at multiple frequency bands. One particular example which is of great practical value is when Z_{gs} is just the intrinsic gate-source capacitance, C_{gs} , and hence Z'_s has to be an inductor as in the single-band common-source LNA in [64] [62] [61]. For negligible passive loss ($R_{\min} \approx 0$) and a real-value impedance Z_{in} , R_{in} (e.g., 50Ω for most practical cases), the source inductor is given by

$$L_s = \frac{R_{in} C_{gs}}{g_m} \approx \frac{R_{in}}{\omega_T} \quad (4.3)$$

This will result in a passive network for Z_g that will minimize $Z_g + Z_{gs} + Z'_s$ for all the frequencies of interest. One example of such design can be found in subsection 4.2.2.

The optimum source inductance depends on the cut-off frequency, ω_T , and hence process parameters, as (4.3) suggests. Ignoring C_{gd} , in a deep short-channel MOS transistor biased in the velocity saturation region, ω_T is approximately given by

$$\omega_T \cong \frac{g_m}{C_{gs}} = \frac{3}{4} \mu_n \frac{E_C}{L_{eff}} = \frac{3}{4} \frac{v_{sat}}{L_{eff}} \quad (4.4)$$

where μ_n is electron mobility in the channel, E_C is the critical field, v_{sat} is the saturation velocity, and L_{eff} is transistor's effective channel length. Therefore, for a given deep sub-micron CMOS technology with constant channel length where carriers are velocity saturated, the value of L_s is almost fixed and is independent of the bias current and the device size. For a bipolar transistor, ω_T generally has a current dependency. However, if junction capacitors are negligible for a transistor biased with a high collector current, this current dependency is small and again the value of L_s is independent of bias current. In a

long-channel MOS transistor, ω_T depends on the bias current and the device width and so will L_s .

4.2.1.3 Noise Matching

An important design parameter in receiver design, which is the measure of receiver noise, is the noise factor, F , (also known as noise figure, NF , when expressed in dB). The definition of noise factor of any transducer (*e.g.*, LNA, mixer, filter, etc.) given by [75] is

$$F = \frac{N_{total}}{N_{source}} \quad (4.5)$$

where N_{total} is the total noise power per unit bandwidth available at the output port¹¹ at a corresponding output frequency when the noise temperature of its input termination is standard 290K at all frequencies and N_{source} is that portion of N_{total} engendered at the input frequency by the input termination at the standard noise temperature¹², 290K.

Any noisy 2-port network can be represented by a noiseless 2-port network with input equivalent voltage, e_n , and current sources, i_n , [78], as shown in Figure 4.4. Then, the noise-factor, F , will be given by:

$$F = \frac{\overline{i_s^2} + \overline{|i_n + Y_s e_n|^2}}{\overline{i_s^2}} \quad (4.6)$$

Where Y_s is the reference source admittance (*e.g.*, $Y_s=1/50\Omega$) for the noise-figure and i_s is the noise current associated with it.

¹¹ Actually, noises can be referred to any other node, *e.g.*, input node, in the circuit.

¹² While noise figure is a useful parameter in practice, it is an incomplete measure of an LNA's performance, as it is desirable to have a low noise figure *while* maintaining a high gain. For example, feedback can be used to reduce F as close to unity as possible, at the price of lowering the gain in the process [66],[76]. Cascading multiple stages of such feedback amplifiers to recover the original gain will result in a noise factor larger than or equal to the noise factor of the original amplifier without feedback [77]. A more accurate measure of an amplifiers noise performance, called the noise measure, M , is defined in [66] to take the effects of both gain and NF into account.

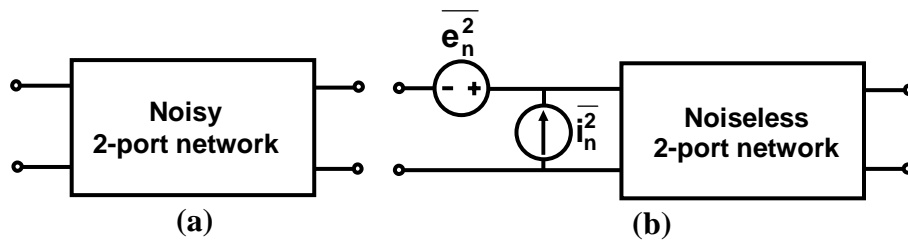


Figure 4.4: General representation of any noisy 2-port (a) and its equivalent circuit (b)

In general, equivalent input voltage and current sources are correlated. The effect of adding components in series or parallel to the input of the network on the equivalent input voltage and current noise sources can be easily modeled by the *noise-source transformations* (Appendix B).

Now, we will find an expression for the noise figure of the general single-stage common-source amplifier of Figure 4.3. While it is possible to include all the different noise sources in the calculations, we will make certain simplifying assumptions to keep the expressions tractable. In the following calculations, we assume that the only dominant noise sources are the drain and gate-induced current source, i_{nd} and i_{ng} [79] for the MOS transistor and collector and base shot noise currents, i_{nc} and i_{nb} , for the bipolar transistor. It is also assumed that passive impedances shown in Figure 4.3 do not contribute any noise. The noise of any physical input resistance, r_g , at the input appears as an additional term, r_g/R_s , in the expressions for F . Practically, r_g and r_b are very important in determining the NF , as well as input impedance of the LNA. They determine the minimum noise-factor (F_{\min}) of a transistor [67].

Using these simplifying assumption, the equivalent input current and voltage sources for the amplifier in Figure 4.3 can be calculated to be

$$\begin{cases} i_n = \alpha_{nd} \cdot i_{nd} + \alpha_{ng} \cdot i_{ng} \\ e_n = Z_{nd} \cdot i_{nd} + Z_{ng} \cdot i_{ng} \end{cases} \quad (4.7)$$

where,

$$\alpha_{ng} = \frac{Z_{gs}(1 - g_m Z_{gd})}{Z_{gs} + Z'_s(1 + g_m Z_{gs}) - g_m Z_{gs} Z_{gd}}, \quad Z_{ng} = -\frac{g_m Z_{gs} Z'_s Z_{gd}}{Z_{gs} + Z'_s(1 + g_m Z_{gs}) - g_m Z_{gs} Z_{gd}} \quad (4.8)$$

$$\alpha_{nd} = -\frac{Z_{gs} + Z_{gd}}{Z_{gs} + Z'_s(1 + g_m Z_{gs}) - g_m Z_{gs} Z_{gd}}, \quad Z_{nd} = -\frac{Z_{gd}(Z_{gs} + Z'_s)}{Z_{gs} + Z'_s(1 + g_m Z_{gs}) - g_m Z_{gs} Z_{gd}}$$

combining (4.6) and (4.7) results in the following expression for the noise factor, F ,

$$F = 1 + |\alpha_{nd} + Y_s Z_{nd}|^2 \cdot \frac{\overline{i_{nd}^2}}{i_s^2} + |\alpha_{ng} + Y_s Z_{ng}|^2 \cdot \frac{\overline{i_{ng}^2}}{i_s^2} + \frac{2 \operatorname{Re}\left\{(\alpha_{nd} + Y_s Z_{nd})(\alpha_{ng} + Y_s Z_{ng})^* \cdot \overline{i_{nd} i_{ng}^*}\right\}}{i_s^2} \quad (4.9)$$

where the second term is due to drain current noise, the third term is caused by gate-induced current noise and the last term is the result of the correlation between the two noise sources (a similar correlation term exists between the collector and base shot noise of a bipolar transistor [79]).

Note that (4.9) is quite general and can be used for the design of broad-band, narrow-band, or concurrent multi-band LNAs using any kind of transistor, as long as the small-signal noise model of the transistor is known. We will use this expression to compare the effect of various noise sources in different topologies.

In the case of a MOS transistor, noise current densities are known to be [79]

$$\begin{aligned} \overline{i_{nd}^2} &= 4kT\gamma g_{d0} \Delta f \\ \overline{i_{ng}^2} &= 4kT\delta g_g \Delta f \quad , \quad g_g = \frac{\omega^2 C_{gs}^2}{5g_{d0}} \\ \overline{i_{nd} i_{ng}^*} &= c^* \cdot \sqrt{\overline{i_{nd}^2}} \sqrt{\overline{i_{ng}^2}} \end{aligned} \quad (4.10)$$

where k is the Boltzman constant, T is the absolute temperature, γ is the excess noise-factor of MOS transistor, δ is the gate-noise coefficient, g_{d0} is the zero-bias drain conductance, g_g is the gate conductance, and c^* is the complex conjugate of the correlation coefficient between gate and drain noise currents.

We can simplify (4.8) if we ignore Z_{gd} (setting $Z_{gd} = \infty$), assuming it is dominated by the small gate-drain capacitor, C_{gd} (*i.e.*, high impedance compared to other impedances in

the circuit at the frequency of interest). Also, we can use the noise transformation of (A.1) to include the effect of an arbitrary gate series impedance, Z_g . Under these assumptions the coefficients in (4.7) will become

$$\begin{aligned} \alpha_{nd} &= \frac{1}{g_m Z_{gs}} & , & \quad \alpha_{ng} = 1 \\ Z_{nd} &= \frac{Z_g + Z_{gs} + Z_s}{g_m Z_{gs}} & , & \quad Z_{ng} = Z_g + Z_s \end{aligned} \quad (4.11)$$

which can be used in (4.9) to estimate the noise figure of the LNA.

To gain more design insight, for the time being let us focus on the effect of the drain current noise, which is often the most dominant noise source in the amplifier. In this case, the noise factor is given by

$$F = 1 + \left| 1 + Y_s (Z_g + Z_{gs} + Z'_s) \right|^2 \cdot \frac{1}{g_m^2 |Z_{gs}|^2} \cdot \frac{\overline{i_{nd}^2}}{i_s^2} \quad (4.12)$$

Since Z_g , Z_{gs} and Z'_s are assumed to be passive networks, and Y_s is a real admittance in all the practical cases (*e.g.*, $1/50\Omega$), the minimum value of the first term of the product above occurs when

$$Z_g + Z_{gs} + Z'_s = 0 \quad , \quad \forall \omega_i \quad (4.13)$$

for all frequency bands, ω . For this to be possible, all three passive networks should be lossless. Therefore, in practice, one should choose the passive networks, Z_g , Z_{gs} , and Z'_s to minimize $Z_g + Z_{gs} + Z'_s$ at *each* center frequency of interest, ω_i . We will refer to this minimum real value at each center frequency as $R_{min}(\omega_i)$. This is the same constraint that we referred to in the previous subsection on the input matching of concurrent low noise amplifiers.

The abovementioned general constraint for a concurrent multi-band LNA should also work in the special and more straightforward case of a single-band LNA. In this case, if Z_{gs} is simply the gate-source capacitance, and if Z_g and Z'_s networks consist of single inductors, we can satisfy (4.13) by setting

$$(L_s + L_g)C_{gs}\omega_0^2 = 1 \quad (4.14)$$

where ω_0 is the center frequency of interest in the single-band LNA. This is the same design equation derived and used in [61].

In addition to minimization of $Z_g + Z_{gs} + Z'_s$ at *each* center frequency of interest, (4.12) suggests that using higher Z_{gs} and higher device g_m can lower the NF further. One simple way of obtaining a large Z_{gs} is to keep the Z_{gs} network as simple as the intrinsic gate-source capacitance, C_{gs} , *i.e.*, using no explicit component between the gate and the source.

Different transistor technologies result in different noise performances. To compare different technologies, we can rewrite the NF expression of (4.12) as the following general expression valid for both MOS and bipolar transistors

$$F = 1 + 2k_L \frac{I R_s}{V_{char}} \left(\frac{\omega}{\omega_T} \right)^2 \quad (4.15)$$

$$k_L = \left(1 + \frac{R_{min}(\omega)}{R_s} \right)^2$$

where ω_T is the small-signal unity frequency of the transistor¹³ and I is the drain (or collector) current. The characteristic voltage, V_{char} , is defined as $V_{char} = 4kT/q$ for a bipolar transistor, and $V_{char} = (V_{GS} - V_T)/\gamma$ and $V_{char} = E_c L/\gamma$ for a long-channel and short-channel velocity-saturated MOS transistor, respectively.

Keeping in mind that to arrive at (4.15) we ignored the effect of the gate-induced current noise (or base shot noise), as well as the gate (base) series resistance noise, we can use (4.15) to make approximate comparison between the noise performance of bipolar and MOS transistors. It can be seen from (4.15) that NF decreases with increasing V_{char} , assuming constant ω_T . Table 4.1 shows the values of V_{char} and ω_T for a bipolar junction

¹³ Note that ω_T is a fixed value for a given deep short-channel MOS transistor biased in velocity saturation region, but it depends on current and device width in a long-channel MOS transistor. ω_T is current dependent in bipolar transistor, but the dependency is smaller for large collector currents and smaller junction capacitors.

transistor as well as a few typical short-channel MOS transistors¹⁴. It is also noteworthy that under these assumptions, a CMOS LNA will have a smaller NF compared to its bipolar counterpart because of its higher V_{char} ¹⁵. Nevertheless, this simplistic analysis is not completely adequate and hence a more accurate comparison will be performed next.

Process Technology	E_C (V/m)	V_{char} (V)	ω_T (rad/s)
Silicon Bipolar ($\tau_F = 3.67$ ps)	N/A	0.140	$2\pi \times 37$ -GHz @ 10 mA
0.35- μm CMOS ($L_{\text{eff}} = 0.27$ μm)	5.46×10^6	0.74	$2\pi \times 42$ -GHz
0.25- μm CMOS ($L_{\text{eff}} = 0.21$ μm)	4.27×10^6	0.45	$2\pi \times 59$ -GHz
0.18- μm CMOS ($L_{\text{eff}} = 0.16$ μm)	3.02×10^6	0.24	$2\pi \times 63$ -GHz
0.15- μm CMOS ($L_{\text{eff}} = 0.13$ μm)	3.57×10^6	0.26	$2\pi \times 102$ -GHz

Table 4.1: Comparison of V_{char} , and ω_T in different sub-micron CMOS processes

Taking the effect of the input resistance, gate-induced noise or base-shot noise into account, the following expression can be derived for the NF

$$F_{\text{Bipolar}} = 1 + \frac{r_b}{R_s} + 2k_L \frac{I_C R_s}{V_{\text{char}}} \left(\frac{\omega}{\omega_T} \right)^2 + \left(k_L + \frac{1}{\left(4 \left(\frac{\omega}{\omega_T} \right) \cdot \frac{I_C R_s}{V_{\text{char}}} \right)^2} \right) \cdot 2 \frac{I_C R_s}{V_{\text{char}} (\beta + 1)} \quad (4.16)$$

$$F_{\text{CMOS}} = 1 + \frac{r_g}{R_s} + k_L \left(\frac{\omega C_{gs}}{g_m} \right)^2 \cdot \gamma g_{d0} R_s + \left(k_L + \left(\frac{1}{\omega C_{gs} R_s} \right)^2 \right) \cdot \delta \frac{\omega^2 C_{gs}^2}{5 g_{d0}} R_s + 2\sqrt{k_L} \frac{(\omega C_{gs})^2}{g_m} \cdot |c| \cdot \sqrt{\frac{\gamma \delta}{5}} \cdot R_s$$

Note that no assumptions about the single-band operation of the amplifier were made and hence these equations are valid in the general case of a concurrent multi-band LNA.

¹⁴ The E_C values in Table I are derived from curves of $g_m \cdot V_{\text{gs}}$ and $g_{d0} \cdot V_{\text{gs}}$ obtained from simulation using BSIM3v3 models and assuming $g_{d0}/g_m = 2(V_{\text{gs}} - V_{\text{th}})/E_C L$ (*i.e.*, deep velocity saturated device). Also we assume a γ of 2 ([80],[81]) and use (4.4) to obtain ω_T of MOS transistors.

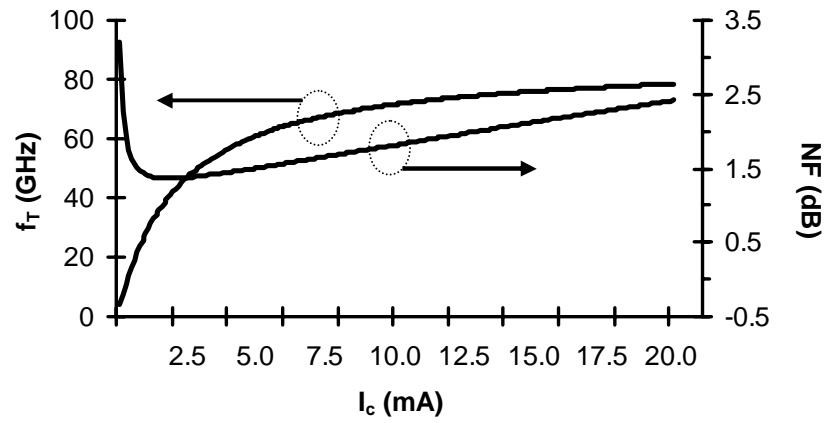
¹⁵ It should be noted that the same V_{char} appears in the phase-noise expressions of ring oscillators resulting in a similar argument suggesting that ring oscillators in current CMOS technologies offer lower phase noise than their bipolar counterparts [82].

Figure 4.5 (a) shows plots of the noise figure and ω_T vs. collector current for a bipolar transistor using (4.16). The contributions of different noise sources to the overall noise factor, F , are shown in Figure 4.5 (b).

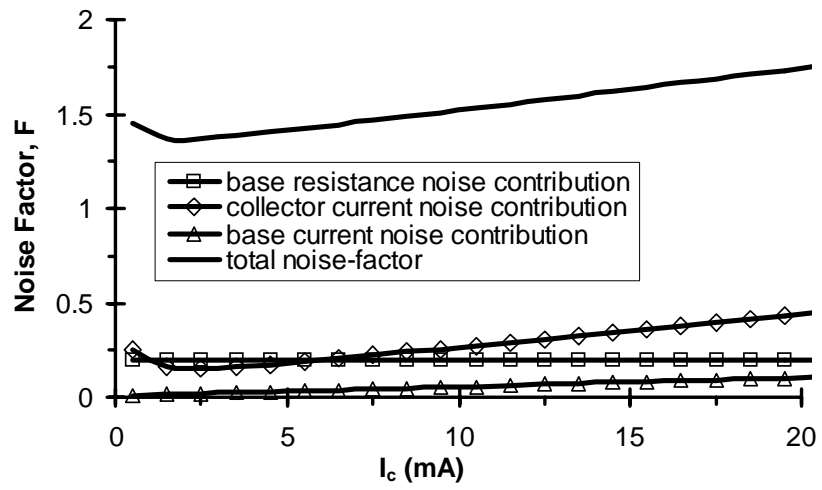
Now we can make a few observations in this common emitter configuration. First, at low frequencies compared to ω_T , NF is dominated by the base shot-noise, while at higher frequencies, the collector shot noise is the primary noise contributor. Second, for large collector currents, collector shot noise dominates the NF and therefore increasing the collector current deteriorates the noise factor, F , in a linear fashion. For smaller collector currents, the effect of base shot noise on the NF increases and the total NF degrades again. Third, a reduction in the collector current will lower the cut-off frequency¹⁶, ω_T , and hence increases the NF . As can be seen, this is similar to the well-known behavior of a single bipolar transistor amplifier where the F_{min} reaches a minimum for a certain collector current [67].

In the case of MOS transistors, there are more degrees of freedom in the design, such as finger width, W_f , and the number of fingers, n_f . It is clear that the fingers should be as short as the technology allows to minimize r_g for any given overall device width, W . Of course, we can control W by adjusting n_f ($W=W_f n_f$). A larger W results in a smaller r_g and hence a smaller gate-resistance noise contribution. However, while a larger W increases transistor's transconductance, g_m , it also increases the drain current consumption and has a negative overall effect on drain noise current contribution to amplifier's NF . Therefore, there's an optimum W and hence an optimum n_f resulting in the lowest NF in this topology (Figure 4.6). This approach does not compromise the voltage gain significantly, as it is shown in the next section that the voltage gain of this amplifier is independent of device transconductance and the number of fingers to the first order.

¹⁶ More accurately, ω_T is given by $\omega_T^{-1} = \tau_T = \tau_F + C_{je}/g_m + C_{\mu}/g_m$



(a)



(b)

Figure 4.5: (a) NF and f_t for a bipolar transistor with $\tau_F=3.67\text{ps}$ (b) Different noise contributions to the total NF from (4.16) (NF numbers for 5.8 GHz)

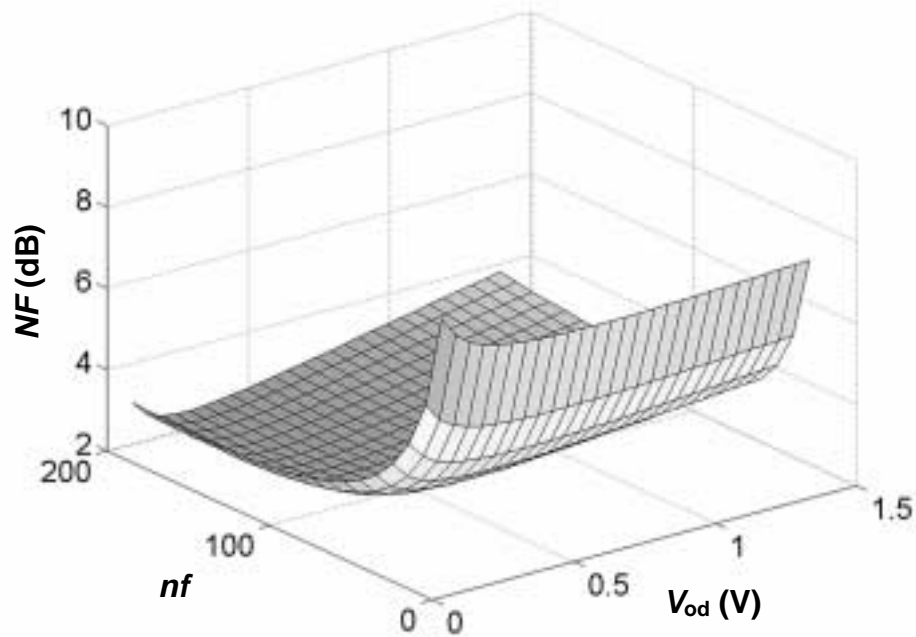


Figure 4.6: NF of a 0.18 μm CMOS transistor at 5.8 GHz with finger width of 2 μm vs. n_f and V_{od}

The other parameter of interest is the gate-source overdrive voltage, $V_{od}=V_{gs}-V_{th}$ of the MOS transistor. For small values of V_{od} , g_{d0} and g_m increase linearly with V_{od} until velocity saturation occurs and then g_m becomes constant. Meanwhile, g_{d0} and consequently the device noise keep increasing with V_{od} . As can be seen from (21-2), the drain noise contribution to F is proportional to g_{d0} and inversely proportional to the square of g_m . Therefore, NF drops with V_{od} in the beginning and then rolls back up, as can be seen in Figure 4.7(a). It also shows graphs of I_d , g_m and g_{d0} vs. V_{od} for the same transistor in a typical 0.18 μm CMOS process. As can be seen from the figure, further increase of V_{od} beyond the optimum NF point will degrade the noise factor and increase the power dissipation. The individual contributions of different noise sources of the same transistor to the total NF are shown in Figure 4.7(c).

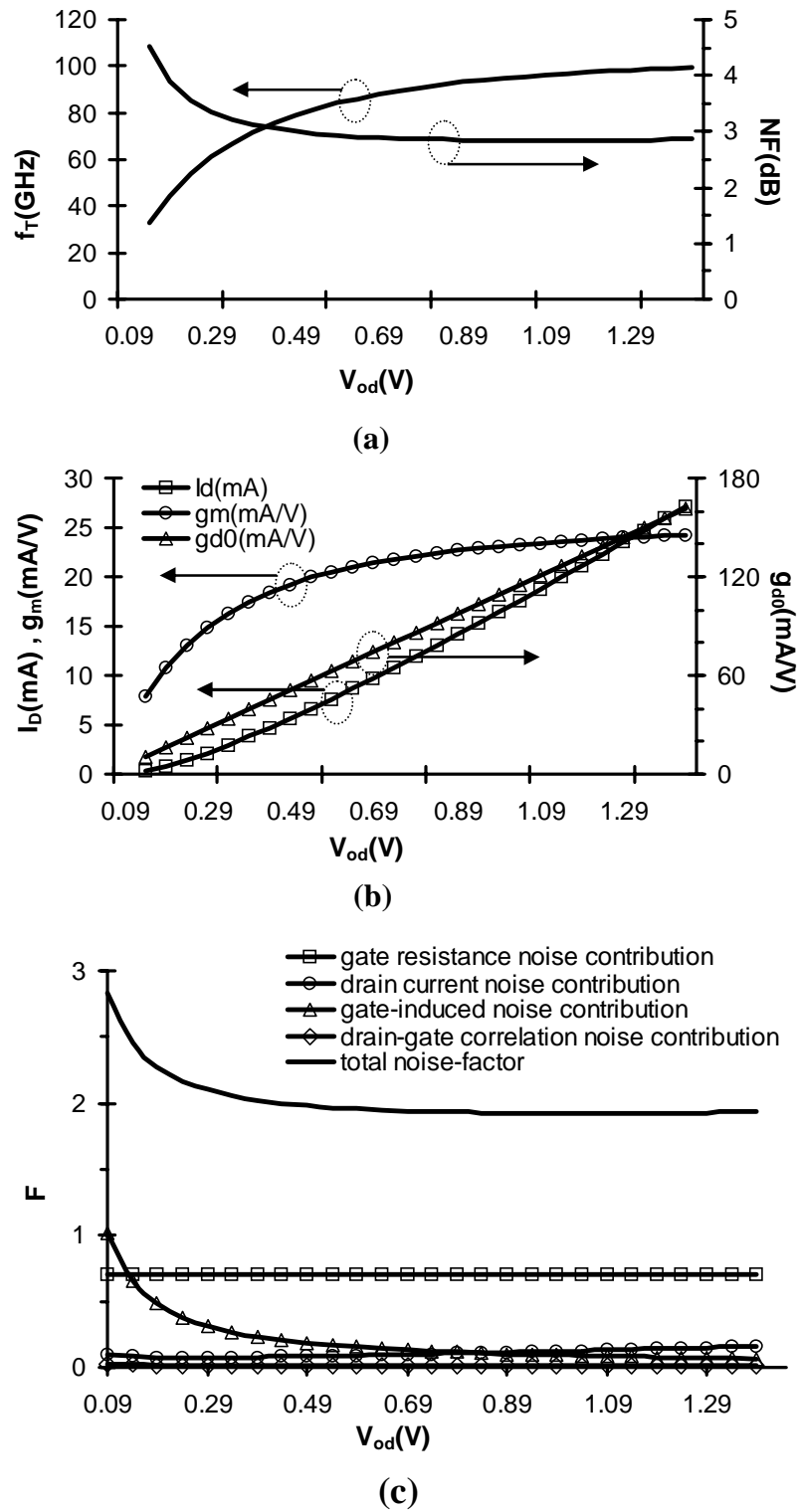


Figure 4.7: (a) NF , f_T of a $20 \times 2.5 \mu / 0.18 \mu$ CMOS transistor. (b) I_D , g_m , g_{d0} of the transistor. (c) Different noise contributions to the total NF from (4.16) (NF numbers at 5.8 GHz)

In practice, passives and substrate resistance noise add to the NF , specially in high frequency circuits where their relative contributions can be substantial [83]. Also, it is noteworthy that the noise of the equivalent channel-resistance, r_{gs} ,¹⁷ in series with C_{gs} at high frequencies is already taken into account in the gate-induced noise expressions in (4.10). Some authors (*e.g.*, [84]) consider the channel resistance noiseless while others (*e.g.*, [63]) modeled it as a noisy resistor. However, it should be noted that channel resistance and gate-induced noise originate from the same distributed gate effect (or non-quasistatic effect) in MOS transistors and the complete noise expressions similar to (4.10) should be used [79]. Although its noise is already taken into account, channel resistance, r_{gs} , will affect the expressions for input matching and should be considered in the design process [85] [84].

Once again, we would like to remind the reader that the above discussion is equally valid for concurrent multi-band LNAs, as well as single-band implementations, as no explicit assumptions regarding the number of frequency bands have been made.

4.2.1.4 Load Circuit, Output Matching and Gain

While the input and output of a stand-alone LNA usually need to be matched to 50Ω to transfer the power efficiently using transmission lines, the output of an LNA in an integrated front-end does not necessarily have to be matched in a similar way. Usually an integrated LNA drives the capacitive input of the first down-conversion mixer in the receiver chain and hence it is not desirable to match the output to a real impedance. This difference also explains why it is more common to report some form of power gain (*e.g.*, G_p or S_{21}) for stand-alone LNAs, and the voltage gain, A_v , for the LNAs in integrated front-end circuits. The NF expression for the receiver using voltage-gain and input-referred voltage sources can be derived when the output of the LNA is not impedance matched [56].

Assuming no body-effect ($g_{mb}=0$) and a small C_{gd} ($Z_{gd} = \infty$), the voltage gain expression of (A-2) simplifies to

¹⁷ It should be noted that this channel-resistance is different from r_{on} of MOS transistor in linear(ohmic) region.

$$|A_v| = \left| \frac{V_{out}}{V_{in}} \right| = \left| \frac{g_m Z_{gs} Z'_L}{Z_{in}} \right| \quad (4.17)$$

which can be used to calculate the gain at all frequencies. At the frequency bands of interest where (4.13) holds for minimum NF , (A-2) further reduces to

$$|A_v| = \left| \frac{Z'_L}{Z'_s + \frac{R_{min}}{g_m Z_{gs}}} \right| \approx \left| \frac{Z'_L}{Z'_s} \right| \quad (4.18)$$

If Z_s is implemented as an inductor to provide the real part of the input impedance, its value is given by (4.2) which is almost independent of the bias current in a deep velocity-saturated short-channel MOS transistor and also in a bipolar transistor as mentioned in subsection 4.2.1.2. Therefore, voltage gain given by (4.18) will be independent of current to the first order. In this case, increasing the bias current will only increase the NF with no significant improvement in A_v .

To achieve the highest gain and selectivity at the frequencies of interest, it is desirable to use a multi-resonant load at the output whose impedance is maximum at the frequencies of interest. An example of such load networks will be shown in the subsection 4.2.2.

4.2.1.5 Practical Considerations

The derivations in previous sections were general and in theory can be applied to design concurrent low-noise amplifiers supporting any number of frequency bands. However, in practice, the number of bands can not be arbitrarily large due to a number of principal reasons.

As the amplifier operates for a higher number of bands, the large-signal behavior at each band deteriorates. Fundamentally, this can be traced back to the fact that the total dc current and the allowable voltage swing across the transistor remain unchanged, however the device needs to amplify more signals added together. From the basic illustrations in Figure 4.8, we can observe that the addition of signals at different frequency bands results in a signal with larger peaks, demanding a more linear design for the amplifier. This latter

generally comes at a cost of reduced gain, reduced voltage-swing, and a larger current consumption. The penalty in linearity is more critical in the design of multi-band power-amplifiers as will be discussed later in Section 4.2.2.2.

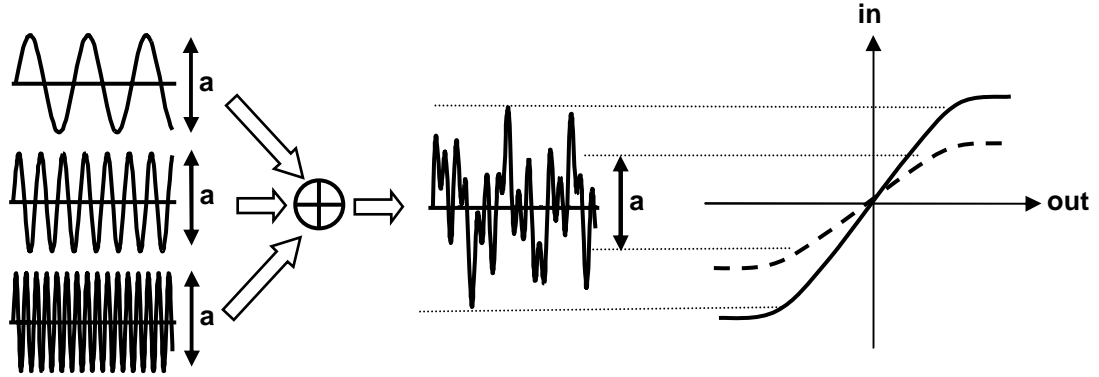


Figure 4.8: Basic illustration revealing that the combination of multi-frequency signals requires a more linear amplifier design

Using the newly defined metrics for the characterization of nonlinearity in concurrent multi-band systems in Chapter 3, the aforementioned penalty can be formally derived. The derivations of nonlinearity measures of these systems in terms of device nonlinearity are similar to those of single-band versions [38]. We can also relate these cross-band nonlinearity measures to the single-band ones. Assuming the concurrent block (*e.g.*, amplifier) output has a third polynomial dependence on the input,

$$V_{out} = a_1 V_{in} + a_2 V_{in}^2 + a_3 V_{in}^3 \quad (4.19)$$

When signals at both bands possess the same amplitude, we can calculate the in-band and cross-band 1-dB compression points defined in Section 3.4,

$$CP1_{inband} = \sqrt{\frac{4}{3}(10^{-0.1} - 1) \cdot \frac{a_1}{a_3}} \quad CP1_{crossband} = \sqrt{\frac{2}{3}(10^{-0.1} - 1) \cdot \frac{a_1}{a_3}} \quad (4.20)$$

As can be seen from equations (4.20), the cross-band 1-dB compression occurs 3 dB earlier than the in-band one. This suggests that for the same amount of nonlinearity, a concurrent multi-band block needs to be 3 dB more linear than its single-band counterpart to demonstrate the same amount of linearity in each band. If different applications at various

bands have different maximum signal powers, the concurrent multi-band block has to be 3 dB more linear for the strongest signal when compared to its single-band counterpart.

In the analysis above, the nonlinearity was assumed to be memoryless. In other words, it is implicit in equation (4.19) that nonlinearity terms are equal for all frequencies. In practice, this includes effects such as nonlinearities in device transconductance and resistors. Frequency dependent nonlinearity terms arising from nonlinear capacitors can not be modeled in this manner and need to be treated differently. Extensions to the simple model of (4.19) such that it also includes frequency dependent terms should be developed in a similar fashion to the case for single-band radios (*e.g.*, [38]).

Additionally, as the number of frequency bands increases, more passive components are required to shape the input and output characteristic of the amplifier. In practice, these passive components (especially inductors) are lossy and a larger number of them can degrade the amplifier performance considerably. More lossy passive components in the input matching circuitry correspond to a higher loss at the input port that directly adds to the total noise of the amplifier. For instance, input return-loss of a dual-band and a triple-band matching circuitry for two values of inductor quality factor are shown in Figure 4.9. As inductors' quality factor decreases, the input matching suffers due to the increase of resistive loss (*i.e.*, larger $R_{min}(\omega_k)$) in the matching circuitry. Although the added resistive part can be considered as a part of input matching design (*e.g.*, (4.2)), the loss associated with it degrades the noise-figure of the amplifier.

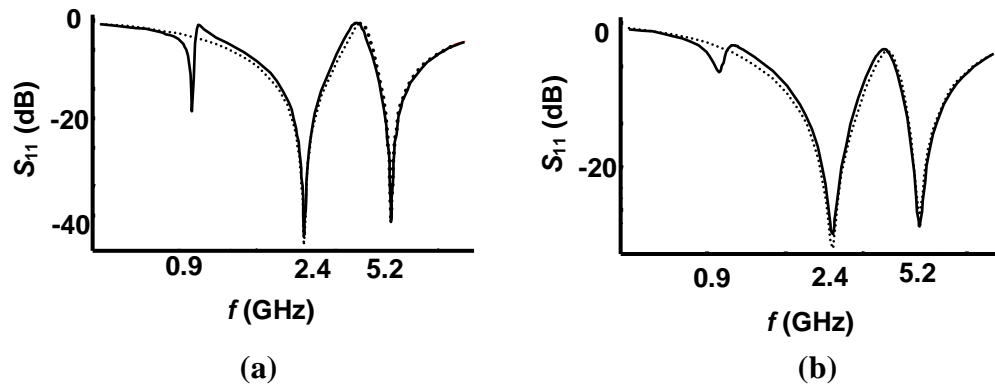


Figure 4.9: Simulated return-loss of a dual-band (dotted-curve) and a triple-band (solid-curve) input matching circuitry (a) $Q_{ind}=100$ (b) $Q_{ind}=10$

At the output, a larger number of lossy passives correspond to a lower equivalent impedance at each band that usually results in a slightly lower gain. A small voltage-gain reduction is generally not as harmful to the system performance as the noise-figure degradation that was previously mentioned. As a case in point, impedance-functions for a triple-band load is compared to a dual-band version at the same center frequencies and for the driving capacitive load in Figure 4.10(a). The results have been derived using a realistic frequency-dependent Q for on-chip inductors, as shown in Figure 4.10(b). Note the slight difference in the peak value of these curves. The frequency of notch (*i.e.*, zero in impedance function) is adjusted in both cases to achieve equal peak values. In the inductively degenerated amplifier that was discussed before, the load impedance should increase with frequency if a constant gain at all bands is desired, since the gain is inversely proportional to frequency-increasing value of Z_s (4.18).

The single-band load's impedance at those frequencies is also plotted for comparison. The large difference between the value at single-band and multi-band loads, in particular at lower frequencies, is due to unrealistically large inductors to tune the fixed load capacitance. In practice, the value of the on-chip spiral inductor is smaller and hence the single-band impedance gain values are lower than those shown in Figure 4.10(a).

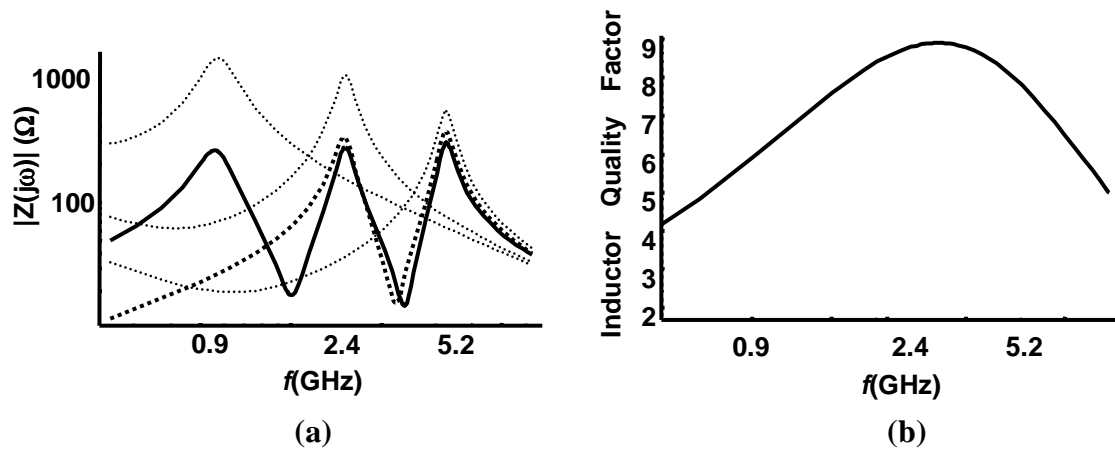


Figure 4.10: (a) Simulated results comparing the value of triple-band (solid-curve), dual-band (bold dotted-curve) and single-band (dotted-curve) impedance functions (b) Typical curve for the quality factor of on-chip spiral inductors that is used to generate impedance function curves

To summarize, although the concurrent ideas can be used in theory for any number of bands, designing circuits for an excessively larger number of bands *might* result in intolerable penalties in the performance of those systems due to practical considerations.

4.2.2 Concurrent LNA Design Examples and Measurement Results

Having established the theoretical framework for the design of concurrent multi-band LNAs, in this section we demonstrate a few examples of dual- and triple-band versions with different topologies.

While (A-1) and (A-3) provide numerous ways to design the input matching network for any number of frequency bands, we can use the more simplified expressions in (4.1) and (4.13) to achieve simultaneous input matching and minimum noise figure at two frequencies. We note that (4.2) can also be satisfied for multiple frequencies if Z_{gs} and Z_s are dual circuits, *i.e.*, $Z_{gs}Z_s=k$, where $k=R_{in}/g_m$ is constant. However, as expected from equation (4.13), the choice of passive networks for Z_{gs} affects the noise-figure of the amplifier considerably. Experimental results of various implemented concurrent amplifiers will be presented to verify the theoretical claims of this Chapter.

4.2.2.1 A High-Performance Concurrent Dual-Band LNA

In this subsection, the design and implementation of a concurrent dual-band low-noise amplifier operating at 2.45 GHz and 5.25 GHz, will be presented.

As mentioned earlier, we need to maximize Z_{gs} in order to minimize the NF . One way to obtain a reasonably large Z_{gs} is to use a transistor with minimum channel length and no extra passive elements between the gate and the source. The condition set by (4.2) can be satisfied using a single on-chip source degeneration inductor similar to the single-band cases of [61] and [62]. Since passive components realized on silicon substrate are normally very lossy, having them at the input of the amplifier seriously degrades the NF of the LNA. To fulfill (4.13) at both frequencies, a parallel LC network in series with the inevitable inductance of the bonding wire and package lead is used as shown in Figure 4.11. The parallel LC network of Z_g is designed to resonate with $Z_{gs}+Z_s$ at both frequency bands of

interest. Neglecting pad capacitance, gate-drain capacitance, and other parasitic effects, values of input matching components can be derived from

$$\begin{aligned} (L_s + L_b)L_g C_g C_{gs} &= \frac{1}{\omega_1^2 \omega_2^2} \\ \frac{1}{(L_s + L_b) \frac{C_g C_{gs}}{C_g + C_{gs}}} + \frac{1}{L_g C_g} &= \omega_1^2 + \omega_2^2 \\ g_m \frac{L_s}{C_{gs}} &= R_s \quad (50\Omega) \end{aligned} \quad (4.21)$$

For a fixed value of wirebond inductance and assuming $g_m/C_{gs} \approx \omega_T$, the above set of equations provides unique solutions for L_g , C_g and L_s .

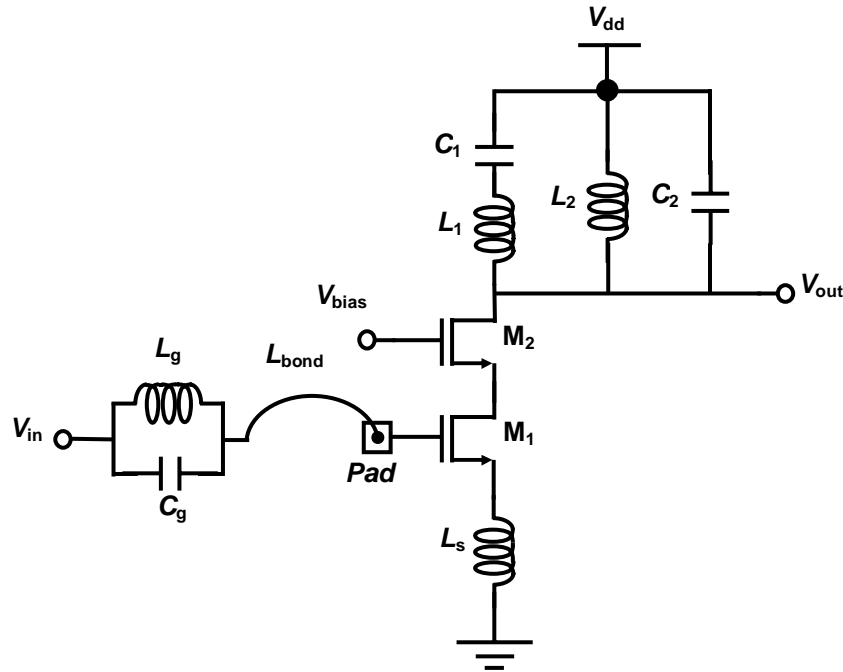


Figure 4.11: Concurrent dual-band CMOS LNA (biasing circuitry not shown)

The drain load network should exhibit high impedance only at frequencies of interest in order to achieve concurrent multi-band gain. This requirement can be fulfilled by adding a series LC branch in parallel with the parallel LC tank of a single-band LNA, as shown in Figure 4.11. Each series LC branch introduces a zero in the gain transfer function of the LNA at its series resonant frequency that determines the frequency of the notches in the transfer function. This notch is used to enhance the image rejection of the receiver, as

discussed in subsection 3.2.6 and shown in Figure 3.8. Equation (4.16) was used to obtain the optimum device size and the dc current.

A concurrent dual-band CMOS LNA was implemented in a $0.35\ \mu\text{m}$ BiCMOS technology using only CMOS transistors and operates at 2.45 GHz and 5.25 GHz. The input parallel resonator is made using a 0.9 pF porcelain multi-layer capacitor and a 2.7 nH chip inductor.

Figure 4.12 shows the measured voltage gain, A_v , and input reflection coefficient, S_{11} , of the amplifier up to 10 GHz. The LNA achieves narrow-band voltage gains of 14 dB and 15.5 dB, input return losses of 25 dB and 15 dB, and noise figures of 2.3 dB and 4.5 dB at 2.45 GHz and 5.25 GHz, respectively. In the course of noise-figure measurements, special attention was paid to *avoid* methods outlined in [86]. The designed LNA draws 4 mA of current from a 2.5-V supply voltage. The notch due to the LNA is about 40 dB deeper than the peaks, which directly translates to the same amount of improvement in image rejection. Due to the large difference between the notch and pass-band frequencies, no elaborate tracking loops such as those proposed in [87] are necessary to obtain extra image rejection. The single-ended nature of the LNA makes external Baluns unnecessary. Measurements of 6 different chips with 3 different boards and off-chip components show good repeatability without using the sliding capacitor input matching adjustment commonly-used in a single-band case [88].

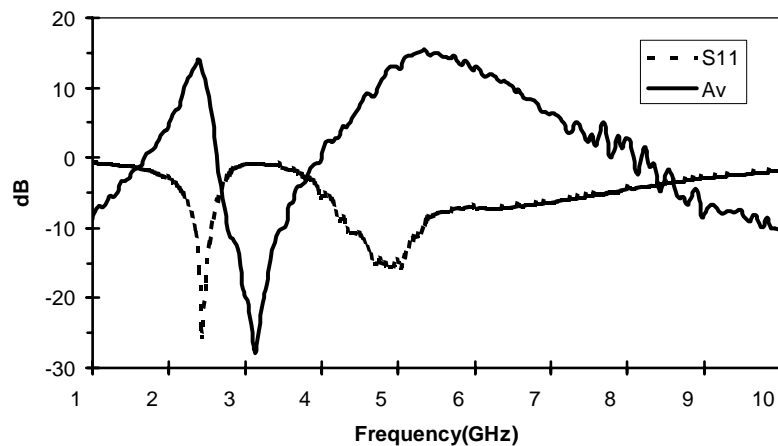


Figure 4.12: Voltage-gain and S_{11} in concurrent dual-band CMOS LNA of Figure 4.11

This concurrent dual-band LNA demonstrates input-referred in-band $IP3$ s of 0 dBm and 5.6 dBm, and in-band $CP1$ s of -8.5 dBm and -1.5 dBm at 2.45 GHz and 5.25 GHz bands, respectively. For this particular frequencies, two tones at 2.50 GHz and 5.15 GHz can combine through the fourth-order nonlinearity to produce an in-band signal at 2.35 GHz (*i.e.*, $3 \times 2.50 - 1 \times 5.15 = 2.35$). The measurements show that this input referred $IP4_{crossband}$ is 7.5 dBm. The LNA exhibits a $CP1_{2.4 \rightarrow 5.2}$ of -11.5 dBm and a $CP1_{5.2 \rightarrow 2.4}$ of -5.7 dBm. Note the 3 dB difference in in-band and cross-band compression points, as predicted by (4.20).

Table 4.2 summarizes the measured performance of the fabricated concurrent dual-band LNA depicted in Figure 4.13. The chip occupies an area of 0.8 mm \times 0.8 mm including pads and ESDs.

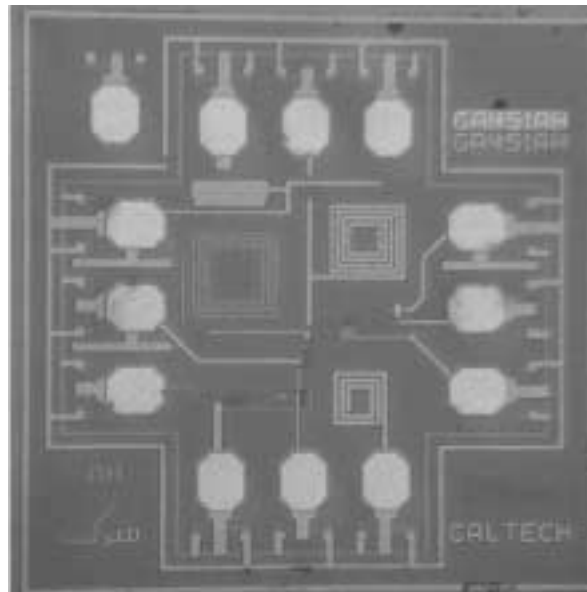


Figure 4.13: Chip micrograph for the concurrent dual-band CMOS LNA in Figure 4.11

Frequency	2.45 GHz	5.25 GHz
Voltage Gain	14 dB	15.5 dB
S_{11}	-25 dB	-15 dB
NF	2.3 dB	4.5 dB
Input $IP_{3\text{in-band}}$	0.0 dBm	5.6 dBm
Input $CP_{1\text{in-band}}$	-8.5 dBm	-1.5 dBm
Input $CP_{1A>B}$	$CP_{12.4>5.2} = -11.5$ dBm	$CP_{15.2>2.4} = -5.7$ dBm
Input $IP_{4\text{cross-band}}$	7.5 dBm	
DC Current	4 mA	
Supply Voltage	2.5 V	
Active Device	0.35- μm CMOS transistors	

Table 4.2: Performance summary of the concurrent dual-band CMOS LNA

Table 4.3 compares the performance of this concurrent dual-band LNA with previously published single-band LNAs working in one of the same frequency bands. The NF , S_{11} and power dissipation are comparable or better than previously published non-concurrent single-band CMOS LNAs.

Ref.	Tech.	Freq.	NF(dB)	Gain (dB)	S_{11} (dB)	IP_3 (dBm)	$CP_{1\text{dB}}$ (dBm)	Power
[89]	0.25- μm PHEMT	5.4GHz	0.76	16	-15	N/A	N/A	N/A
[91]	0.4- μm GaAs	5.2 GHz	1.7	14.5	N/A	-10 (Input)	N/A	3 mA (3 V)
[90]	GaAs HBT	5.7 GHz	2.9	16.2	-7	7 (Output)	21 (Output)	21 mA (3.5 V)
[92]	SiGe HBT	5.8 GHz	1.6	17	N/A	N/A	N/A	7.5 mA (4.5 V)
[93]	0.6- μm CMOS	2.4 GHz	2.3	17.5 (A_v)	-19	1.8 (Input)	-9 (Input)	8 mA (3.3 V)
[87]	0.24- μm CMOS	5 GHz	4.8	18 (A_v)	-12	N/A	N/A	3.6 mA (2 V)
[94]	0.25- μm CMOS	5 GHz	2.5	16 (G_p)	-9.5	N/A	N/A	16 mA (3 V)
This Work [45]	0.35-μm CMOS	2.45 GHz	2.3	14 (A_v)	-25	0 (Input)	-8.5 (Input)	4 mA (2.5 V)
		5.25 GHz	4.5	15.5 (A_v)	-15	5.6 (Input)	-1.5 (Input)	

Table 4.3: Comparison of existing single-band CMOS LNAs and the concurrent multi-band LNA at the same frequency bands (S-band and C-band)

4.2.2.2 A Fully Integrated Concurrent Dual-Band Amplifier¹⁸

As mentioned in the introduction to 4.2.2, one simple method to achieve impedance matching at the input is by using a pair of dual networks for Z_{gs} and Z_s . In the design depicted in Figure 4.11, the intrinsic gate-source capacitor of the input transistor, C_{gs} , together with an inductor at the source, L_s , form the dual pair. More passive components were used at the transistor input (*i.e.*, L_g , C_g , and L_b) so as to satisfy the minimum noise-figure condition given in (4.13).

Other dual-network pairs for Z_{gs} and Z_s can be employed such that the condition in (4.13) is satisfied at multiple frequency bands without the need for extra passive components at the input. In subsections 4.2.2.2 and 4.2.2.3, concurrent dual- and triple-band amplifiers that realize the input matching condition without the use of Z_g , will be presented. Note that the networks of Z_{gs} and Z_s have the same order because of duality. Therefore, given a zero value for Z_g , in order to satisfy the condition in (4.13) at n frequency bands, both Z_{gs} and Z_s should be of order n (*i.e.*, each comprises of n passive components). For a dual-band amplifier, an inductor in parallel with the intrinsic gate-source capacitance, C_{gs} , form a parallel second-order system. The dual network can be implemented as a series LC combination at the source of transistor. The schematic of a dual-band amplifier with the described input matching circuitry is shown in Figure 4.14. A large coupling capacitor, C_{coup} , is used to separate the dc bias of gate and source of the transistor for proper biasing. For a given value of bias current, the values of g_m and C_{gs} can not be set independently. Hence an extra capacitor, C_{gs1} , is connected between the gate and source of input transistor to assist in satisfying the input matching conditions. The dc current is supplied through the current source I_{bias} and the dual-resonance tank is similar to the one described previously in subsection 4.2.2.1. Assuming ideal lossless passive components, design equations for input matching circuitry in this case are:

¹⁸ This section summarizes the design details of an earlier attempt towards fully integrated concurrent LNAs.

$$C_{gs,total} = C_{gs} + C_{gs1} = \sqrt{\frac{g_m}{R_s}} \times \frac{1}{|\omega_1 - \omega_2|}$$

$$L_g C_{gs,total} = L_s C_s = \frac{1}{\omega_1 \omega_2} \quad (4.22)$$

$$g_m \frac{L_g}{C_s} = R_s \quad (50\Omega)$$

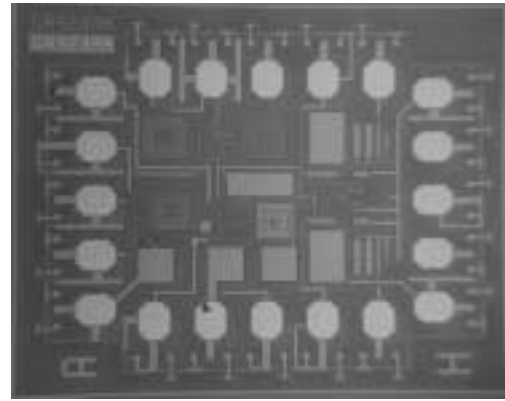
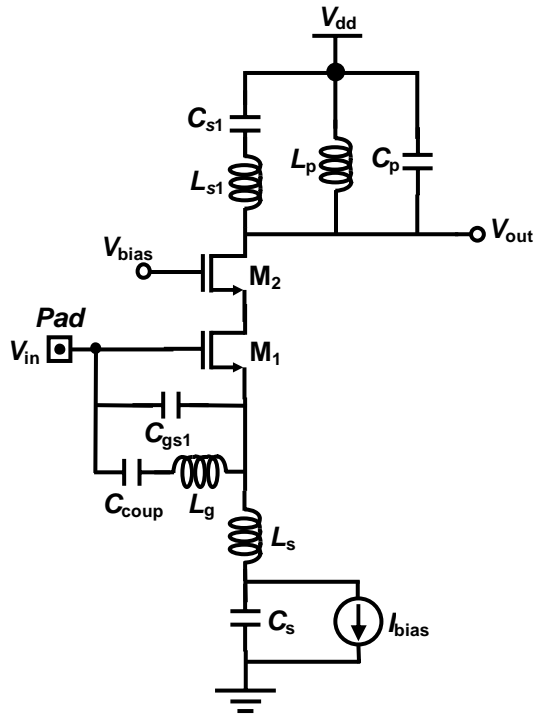


Figure 4.14: Schematic and layout of an integrated dual-band CMOS amplifier

Based on the described topology, a concurrent dual-band amplifier at 2.45- and 5.25-GHz frequency bands is implemented in the 0.35 μm BiCMOS technology using only CMOS transistors (Figure 4.14). The voltage-gain and input return-loss of the fabricated amplifier using on-chip probing measurement system are shown in Figure 4.15. The concurrent amplifier provides a voltage-gain of more than 10dB at each frequency band, while consuming 3mA from a 3V supply. The in-band third order intermodulation points of this amplifier, $IIP3_{\text{in-band}}$, are 5- and 7-dB at the two frequency bands, respectively.

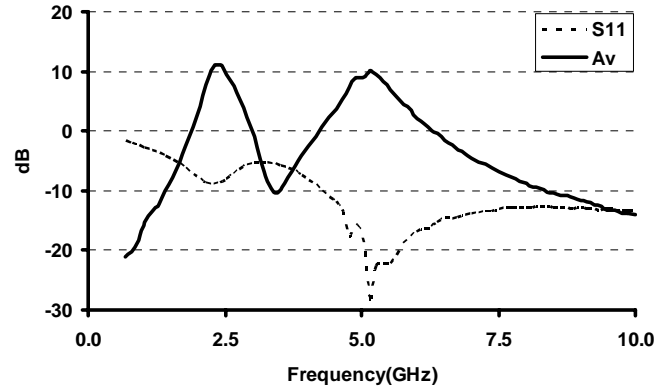


Figure 4.15: Voltage-gain and return-loss of concurrent dual-band amplifier of Figure 4.14

Noise measurements of this amplifier show that noise-figure at the two frequency bands is larger than 10dB. The large value of noise-factor can be traced back into a decrease in the value of Z_{gs} in the architecture of Figure 4.14. In fact, by applying the matching conditions of (4.2) and (4.13) and assuming a $Z_g=0$, a simplified noise-figure expression for this type of concurrent multiband amplifier can be derived. From (4.13) and assuming lossless passive components for Z_{gs} and Z_s , we find that Z_{gs} and Z_s have the same magnitude at all the frequency band of interest, ω_i .

$$\left| Z_{gs}(j\omega) + Z_s(j\omega) \right|_{\omega=\omega_i} = 0 \Rightarrow Z_{gs}(j\omega_i) = -Z_s(j\omega_i) = \pm j |Z_{gs}(j\omega_i)| \quad (4.23)$$

By using (4.2) and (4.23), the magnitude of Z_{gs} can be obtained as following.

$$\left| Z_{gs}(j\omega_i) \right| = \sqrt{\frac{R_s}{g_m}} \quad (4.24)$$

Therefore, for each of the desired frequencies, ω_i , the simplified noise-factor expression of (4.12) can be reduced to the following:

$$F = 1 + k_L \gamma \left(\frac{g_{d0}}{g_m} \right) \quad (4.25)$$

where k_L is defined in (4.15). Compared to (4.15) that was derived for the amplifier architecture of Figure 4.11, the noise-factor in this case is higher by $(\omega_T/\omega)^2$. Note that the frequency-independent noise-factor in this case resembles the one in common-gate

architectures [60]. Finite quality factor of inductors L_g and L_s increases k_L and deteriorates the amplifier noise-figure further. Also the noise contributions of gate and source resistances as well as the cascode transistor, M_2 , add to the total noise-figure considerably. As previously mentioned, the increase of noise-factor for the amplifier showed in Figure 4.14 is validated by measurements as well. The measurements match closely with simulations for an increased value of MOS transistor excess noise factor, $\gamma=2$, and quality factor of about 6 for spiral inductors. It should be mentioned that (4.25) can be used for a design that uses bipolar transistors by replacing $g_{d0}=g_m$ and $\gamma=0.5$. Hence, comparing to the CMOS design where $g_{d0}/g_m>1$ and $\gamma\approx 2$, a lower noise-figure for the bipolar design can be expected.

4.2.2.3 Fully Integrated Concurrent Triple-Band Amplifiers

Similar to the case described in 4.2.2.2, higher-order dual networks for Z_{gs} and Z_s can be employed to satisfy the input matching conditions in (4.2) and (4.13), without the need for Z_g , at a larger number of frequency bands. A triple-band amplifier design using three passive components for each of Z_{gs} and Z_s is shown in Figure 4.16. The value of input matching components can be derived from the following design equations

$$\begin{aligned}
 C_g &= -\sqrt{\frac{g_m}{R_s}} \times \left(\frac{M}{P} + \frac{1}{S} \right) \\
 \frac{C_g}{C_{gs,total}} &= \frac{L_{sp}}{L_{ss}} = -\left(\frac{S \cdot M}{P} + 1 \right), \quad C_{gs,total} = C_{gs} + C_{gs1} \\
 L_g C_g &= \frac{S}{P} \\
 L_{sp} C_g &= \left(\frac{M}{P} + \frac{1}{S} \right)^2 \\
 g_m \frac{L_{ss}}{C_{gs,total}} &= R_s \quad (50\Omega)
 \end{aligned} \tag{4.26}$$

where M , P , and S are defined as

$$\begin{aligned}
 P &= \omega_1 \omega_2 \omega_3 \\
 M &= -\omega_1 \omega_2 - \omega_2 \omega_3 + \omega_3 \omega_1, \quad \omega_1 < \omega_2 < \omega_3 \\
 S &= \omega_1 - \omega_2 + \omega_3
 \end{aligned} \tag{4.27}$$

At the output, a triple-resonance load is formed by adding another series LC branch in parallel with the dual-band load of previous designs. As a special case, expression (4.25) can also be applied for the concurrent triple-band amplifier in Figure 4.16.

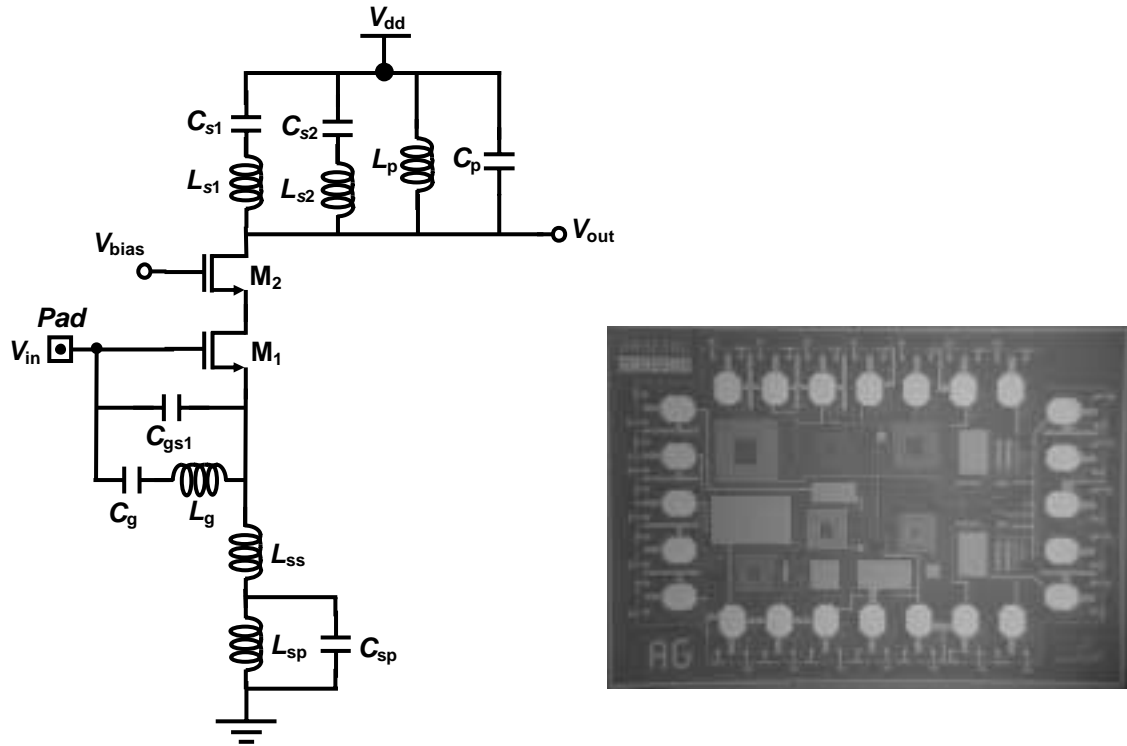


Figure 4.16: Schematic and layout of an integrated triple-band CMOS amplifier

Using the architecture of Figure 4.16, concurrent triple-band amplifiers at 0.9-, 2.45-, and 5.25 GHz *ISM* frequency bands were designed and fabricated in a 0.35 μm BiCMOS technology. Two versions of the same topology using different transistor technologies were fabricated for comparison purposes. The first design uses CMOS transistor and consumes 3mA from a 3V supply, while the second version uses bipolar junction transistors and draws 0.5mA from a 1.5V supply. The voltage-gain and input return-loss of the fabricated amplifiers using on-chip probing measurement system are shown in Figure 4.17. The higher gain in the second version can be attributed to a larger output impedance of bipolar transistors. The measured noise-figure in the middle frequency band is about 6.5dB and 10dB in bipolar and CMOS versions, respectively. The noise-figure at the other two bands

is about 1-2dB higher. These values are consistent with simulation results for a quality factor of about 6 for spiral inductors. Note that although the simplified expression of (4.25) predicts the same noise-figure in all frequency bands, the amplifier noise-figure will have frequency dependent terms due to other contributions to the total noise such as passive losses. The larger value of noise-figure in the CMOS design compared to the bipolar version is consistent with (4.25) and simulations as well.

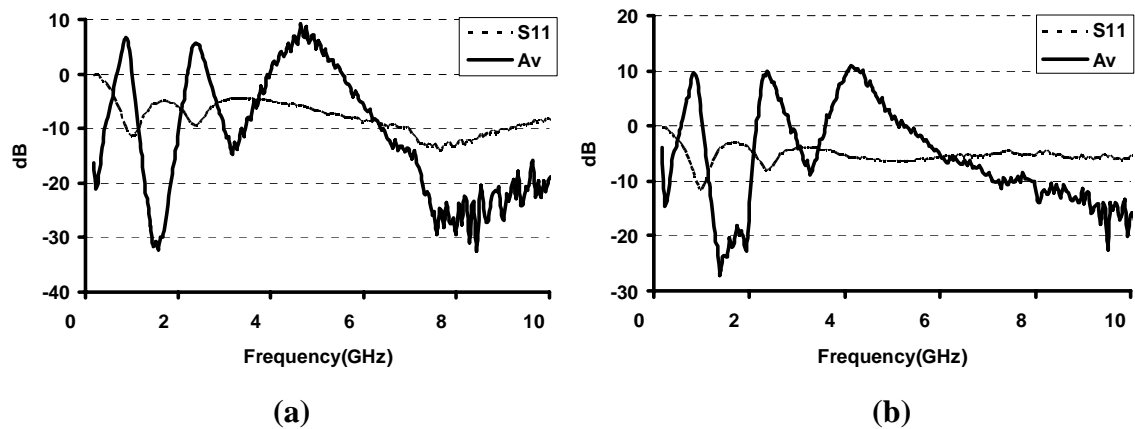


Figure 4.17: Voltage-gain and return-loss of concurrent triple-band amplifiers using the topology in Figure 4.16. (a) CMOS version (b) Bipolar version

4.3 Multi-Band Power Amplifiers

Many of the existing multi-band power-amplifiers follow the generic architecture of Figure 4.2, where a band-select switch picks the appropriate signal path (*e.g.*, [95]). Each path consists of a power transistor and matching elements that are optimized for the designed single frequency band. Power transistors use a substantial part of the, usually expensive¹⁹, semiconductor area in order to generate a large amount of power. Also there would be a considerable requirement in the linearity of band-select switch, particularly if the signals of interest have a non-constant envelope. Therefore, as a modification to the scheme in Figure 4.2, power transistor can be shared among all frequency bands while band-select switches

¹⁹ Chip area in the case of power-amplifiers is more valuable as the substrate material and process is normally based on an expensive compound semiconductor.

pick the appropriate passives at the input and output (*e.g.*, [96]). Other designs use diplexers/combiners or employ electronically tunable components [97] to cover more frequency bands.

In order to remove the band-select switch and save the active area, Bohn et al. [98] have demonstrated a switch-less dual-band power-amplifier that uses dual-resonance input and load matching passive networks for impedance transformation and harmonic termination. Besides removing the switch and/or diplexer, this solution saves on the active area as a single pair of power transistors serves both bands. Similar designs can be done at higher frequencies and using integrated components.

Nevertheless, there is no report of a concurrent power-amplifier yet. Since, power-amplifiers have to handle large-amplitude signals, in a concurrent scenario there may be a significant penalty in the linearity of these blocks, as shown in Figure 4.8. On the other hand, if we opt to operate the power-amplifier in linear regions only (*e.g.*, Class-A), the maximum efficiency of these amplifiers will be limited. It should be noted that in a linear concurrent power-amplifier, the maximum efficiency per frequency band is half of that in a linear single-band case. Driving the concurrent power-amplifier into nonlinear regions, will cause intermodulation products, in-band as well as out-of-band, that are highly undesirable. Schemes that employ pre-distortion at multiple frequency bands might serve as a useful solution for the mentioned problem.

In summary, the design of multi-band power-amplifier is an open field of research. Adding concurrency requirement to these blocks creates more challenges in the design from circuit as well as system viewpoints and can serve as a potentially valuable future research direction.

4.4 Summary

The new concept of concurrent multi-band LNA with the intention of its use as the essential part of a concurrent multi-band receiver is introduced. A general methodology is provided to achieve simultaneous narrow-band gain and input matching while offering a low noise figure in concurrent multi-band LNAs. The efficacy of the proposed methodology is demonstrated through measurement results of a CMOS implementation of the integrated

concurrent dual-band LNA that achieves a superior NF , S_{11} , and power dissipation over previously published non-concurrent and/or single-band LNAs. Multi-band power-amplifiers, in particular the concurrent versions, are still open for further investigation.

Chapter 5

An Experimental Concurrent Dual-Band Receiver

After looking into concurrent multi-band radios from architectural and circuit building block viewpoints in the last two chapters, it is time to put the pieces together to design a complete system. As a case study, the design and implementation of a concurrent dual-band radio receiver for potential use in wireless networking will be discussed in the following sections. This chapter starts with the derivation of some of the RF requirements in the radio for the intended applications. Fully integrated concurrent receiver architecture to fulfill these requirements will be introduced. The novel concurrent image-rejection scheme, previously mentioned in Chapter 3, benefits from a number of original building blocks resulting in a low-power and reduced-area implementation. Details of receiver circuit building blocks and experimental results of the implemented chip will be explained later in the chapter.

5.1 Top-Level Radio Design

As mentioned in Chapter 3, there are many applications where concurrent multi-band radio is beneficial. As a reminder, some of these benefits are to increase the effective bandwidth of the system and to have a more reliable wireless communication due to the added frequency diversity. Recently, wireless communications has become a fast-growing technology that enables convenient and inexpensive network solutions. However, the wireless network specifications vary considerably, as dictated by their target applications

(*e.g.*, short vs. long range, high vs. low data-rate) and even their advocates and sponsors. As a case in point, in the following, we will briefly describe some of these specifications and the way in which they affect the design of radio. A concurrent receiver architecture will be described that can be used as the radio backbone of wireless network receivers at two distinct frequency bands.

5.1.1 WLAN Standards and System Analysis

Currently, there are a number of frequency bands allocated for WLAN applications and standards. Our target frequencies for this implementation are the bands of 2.4 GHz (ISM) and 5.2/5.8 GHz (UNII/ISM) currently being used for the majority of employed WLAN standards. It should be noted that the description of WLAN standards in this section is merely intended for a comprehensive design cycle, from specifications to implementation. Clearly, the concurrent multi-band design can also be used for other applications with different specifications.

The Institute of Electrical and Electronics Engineers (IEEE) has developed technology specifications for both frequency bands under the family of 802.11 standards. IEEE 802.11 standards are mainly intended for high-speed wireless local-area networks (WLAN) applications. Some of the heavyweights in the telecommunications industry introduced another standard at 2.4 GHz called Bluetooth which is mainly intended for short-range and low data-rate communications. This results in very low power radios that, for instance, can connect home appliances and devices in a network. The European Telecommunications Standards Institute (ETSI) has made standards under the family High Performance Radio Local Area Networks (HIPERLAN), Broadband Radio Access Networks (BRAN), at the 5 GHz frequency band intended for high-data rate multimedia LANs such as High Definition TV (HDTV). Table 5.1 summarizes some of the specifications of these standards that mainly set the requirements for radio design and architecture. As the table indicates, the radio requirements for these standards, as intended for short-range applications, is more relaxed than other standards such as the ones used in cellular phones. This will allow for low-power implementations of the radio as will be seen later in this chapter.

To gain a better understanding of standards and our target performance numbers, we will show how the numbers in the table are translated into radio specifications. In particular, in the design of radio receivers, *dynamic range* and *selectivity* are among the most important specifications.

Dynamic range is the difference between the maximum and minimum signal levels the receiver can handle without exceeding the intended bit-error-rate (BER). The maximum input signal level, directly mentioned in standard, is limited by receiver nonlinearities. The minimum level, known as *sensitivity*, is mostly limited by multiple sources of noise in receiver. It can be shown (*e.g.*, [99]) that the receiver's overall noise-figure (*NF*) has to be limited to the following bound

$$NF[\text{dB}] \leq \text{sensitivity}[\text{dB}] - 10\log[C/(I+N)] - 10\log(k_BTB) \quad (5.1)$$

In (5.1), *sensitivity* is usually given as a part of radio specifications; $C/(I+N)$ is the ratio of carrier signal power to the combined power of interference and noise that for any given modulation can be derived from the required BER specification; and k_BTB is the total thermal noise in signal bandwidth, B .

Band Name	ISM		UNII, HIPERLAN	
Frequency	2400 – 2483.5 MHz		5250 ± 75 MHz	5250 ± 100 MHz
Standards	Bluetooth	802.11b	HiperLAN/1	802.11a
Multiple Access	FHSS, TDD	DSSS, FHSS	NPMA	OFDM
Modulation	GFSK (BT=0.5)	DPSK, CCK	GMSK (BT=0.3)	BPSK, QPSK, QAM (16, 64)
Sensitivity	-70dBm	-76dBm	-70dBm	-82 .. -65dBm
Max. Input Level	-20dBm	-10dBm	-20dBm	-30dBm
Channel BW	1MHz	5MHz	23.5MHz	16.6MHz
Max. Data Rate	1Mbit/s	11Mbit/s	23.5Mbit/s	54Mbit/s
Max. Output Power (mW)	100 (class 1)	1000 (USA) 100 (Europe)	1000	40 (5.15-5.25 GHz) 200 (5.25-5.35 GHz)
Range	100m	100m	100m (?)	50m
Application	Short-range cable replacement	High-speed WLAN	High-speed multimedia LAN	High-Speed WLAN
DSSS: Direct Sequence Spread Spectrum FHSS: Frequency Hopping Spread Spectrum TDD: Time Division Duplex NPMA: Non-preemptive Priority Multiple Access OFDM: Orthogonal Frequency Division Multiple Access			BPSK: Binary Phase Shift Keying QPSK: Quadrature Phase Shift Keying QAM: Quadrature Amplitude Modulation GFSK: Gaussian Frequency Shift Keying GMSK: Gaussian Minimum Shift Keying DPSK: Differential Phase Shift Keying CCK: Complementary Clock Coding	

Table 5.1: Summary of a few wireless networking standards at 2.4 GHz and 5 GHz

Additionally, the receiver should be able to detect the signal in the presence of out-of-band strong interferences, referred to as blockers. The ability to recover the weak narrow-band signal among all the blockers is a measure of receiver *selectivity*. The maximum level of blockers that might be present in the receiving environment is a function of frequency and is often specified for the given application. Receiver *selectivity* is limited by nonlinearities and another phenomenon known as *reciprocal mixing*, the result of the down-conversion of the blockers with oscillator phase-noise into the intended signal bandwidth (Chapter 3). Hence, there will be an upper bound on the local oscillator phase-noise at certain offsets determined by such requirements on the blocker rejections (*e.g.*, [99])

$$PN(f_{offset})[dBc/Hz] \leq C[dBm] - 10\log[C/(I+N)] - I[dBm] - 10\log(B) \quad (5.2)$$

In (5.2), C is the signal level that has to be recovered in the presence of interference level I at frequency f_{offset} .

The target receiver *dynamic-range*, NF , and VCO phase-noise of the standards in Table 5.1 are derived in Table 5.2. For comparison purposes, the numbers for the more stringent GSM standard for mobile-phone communication are also mentioned in Table 5.2.

	Bluetooth	802.11b	HiperLAN/1	802.11a	GSM
Dynamic Range (dB)	50	66	50	52	87
Overall NF(dB)	26	19	18.3	15	10
VCO Phase-Noise (dBc/Hz)		-114 @ $f_{offset}=25\text{MHz}$	-85.7 @ $f_{offset}=23.5\text{MHz}$	-93 @ $f_{offset}=20\text{MHz}$	-138 @ $f_{offset}=3\text{MHz}$

Table 5.2: Receiver target numbers for standards in Table 5.1

Once again, it should be noted that the implementation of the concurrent receiver is most valuable in demonstrating the new concept than in satisfying the application-specific radio requirements. Nonetheless, Table 5.2 provides realistic performance goals in designing the radio.

5.1.2 Receiver Architecture

The implemented concurrent dual-band receiver architecture uses the same principal structure as the one explained in Section 3.2.6 (Figure 3.7). Two different versions of the receiver have been fabricated. In the first version, all the blocks are integrated on the chip except that the second down-conversion local oscillators (LO_2 and LO_3) are provided from outside. The second version is fully integrated and all the local oscillators are generated using *one* on-chip phased-locked loop (PLL), as will be described in the following section. The input frequency as well as the LO frequencies are the same in both cases. The complete architecture of the fully integrated receiver is shown in Figure 5.1.

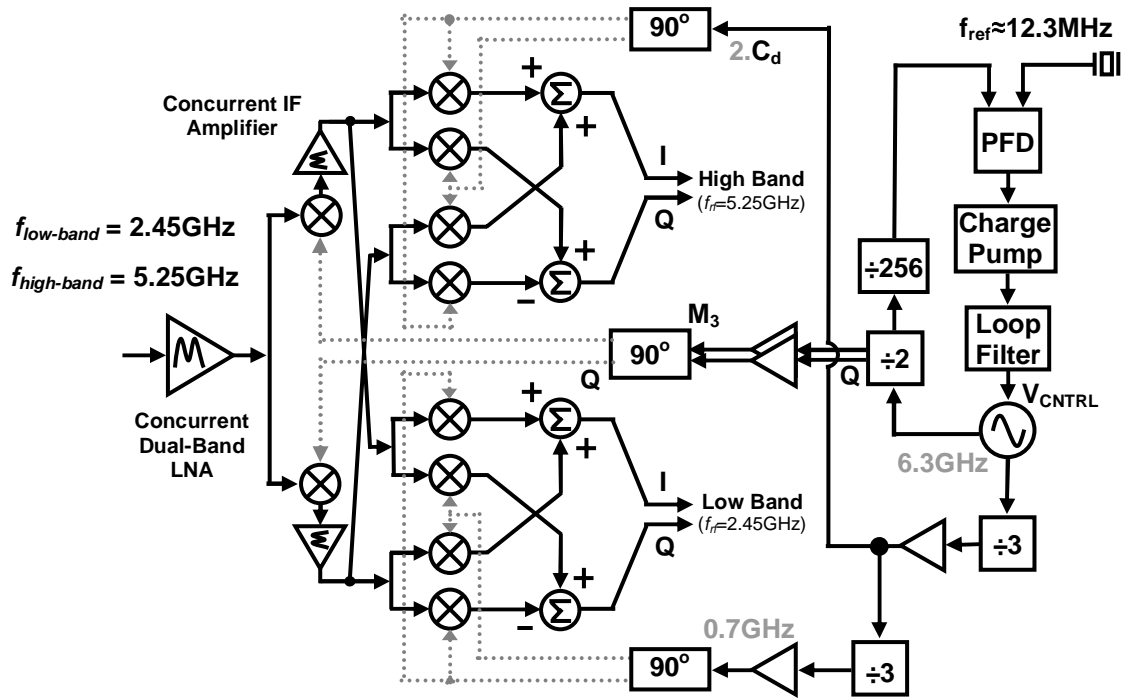


Figure 5.1: Complete schematic of the fully integrated concurrent dual-band receiver

The received signals at two frequency bands are first amplified by a concurrent dual-band low-noise amplifier. The narrow-band response of the LNA around each of the desired frequency bands prohibits the amplification of strong out-of-band signals that might deteriorate the performance of later stages in the receiver chain due to nonlinearity. In a receiver, the gain of each block suppresses the effect of noise of the following stages in the overall performance [46]

$$F_{overall} = F_1 + \frac{F_2 - 1}{G_1} + \frac{F_3 - 1}{G_1 G_2} + \dots \quad (5.3)$$

In (5.3), $F_{overall}$ is the overall noise-factor of the receiver, and F_i and G_i are noise-factor and available gain of the i^{th} stage in the receiver chain.

However, as the signal is amplified along the receiver, its amplitude gets larger and is more likely to drive the following IF stages into undesired nonlinear region of operation, *i.e.*,

$$\frac{1}{IIP3_{overall}} = \frac{1}{IIP3_1} + \frac{G_1}{IIP3_2} + \frac{G_1 G_2}{IIP3_3} + \dots \quad (5.4)$$

In (5.4), $IIP3_{\text{overall}}$ is the input-referred intercept point of the complete receiver, and $IIP3_i$ and G_i are the input-referred intercept point and linear gain of the i^{th} stage in the receiver chain.

Therefore, the gain of LNA should be large enough to suppress the noise of later stages and low enough not to sacrifice the linear behavior of following stages. In order to relax the dynamic-range requirements of the receiver, two gain modes for the concurrent dual-band LNA are devised. When the received signal strength is low (close to sensitivity level) the amplifier has a larger gain. In the case of a large received signal, the amplifier gain is reduced to provide a reasonable level to next stages. In the concurrent case, it is desired to have an independent control of gain for all the desired frequency bands. However, in this implementation of concurrent LNA a single gain-control is applied for both frequency bands.

Assuming symmetric in-phase and quadrature-phases signal paths, the down-conversion scheme proposed by Weaver [8] rejects the image signal completely. Nevertheless component mismatches inherent to any actual implementation, lowers the image-rejection of Weaver architecture considerably. In fact, it can be shown that a mismatch of ΔG and of $\Delta\Phi$ in the gain and phase of in-phase and quadrature paths sets the following limit on the image-rejection (IMR) of the receiver [35],[36].

$$IMR = \frac{(\Delta\Phi)^2 + \left(\frac{\Delta G}{G}\right)^2}{4} \quad (5.5)$$

In order to reach a higher on-chip image-rejection, quadrature mixing in the radio frequency (RF) mixers followed by the use of double quadrature downconversion scheme ([100]) at the intermediate frequency (IF) stage is pursued. The use of complex mixing enhances the image-rejection by an order of magnitude [100]. Furthermore, an even larger on-chip image-rejection is achieved by a combination of frequency planning and the best use of the notch in the dual-band front-end transfer function, as mentioned in Section 3.2.6. The complete frequency planning of the receiver with the frequency details is illustrated in Figure 5.2. As evident from this figure, since the received RF signals are down-converted into two different intermediate frequencies, a dual-band response at the IF stage is considered as well.

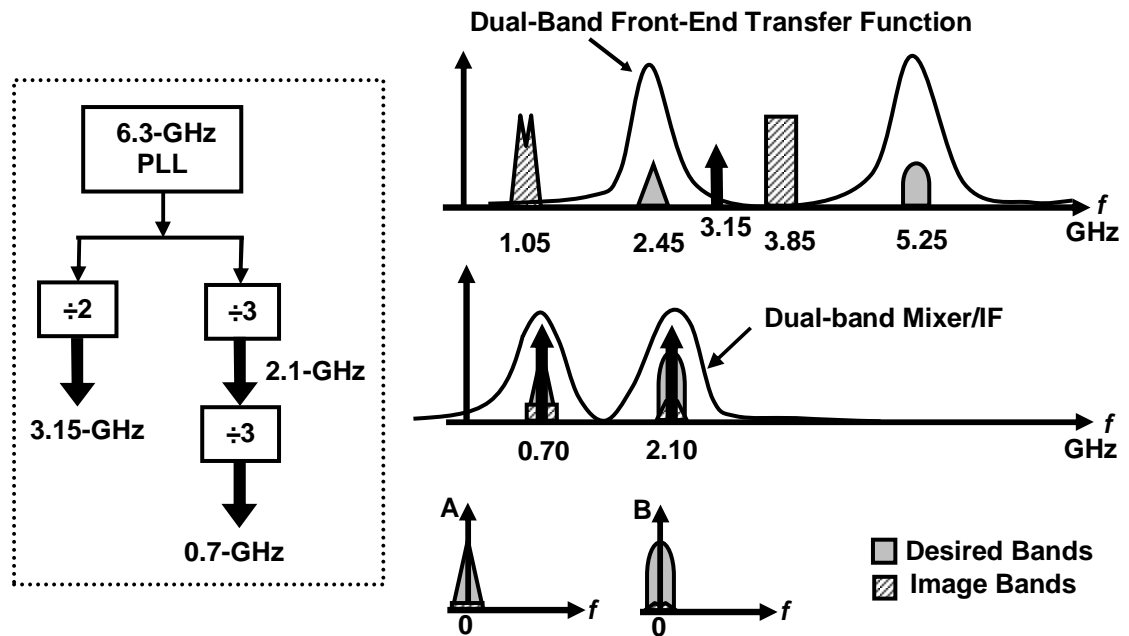


Figure 5.2: Frequency planning of the concurrent dual-band receiver in Figure 5.1

Since high-frequency PLLs consume a considerable amount of battery power and chip area, it was decided to generate all the local oscillator frequencies out of one PLL and high-speed dividers. Channel selection can be achieved at baseband with substantially smaller power consumption.

Compared to other dividers, divide-by-two circuits are generally considered to be easier to design. Additionally, both in-phase and quadrature-phase signals can be extracted from the outputs of divide-by-two and divide-by-four circuits [102]. Hence, a frequency planning scheme in which all the local-oscillator signals are generated from a single oscillator and divide-by-two blocks was conceived (Table 5.3).

f_{LO1}	$f_{LO2}=f_{LO1}/2$	$f_{LO3}=f_{LO1}/4$	
3.42GHz	1.71GHz	0.855GHz	
f_{RF1}	$f_{IF1}=f_{LO1}-f_{RF1}$	$f_{img1}=f_{IF1}+f_{LO1}$	$f_{BB1}=f_{IF1}-f_{LO3}$
2.45GHz	0.97GHz	4.39GHz	115MHz
f_{RF2}	$f_{IF2}=f_{RF2}-f_{LO1}$	$f_{img2}=f_{LO1}-f_{IF2}$	$f_{BB2}=f_{IF2}-f_{LO3}$
5.25GHz	1.83GHz	1.59GHz	120MHz

Table 5.3: Concurrent receiver frequency planning that uses only divide-by-two

The downfall of the aforementioned frequency planning is the closeness of image frequency of each band (*e.g.*, f_{img1}) to the center frequency of the other band (*e.g.*, f_{RF2}). Consequentially, dual-band transfer function of the front-end can not attenuate the image-signals as much²⁰.

Improved frequency planning schemes can be considered that utilize frequency divisions by an integer factor other than two²¹. A frequency planning scheme that exploits a divide-by-three and two divide-by-two blocks to generate all the necessary local-oscillator signals from a 6.6 GHz source is presented in Table 5.4.

f_{VCO}	$f_{\text{LO1}}=f_{\text{VCO}}/2$	$f_{\text{LO2}}=f_{\text{LO1}}/3$	$f_{\text{LO3}}=f_{\text{LO2}}/2$
6.6 GHz	3.3 GHz	2.2 GHz	1.1 GHz
f_{RF1}	$f_{\text{IF1}}=f_{\text{LO1}}-f_{\text{RF1}}$	$f_{\text{img1}}=f_{\text{IF1}}+f_{\text{LO1}}$	$f_{\text{BB1}}=f_{\text{IF1}}-f_{\text{LO3}}$
2.45 GHz	0.85 GHz	4.15 GHz	250 MHz
f_{RF2}	$f_{\text{IF2}}=f_{\text{RF2}}-f_{\text{LO1}}$	$f_{\text{img2}}=f_{\text{LO1}}-f_{\text{IF2}}$	$f_{\text{BB2}}=f_{\text{IF2}}-f_{\text{LO3}}$
5.25 GHz	1.95 GHz	1.35 GHz	250 MHz

Table 5.4: Concurrent receiver frequency planning that exploits divide-by-three and divide-by-two circuit blocks

Compared to the previous case, the image frequency of each band is farther away from the center frequency of the other band that allows for a better image-rejection due to the dual-band front-end transfer function. The final down-converted signals are centered at 250 MHz that will necessitate a wide-band digital circuitry for final channel selection and demodulation.

The frequency plan of Figure 5.2 was selected for the implemented receiver for a variety of reasons. A single PLL at 6.3 GHz and its divided versions can generate all the frequencies required in the receiver. Since the first local oscillator is generated by a divide-by-two, we will have access to both in-phase and quadrature phases of the LO. A passive polyphase filter ([100]) further corrects for any phase imbalance between the two that could

²⁰ It should be mentioned that placing the front-end notch very close to either of the frequency bands results in a lower gain and bandwidth for that band.

²¹ In many cases, analog frequency multiplication can be exploited instead of frequency division.

be due to the potential asymmetric duty-cycle of the 6.3 GHz oscillator. The second and third local oscillator signals are generated with divide-by-threes and are passed through passive polyphase filters for quadrature generation. Generation of in-phase and quadrature-phase signals using polyphase filters will be further discussed in subsection 5.2.4. The image frequencies are located far enough from the frequency bands of interest and will be attenuated by the front-end transfer function substantially. Additionally, the desired signals are down-converted to dc or a very low-IF and can be further processed in digital domain. The strength of the received signal can be measured at baseband and a feedback circuitry can change the gain of low-noise amplifier and other low-frequency variable-gain amplifiers that are not a part of described implementation. In summary, a large dynamic-range at both frequency bands should be expected from the concurrent dual-band receiver in Figure 5.1.

5.2 Receiver Building Blocks

The design of individual building blocks in the receiver is described in the following sections.

5.2.1 Concurrent Dual-Band LNA

The simplified schematic of the concurrent dual-band LNA together with all on-chip component values is shown in Figure 5.3. The values of off-chip input matching components, L_g and C_g , depend on the placement of the chip inside the package and the length of wirebond. In our case, their values were 2.7 nH and 0.5 pF, respectively. $L_{\text{bond-s}}$ at the source of M_1 is implemented using a downbond to the package bottom that is grounded and its value is approximately 0.9 nH.

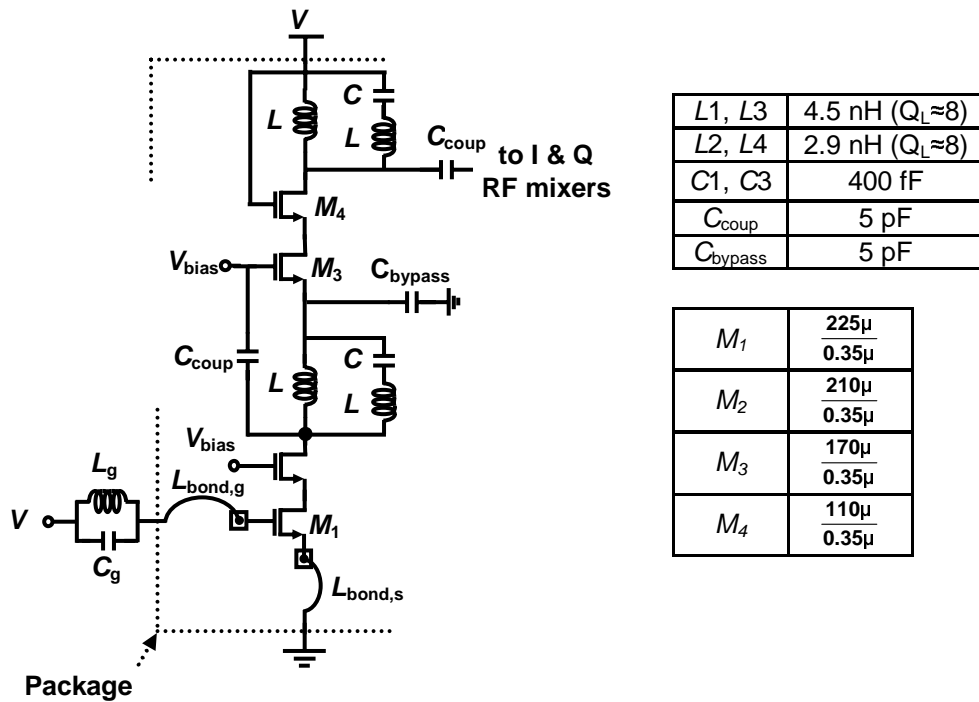


Figure 5.3: Simplified schematic of the concurrent dual-band LNA

In this implementation, the LNA uses a two-stage design where both stages use a cascode structure. With a 3V of power supply, stacking of four transistors does not degrade the performance noticeably and hence a current reuse technique is used in the design, *i.e.*, both stages share the same dc current [101]. At RF, the two stages are separated using a C_{bypass} at the source of M_3 and the output of the first stage at the drain of M_2 is connected to the input of the second stage at the gate of M_3 . The design of both stages followed the guideline of Chapter 4 with the exception that the second stage does not need input matching to 50Ω . Since the LNA is single-ended, all the package and wirebond parasitics at the V_{dd} node will be a part of load and can create unwanted resonant modes. Therefore, this node has been bypassed with a lossy capacitor²².

The LNA is designed to work with 4mA of current from a 3V of supply. Simulations predict a gain of 20dB and 15dB and a noise-figure of 3dB and 4.7dB at 2.4 GHz and 5.2 GHz, respectively.

²² A capacitor at V_{dd} node combined with the wirebond inductor can cause a low-frequency resonant pole. By placing a small series resistor ($\approx 5\Omega$), we can effectively reduce the gain of that mode.

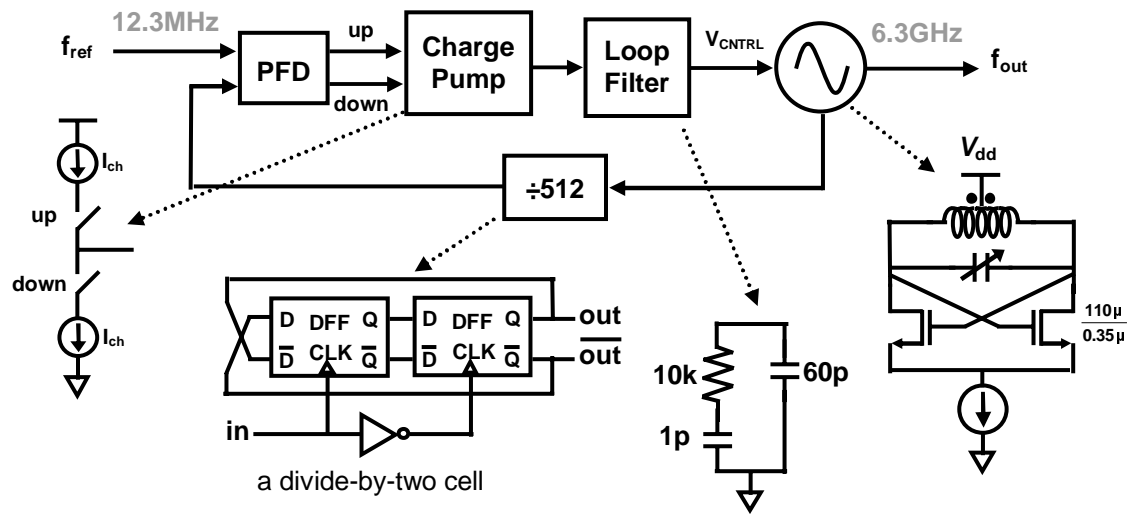


Figure 5.6: Simplified schematic of the 6.3 GHz PLL ²³

Two-stage passive polyphase structures are used to generate in-phase and quadrature-phase LO signals necessary for the image-reject architecture [100]. The output phase of a first-order low-pass/high-pass structure (*e.g.*, RC/CR filter) lags/leads the input phase by 45° at the frequency of its pole (*e.g.*, $\omega_0=1/RC$). Additionally, the outputs of first-order high-pass and low-pass RC filters at the pole frequency have equal amplitudes. A first-order passive polyphase structure uses the 90° phase difference in the output of high-pass and low-pass filters to create the in-phase and quadrature-phase signals at the pole frequency. In a complex frequency domain [100], each stage puts a notch in its pole frequency determined by the product of RC . However, changes in center frequency due to variations in the integrated technology processing as well as component mismatches limit the accuracy of quadrature generation of a first-order poly-phase filter. Higher-order poly-phase structures can generate the in-phase and quadrature signals in a wider frequency span and hence are less affected by process variations [100]. A second-order poly-phase filter is created by cascading two first-order poly-phase filters. Two center frequencies are slightly off-tuned (stagger-tuned configuration) in order to provide a larger range of quadrature generation, as shown in Figure 5.6.

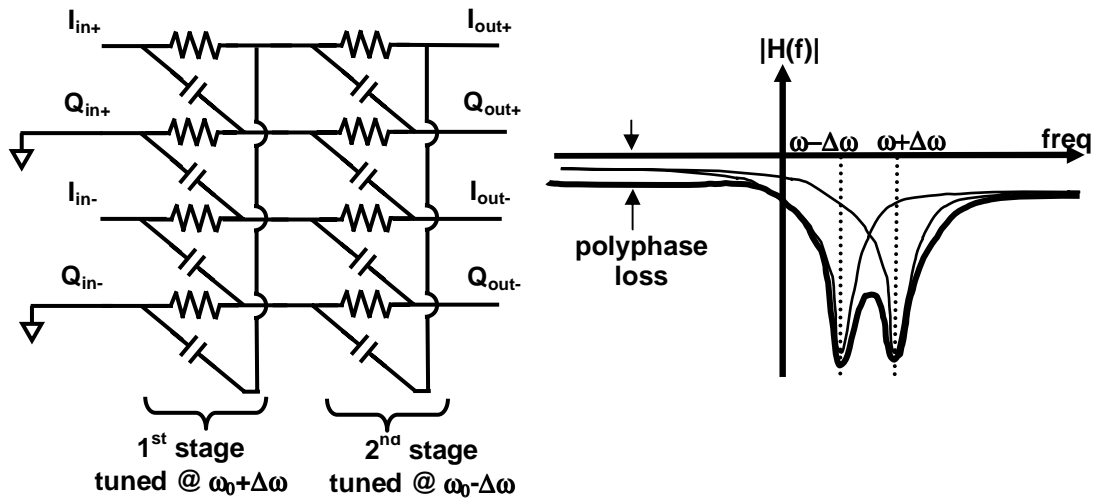


Figure 5.7: (a) Two-stage stagger-tuned poly-phase structure for LO quadrature generation; (b) its frequency response in complex domain

5.2.5 Analog Frequency Dividers

As Figure 5.1 and Figure 5.2 demonstrate, the second down-conversion LOs are generated from the 6.3 GHz signal using a couple of divide-by-three circuits. At first, flip-flop based digital divide-by three was attempted. The basic idea of that design is to have a cascade of 4 D-type flip-flops with alternating clocks which are able to count up to 4 and then reset it each time the counter reaches 3 with a feedback loop (*e.g.*, [102]). However, the timing becomes crucial as the feedback has to respond just in time to reset the signal before the states of flip-flops have changed. 6.3 GHz proved to be too high of a frequency to allow these types of dividers to operate reliably without consuming a large amount of current in a 0.35 μm CMOS technology. Hence, analog implementation of frequency dividers based on injection locking is pursued in this design.

Injection locking, in general, is synchronizing a free-running oscillator with an injected input signal. In injection-locked frequency dividers (ILFD), the frequency of input signal is close to one of the harmonics of the oscillator's free-running frequency. As the input signal gets closer to the harmonic of the oscillator or as its power increases, the oscillator frequency will change to synchronize it with the input signal. ILFDs are advantageous over

the standard flip-flop based design due to a number of reasons. Flip-flop (digital) dividers usually operate well below the cut-off frequency of the active device and consume significant power as their operation frequency increases. Both these issues are attributed to their wide-band operation. In contrast, ILFDs are based on narrow-band oscillators and therefore can operate as close as possible to the device's maximum operation frequency (f_{\max}) with smaller power consumption.

Injection locked frequency dividers based on ring oscillators [103],[104] as well as resonator-based oscillators [105],[106] have been reported. Between the mentioned oscillator topologies, the latter can operate at higher frequencies due to the extra phase shift provided by the resonator. Resonator-based divide-by-two ILFDs have been analyzed and designed [105], and tested up to frequencies close to device cut-off frequency [106]. However, there has not been any reported high-speed resonator-based ILFD implementations of divide-by-three in the literature. Ring oscillators have been used in the core of ILFDs to implement these odd-dividers [104] as well as even dividers [103]. A resonator-based divide-by-three will be described in the following.

Figure 5.8 shows the simplified schematic of the divide-by-two ILFD that uses a cross-coupled differential pair as the oscillator core [105],[106]. The input signal at twice the oscillation frequency is injected at the common source node. Due to the circuit symmetry, odd harmonics of current in the differential pair swing back and forth between the transistors while even harmonics are added up in the common source node and get absorbed by the circuitry at that node. That provides an explanation as to why the common source node is the best node to inject the signal current at even harmonics of the oscillation frequency, especially in the divide-by-two case. Based on this argument, it is clear that in the case of divide-by-three (or other odd harmonics of oscillation frequency) this structure is not optimum. Note that under hard switching condition, each of the transistors in the oscillator core still carries all the even and odd harmonics of the oscillation frequency. An alternative approach is required to combine the desired odd harmonic (*e.g.*, third harmonic in the case of divide-by-three) without disturbing the oscillator functionality at the fundamental frequency.

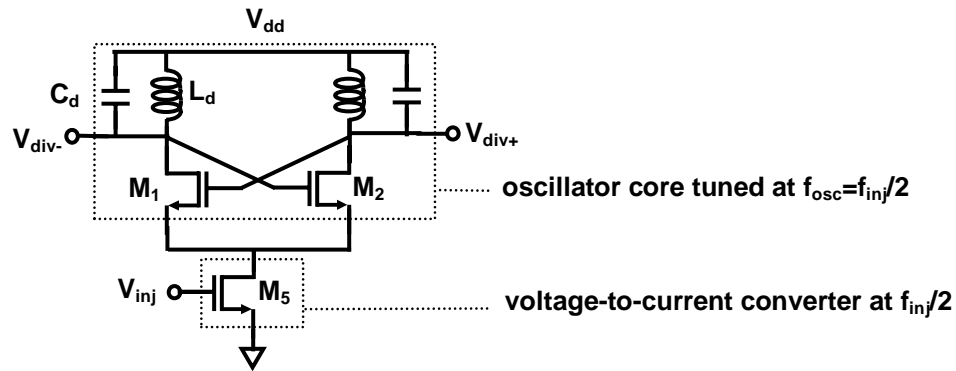


Figure 5.8: Simplified schematic of the divide-by-two ILFD in [105] and [106]

Figure 5.9 illustrates the simplified schematic of the proposed divide-by-three based on the ILFD technique. The top part consisting of cross-coupled pair M_1 and M_2 together with resonance load forms a free-running oscillator as before. However, in this implementation the sources of cross-coupled pair transistors are not connected to a common node as in the previous case. Instead, they are fed by another differential pair that injects the input current. The series LC branch of L_s and C_s form a short circuit at the oscillation frequency which in effect causes the sources of cross-coupled pair M_1 and M_2 to be connected together at the fundamental frequency for a large loop gain and therefore a reliable oscillation. With no input signal, the circuit behavior is similar to a standard cross-couples oscillator at f_{osc} with one minor difference. All the harmonics of the transistor's current expect the fundamental pass through M_3 and M_4 . The fundamental current has a shorter return path through L_s and C_s as shown in Figure 5.10. The series LC branch of L_s and C_s behaves inductively at higher harmonics. At odd harmonics, there would still be a current through this finite impedance path. In order to make this current smaller and consequently get a better coupling of injected signal to the oscillator core, the value of L_s should be increased while the product of $L_s C_s$ is fixed.

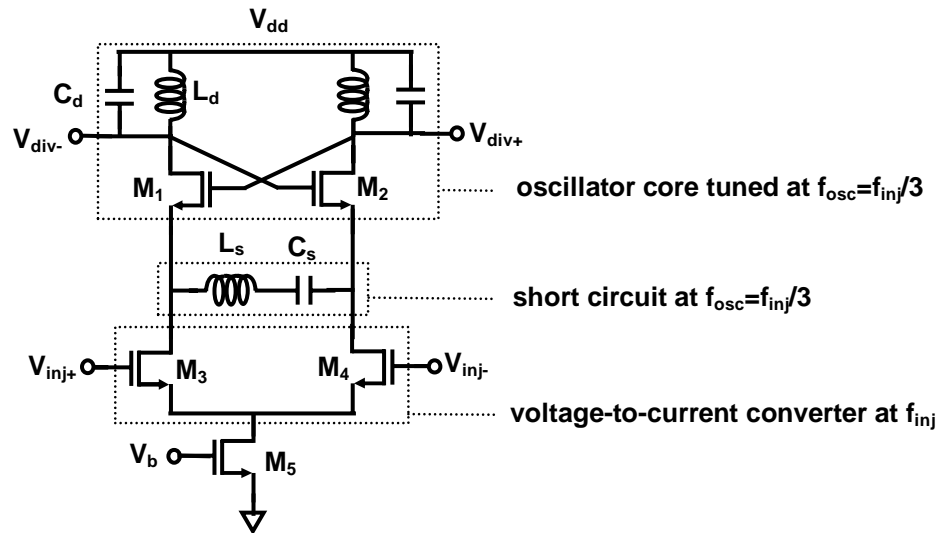


Figure 5.9: Simplified schematic of the proposed divide-by-three ILFD

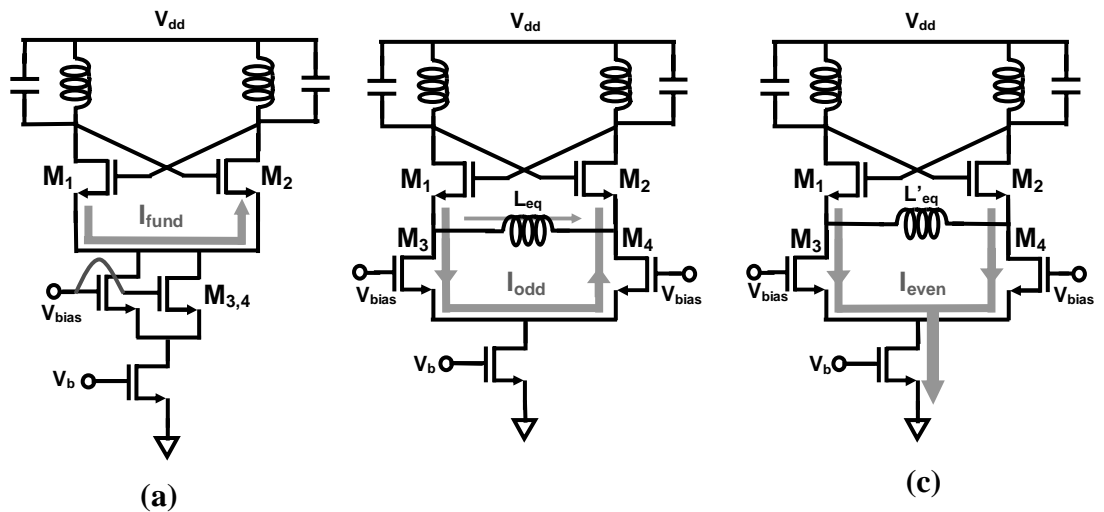


Figure 5.10: Divide-by-three principle of operation under no input signal at (a) fundamental oscillation frequency (b) odd harmonics of oscillation frequency (c) even harmonics of oscillation frequency

For instance, the frequency contents of the shown currents for the first implemented divide-by-three ($f_{inj}=6.3$ GHz) under no input signal power are shown in Figure 5.11. As expected, most of the fundamental components of the current at 2.1 GHz pass through the LC series branch and all other harmonics mainly pass through transistors M_3 and M_4 . Figure 5.11(b)

also confirms that a smaller portion of odd harmonics of the current, rapidly dropping with frequency, passes through the series branch.

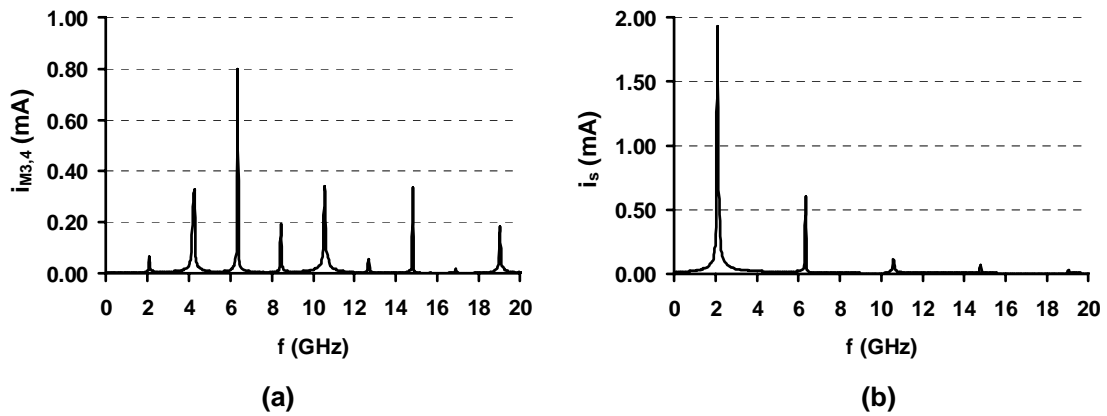


Figure 5.11: Simulated results of the ILFD in Figure 5.9 with no injected input power and for $f_{osc}=2.1$ GHz: (a) frequency contents of current in $M_{3,4}$, (b) frequency contents of current in the LC series branch of L_s and C_s

Since the current in an ordinary differential pair has a similar direction to the oscillator current in Figure 5.10 (b), it can be used to inject any of the odd harmonics to the oscillator core. Therefore, in principal, the structure of Figure 5.9 can be used as an odd frequency divider. However, as we move up to higher odd harmonics, the magnitude signal in the oscillator core decreases and the workable frequency range of the divider degrades as well. It is also worth noting that the divide-by-three ILFD in Figure 5.9 has the advantage of differential input over the divide-by-two circuit of Figure 5.8.

Compared to wide-band flip-flop based dividers, the general disadvantage of ILFDs is their limited tuning range. For instance, the simulated locking-range of the implemented 6.3 GHz ILFD divide-by-three versus the divider current consumption is shown in Figure 5.12. One can remedy the limited locking-range by adding a tunable part in the load capacitor C_d which can be tuned simultaneously with the VCO capacitor in the PLL. Subsequently, the center frequency of divider and the VCO change together.

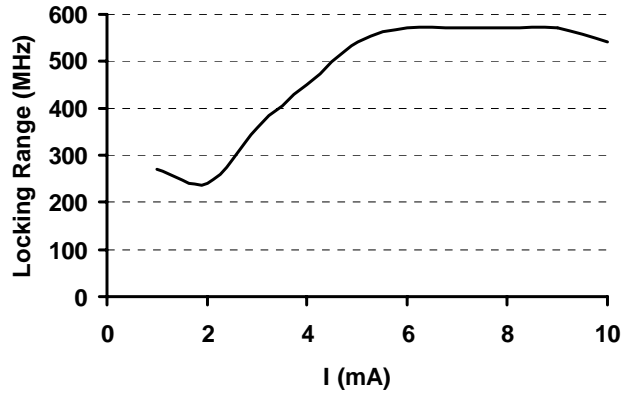


Figure 5.12: Simulated locking-range of the implemented ILFD-based 6.3 GHz divide-by-three versus divider's current consumption

L_d	5.2 nH ($Q_L \approx 7.5$)
C_d	300 fF
L_s	3.3 nH ($Q_L \approx 6.5$)
C_s	1.6 pF

L_d	14 nH ($Q_L \approx 5.5$)
C_d	2.7 pF
L_s	14 nH ($Q_L \approx 5.5$)
C_s	2.7 pF

$M_{1,2}$	$\frac{150\mu}{0.35\mu}$
$M_{3,4}$	$\frac{210\mu}{0.35\mu}$

$M_{1,2}$	$\frac{150\mu}{0.35\mu}$
$M_{3,4}$	$\frac{210\mu}{0.35\mu}$

(a)

(b)

Table 5.5: Component values of the implemented divide-by-three ILFDs in Figure 5.9 (a) 6.3 GHz to 2.1 GHz divider (b) 2.1 GHz to 0.7 GHz divider

Component values of the two implemented divide-by-threes are mentioned in Table 5.5. ILFDs are promising alternatives for high-frequency low-power dividers. In this subsection, we demonstrated an ILFD-based divide-by-three circuit an important block of the frequency generating section in the concurrent dual-band receiver.

5.3 Experimental Results

Both versions of the concurrent dual-band receiver were implemented in a $0.35\ \mu\text{m}$ BiCMOS technology only using CMOS transistor as active devices (Figure 5.13 and Figure 5.14). Each chip employs an area of $2.4\text{mm} \times 2.4\text{mm}$ and incorporates 48 pads mainly placed for test purposes. In the fully integrated revision of the chip fabricated later, certain parts of the layout were also changed in order to minimize line parasitics and to boost the overall dynamic range of the receiver. The designs were intended for a 3-metal layer version of the process with the thick top metal of $3\ \mu\text{m}$. Unfortunately, the fully integrated version was fabricated in a 4-metal version of the process due to an oversight by the foundry. The thickness of the third layer that is used to implement all inductors and other high-frequency routings in this process is about a fifth of the original one and hence the quality factor of all inductors is dramatically reduced. Therefore, the fully integrated version of the chip could not be measured successfully despite effort taken to this effect.

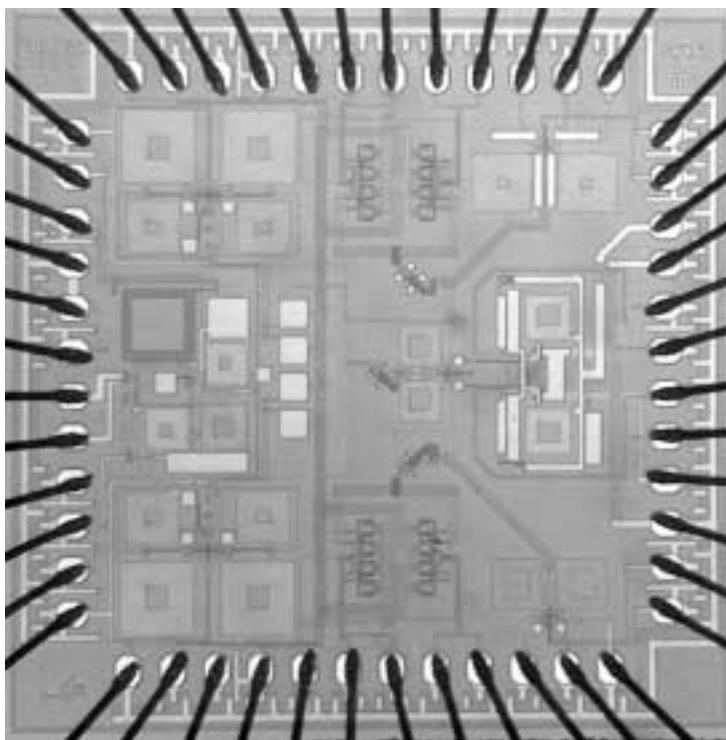


Figure 5.13: Die micrograph of the first version of concurrent receiver (off-chip LO)

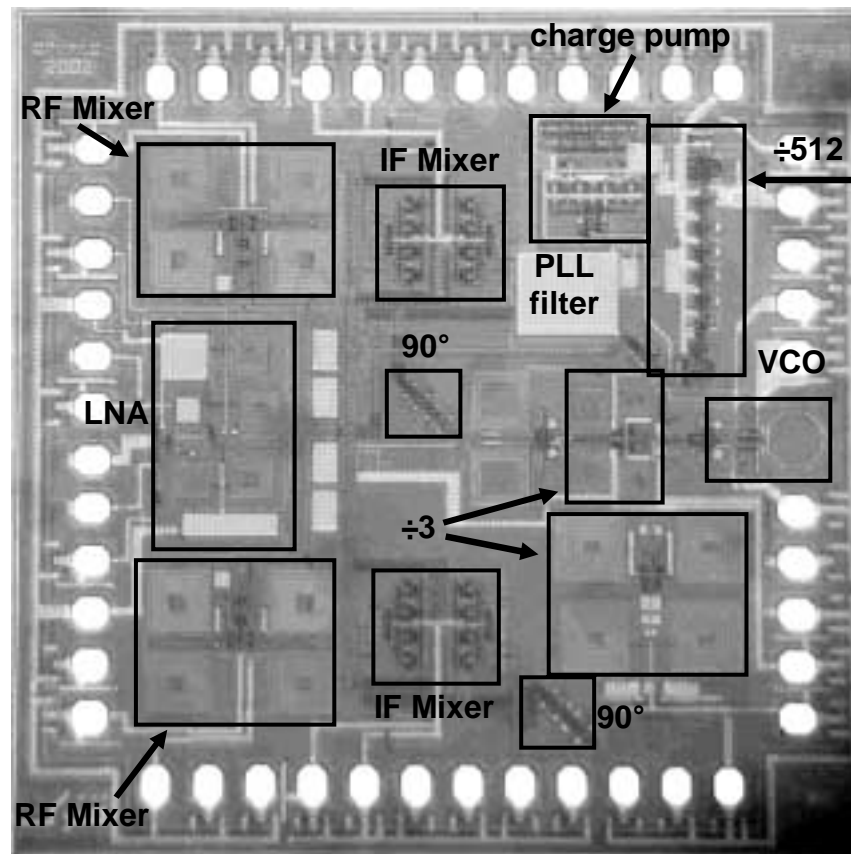


Figure 5.14: Die micrograph of the second version of concurrent receiver (fully integrated)

In order to measure the earlier version of the chip, it was packaged in a 48-pin Thin Quad Flat Package (TQFP) and mounted on a custom-made high-frequency Printed Circuit Board (PCB) (Figure 5.15). Several jumpers and SMA connectors on the PCB allowed for separate control and monitoring of power-supply and signals in different parts of the receiver chip. The on-chip VCO that generated the first LO signal was locked to a reference signal using an off-chip PLL programmed via the serial port of a laptop. The other two LO signals were fed by sweep signal generators. To emulate the concurrent signal reception, output signals of two sweep generators, one for each band, were combined before feeding the receiver input with a low-loss cable. A typical measurement setup is shown in Figure 5.16.

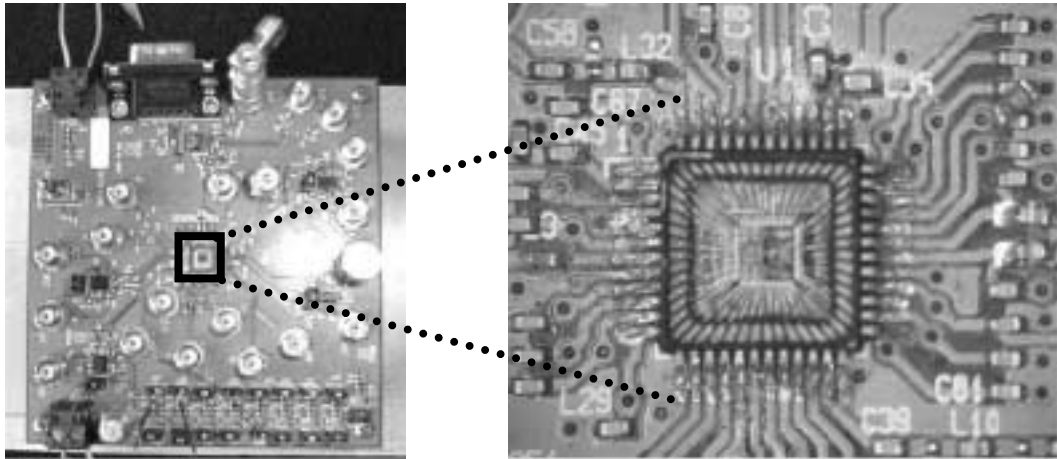


Figure 5.15: Test board to measure the performance of concurrent receiver

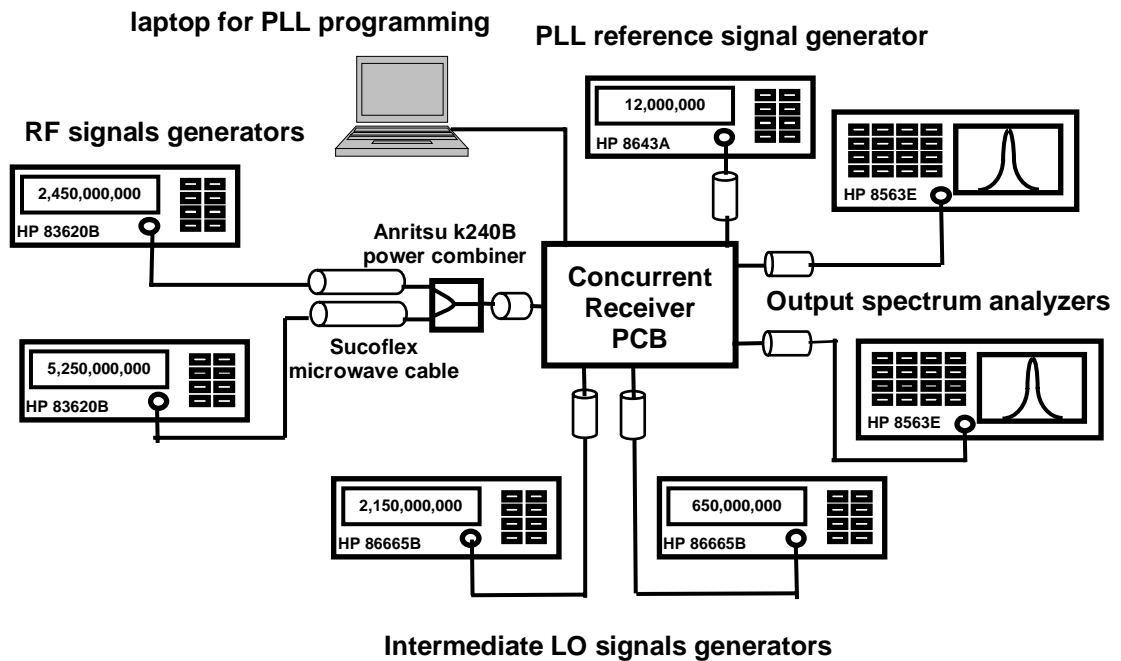


Figure 5.16: Typical measurement setup for the concurrent receiver

The measured gain of the receiver at the two bands of interest is illustrated in Figure 5.17. The gain is almost 10dB lower than the designed value. Post-processing of the simulation results revealed that lossy long ground lines in the LNA block are responsible for the loss of

gain. The slight change in the position of the second frequency band is attributed to the same layout issue. The layout has been fixed in the new fully integrated version of the concurrent receiver.

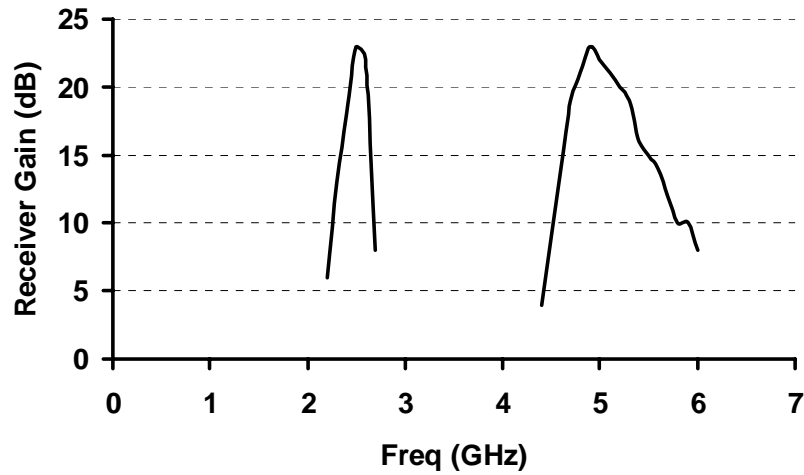


Figure 5.17: Measured gain of the concurrent receiver at two bands of interest.

The linearity performance of the receiver has to be evaluated in a method similar to that mentioned in the concurrent LNA case (Section 4.3.1.5). As a sample, the large-signal behavior of the receiver at the higher frequency band is shown in Figure 5.18.

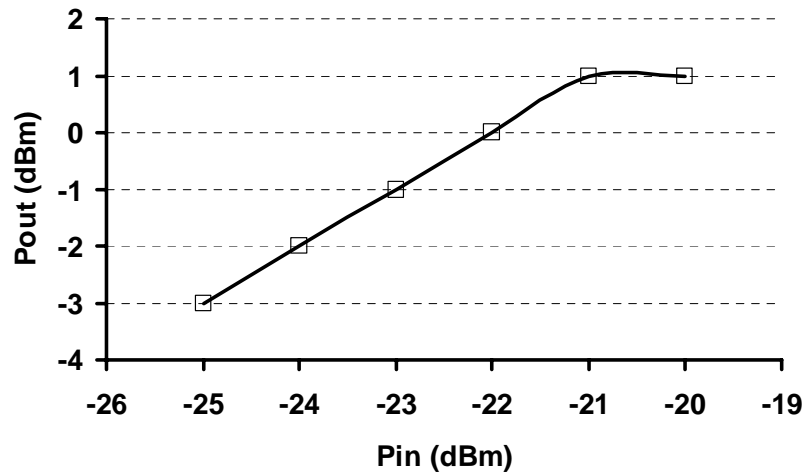


Figure 5.18: Large-signal gain characteristic of the receiver at the higher frequency band

The performance of the receiver is summarized in Table 5.6. The concurrent receiver yields a NF of better than 10dB at both bands that is an acceptable number for WLAN standards. In fact, the NF has been deteriorated due to the loss of LNA gain caused by layout issues. The on-chip image-rejection for the low band is about 69dB owing to the combination of image-reject architecture and the notch in concurrent LNA transfer function. The image-rejection at the high band is smaller (around 30dB) due to several factors. First, the LNA transfer function does not have a notch at that image frequency. Second, the second peak is slightly lower than the design value. Also, despite all the effort in the layout, path mismatches determining the image-rejection of this architecture demonstrate their effect more severely at higher frequencies. Moreover, this amount of image-rejection will be improved further due to the selectivity of the dual-band antenna and the consequent dual-band bandpass filter.

Frequency	2.45 GHz	5.25 GHz
Receiver Gain	23 dB	19 dB (peak: 23dB @ 4.9GHz)
S_{11}	< -12 dB	< -12 dB
NF	< 10 dB	< 10 dB
Input $IP3_{in-band}$	-8 dBm	-12 dBm
Input $CP1_{in-band}$	-17 dBm	-20 dBm
Input $CP1_{A>B}$	$CP1_{2.4>5.2} = -20$ dBm	$CP1_{5.2>2.4} = -16$ dBm
Image Rejection	≈ 69 dB	≈ 30 dB
DC Current	signal path (LNA + mixers): 28 mA LO path (VCO + buffers): 30 mA	
Supply Voltage	3 V	
Active Device	0.35- μ m CMOS transistors	
Die Area	2.4mm x 2.4mm	
Package	48-pin TQFP	

Table 5.6: Concurrent dual-band receiver performance summary

The fully integrated version of the concurrent dual-band receiver, which could not be measured due to the unfortunate mistake in the process run, was designed to alleviate the layout problems of the first chip and was expected to achieve a better gain, NF and image-rejection.

5.4 Summary

The design and implementation of the first concurrent dual-band receiver were described in this chapter. The receiver operates at 2.4 GHz and 5.2 GHz WLAN frequency bands simultaneously and can be used to enhance the data-rate and robustness of the wireless communication. In addition to the novel concurrent image-reject architecture, diligent frequency planning allows for the use of only one frequency synthesizer in the entire receiver, thereby reducing chip area and power consumption. Moreover, the concurrent receiver benefits from a number of novel building blocks such as concurrent dual-band amplifiers, mixers, and analog divide-by-three circuitry.

Chapter 6

Oscillators with Multi-Band Resonators

Oscillators are essential building blocks in many electrical systems, such as radio transceivers and digital electronics circuitry. When placed in a frequency-stabilizing feedback loop (such as a PLL), voltage- or current-controlled oscillators are used to generate an accurate frequency or time reference. Therefore, time waveform as well as frequency components of oscillators output are two major characteristics of such systems. In radio transceivers, local oscillators typically generate periodic waveforms that are used for the up- / down-conversion or sampling of the main information signal. As discussed in Chapters 2, in multi-band and multi-mode radio architectures, in order to process the information in various frequency bands, a number of local-oscillator (LO) frequencies are usually needed. More importantly, in concurrent radios described in Chapter 3, numerous LO frequencies are required at the same time. Since oscillators consume a substantial part of the chip area and battery power, methods to generate all these necessary LO waveforms in a compact design are very appealing. In Chapters 2, 3 and 5, we gave examples of radio architectures where elegant frequency planning allowed for the use of one oscillator core in addition to frequency dividers for the whole (concurrent) multi-mode systems. In this chapter we will discuss the simultaneous generation of two frequencies by an oscillator.

A large number of the electrical oscillators can be modeled by a nonlinear second-order differential equation. In these systems, the frequency of periodic oscillation is determined by a second-order resonator (*e.g.*, a series or parallel *LC*) connected to a nonlinear active core. In non-concurrent multi-band and multi-mode systems, where the LO tones for different modes/bands of operation are not simultaneously needed, the appropriate LO tone

can be selected by switching among multiple resonators all connected to a single active core [133].

In this chapter, we will focus on a special class of electrical oscillators with higher-order nonlinear differential equations. As will be shown, multi-resonance networks (*e.g.*, higher-order *LC* configurations) connected to a nonlinear active core, belong to this class of oscillators. These oscillators are capable of oscillations at either of their resonance frequencies as well as simultaneous oscillations at more than one frequency under certain conditions. As it will be shown with a few examples, multi-resonant oscillators can be used in the future novel multi-mode and multi-band radio systems.

In the rest of this chapter, an analysis of phase-noise (frequency fluctuations due to noise) in oscillators with general types of resonator load (*i.e.*, multi-band) will be presented. The analysis is based on a physical interpretation of *quality factor* (Q) in resonator-based oscillators and will lead to the design of low-phase noise oscillators using enhanced resonator structures.

6.1 Time-Domain Response of Multi-Frequency Oscillators

The output of most of the oscillators that are used in radio systems has a periodic waveform with a general form

$$x(t) = \sum_n A_n \cos(n\omega_0 t + \varphi_n) \quad (6.1)$$

Hence, the oscillator output can have energy at the fundamental frequency, ω_0 , and its harmonics. In resonator-based oscillators with a low resonator loss, the amplitude of harmonic terms are often substantially smaller than the amplitude of fundamental term.

However, in many radio architectures, particularly in multi-mode and multi-band systems, the required local-oscillator tones are not harmonically related. With the goal of designing efficient architectures for such systems, we would like to investigate the possibility of generating all the desired LO tones in one oscillator. The output waveform of such an oscillator would be

$$x(t) = \sum_n A_n \cos(\omega_n t + \varphi_n) \quad (6.2)$$

where in (6.2), the angular frequencies, ω_n , are not necessarily harmonically related. More generally, the ratios of these frequencies might be irrational resulting in a non-periodic waveform.

Oscillators that can simultaneously generate multiple frequencies have been studied in the literature [121]-[129]. After reviewing some of the previous work on multi-frequency oscillators, we will perform an analysis on an oscillator with a dual-resonance load. The analysis will show that simultaneous oscillations at two frequencies in that oscillator are indeed possible, making it suitable as a unique building block in multi-mode and multi-band radio architectures. As an introduction, we will initially review some of the features of the widely used second-order oscillator. We will demonstrate that these oscillators are incapable of generating non-periodic waveforms of the type expressed in (6.2). Therefore, we will focus on higher-order resonators to generate a set of non-harmonically-related frequencies.

6.1.1 A Brief Overview of Second-Order Oscillators

As mentioned before, a large class of practical oscillators can be sufficiently represented with a second-order nonlinear differential equation. A second-order passive resonator connected to a nonlinear active device often serves as an accurate model for second-order electrical oscillators (Figure 6.1).

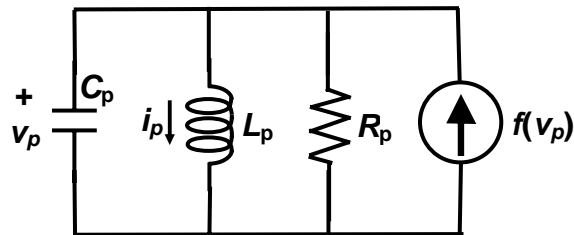


Figure 6.1: A simple model for a second-order electrical oscillator

In Figure 6.1, $f(V_p)$ represents the current generated by the active device as a nonlinear function of voltage across resonator. This nonlinearity is essential in maintaining a stable oscillatory waveform after an oscillation grows up. The effect of loss terms that are present in every real oscillator are captured in the parallel resistor, R_p . By defining the normalized capacitor voltage and inductor current as independent state variables, the nonlinear differential equation of the second-order oscillator can be formed in the following canonical representation

$$\dot{\mathbf{X}} = \begin{bmatrix} 0 & -\frac{1}{\sqrt{L_p C_p}} \\ \frac{1}{\sqrt{L_p C_p}} & 0 \end{bmatrix} \mathbf{X} + \begin{bmatrix} \frac{1}{\sqrt{C_p}} f\left(\frac{x_1}{\sqrt{C_p}}\right) - \frac{x_1}{R_p C_p} \\ 0 \end{bmatrix} \quad (6.3)$$

where

$$\mathbf{X} = \begin{bmatrix} \sqrt{C_p} v_p & \sqrt{L_p} i_p \end{bmatrix}^T \quad (6.4)$$

We can easily show that if $f'(v_p).R_p > 1$ a periodic oscillation with the angular frequency given by $\omega_0 = 1/\sqrt{L_p C_p}$ will start up²⁴, where $f'(v_p)$ is the time-derivative of $f(v_p)$. The exact solution to the above differential equation depends on the form of nonlinearity function $f(V_p)$. However, a number of general results apply to the two-dimensional (*i.e.*, second-order) nonlinear differential equations. In particular, a powerful theorem by Poincaré and Bendixson states that any solution for the nonlinear differential equation in two dimensions converges to either a periodic waveform, a fixed-point (*i.e.*, no transient) or a combination of the two [134].

Interestingly, based on the Poincaré-Bendixson theorem, generation of multiple tones with irrational ratios in second-order systems resulting in non-periodic waveform is prohibited. More specifically, oscillators with second-order resonators are generally incapable of providing all the necessary LO signals that might be needed for a (concurrent) multi-band system. In the next sections, we will discuss the possibility of generating non-

²⁴ Intuitively, the inequality $f'(v_p).R_p > 1$ can be derived by finding the condition in which the closed loop-gain of the oscillator becomes larger than one, *i.e.*, $g_m.R_p > 1$ where g_m is the small-signal transconductance of the active device with the nonlinear function f .

periodic waveforms similar to the ones expressed in (6.2) with higher-order resonators in an oscillator.

As an example of a second-order nonlinear system, we will consider the oscillator in Figure 6.2. The cross-coupled differential-pair configuration with a simple LC resonant load along with its variations have become a popular choice for integrated high-frequency oscillators [132]. Intuitively and in circuit terms, an effective negative resistance is formed by the cross-coupled differential pair and the passive resonator makes the necessary phase shift of 360° at the appropriate frequency to maintain an oscillation. Later, we will analyze an oscillator that has the same active core (*i.e.*, negative-resistance), but uses a higher-order resonator structure.

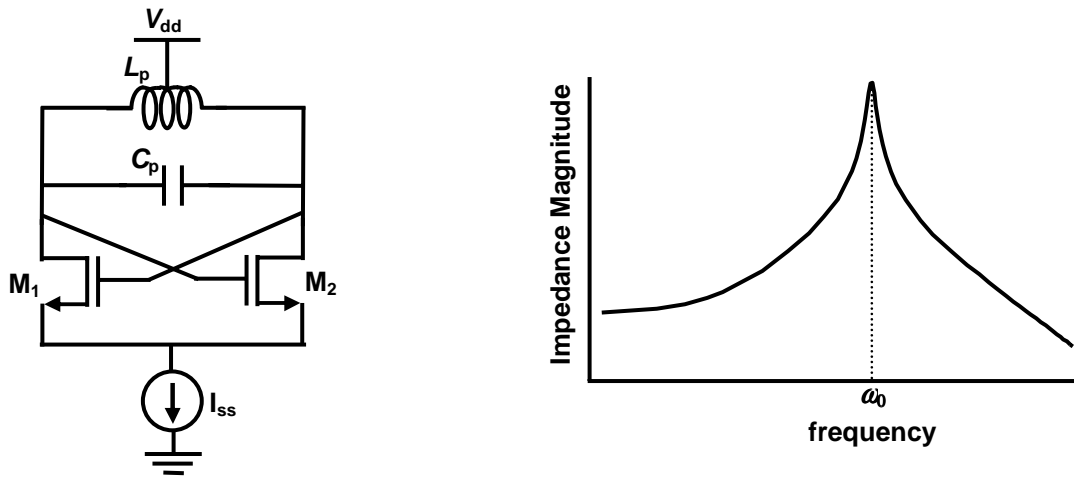


Figure 6.2: Cross-coupled pair oscillator with a simple second order LC resonator and the plot of resonator's impedance magnitude

Assuming that during the entire oscillation cycle, the current of MOSFET transistors, M_1 and M_2 are governed by a square-law equation with respect to their gate-source voltage, *i.e.*,

$$I_{M_{1,2}} = k(V_{GS} - V_T)^2 \quad (6.5)$$

Then the nonlinear function, $f(V_p)$, can be simply written as²⁵

²⁵ Note that usually transistors M_1 and M_2 enter the triode and cut-off region during the oscillation cycle and hence the nonlinear function $f(V_p)$ is more complicated and can not be expressed in a simple form of (6.6).

$$I_{M_1} - I_{M_2} = f_{MOSFET}(v_p) = k \cdot v_p \cdot \sqrt{\frac{2I_{ss}}{k} - v_p^2} \quad (6.6)$$

If bipolar junction transistors, Q_1 and Q_2 are used instead, the nonlinear function will then be

$$I_{Q_1} - I_{Q_2} = f_{BJT}(v_p) = I_{ee} \cdot \tanh\left(\frac{v_p}{2V_{th}}\right) \quad (6.7)$$

where $V_{th} = 4k_B T/q$ is the thermal voltage that has a value of about 25.8mV at room temperature.

6.1.2 A Brief Review of Previous Work

Oscillator with higher-order nonlinear differential equations and the possibility of simultaneous multi-frequency oscillations have been studied for a long time. In one of the early works, van der Pol analyzed a certain triode oscillator with two degrees of freedom created by two coupled resonators²⁶ (Figure 6.3) [121]. Similar to the second-order case of (6.3), the fourth-order nonlinear differential equation for this case can be formed, revealing two resonant modes. Van der Pol showed that if the nonlinear function, f , can be modeled with a third-order polynomial²⁷, simultaneous oscillations at two frequencies is unstable.

In his approach, a hypothetical solution similar to (6.2) that is the sum of both resonant modes is inserted into the nonlinear differential equation. After simplifying the problem based on physical intuition, he proves that under no condition both resonant amplitudes can be nonzero. The underlying assumption in his derivation was the non-existence of higher harmonics and intermodulation terms in the solution for highly selective tanks.

²⁶ Interestingly, this particular type of oscillator that uses coupled inductors show a better phase-noise performance compared to the resonators without coupling terms and will be covered later in this Chapter.

²⁷ The current in the triode as a function of grid voltage represents the nonlinear function in Figure 6.3.

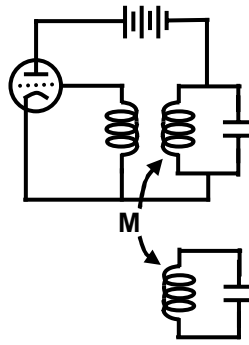


Figure 6.3. Triode oscillator with two degrees of freedom analyzed in [121]

Schaffner showed that an oscillator with two-degrees of freedom, under certain conditions, can oscillate simultaneously at two different frequencies [122]. The ratio of the frequencies may either be rational (*synchronous* oscillation) or irrational (*asynchronous* oscillation). Asynchronous solutions are not periodic and are referred to as “*almost-periodic*” or “*quasi-periodic*” solutions in the literature [131]. Schaffner needed a 5th order nonlinear term in the power series expansion of current-to-voltage characteristic of the active part to achieve stable simultaneous oscillations. A method of equivalent linearization of the nonlinear differential equation is pursued in his paper. In this approach, formally known as *averaging method*, the structure of the solution is determined by the unperturbed linear equation. Then, the average amplitudes are established by a linearized equation that is equivalent to the original nonlinear equation in power (*i.e.*, the difference between the original non-linear equation and the linearized one shrinks with a certain power). This method has been pursued by others in analyzing simultaneous multi-frequency oscillations in other cases such as Class-C oscillators [123] and coupled-resonator oscillators similar to Figure 6.3 [124].

Endo and Mori have used the same linearization principal in analyzing simultaneous multi-mode solutions in ladder networks of nonlinear oscillators with van der Pol dynamics [125]. Their matrix-based analysis method, referred to as *mode-analysis* method, has been used by others to investigate simultaneous oscillations in coupled van der Pol oscillators that models the myoelectrical activity in the human large intestine [126].

More recently, Chua and Endo provided a rigorous mathematical foundation for the mode-analysis method using integral manifolds to analyze the periodic and quasi-periodic oscillations in various types of coupled oscillators [127],[128].

Finally, it should be mentioned that in a number of multi-frequency oscillators, synchronous or asynchronous, linear combination(s) of the resonant frequencies might appear in the solution as well [129].

6.1.3 Problem Formulation of a Fourth-Order System

In this section, we will perform an analysis on a fourth-order oscillator that is formed by connecting a dual-band resonator to a nonlinear active network (Figure 6.4). Once again, $f(V_p)$ is the active network's non-linear current characteristic and R_p represents the equivalent resistance of the entire tank²⁸.

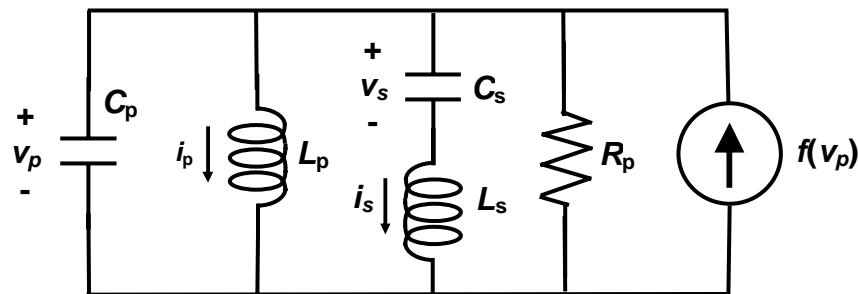


Figure 6.4: The simple model used to analyze the oscillator in Figure 6.6

In the following, in order to analyze the fourth-order oscillator of Figure 6.4, the nonlinear differential equation describing the system will be formed as a combination of a linear section and a nonlinear perturbation component. The structure of the solution of the complete nonlinear system is then hypothesized by means of the solution to the linear

²⁸ The physical sources of this resistance in the resonator include the ohmic loss of the inductors and capacitors, the loss in semiconductor substrate, and the finite output resistance of active devices. Derivation of an analytical solution to the problem with the consideration of all these individual sources, although straight forward and similar to the simplified case, is more tedious and does not offer any fundamental difference in the final conclusions. For instance, the nonlinear differential equation including some of these individual sources of loss is briefly described in Appendix C. In any case, the exact numerical solution, even with

section. Then, similar to averaging methods that were briefly mentioned in subsection 6.1.2, assuming slowly varying amplitude for the solution and using a polynomial expansion for the nonlinear terms, nonlinear differential equations for the slowly-varying (*i.e.*, average) amplitude will be derived. Finally, the steady-state solutions of interest are found and their stability is checked via standard methods used in analyzing nonlinear dynamical systems [134].

The impedance function of the resonator of Figure 6.4 reveals two resonant peaks at ω_1 and ω_2 with a notch at a frequency, ω_s , in between the two (Figure 6.5). As shown in Figure 6.5, by placing the notch frequency closer to either of the resonant frequencies, the impedance magnitude at the other frequency increases.

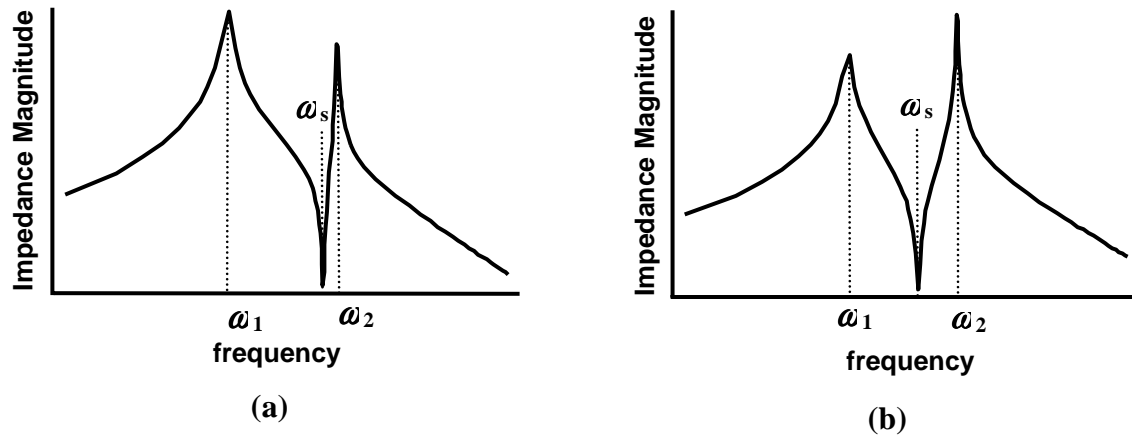


Figure 6.5: Impedance magnitude of the fourth-order resonator of Figure 6.4 when ω_s is closer to: (a) ω_2 , (b) ω_1

The dual-band resonant load has four independent energy storing elements resulting in a fourth-order system. By defining normalized inductor currents and capacitor voltages as independent state variables and applying Kirchoff's current and voltage laws, the circuit in Figure 6.4 can be described using the following set of nonlinear equations in matrix form

complete models for each component, can always be found using circuit simulators. The solution to the simplified case captures all the essence intended here.

$$\dot{\mathbf{X}} = \begin{bmatrix} 0 & \omega_p & 0 & 0 \\ -\omega_p & 0 & -\omega_c & 0 \\ 0 & \omega_c & 0 & -\omega_s \\ 0 & 0 & \omega_s & 0 \end{bmatrix} \mathbf{X} + \begin{bmatrix} 0 \\ \frac{1}{\sqrt{C_p}} f_t\left(\frac{x_2}{\sqrt{C_p}}\right) \\ 0 \\ 0 \end{bmatrix} \quad (6.8)$$

where

$$\mathbf{X} = \left[\sqrt{L_p} i_p \quad \sqrt{C_p} v_p \quad \sqrt{L_s} i_s \quad \sqrt{C_s} v_s \right]^T \quad (6.9)$$

and where ω_p and ω_s are resonance frequencies for the parallel and series LC branches, respectively, and ω_c is a frequency term associated with the coupling between the series and parallel branches. More specifically,

$$\omega_p = \frac{1}{\sqrt{L_p C_p}}, \quad \omega_s = \frac{1}{\sqrt{L_s C_s}}, \quad \omega_c = \frac{1}{\sqrt{L_s C_p}} \quad (6.10)$$

Also, the nonlinear function, f_t , consists of the current flowing through the active network, f , and the current through resistor R_p .

$$f_t(v_p) = f(v_p) - v_p / R_p \quad (6.11)$$

Basic circuit theory can be used to show that oscillation starts to build-up from a zero condition if the small-signal loop gain is greater than one, *i.e.*, $g_m R_p > 1$, where g_m is the transconductance of the active device. More systematically, we can obtain the same result by looking at the location of the eigenvalues of the Jacobean matrix of the zero solution of (6.8) [134]

$$\mathbf{J} = \begin{bmatrix} 0 & \omega_p & 0 & 0 \\ -\omega_p & \frac{1}{C_p} \cdot \left. \frac{df_t(x)}{dx} \right|_{x=0} & -\omega_c & 0 \\ 0 & \omega_c & 0 & -\omega_s \\ 0 & 0 & \omega_s & 0 \end{bmatrix} = \begin{bmatrix} 0 & \omega_p & 0 & 0 \\ -\omega_p & \left(g_m - \frac{1}{R_p} \right) \cdot \frac{1}{C_p} & -\omega_c & 0 \\ 0 & \omega_c & 0 & -\omega_s \\ 0 & 0 & \omega_s & 0 \end{bmatrix} \quad (6.12)$$

The characteristic equation of the Jacobean can be written as

$$|\mathbf{J} - \lambda \mathbf{I}| = \lambda^4 - \left(g_m - \frac{1}{R_p} \right) \cdot \frac{1}{C_p} \cdot \lambda^3 + (\omega_p^2 + \omega_s^2 + \omega_c^2) \cdot \lambda^2 - \left(g_m - \frac{1}{R_p} \right) \cdot \frac{1}{C_p} \cdot \omega_s^2 \cdot \lambda + \omega_p^2 \omega_s^2 \quad (6.13)$$

By applying Ruth-Hurwitz method to the characteristic equation of (6.13), we will find that $g_m R_p > 1$ is the necessary condition to have right-hand plane (RHP) roots leading to an amplitude growth and possible oscillation.

The matrix formulation of the problem as in (6.8) is useful for applying a variety of techniques to find the solutions of this system [134]. With a little bit of algebraic manipulation, a single equation for one of the state variables (*e.g.*, normalized tank voltage, x_2 , in this case) can also be derived as,

$$x_2^{(4)} + (\omega_p^2 + \omega_s^2 + \omega_c^2)x_2^{(2)} + (\omega_p^2 \omega_s^2)x_2 = \frac{d^3}{dt^3} g(x_2) + \omega_s^2 \frac{d}{dt} g(x_2) \quad (6.14)$$

$$g(x_2) = \frac{1}{\sqrt{C_p}} f_t \left(\frac{x_2}{\sqrt{C_p}} \right)$$

where $x_2^{(n)}$ represents the n^{th} derivative of x_2 with respect to time. As a reminder, x_2 is the normalized tank voltage and $g(x_2)$ is the normalized current characteristic of the active device and tank loss. We assume that $g(x_2)$, a nonlinear function of x_2 , is analytic and can be expressed as a converging Taylor series expansion with respect to x_2 , *i.e.*,

$$g(x_2) = \sum_{i=1}^{\infty} k_i x_2^i \quad (6.15)$$

where

$$k_i = \frac{1}{i!} \frac{d^i}{dx_2^i} g(x_2) \quad (6.16)$$

The first coefficient in the above series, k_1 , will be a part of linearized differential equation and is equal to

$$k_1 = \frac{g_m - 1/R_p}{C_p} \quad (6.17)$$

which is the effective negative conductance divided by the total tank capacitance.

For instance, if the cross-coupled pair showed in Figure 6.2 is used as the nonlinear function for the discussed fourth-order system (Figure 6.6), the Taylor expansion coefficients of the nonlinear function, f , based on (6.6) and (6.7) are

$$g_{MOSFET}(x_2) = \frac{1}{\sqrt{C_p}} \cdot \left[\left(g_m - \frac{1}{R_p} \right) \frac{x_2}{\sqrt{C_p}} - \frac{1}{4} g_m \left(\frac{k}{I_{ss}} \right) \left(\frac{x_2}{\sqrt{C_p}} \right)^3 - \frac{1}{32} g_m \left(\frac{k}{I_{ss}} \right)^2 \left(\frac{x_2}{\sqrt{C_p}} \right)^5 + O(x_2^7) \right] \quad (6.18)$$

where

$$g_m = \sqrt{2kI_{ss}} \quad (6.19)$$

and

$$g_{BJT}(x_2) = \frac{1}{\sqrt{C_p}} \cdot \left[\left(g_m - \frac{1}{R_p} \right) \frac{x_2}{\sqrt{C_p}} - \frac{1}{3} g_m \left(\frac{g_m}{I_{ee}} \right)^2 \left(\frac{x_2}{\sqrt{C_p}} \right)^3 + \frac{2}{15} g_m \left(\frac{g_m}{I_{ee}} \right)^4 \left(\frac{x_2}{\sqrt{C_p}} \right)^5 + O(x_2^7) \right] \quad (6.20)$$

for a bipolar junction transistor where

$$g_m = \frac{I_{ee}}{2V_{th}} \quad (6.21)$$

Note that g_m is the small-signal transconductance of each transistor for a balanced differential pair. Clearly, even order terms in the above series are zero because of the symmetric differential structure.

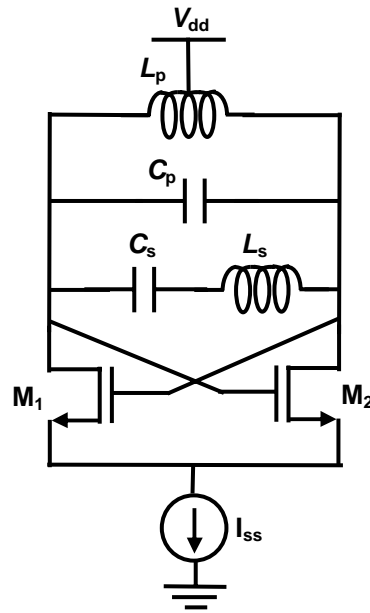


Figure 6.6: Cross-coupled pair oscillator with the fourth-order dual-resonance tank depicted in Figure 6.4

6.1.4 Multi-Frequency Oscillations in Fourth-Order System

To analyze the multiple responses of the oscillator, an approximate averaging method based on linearized differential equation, similar to the methods that were discussed in subsection 6.1.2, will be used. Using (6.15), the nonlinear differential equation in (6.14) can be split into a linear differential equation and nonlinear perturbation terms.

$$\begin{aligned}
 x_2^{(4)} - (k_1)x_2^{(3)} + (\omega_p^2 + \omega_s^2 + \omega_c^2)x_2^{(2)} - (k_1\omega_s^2)x_2^{(1)} + (\omega_p^2\omega_s^2)x_2 \\
 = \sum_{i>1} k_i \left(\frac{d^3}{dt^3}(x_2^i) + \omega_s^2 \frac{d}{dt}(x_2^i) \right)
 \end{aligned} \tag{6.22}$$

The solution to the linear differential equation (left-hand side of (6.22)) has the general form of

$$x_2(t) = \sum_{i=1}^4 \exp(\alpha t) \tag{6.23}$$

where the values of α can be found from the following fourth-order polynomial equation:

$$\alpha^4 - (k_1)\alpha^3 + (\omega_p^2 + \omega_s^2 + \omega_c^2)\alpha^2 - (k_1\omega_s^2)\alpha + (\omega_p^2\omega_s^2) = 0 \quad (6.24)$$

In an oscillatory solution, the roots of (6.24) appear in complex conjugate pairs, *i.e.*, $\alpha = \tau_1 \pm i\omega_1$ and $\alpha = \tau_2 \pm i\omega_2$. For oscillation start-up, the values of τ_1 and τ_2 have a positive sign showing an amplitude growth. As the amplitude grows up, the nonlinear terms in (6.22) should also be considered to calculate the steady-state response of the solution. The oscillation frequencies, ω_1 and ω_2 are derived from

$$\omega_{1,2}^4 - (\omega_p^2 + \omega_s^2 + \omega_c^2)\omega_{1,2}^2 + \omega_p^2\omega_s^2 = 0 \quad (6.25)$$

Based on the above arguments for the linear equation, the general solution for the nonlinear differential equation (6.22) is postulated as

$$x_2(t) = a_1(t) \cdot \cos(\omega_1 t + \phi_1) + a_2(t) \cdot \cos(\omega_2 t + \phi_2) \quad (6.26)$$

Plugging (6.26) in (6.22), using the nonlinear power series of up to a 3rd order, and assuming that high order derivatives of a_1 and a_2 are negligible (slowly varying amplitudes) results in the following set of equations

$$\begin{aligned} a_1[\omega_1^4 - (\omega_p^2 + \omega_s^2 + \omega_c^2)\omega_1^2 + \omega_p^2\omega_s^2] &= \left(k_1\dot{a}_1 + \frac{9}{4}k_3\dot{a}_1a_1^2 + \frac{3}{2}k_3\dot{a}_1a_2^2 + 3k_3a_1\dot{a}_2a_2 \right) (-3\omega_1^2 + \omega_s^2) \\ a_2[\omega_2^4 - (\omega_p^2 + \omega_s^2 + \omega_c^2)\omega_2^2 + \omega_p^2\omega_s^2] &= \left(k_1\dot{a}_2 + \frac{9}{4}k_3\dot{a}_2a_2^2 + \frac{3}{2}k_3\dot{a}_2a_1^2 + 3k_3a_2\dot{a}_1a_1 \right) (-3\omega_2^2 + \omega_s^2) \\ 2[2\omega_1^2 - (\omega_p^2 + \omega_s^2 + \omega_c^2)]\dot{a}_1 &= (\omega_1^2 - \omega_s^2) \left(k_1a_1 + \frac{3}{4}k_3a_1^3 + \frac{3}{2}k_3a_1a_2^2 \right) \\ 2[2\omega_2^2 - (\omega_p^2 + \omega_s^2 + \omega_c^2)]\dot{a}_2 &= (\omega_2^2 - \omega_s^2) \left(k_1a_2 + \frac{3}{4}k_3a_2^3 + \frac{3}{2}k_3a_2a_1^2 \right) \end{aligned} \quad (6.27)$$

In the postulated solution in (6.26), harmonic and cross-coupling terms between two modes have been neglected because of the highly-selective resonator and hence have not been considered in (6.27) either.

In steady-state, the amplitudes would be fixed and $\dot{a}_1 = \dot{a}_2 = 0$. Applying this condition to (6.27) and solving the corresponding equations results in 4 different solutions for (a_1, a_2) :

$$\begin{cases} a_1 = 0 \\ a_2 = 0 \end{cases}, \quad \begin{cases} a_1 = 0 \\ a_2 = \sqrt{-\frac{4 k_1}{3 k_3}} \end{cases}, \quad \begin{cases} a_1 = \sqrt{-\frac{4 k_1}{3 k_3}} \\ a_2 = 0 \end{cases}, \quad \begin{cases} a_1 = \frac{2}{3} \sqrt{\frac{k_1}{k_3}} \\ a_2 = \frac{2}{3} \sqrt{\frac{k_1}{k_3}} \end{cases} \quad (6.28)$$

To check the stability of each of the steady-state solutions in (6.28), we form the Jacobean matrix of the final two equations in (6.27)

$$\begin{cases} \dot{a}_1 = \beta_1 \left(k_1 a_1 + \frac{3}{4} k_3 a_1^3 + \frac{3}{2} k_3 a_1 a_2^2 \right) \\ \dot{a}_2 = \beta_2 \left(k_1 a_2 + \frac{3}{4} k_3 a_2^3 + \frac{3}{2} k_3 a_2 a_1^2 \right) \end{cases} \quad (6.29)$$

where

$$\beta_i = \frac{(\omega_i^2 - \omega_s^2)}{2[2\omega_i^2 - (\omega_p^2 + \omega_s^2 + \omega_c^2)]}, \quad i=1,2 \quad (6.30)$$

Each set of the solutions in (6.28) is stable only if the eigenvalues of the Jacobean have negative real part. For the first set of solutions when both amplitudes are zero (*i.e.*, no oscillation occurring), the characteristic equation of the Jacobean can be written as

$$\begin{cases} a_1 = 0 \\ a_2 = 0 \end{cases} \Rightarrow |J - \lambda I| = \begin{vmatrix} \beta_1 k_1 - \lambda & 0 \\ 0 & \beta_2 k_1 - \lambda \end{vmatrix} \quad (6.31)$$

As once showed before, if $k_l > 0$ (or equivalently $g_m R_p > 1$) both roots of the characteristic equation will have positive signs proving the instability of this solution.

The second and third sets of solutions in (6.28) correspond to cases where oscillation takes place at one of the resonant frequencies: ω_1 or ω_2 . The characteristic equation when oscillation at ω_2 occurs is

$$\begin{cases} a_1 = 0 \\ a_2 = \sqrt{-\frac{4 k_1}{3 k_3}} \end{cases} \Rightarrow |J - \lambda I| = \begin{vmatrix} -\beta_1 k_1 - \lambda & 0 \\ 0 & -2\beta_2 k_1 - \lambda \end{vmatrix} \quad (6.32)$$

In this case, with $k_1 > 0$ and $k_3 < 0$, the roots of the characteristic equation of (6.32) have negative signs showing a stable solution. Clearly, the same conclusion can be derived for the case where oscillation occurs at ω_1 . In other words, the nonlinear fourth-order system is capable of producing stable oscillation at either of its resonant modes.

It is worth mentioning that the oscillation amplitude in these cases can also be derived based on energy arguments. Assuming an oscillation at one of the resonant modes, *i.e.*, ω_1 , the total stored energy in the resonator can be written as

$$\begin{aligned} E_{resonator} &= \frac{1}{2} L_p i_p^2 + \frac{1}{2} C_p v_p^2 + \frac{1}{2} L_s i_s^2 + \frac{1}{2} C_s v_s^2 \\ &= \frac{1}{2} \sum x_i^2 = \frac{1}{2} \mathbf{X}^T \mathbf{X} \end{aligned} \quad (6.33)$$

where the normalized variables defined in (6.8) were used to derive the second line of (6.33). Using the differential equations in (6.8), we can show that the rate of energy change in resonator can be simplified to

$$\frac{dE_{resonator}}{dt} = \frac{1}{2} \frac{d(\mathbf{X}^T \mathbf{X})}{dt} = v_p f_t(v_p) \quad (6.34)$$

which is not surprisingly equal to the total power entering into (or flowing outward of) the resonator. For a steady-state stable oscillation, the rate of resonator energy change in every period is zero. Hence

$$\int_0^T \frac{dE_{resonator}}{dt} dt = \int_0^T v_p f_t(v_p) dt = 0 \quad (6.35)$$

Assuming that the oscillator is generating only one of its resonant modes in steady-state, we may write

$$v_p(t) = a_1 \cdot \cos(\omega_1 t + \phi_1) \quad (6.36)$$

For a known nonlinear function, $f_t(v_p)$, the oscillation amplitude, a_1 , can then be derived by replacing the steady-state solution of (6.36) in the expression (6.35). For a third-order nonlinear function of $f_t(v_p)$, we can easily show that the amplitudes will be the same as predicted by (6.28) proving consistent results²⁹.

The fourth solution in (6.28) corresponds to simultaneous oscillations at both resonant frequencies, ω_1 and ω_2 . The characteristic equation in this case is

²⁹ The derivation of oscillation amplitude based on energy arguments is a general method and can be applied to any other higher-order resonator as well. In particular, for any oscillator that, similar to Figure 6.4, can be

$$\begin{cases} a_1 = \frac{2}{3} \sqrt{-\frac{k_1}{k_3}} \\ a_2 = \frac{2}{3} \sqrt{-\frac{k_1}{k_3}} \end{cases} \Rightarrow |J - \lambda I| = \begin{vmatrix} -\frac{2}{3}\beta_1 k_1 - \lambda & \frac{4}{3}\beta_1 k_1 \\ \frac{4}{3}\beta_2 k_1 & -\frac{2}{3}\beta_2 k_1 - \lambda \end{vmatrix} \quad (6.37)$$

$$= \lambda^2 - \frac{2}{3}(\beta_1 + \beta_2)k_1 \lambda - \frac{4}{3}\beta_1 \beta_2 k_1^2$$

As (6.37) indicates, eigenvalues of the Jacobean matrix have opposite signs showing a saddle point (Figure 6.7). In other words, for the fourth-order system of discussion and assuming a third-order nonlinear expansion, simultaneous multi-frequency oscillations is not a stable response.

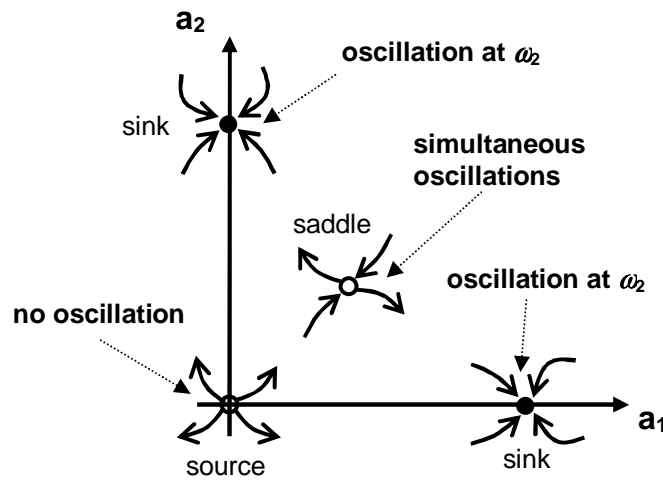


Figure 6.7: Graphical representation of the stability of multiple solutions to (6.14) for a 3rd order power expansion of the nonlinear voltage-current characteristic

While this results shows that it is not possible to maintain two simultaneous asynchronous tones in a third-order oscillator, it should not be generalized to higher-order systems. Following the same procedure for higher order nonlinearities *does* result in simultaneous oscillations under certain conditions for the coefficients in the power series. The results for a fifth order nonlinearity expansion is presented in Appendix D. We will not

modeled with a parallel combination of a resonator and a nonlinear current source as a function of resonator voltage, the steady-state resonator amplitude is identical to what we derived using (6.35).

show the same algebraic analysis in this chapter for the brevity and will limit ourselves to the simulation results showing the possibility of such simultaneous oscillations.

Practically, the steady-state response of oscillators depends on the bias conditions as well as its initial conditions. In Appendix D, we show a set of bias conditions for the generation of stable simultaneous oscillations in a particular example. In addition, if a nonlinear system has multiple attractors or sinks in the state-space (*i.e.*, two in Figure 6.7), the steady-state solution will depend on the initial conditions [134]. Loosely speaking, by setting the initial conditions closer to one of the stable points, the output will converge to that solution. The basin of attraction for the stable points depends on the nonlinear function [134] and often is found numerically. Through a number of circuit simulations of multi-frequency oscillators such as the one in Figure 6.6, we observed that by increasing the loop-gain at one of the possible output frequencies, the oscillator tends to oscillate at that mode. This observation might correspond to an increase in the size for the region of attraction of that stable mode. Note that for the same resonant frequencies and passive quality factors, by changing the position of zero (ω_s in Figure 6.5) in the resonator impedance magnitude function, the value of loop-gain can be modified.

As an example, consider a cross-coupled oscillator of Figure 6.6 with a dual resonance load at frequencies $\omega_1=1.26$ GHz and $\omega_2=7$ GHz. The zero in dual-resonator impedance function, ω_s , is set at 3.8 GHz. For a given load capacitor, C_p , the values for other tank passives can be calculated from (6.25) to be: $C_p=2.63$ pF, $L_p=1.77$ nH, $C_s=5.6$ pF, and $L_s=0.31$ nH. From our circuit simulations it was revealed that for moderate nonlinearity, this circuit will oscillate at the lower resonant frequency with a higher loop gain (Figure 6.5 (a)). However, if we move ω_s closer to ω_1 , the oscillation will happen at the higher frequency, ω_2 (Figure 6.5 (b)). The predicted simultaneous oscillations for higher-order nonlinearity terms in the power series expansion (*e.g.*, Appendix D) can be observed in circuit simulations too (Figure 6.8). As previously mentioned, in most cases the nonlinearity terms can be modified by simply changing the bias condition. Notice the quasi-periodic nature in the time-domain response of the oscillator confirming an asynchronous oscillation.

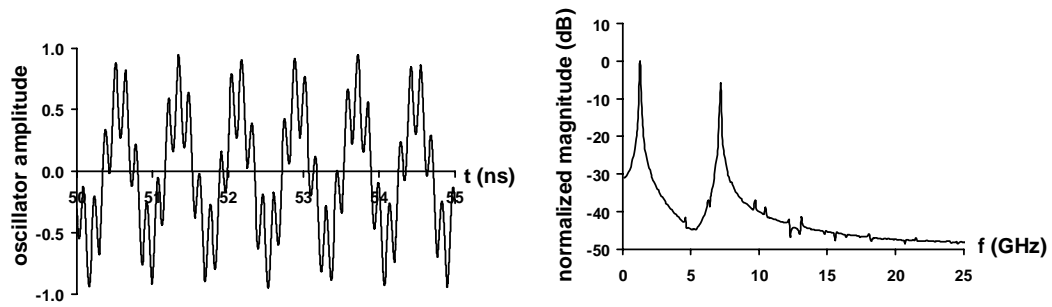


Figure 6.8: Simulation results showing asynchronous oscillations in Figure 6.6

As another example and in order to illustrate the occurrence of synchronous simultaneous oscillations in a different oscillator topology, a Colpitts-type oscillator with a fourth-order resonator is shown in Figure 6.9. The dual-band resonator is tuned at two harmonically related frequencies of 500 MHz and 7.5 GHz. Simulation results reveal the possibility of synchronous oscillations under certain bias conditions in addition to a response at either of the frequencies. A small presence of cross-coupling terms between the two modes is apparent in frequency spectrum of this example. Synchronous oscillations can be studied using the general methods discussed in subsection 6.1.2.

In summary, oscillators with multi-band resonators are capable of generating oscillations at either of their resonant frequencies as well as simultaneous synchronous or asynchronous oscillations at a combination of those frequencies. In this chapter, we performed analysis on one class of these oscillators with a dual-band resonator and demonstrated the possibility of simultaneous asynchronous oscillations under certain conditions. Simultaneous oscillations can also be observed in circuit simulators with more complete and realistic nonlinearity functions. Some of the potential applications of multi-frequency oscillators will be discussed in the next subsection.

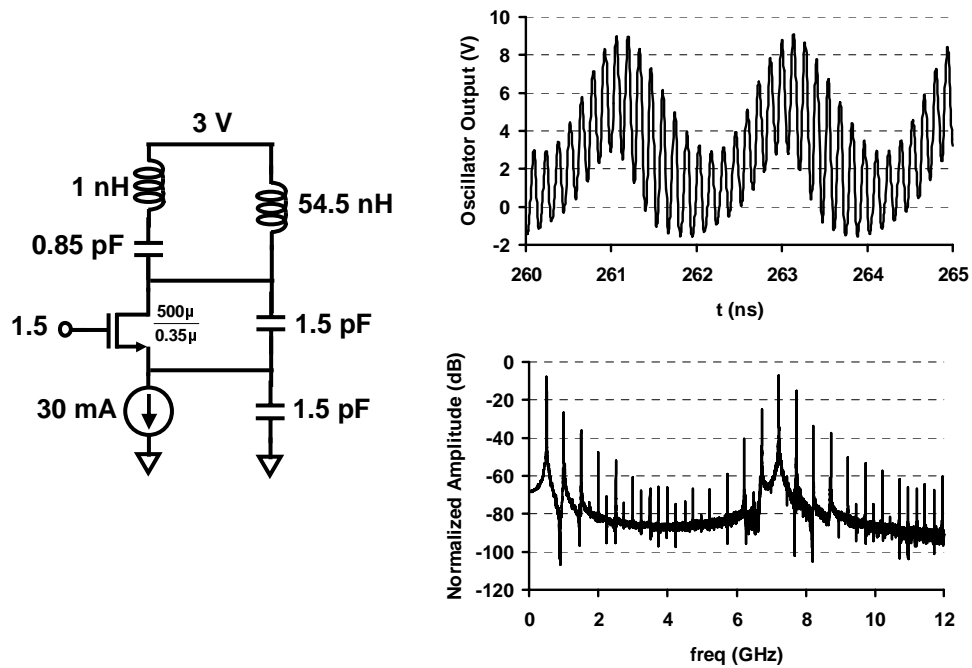


Figure 6.9: Dual-band Colpitts-type oscillator generating synchronous oscillations

6.1.5 A Few Potential Applications of Multi-Frequency Oscillations

In many instances, the observed simultaneous oscillations are parasitic and undesirable. However, synchronous oscillation may be used in generating power at high frequencies which are exact multiples of a lower frequency of oscillation [122]. For example, power at a higher harmonics can be extracted while the oscillation at lower frequency is possibly synchronized to an outside source (*harmonic loading*).

Another traditional application of simultaneous oscillations is in touch-tone phones where a system known as dual-tone multi-frequency (DTMF) is used to represent each key on the touch pad. Dual-frequency oscillators, capable of generating any one of 16 combinations of two frequencies, have been used in such systems [130].

Multi-band and multi-mode systems can benefit from a single oscillator that generates multiple unrelated frequencies simultaneously. For instance, a potential architecture of a single-chain concurrent receiver that uses a multi-band oscillator is shown in Figure 6.10.

In this scheme, all the desired channels from multiple frequency bands are down-converted to a low frequency (low-IF or DC) for further processing in digital domain.

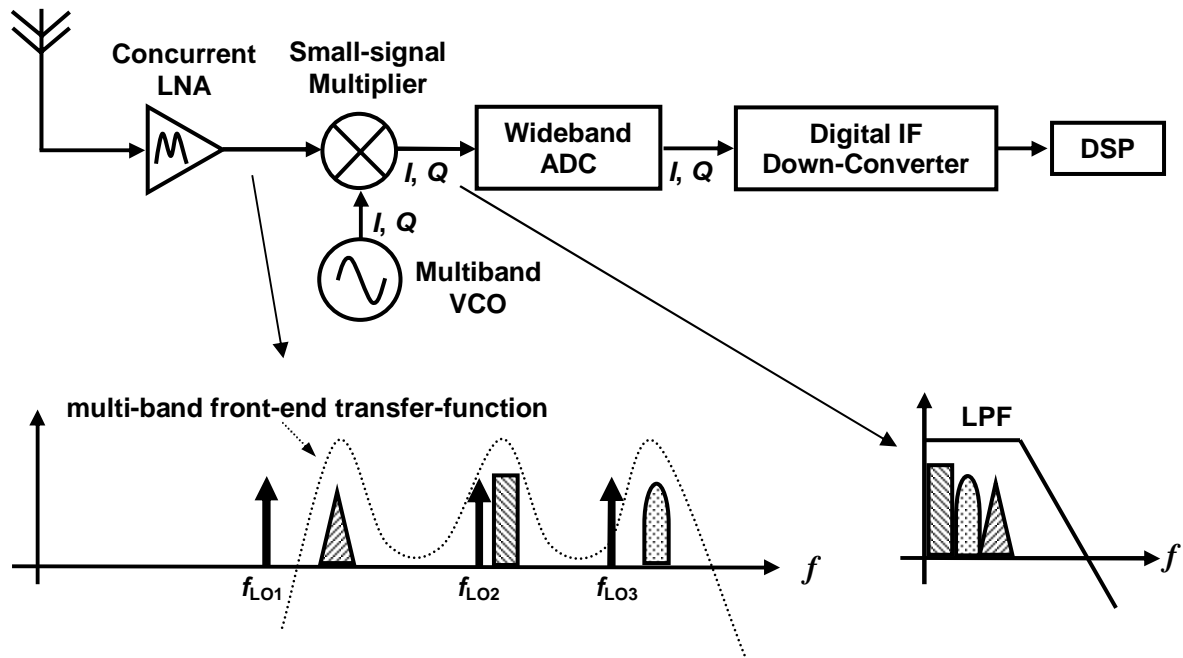


Figure 6.10: A potential single-chain concurrent receiver using a multi-band oscillator

There are still quite a number of remaining issues in the context of multi-band oscillators that needs to be addressed in the future. The phase-noise formulation of multi-band oscillators is still an open research topic. Also the behavior of asynchronous oscillator in frequency-locking loop(s) is another open aspect for later investigations.

6.2 Phase-Noise of Oscillators with a Generalized Resonator Structure

As it was mentioned in the introduction to this chapter, time waveforms and frequency components are two major characteristic features of oscillators. However, both of these features tend to fluctuate due to different sources of noise present at the core of oscillators. The mentioned frequency and time instability of oscillators deteriorates the performance of the systems that use them. As a result, predicting the oscillator frequency and time instabilities as well as developing methods to minimize them are active areas of research [110]-[112].

With a few exceptions, most of the recent literature has focused on achieving a better performance in a limited number of oscillator topologies, such as the one shown in Figure 6.2, with similar principal guidelines: superior integrated technology (*i.e.*, transistors with improved frequency response), enhanced inductors, and more power of the resonator improve the performance. Little attention has been paid to other resonator structures that can potentially improve the operation of such oscillators. At the same time, there have been a few reports of improvements in oscillators that use other forms of resonator structures [113]-[114]. It is hence reasonable to consider other oscillator topologies with the same active core that use a different resonator structure (Figure 6.11). In particular, we are interested in the general behavior of higher-order passive resonators. We will investigate whether oscillators with other resonator structures can have a better performance, *i.e.*, lower power consumption for a given phase-noise or a lower phase-noise for a given power as compared to the more conventional circuit topology of Figure 6.2. Also we will verify the validity of prior claims of improvements from a broader perspective.

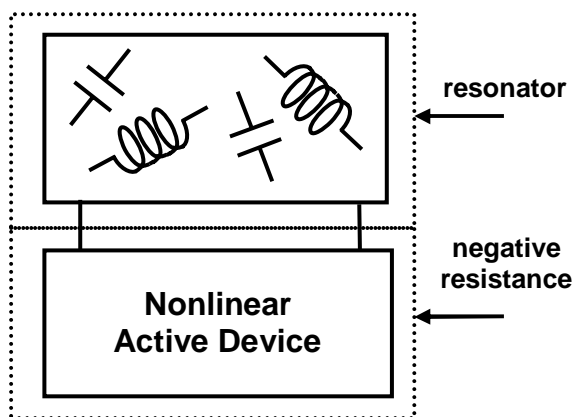


Figure 6.11: General model of a negative-resistance oscillator with a resonator

An example of a fourth-order system that uses 4 energy-storing elements (*i.e.*, inductors and capacitors) is shown in Figure 6.6. As we showed earlier, oscillators that use higher-order resonator structures (*i.e.*, with multi-band frequency response) can generate stable simultaneous multi-frequency oscillation waveforms at multiple frequencies, as well as oscillation at a single frequency. In this section, we focus on the case of an oscillator

generating an output at only one of its possible resonant frequencies and simultaneous oscillation at multiple frequencies is not considered for our phase-noise analysis³⁰.

Since phase-noise dependency on the resonator quality factor for a second-order system has been shown in various publications [39]-[112], we will start by analyzing the quality factor of a general resonator. Using circuit theory and physical arguments, we will show the effect of resonator topology on the quality factor and will demonstrate methods to improve it. We'll also derive general expressions that relate the quality factor to the resonator impedance function at the oscillation frequency without detailed knowledge of the resonator structure. Phase noise analysis of oscillators with a general resonator structure is carried out in Section 6.2.2. In particular, we will explain how we can apply the already developed phase-noise models for second-order systems in a general resonator structure. Multiple examples that are discussed in Section 6.2.2 confirm the claims of this chapter. At the same time, phase-noise improvements in oscillators that use enhanced resonators based on discussions of Section 6.2.1 will be illustrated.

6.2.1 Resonator Quality Factor

Previous approaches to the analysis of the oscillator phase-noise conclude that the phase-noise of a second-order oscillator improves with the resonator quality factor, Q [39]-[112]. We will extend this claim to general passive resonators consisting of multiple energy-storing elements. After deriving simple forms for a physical definition of quality factor in a general passive resonator structure, we will show that phase-noise depends on Q similar to the second-order system.

The term quality factor has been used with several definitions in the literature (*e.g.*, [115],[116]). One, particularly useful in filtering applications, defines the quality factor of a

³⁰ As we will show in the coming sections, the developed phase-noise models for second-order oscillators can also be used to evaluate the phase-noise of oscillators with higher-order resonator structures, if they oscillate at only one of their resonant frequencies. However, multi-frequency oscillations are governed by higher-order nonlinear differential equations (subsection 6.1.4), and hence their phase-noise performance can not be analyzed with the models derived for second-order oscillators. Constructing concepts and theories for the analysis of phase-noise of multi-frequency oscillations is an open and interesting topic for future investigation.

second-order system as a measure of broadness of its frequency-domain transfer function around the center of its bandpass characteristic [115]

$$Q_{filter} = \frac{\omega_0}{\Delta\omega_{-3dB}} \quad (6.38)$$

where $\Delta\omega_{3dB}$ is the difference of two frequencies at which the magnitude of frequency-domain transfer function drops by 3dB (*i.e.*, one-half the power) from its value at the center frequency, ω_0 . Based on this definition, a higher-quality factor implies a narrower spectrum around ω_0 . In the time-domain, a higher quality factor means a slower exponential decay rate of the impulse response due to loss.

A physically more meaningful definition of quality factor in resonance is given as [116]

$$Q_{energy} = 2\pi \cdot \frac{\text{total energy stored in the resonator}}{\text{energy dissipated in one oscillation cycle}} \quad (6.39)$$

The definition in (6.39) is more general and can be applied to resonators as well as single energy-storing elements such as inductors and waveguides.

For a second-order resonator one can easily show that these two definitions are interchangeable. This equality of definitions for a second-order system might *prematurely* lead one to believe that a narrower frequency spectrum in general implies a higher ratio of stored-to-dissipated energy for all resonators.

One can increase the order of resonator by adding more energy-storing elements in a way that forces the resonator frequency spectrum to roll off faster resulting in a narrower spectrum. In general, peaks in the resonator frequency-domain transfer function are due to the presence of poles close to (or on) the imaginary axis and dips are due to zeros. Hence adding zeros close to ω_0 , in the resonator transfer function is one way of forcing it to roll-off faster close to ω_0 , as graphically illustrated in Figure 6.12. Zeros can be easily implemented by adding series *LC* branches in parallel to the familiar second-order resonator (parallel *LC*). As an example, we can form a sixth-order resonator by adding two zeros to the second-order parallel *LC* (Figure 6.13). The impedance magnitude of this sixth-order resonator is plotted in Figure 6.12 together with a second-order resonator with the same peak frequency. Although the frequency roll-off appears faster farther away from the center peak frequency, the same is not quite obvious for the roll-off close to the center frequency.

We will show that the energy-based quality factor, Q_{energy} , of the resonator cannot be enhanced using this technique and no improvement in close-in phase-noise for the oscillator using the improved resonator can be achieved³¹. However, we will demonstrate the possibility of using mutual inductances in order to increase the Q_{energy} of a resonator and hence improve the oscillator phase-noise

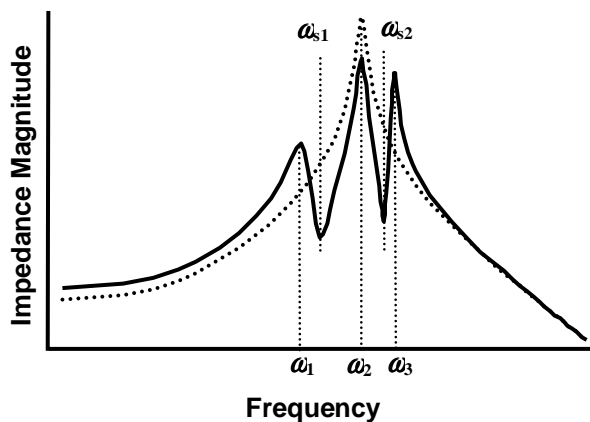


Figure 6.12: Frequency spectrum magnitude of a sixth-order and a second-order resonator (a sixth-order resonator structure is shown in Figure 6.13)

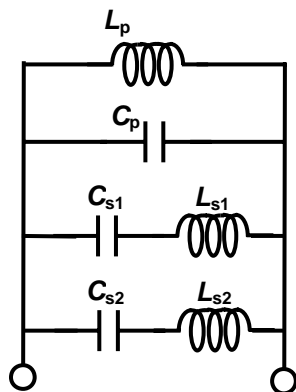


Figure 6.13: A sixth-order triple-band resonator

³¹ Although close-in phase-noise can not be improved using this technique, one might anticipate lowering of the far-out phase-noise at frequencies close to the null in the impedance transfer function of the resonator. However, in practice the phase-noise is usually limited by flat thermal noise of active elements outside of unaffected by the resonator (*e.g.*, output buffers), at these far frequencies. Therefore, no major improvements can be expected.

6.2.1.1 Resonator Quality Factor without Coupling Terms

In this subsection, first we will derive an upper bound on the quality factor of a passive resonator structure consisting of inductors and capacitors *without* any magnetic coupling terms between the inductors. Let's start from the total dissipated power in such a resonator where each element has a certain quality factor. At a single frequency of oscillation, ω_0 , the total dissipated power in resonator, $P_{d,total}$, is the sum of dissipated power in each of its component.

$$P_{d,total} = \sum_{\text{inductors}} P_{d,ind} + \sum_{\text{capacitors}} P_{d,cap} \quad (6.40)$$

where $P_{d,ind}$ and $P_{d,cap}$ represent the dissipated power of each inductor and capacitor, respectively. Using (6.39) for each element, we can further write

$$P_{d,total} = \sum_{\text{inductors}} \omega_0 \frac{E_{M,ind}}{Q_{ind}} + \sum_{\text{capacitors}} \omega_0 \frac{E_{E,cap}}{Q_{cap}} \quad (6.41)$$

where $(Q_{ind}, E_{M,ind})$ and $(Q_{cap}, E_{E,cap})$ represent the quality factor and the average stored magnetic/electric energy of each individual inductor and capacitor, respectively. Denoting the highest quality factor of all the inductors and all the capacitors in the resonator with $Q_{ind,MAX}$ and $Q_{cap,MAX}$, respectively, and using (6.41) we can write

$$P_{d,total} \geq \omega_0 \sum_{\text{inductors}} \frac{E_{M,ind}}{Q_{ind,MAX}} + \omega_0 \sum_{\text{capacitors}} \frac{E_{E,cap}}{Q_{cap,MAX}} \quad (6.42)$$

that can be further simplified to

$$P_{d,total} \geq \frac{\omega_0 E_M}{Q_{ind,MAX}} + \frac{\omega_0 E_E}{Q_{cap,MAX}} \quad (6.43)$$

where E_M and E_E are the average stored magnetic and electric stored in the resonator, respectively. The equality will hold when all of the quality factors of inductors are equal and so are the quality factor of capacitors.

Later section 6.2.1.3, we will show that for a resonator at each single resonance frequency, the total stored magnetic and electric energy per cycle are equal, *i.e.*,

$$\sum_{\text{inductors}} E_{M,ind} = \sum_{\text{capacitors}} E_{E,cap} \quad (6.44)$$

Then (6.43) can be simplified to

$$P_{d,total} \geq \omega_0 \frac{E_M}{2} \left(\frac{1}{Q_{ind,MAX}} + \frac{1}{Q_{cap,MAX}} \right) \quad (6.45)$$

Replacing (6.43) in the energy-based expression for resonator quality factor in (6.39) results in an upper bound for the energy-based quality factor, Q_{energy} , of any high-order passive resonator consisting of inductors and capacitors without coupling terms in resonance

$$Q_{energy} \leq 2 \left(\frac{1}{Q_{ind,MAX}} + \frac{1}{Q_{cap,MAX}} \right)^{-1} \quad (6.46)$$

It is noteworthy that this upper bound on Q_{energy} is equal to the quality factor of a second order resonator achieved using the inductor and capacitor with the highest Q in the set. This result has very important practical implications: *no combination of inductors and capacitors without coupling terms can achieve a higher quality factor than that of a single inductor element in parallel with a capacitor forming a second order resonator.*

In the following section, we will show that the phase-noise of any oscillator using a general passive resonator depends on the Q_{energy} of the resonator. Hence, no improvement in the phase-noise can be expected beyond what is offered by a second-order system under the above conditions. Reported improvements in resonator quality factor and oscillator phase-noise by means of more complicated resonator structures such as the ones in [114] can only be attributed to the use of better passive components (*i.e.*, bondwire inductors with a higher quality factor) and not to the topology of the specific resonator used.

6.2.1.2 Resonator Quality Factor Including Coupling Terms

A higher quality factor can indeed be obtained if we use passive structures that can fundamentally store more energy per cycle. Coupled inductors are one such example, where magnetic energy is not only stored in the self-inductance of the inductors, but also in their mutual inductance. Compared to separate inductors in a resonator structure, closely-spaced inductors with similar individual quality factors can result in a higher overall stored

magnetic energy due to the coupling while having the same loss. So resonators that use coupled inductors (*e.g.*, transformers) *can in principal* have a higher quality factor if designed properly. To better understand this effect, let us write the total magnetic stored energy, E_M , in a resonator in the presence of coupling terms between inductors

$$E_M = E_{M, self} + E_{M, mutual} \quad (6.47)$$

where

$$E_{M, self} = \sum_{\text{inductors}} E_{M, self} = \sum_{n=1}^N \frac{1}{2} L_n i_n^2 \quad (6.48)$$

and

$$E_{M, mutual} = \sum_{m=1}^N \sum_{n=1}^N M_{mn} \cdot i_m \cdot i_n \quad (m \neq n) \quad (6.49)$$

and where L_n is the self-inductance of n th inductor carrying current i_n and M_{mn} is the mutual inductance between inductors m , n carrying currents i_m , i_n , respectively, and N is the total number of inductors. The ratio of stored-energy to the dissipated power in this system is higher if the total energy stored in coupling terms, $E_{M, mutual}$, is positive. Note that the total stored energy will be lowered if the coupling terms add with a negative sign. In summary, the quality factor of a resonator using coupled inductors can be higher or lower than that for the non-coupled case depending on the sign of $E_{M, mutual}$, *i.e.*,

$$Q_{energy} \begin{cases} > Q_{ind} & \text{if } E_{M, mutual} > 0 \\ < Q_{ind} & \text{if } E_{M, mutual} < 0 \\ = Q_{ind} & \text{if } E_{M, mutual} = 0 \end{cases} \quad (6.50)$$

where, for simplicity, we have assumed an identical quality factor, Q_{ind} , for all the inductors.

To have the maximum improvement in the stored coupled energy in (6.48), the currents through different inductors should be in-phase, bearing in mind that in steady-state inductor currents can be represented using phasors. If they are in opposite phases, they will have a destructive effect by reducing the total stored energy. To show the aforementioned effects in real circuits, consider two resonators in Figure 6.14. If we assume perfect coupling between the coupled inductors ($k=1$), the same E voltage appears across both of them. In the

resonator of Figure 6.14 (a), the current through both inductors will be in-phase and equal because of the symmetry of the circuit and thus the overall quality factor of the resonator increases (exactly twice its uncoupled value). In the resonator of Figure 6.14 (b), the current through coupled inductors will have opposite phases because capacitor current leads the resonator voltage by 90° and inductor current lags the same voltage by 90° . Therefore, the overall quality factor of this structure is lowered compared to the uncoupled case. From this illustrative example, it is clear that quality factor enhancement is *not* a universal property of all resonators using coupled-inductors and depends on the resonator topology as well. The improved phase-noise performance in transformer-based oscillators [113] is due to an increase of Q_{energy} of such structures, as described above.

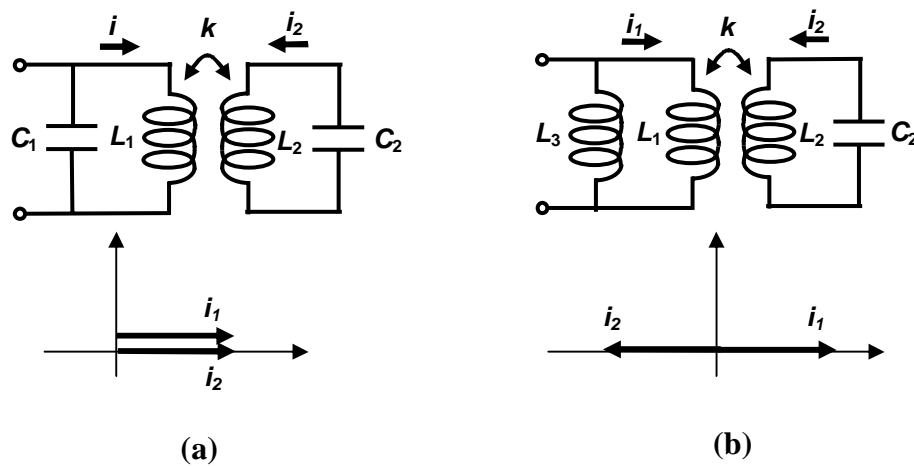


Figure 6.14: Two examples of resonators that use coupled inductors: (a) Quality factor increases, since coupling energy adds to total stored energy (i_1 and i_2 in-phase). (b) Quality factor decreases, since coupling energy subtracts from total stored energy (i_1 and i_2 out-of-phase)

6.2.1.3 Useful Expressions for Resonator Quality Factor

We will conclude this section by deriving the oscillation condition based on energy arguments that will lead to approximate, yet practical, expressions for the quality factor in a general resonator structure. From basic circuit or electromagnetic theories we know that in

any linear one-port passive network in steady-state, the driving-point impedance at a specific frequency, $Z(j\omega)$, can be expressed as [115],[116]³²

$$Z(j\omega) = R(\omega) + jX(\omega) = \frac{2P_{d,total} + 4j\omega[E_M(\omega) - E_E(\omega)]}{|I|^2} \quad (6.51)$$

where $P_{d,total}$, $E_M(\omega)$, and $E_C(\omega)$ are total dissipated power, magnetic and electric stored energy of the passive network, respectively, and I is the current phasor of at the port (Figure 6.15).

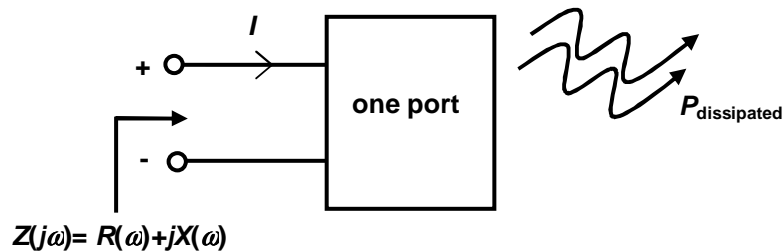


Figure 6.15: Impedance definition of a one-port network

Using (6.51), we can see that the dissipated power in such a system is proportional to the real part of driving point impedance, as anticipated physically

$$P_{d,total} @ \omega_0 = \frac{1}{2}|I|^2 \operatorname{Re}(Z(j\omega_0)) = \frac{1}{2}|I|^2 R(\omega_0) \quad (6.52)$$

For an oscillator in steady-state, the loss in the resonator is compensated with the energy delivered by the active part and the resonator provides a 360° (or zero) phase shift at the oscillation frequency. In other words, the resistive part of resonator is compensated by an effective negative resistance of the nonlinear active device at the fundamental frequency while the imaginary part of the resonator impedance should be zero³³ [117]. So based on the

³² The circuit theory proof of (6.51) uses the application of Tellegen's theorem in electrical networks at steady-state. Based on Tellegen's theorem, for any set of branch currents, I_m , satisfying $\sum I_m = 0$ at every node and any set of branch voltages, V_n , satisfying $\sum V_n = 0$ for every loop, we will have $\sum V_n I_n = 0$. Note that in a physical network, Tellegen's theorem is a statement of conservation of energy.

Similarly, by applying the complex Poynting theorem, valid for the power flow of an electromagnetic wave into any isotropic medium, to the one-port circuit network of interest in Figure 6.15, the input impedance of (6.51) can be derived.

³³ In the discussion above, we assumed that all the dynamics in the active device (e.g., intrinsic capacitors, etc.) are absorbed in the passive resonator (Figure 6.4).

above argument and using (6.51) for any general passive resonator in an oscillator, at the resonance frequency, ω_0 , we have

$$E_M(\omega)\Big|_{\omega=\omega_0} = E_E(\omega)\Big|_{\omega=\omega_0} \quad (6.53)$$

which proves our previous claim in (6.44). We are already familiar with this expression for the second-order systems: energy oscillates back-and-forth between magnetic stored energy of the inductor and electric stored energy of the capacitor. Expression (6.53) can be used as a simple physical definition to calculate the oscillation frequency for any resonator.

At the same time, one can show that the overall stored energy in a *lossless* network is proportional to the derivative of the imaginary part of its driving point impedance with respect to the angular frequency [115],[116], *i.e.*,

$$E_{stored} @ \omega_0 = \frac{1}{4}|I|^2 \frac{dX(\omega)}{d\omega}\Big|_{\omega_0} = \frac{1}{4}|V|^2 \frac{dB(\omega)}{d\omega}\Big|_{\omega_0} \quad (6.54)$$

Where $X(\omega)$ and $B(\omega)$ are imaginary parts of the driving-point impedance and admittance functions, called reactance and susceptance, respectively, and V is the phasor of steady-state voltage across the one-port network. Different proofs of (6.54) using circuit theory (*e.g.*, a variation of Tellegen's theorem) or electromagnetic theory (*e.g.*, a variation form of Poynting theorem) exist in the literature [115],[116]³⁴. For general *low-loss* resonators where the resonant frequencies are far apart, (6.54) is still a reasonable approximation at each resonant frequency. We will explain these conditions more rigorously in the next subsection.

Now using (6.52) and (6.54), the energy-based definition of the quality factor can be written as

$$Q_{energy} = 2\pi \frac{E_{stored}/cycle @ \omega_0}{E_{dissipated}/cycle @ \omega_0} \cong \frac{\omega_0}{2} \cdot \frac{\frac{dX(\omega)}{d\omega}\Big|_{\omega_0}}{R(\omega_0)} \quad (6.55)$$

³⁴ In the variation form of Tellegen's theorem, the summation discussed in ³² is applied to the derivatives of currents and voltages in the network that still satisfy the kirchoff's laws, *i.e.*, $\sum dV_n/dt=0$ and $\sum dI_n/dt=0$ and hence from Tellegen's Theorem $\sum I_n(dV_n/dt)=0$ and $\sum (dI_n/dt)V_n=0$.

Since at the resonant frequency or at a very close frequency to it, the derivative of impedance magnitude and its real part is zero³⁵, the expression in (6.55) can be further simplified to

$$Q_{energy} \equiv \frac{\omega_0}{2} \cdot \left. \frac{d\Phi(\omega)}{d\omega} \right|_{\omega_0} \quad (6.56)$$

where $\Phi(\omega)$ is the phase response of the resonator impedance function. The form of (6.56) was suggested before [118] in the context of feedback model of second-order oscillators. Here, we show its generality for all passive resonator structures using energy arguments.

Note that (6.55) and (6.56) are general expressions for *all passive structures at resonance* and should be used instead of the widely used definition for one-port networks where the quality factor is defined as the ratio of imaginary to the real part of impedance function.

6.2.2 Phase Noise

The power spectrum density of an ideal oscillator consists of delta-functions at the oscillation frequency and its harmonics. However, the spectrum of any real oscillator will have skirts around these delta-functions due to the noise present in the oscillator core. Phase-noise quantifies this spectral impurity by comparing the oscillator power at the oscillation frequency to the power at its vicinity (Figure 6.16)

$$\text{Phase Noise at } \Delta\omega \text{ offset from } \omega_0 = \frac{\text{oscillator output power in 1Hz bandwidth around } \Delta\omega \text{ offset from } \omega_0}{\text{total oscillator output power around } \omega_0} \quad (6.57)$$

³⁵ The impedance magnitude function has peaks/nulls at parallel/series resonant frequencies.

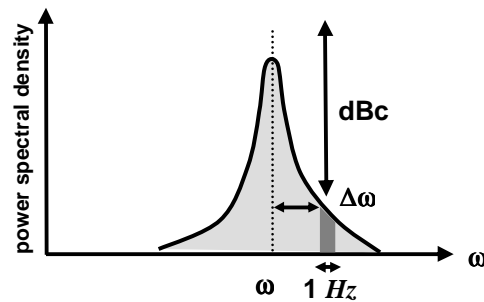


Figure 6.16: Illustration of phase-noise definition per unit bandwidth

Hence oscillators with a smaller phase-noise number will have a purer power spectrum density around the oscillation frequency. Despite its deceptively simple look, calculation of oscillator output spectrum in the presence of noise is not always easy and many efforts have been dedicated to this task for over half a century [39]-[112]. The linear time-invariant analysis of the problem given by Leeson in [39] provides a simple expression for phase-noise that has been used extensively by designers for decades. Probably, it is due to the simplicity of the expressions in [39] that the more concrete analysis by Lax in [109] has not been given the same attention by the circuit design community. Since oscillators are a major building block in most communication circuits and their phase-noise affects the sensitivity of the radio system, attention has been given to accurate analysis of phase-noise in integrated oscillators recently [110]-[113]. Approaches vary quite a bit, with [110] emphasizing on the time-varying aspect of the nonlinear problem, deriving a phase-noise expression that can help in designing oscillators with a lower phase-noise number. The exact solution of the stochastic nonlinear problem is possible and the results can be integrated into a circuit simulator [111]. More recently the problem of noise in integrated oscillators has been once again traced back in its physical origin of diffusion processes via the concept of virtual damping [112].

In this section, we will first argue that many resonator structures can be modeled with a second-order resonator for frequencies close to resonance and the conditions that allow us to do so. Then, using the well-known models to calculate phase-noise for second-order systems, we will show a general link between the phase-noise of an oscillator and Q_{energy} of its resonator.

From the early works of Foster [119], we know that for any lossless network, the reactance function can be represented as

$$X(\omega) = \sum_{n=1} \frac{2a_n \omega}{\omega^2 - \omega_n^2} - \frac{1}{\omega C_0} + \omega L_\infty \quad (6.58)$$

where ω_n are the poles of the network and a_n is the residue of the pole ω_n . The capacitor C_0 models that pole at zero frequency while the inductor L_∞ model the pole at infinity. If ω_n s are not very close, for frequencies close to any of the poles, say ω_k , the k^{th} term in the sum dominates and (6.58) simplifies to

$$X(\omega) \Big|_{\omega \text{ close to } \omega_k} \approx \frac{2a_k \omega}{\omega^2 - \omega_k^2} \quad (6.59)$$

Differentiating the susceptance (inverse of (6.59)) and use of (6.54) gives

$$a_k = -\frac{1}{(dB/d\omega)_{\omega=\omega_k}} = -\frac{|V|^2}{4 \cdot E_{\text{stored}}} \quad (6.60)$$

From comparing (6.58)-(6.60) to the results for a second order parallel LC resonator, we can derive the equivalent capacitor and inductor for a complex network in resonance

$$C_{eq} = \frac{-1}{2a_k} = -\frac{2 \cdot E_{\text{stored}}}{|V|^2}, \quad L_{eq} = \frac{-2a_k}{\omega_k^2} = -\frac{|V|^2}{2 \cdot E_{\text{stored}} \cdot \omega_k^2} \quad (6.61)$$

If the poles of the network are low-loss³⁶, the effect of loss can be lumped into a single resistor in parallel with the equivalent second order resonator

$$R_{eq} = \frac{|V|^2}{2 \cdot P_{\text{dissipated}}} = R(\omega_0) \quad (6.62)$$

The quality factor of this equivalent second order system is the same as one expects from (6.55). The equivalent model derived above can be used to calculate the phase-noise in oscillators using the previously developed theories for second order systems.

First, we want to show how the results obtained in this section can be applied to the phase-noise model in [110]. This model starts with calculating the effect of injected noise to

³⁶ This assumption is along the same line that led us to deriving (6.56). Both assumptions are to assure that in the neighborhood of resonance that we are interested in, the dominant effect comes from the corresponding pole and not from other poles of the resonator. If these conditions are not satisfied, the null in the impedance transfer function becomes shallower due to loss as the poles get closer.

phase displacements for a resonator at oscillation. According to [110] the transfer function of injected impulse current at different times to excess phase in the oscillating output is a periodic function of time, called the *impulse sensitivity function* (the ISF is shown with $\Gamma(\omega_0 t)$ hereafter) and directly affects the phase-noise expression of oscillators. Although direct calculation of ISF in general is possible, it gets more difficult for higher-order resonators. An example of the direct calculation of ISF for a fourth-order resonator is given in the Appendix E.

For a general resonator with impedance function $Z(s)$ that is already oscillating at $\omega=\omega_0$, the effect of impulse current at $t=t_0$ on its output can be calculated using

$$V(t) = V_{unperturbed}(t) + L^{-1}\{Z(s) \cdot e^{-st_0}\} \quad (6.63)$$

In (6.63) $V_{unperturbed}(t)$ is resonator's oscillating output before injecting the impulse current and L^{-1} is the inverse Laplace transform. Clearly the effect of the second part of (6.63) is also oscillation at $\omega=\omega_0$ which combined with the pre-injection term yields an oscillation with a different phase shift³⁷. Since the effect of passive resonator is only to shape the ISF through (6.63), the derivations and discussions in [110] will remain valid for a complicated resonator structure by merely using the equivalent values of (6.61)-(6.62). The link to the physical resonator stored energy is still preserved through those expressions.

The phase-noise model of [109] starts off by the Taylor expansion of the impedance function around the resonance frequency of a second-order system. Similarly we can write

$$Z(j\omega)\Big|_{\text{close to } \omega_0} \cong j \frac{dX(\omega)}{d\omega}\Big|_{\omega=\omega_0} (\omega - \frac{\omega_0}{2}) + R(\omega_0) + jX(\omega_0) + \frac{dR(\omega)}{d\omega}\Big|_{\omega=\omega_0} (\omega - \omega_0) \quad (6.64)$$

The standard procedure for second-order systems in [109] can be followed to derive the Langevin equation for the phase of the oscillator. In the standard second-order LC system $dX(\omega)/d\omega$ at resonant frequency is simply the value of inductor, L . The result will be the familiar phase-noise dependency on $\omega_0 L/R$ that is called the tank quality factor. However in the general case of (6.64) the phase-noise will depend on $\frac{\omega_0}{2} \cdot \frac{dX(\omega)}{d\omega}\Big|_{\omega_0} / R(\omega_0)$ which is the

familiar energy-based definition of quality factor (expression (6.55)). This result agrees favorably with [112] where the phase-noise treatment is based on the physical phase diffusion model. There, it is showed that for the second-order LC system, the phase-noise is directly related to the total stored energy in the tank and inversely proportional to the thermal energy stored in the system.

In summary, we first argued that any complex resonator structure with multiple poles (resonant frequencies) that are sufficiently far apart, behaves similar to a second order system close to its resonant frequency. This link has been made based on energy arguments. Hence, phase-noise models that are expressed for second order systems can be further expanded to higher-order systems for frequencies close to the oscillation frequency³⁸.

6.2.3 Circuit Examples

A cross-coupled pair oscillator with different resonator topologies has been investigated to verify the claims in this chapter. A simple second-order LC resonator is compared with more complicated fourth- and sixth-order systems in Figure 6.6 and Figure 6.13. Also a resonator formed by transformers, as suggested in [113], has been investigated (Figure 6.17). It can be shown that the transformer-based resonator in [113] also forms a fourth-order system. The values of component are chosen so that the peak resonance frequency of the second-order system is the same as other resonator structures. Also the zeros in the impedance transfer function of resonators are picked so that the oscillators have the highest loop-gain at the desired frequency. We have also assumed that all the inductors used have the same quality factor.

³⁷ More accurately, the second term can have multiple oscillations for a general resonator (for an example in a fourth-order system, refer to Appendix D). However, since the resonator is in the oscillation loop and the injected current noise is small, other oscillation modes will not be triggered.

³⁸ This argument is not necessarily correct for far-out phase-noise that can have peaks and nulls due to other poles and zeros in the resonator. However, if the poles are sufficiently far apart, these peaks will be within the thermal-noise floor of phase-noise.

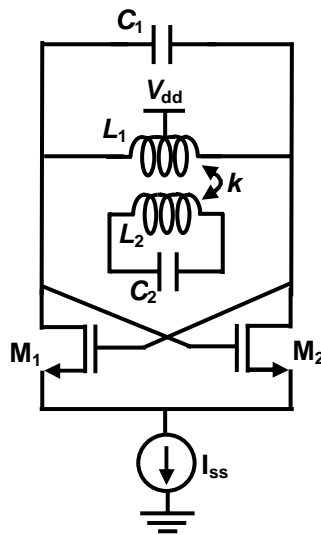


Figure 6.17: Cross-coupled pair oscillator with a fourth-order resonator implemented using transformers

For each resonator structure, the magnitude of the impedance function is compared with that of the second-order LC resonator in Figure 6.18. The stored and dissipated energies have been accurately calculated for each structure using a custom Mathematica [120] routine. The quality factor calculated by this method agrees very accurately with expressions given in (6.55) and (6.56)³⁹. The phase-noise of oscillators using all these resonators has been simulated using SpectreRF (that uses a method similar to [111]). All results give the same number confirming the previous claim that phase-noise only depends on the resonator quality factor and is independent on resonator structure details. In the transformer-based structure, the quality factor can be as high as twice that of a single inductor for perfect coupling ($k=1$) and decreases as the coupling is lowered. Figure 6.18 shows the result for $k=0.9$ that corresponds to the overall resonator quality factor of 19 when inductors have quality factor equal to 10. A summary of the quality factor of these structures is shown in Table 6.1.

³⁹ For these structures and for inductor quality factors as low as 5, only an error of less than 3% is introduced in the calculations. For inductor quality factors of 10 and higher, the error is less than 1%.

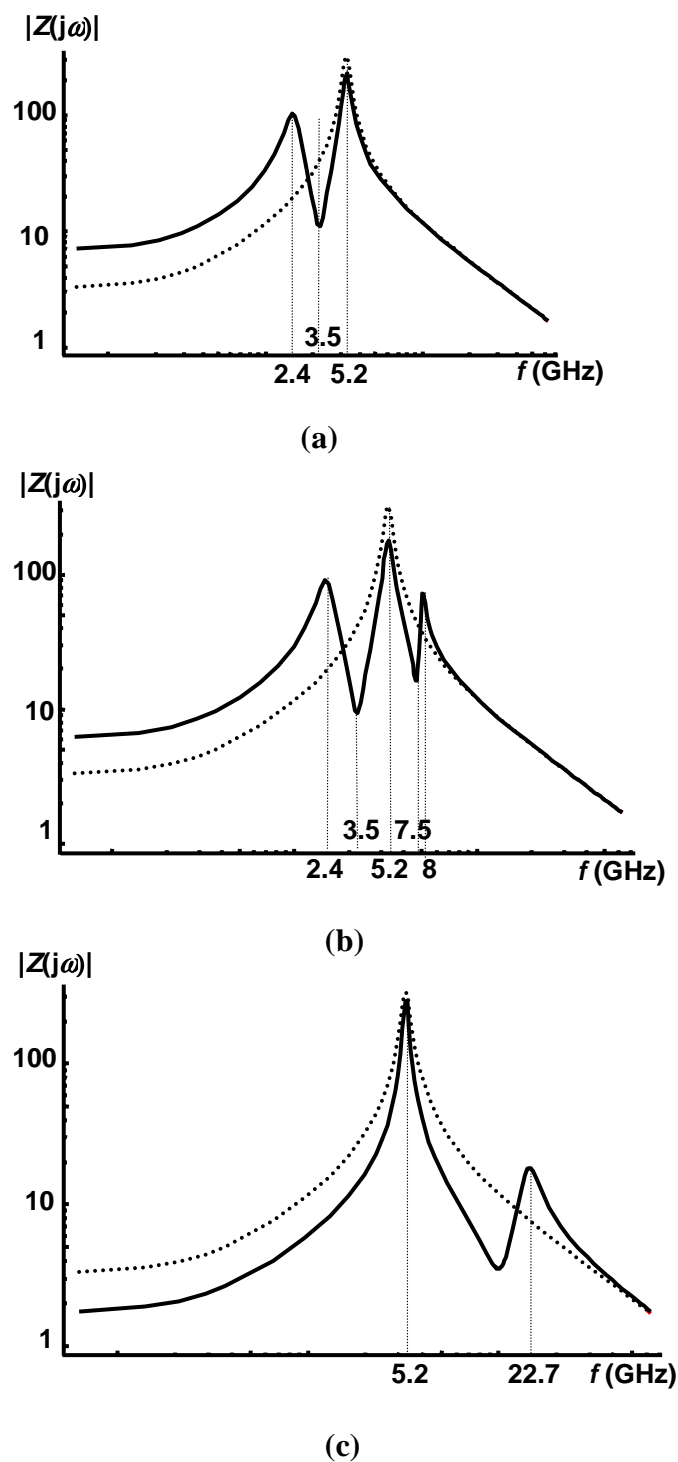


Figure 6.18: Impedance magnitude of the higher-order resonators (solid-curves) compared to the second-order LC resonator of Figure 6.2 (dotted curves) (a) fourth-order resonator used in oscillator of Figure 6.6 (b) sixth-order resonator used in oscillator of Figure 6.13 (c) fourth-order transformer-based resonator used in oscillator of Figure 6.17 [Coupling-factor $k=0.9$ is assumed in this figure]

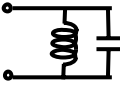
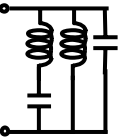
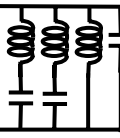
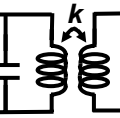
	Q_{ind}	$Q_{\text{impedance}} \equiv \frac{X(\omega_0)}{R(\omega_0)}$	$Q_{\text{phase}} \equiv \frac{\omega_0}{2} \cdot \frac{d\Phi(\omega)}{d\omega} \Big _{\omega_0}$	$Q_{\text{energy}} \equiv \frac{\omega_0}{2} \cdot \frac{dX(\omega)}{d\omega} \Big _{\omega_0} \cdot R(\omega_0)$
	10	0	10	10
	10	0	9.5	9.6
	10	0	9.6	9.6
	10	0	(k=1.0) 19.8	(k=1.0) 19.9
			(k=0.5) 14.8	(k=0.5) 14.8

Table 6.1: Quality factor comparison for different resonator structures

Based on the arguments of Section 2, one can store more energy in the coupling terms for a larger number of inductors in the resonator to achieve an even better phase-noise for the oscillator. As one example, a resonator using three identical coupled inductors is shown in Figure 6.19. We can show that for this structure, the quality factor reaches three time the quality factor of each inductor as the coupling factor gets closer to one. Following the discussions of this chapter, it should not come as a surprise that the phase-noise of an oscillator based on this structure is better than previously discussed oscillator that have the same oscillation amplitude and use inductors with a similar quality factor in their resonator. Simulated phase-noise performance of oscillators at 5 GHz with an identical core using the abovementioned resonator structures are presented in Figure 6.20 for comparison. SpectreRF is used to simulate the phase-noise and the oscillators are designed in a 0.35 μm CMOS technology. Inductor quality factor of 10 and coupling coefficient of $k=0.95$ is assumed in all cases. The improvement in phase-noise is consistent with a similar increase in the energy-based quality factor that is the direct result of storing more energy in coupling

terms. Further improvements in oscillator phase-noise are still possible by storing more energy in a system of coupled elements in a resonator.

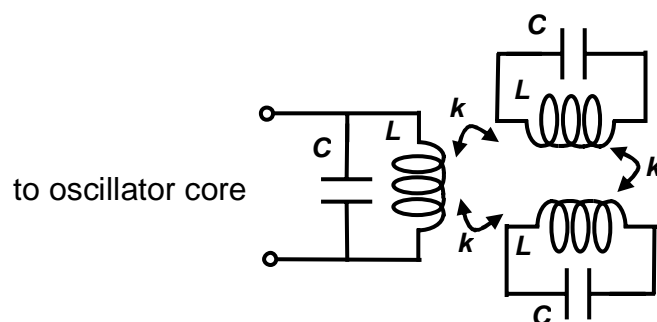


Figure 6.19: A proposed combination of three coupled inductors in a resonator structure to achieve a higher energy-based definition of quality factor that results in an enhanced phase-noise performance if inserted in an oscillator core.

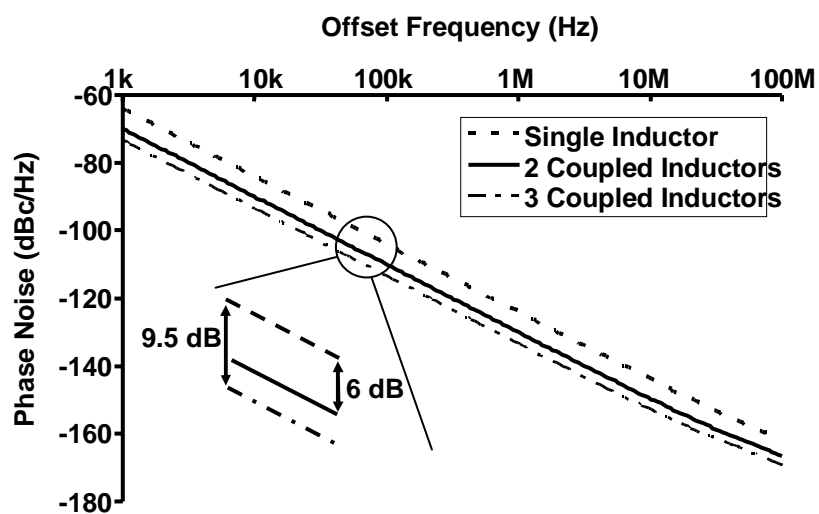


Figure 6.20: Simulated phase-noise of three cross-coupled oscillators at 5 GHz having a common core with different resonator structures in Figure 6.2, Figure 6.17, and Figure 6.19. Oscillation amplitude is 0.830 V, 0.805 V and 0.795 V for these cases, respectively.

6.3 Summary

In this chapter, we analyzed the performance of nonlinear oscillators with multi-band resonator structures. At first, we proved the possibility of simultaneous multi-frequency oscillations under certain conditions in a fourth-order nonlinear oscillator that uses a dual-band resonator. These simultaneous multi-frequency oscillations will have a variety of applications, particularly in the design of efficient multi-band and multi-mode radio systems.

In the second part of this chapter, a noise analysis of negative-resistance oscillators with general resonators is performed. By observing energy relations in a general resonator and following the steps of prior literature on phase-noise, it is shown that the oscillator phase-noise depends only on the energy-based definition of quality factor. The results not only can explain the phase-noise improvements in previously reported oscillators, but also can be used to design low phase-noise oscillators. One particular result of the analysis shows that no combination of inductors and capacitors without coupling can achieve a lower phase-noise than a second-order LC resonator with the same quality factor. However, by storing more energy in the coupling terms between elements in a properly-desired configuration, one *can* increase the resonator quality factor and hence enhance the phase-noise of oscillator using that resonator.

Chapter 7

A Multiple-Antenna Phased-Array Radio

Based on Shannon's capacity theorem [2], the maximum data-rate of any communication system increases with bandwidth and signal-to-noise ratio (*SNR*) enhancement. Due to the finite available frequency spectrum and numerous wireless users and applications, increasing the data-rate by using more bandwidth is often an unattractive solution. At the same time, there are a few practical limitations to increasing signal-to-noise ratio at the receiver: in addition to the conventional sources of additive noise and loss in signal power, *multi-path fading* and *co-channel interference* also degrade the received signal-to-noise-and-interference ratio, *SNIR*, substantially. The loss of the received signal in a fading environment can be compensated by a substantial increase in the power of the transmitted signal that in turn raises the interference level to other receivers and lowers their *SNIR*.

However, multiple-antenna systems can result in an effective increase of data-rate for the wireless communication system by battling against channel fading and/or co-channel interference. By properly combining the signal power of multiple antenna elements, we can simultaneously increase the level of the desired signal and decrease the interference level. Consequently, the *SNIR* of multiple-antenna systems is higher than single-antenna systems leading to a higher data-rate for the former.

In this chapter, after a brief discussion of the effectiveness of multiple-antenna systems, an implementation of a phased-array system at 24 GHz in a silicon-based technology will be described.

7.1 Brief Overview of Multiple-Antenna Systems

In this section, we will show a few schemes that use multiple antennas to enhance the effective data-rate of communication. At this point, a distinction between line-of-sight (LOS) communication and communication in multi-path fading channels will be made. In the case of line-of-sight communication, the signal travels from the transmitter to the receiver in a straight line (Figure 7.1 a). In a multi-path fading channel, multiple replicates of the transmitted signal that are reflected from various scatterers reach the receiver at different times with different amplitudes and phases (Figure 7.1 b). Radio astronomy is an example of LOS communication while most indoor communication schemes such as wireless local area networks (WLAN) are conducted in a predominantly fading channel. Due to the statistical nature of fading channels, the properties of the received signal might change significantly with small variations⁴⁰ in the position of transmitter and/or receiver (*e.g.*, [3]).

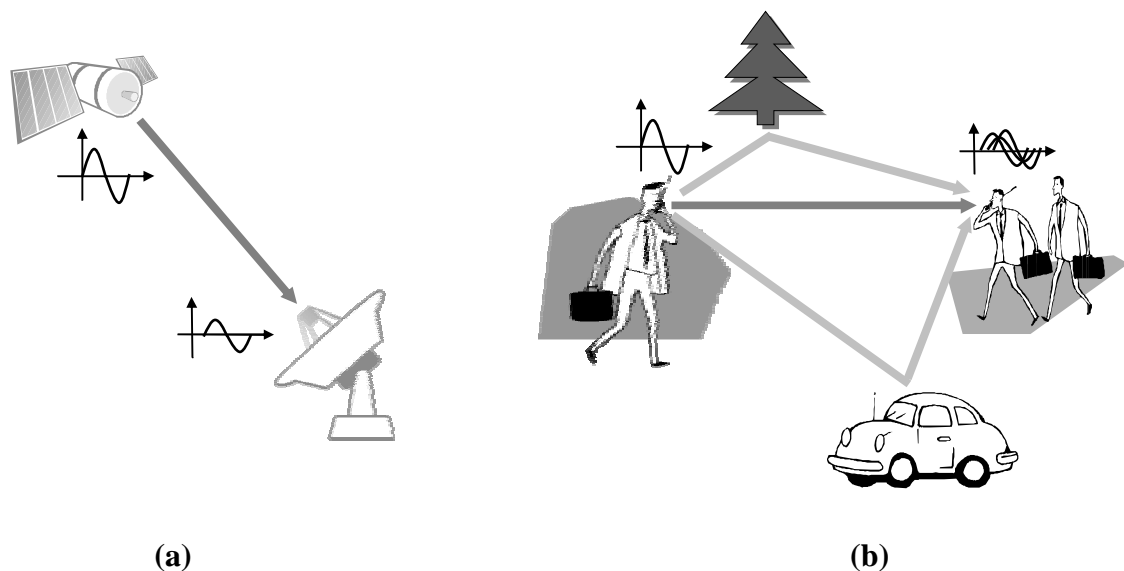


Figure 7.1: Wireless communication channels (a) line-of-sight (b) multi-path fading

Spatially separated antennas can be used to enhance the performance of wireless communication in both cases. For a single antenna element, a pattern identifying the

direction of the transmitted (received) signal power is called the *antenna pattern* [135]. The shape of the antenna pattern is a function of antenna shape and size and usually consists of a main lobe and several side-lobes. As depicted in Figure 7.2 a, an antenna with a wide main lobe is more susceptible to transmitting (receiving) interference signals. As will be discussed in the following sections, an array of antennas can be used to form an effective narrow beam in a LOS communication scheme (Figure 7.2 b) in order to minimize the interference levels and hence increase system's overall efficiency (*i.e.*, higher capacity for the same power).

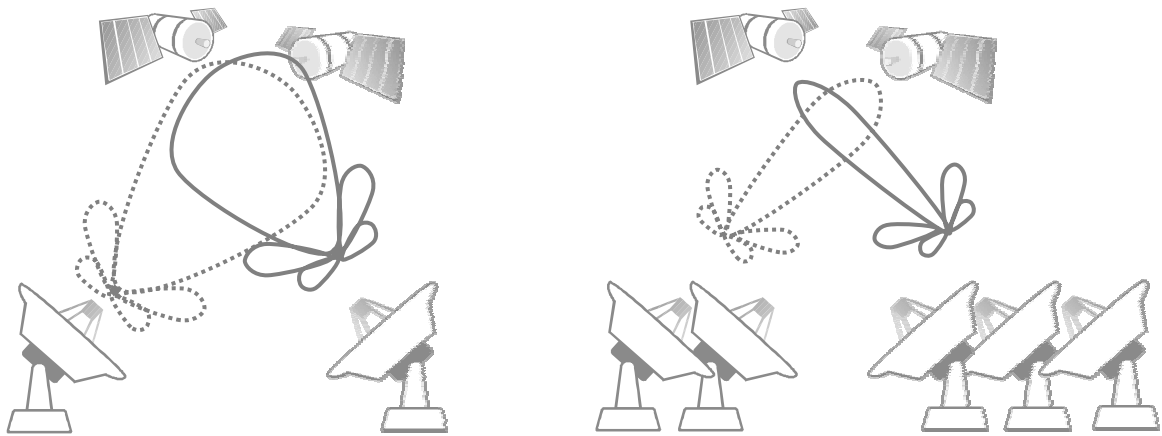


Figure 7.2: Narrower antenna beams using multiple-antenna elements

In a statistically fading environment, due to multiple reflections in the surroundings, the received signal level varies rapidly as the distance between the transmitter and receiver is altered by only a fraction of a wavelength [136]. Figure 7.3 depicts the characteristic of a received signal envelope in a typical fading channel [137]. Hence, spatially separated antennas can be used to extract more information from these large amplitude fluctuations in a fading channel, leading to an effectively higher data-rate [136].

⁴⁰ These small alterations could vary from a fraction to multiples of the signal wavelength depending on the size and type of scatterers.

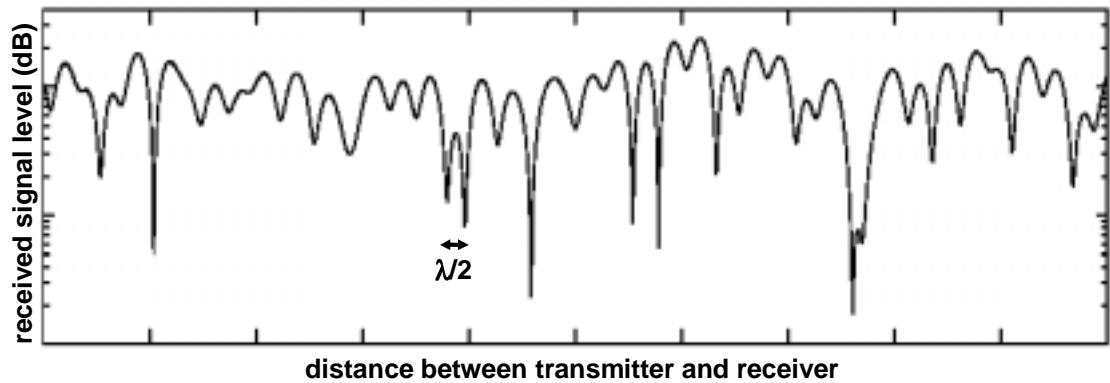


Figure 7.3: Characteristic of a received signal envelope in a typical fading channel (courtesy of [137])

7.1.1 Spatial Diversity

Spatially separated antennas at the receiver and the transmitter can enhance the performance of the communication system (*i.e.*, higher data-rate) in a fading channel. Performance improvement using spatial diversity can be achieved at the receiver, the transmitter, or both, simultaneously. In the following subsections, we will address these possibilities.

7.1.1.1 Receiver Diversity

If multiple receiving antennas are sufficiently spaced apart from one another, their received signal levels are almost independent in a statistically fading channel (Figure 7.3). A decision circuit can simply pick the antenna that offers the highest signal-to-noise ratio (selection diversity) or more optimally it can combine the weighted signals from different antennas in a manner that achieves the highest possible SNR (maximal ratio combining) [136]. Figure 7.4 shows a simplified schematic of a diversity receiver based on the latter method where the signal from each antenna element is weighted by the complex number $A_i e^{j\phi_i}$ prior to combining. In later sections, we will discuss the various receiver architecture possibilities that exist for signal weighting and combining in the context of phased-array receivers.

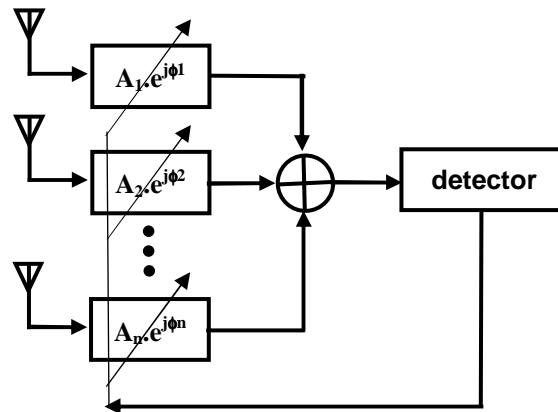


Figure 7.4: Simplified scheme of a maximal ratio combining receiver using spatial diversity

7.1.1.2 Transmitter Diversity

Similarly, in a statistically fading channel transmitted signals from spatially separated transmitting antennas experience independent fades as they reach the receiver [136]. If channel properties from the transmitter array to the receiver are known, the transmitter can shape the signal fed to each antenna element in such a way that after propagation in the fading environment all signals combine constructively at the receiver end. Multiple transmitting antennas in this configuration effectively create a signal that arrives at receiver with the best possible “form” (*i.e.*, highest SNIR) without increasing the overall transmitted power (*e.g.*, [138]), hence the name *beam-forming*.

Even in the case where the communication channel is unknown to the transmitter, by transmitting different signals from various antennas over time, a larger signal-to-noise at the receiver can be achieved which increases the overall capacity and performance. In these systems, the information is *coded* using different symbols, S_i , that are transmitted via multiple transmitting antenna elements at consecutive time frames⁴¹, hence the name *space-time coding* [139],[141] (Figure 7.5)⁴².

⁴¹ The channel properties are usually assumed constant during each time frame.

⁴² Interestingly, the same coding scheme can be applied by transmitting the coded symbols in multiple frequency carriers instead of consecutive time frames (*space-frequency coding*). Multi-band radio systems that were discussed in previous chapters are a useful platform for this type of coding. Additionally, one can

As a more general case, we can imagine multiple-input multiple-output, MIMO, systems with m transmitting antenna elements and n receiving antenna elements. Assuming independent communication channels from each transmitting antenna to a receiving antenna, it can be shown [140] that besides the achieved diversity gain, the capacity of a MIMO system increases with the number of antenna elements. Space-time coding has been extensively used for MIMO systems to achieve a higher overall capacity for the communication channel [141] (Figure 7.5).

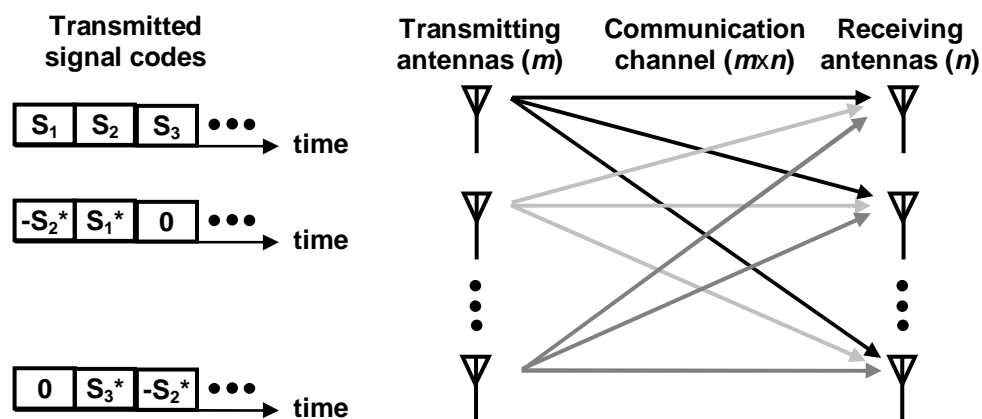


Figure 7.5: Illustration of a MIMO system and space-time coding at the transmitter

7.1.2 Phased Array

One way to make the most efficient use of transmitted signal power and to battle against the interference simultaneously is to form a directional communication link. Phased arrays are multiple-antenna systems that can *electronically* change the direction of signal transmission and reception. Naturally, one of the first applications of the phased-array systems was to form electronic radar in the military for airborne, space, and other applications [142].

Imagine a plane-wave that reaches a linear array of antennas, as shown in Figure 7.6. The general propagation expression for a plane electromagnetic wave is

imagine systems that use all of the three dimensions: time, frequency, and space for a high-performance communication.

$$\vec{E}(\vec{r}, t) = \vec{E}_0 \exp[j(\omega t \pm \mathbf{k} \cdot \vec{r})] \quad , \quad \vec{H}(\vec{r}, t) = \vec{H}_0 \exp[j(\omega t \pm \mathbf{k} \cdot \vec{r})] \quad (7.1)$$

where t is time, \vec{r} is the distance the wave has traveled, ω is the angular frequency, and \mathbf{k} is the propagation vector with the magnitude given by

$$|\mathbf{k}| = \omega \sqrt{\mu \epsilon} \quad (7.2)$$

In (7.2) μ and ϵ are permeability and permittivity of the propagation medium, respectively. The argument of the exponential in (7.1) (*i.e.*, $\omega t \pm \mathbf{k} \cdot \vec{r}$) is the phase difference of the received signal at multiple antenna elements and is proportional to the angular frequency. Since the distance that the incidence wave has traveled at each antenna port is different depending on the incidence angle, θ , there will be a corresponding phase shift in the received signal for each received path⁴³. From Figure 7.6, it can be seen that if d is the distance between two adjacent antenna elements⁴⁴, the phase difference between adjacent paths is proportional to $d \cdot \sin(\theta)$. For a single-frequency signal, the phase difference of the paths can be compensated by providing an appropriate phase shift of ϕ_m in each of the receiver chains. Additionally, the amplitude at each path can be individually controlled via an adjustable gain of A_m . Therefore, for an array size of n , the array output is

$$V(t) = \sum_{m=1}^n A_m \cdot e^{jm(kd \sin(\theta) - \phi_m)} \quad (7.3)$$

Based on the phase shifts that are provided at each receiver path, the final combined signal can be amplified or rejected. More generally, if both signal phase and amplitude can be controlled at each path, signal amplification and rejection in multiple directions is

⁴³ Although the discussions are regarding phased-array receivers, most of the arguments are applicable to phased-array transmitters as well.

⁴⁴ In a phased-array system, the distance between adjacent antenna elements affects the equivalent antenna pattern of the whole array [135]. Usually in a linear array, the elements are separated by half a wavelength, $\lambda/2$. Antenna separation for the spatial diversity schemes discussed in subsection 7.1.1 depends on the fading environment that is in turn a function of size, number, and location of the scatterers in the proximity of receivers/transmitters. To achieve uncorrelated signals at the antennas for a maximum spatial diversity gain, the antenna separation should be about 2-3 wavelengths for small-size scatterers and in the order of 10 wavelengths for large-size scatterers [139].

possible (e.g., [143]). By proper adjustments of the weights, a large immunity to undesired interference signals coming from certain directions can be achieved in the so-called *adaptive arrays* (e.g., [143]).

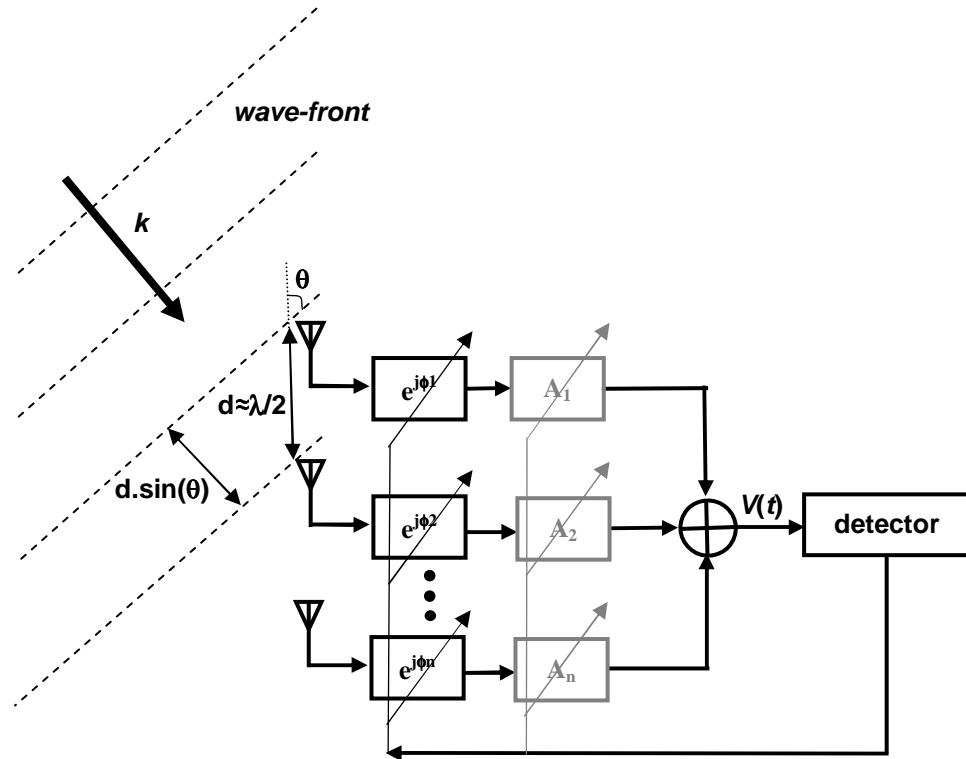


Figure 7.6: Phased-array concept (gain control block is only necessary when controlling multiple peaks and nulls is desired)

Phased arrays provide system advantages for a number of reasons: The combination of a higher signal power due to signal combining and a lower interference level due to nulling results in a higher signal-to-noise and interference ratio, SNIR. A higher SNIR can be used to increase the communication data-rate or reduce the transceiver's power-consumption. At the same time, more directionality opens the possibility of more efficient frequency re-use when a large number of users share limited frequency resources, such as cellular-phone applications. It is worth reminding the reader that phased-array techniques can be employed in the receiver, transmitter, or both.

Before discussing various radio architectures for the implementation of a generic phased-array system, we will show how the signal-to-noise ratio of a phased-array system is increased compared to a single chain receiver. For a single-chain receiver assume that the signal and noise power levels at the antenna input are S_{IN} and N_{IN} , respectively. Therefore, the input signal-to-noise ratio, SNR_{IN} is

$$SNR_{IN} = \frac{S_{IN}}{N_{IN}} \quad (7.4)$$

Since each receiver provides the same gain for the input signal and noise, assuming that the input referred noise power of each receiver chain is represented as N_{RX} , the output signal-to-noise ratio of each receiver, SNR_{OUT} can be calculated from

$$SNR_{OUT} = \frac{S_{IN}}{N_{IN} + N_{RX}} \quad (7.5)$$

Clearly in a single-chain receiver, the ratio of signal power to the noise power degrades as we move from the input to the output. In other words, a single-chain receiver is incapable of improving the SNR_{IN} without any signal processing. We will now show that the input signal-to-noise ratio can be improved in a multiple-antenna phased-array receiver.

Assume that the signal and noise power levels at the input of i^{th} antenna are $S_{IN,i}$ and $N_{IN,i}$, respectively. Also suppose that the input referred noise power and the power-gain of each receiver chain are $N_{RX,i}$ and G_i , respectively. For the desired incidence angle, the n signal paths in the receiver change their corresponding phases, Φ_i , so that their outputs add coherently (Figure 7.6). In other words, since the signals at all antenna inputs are merely phase shifted versions of each other, they are all correlated and they are added in phase at the array output. Consequently, the output signal is a *voltage summation* of the signals of all the paths. Assuming identical input signal power levels, S_{IN} , and equal receiver gains, G , the total output power, S_{OUT} , will then be

$$S_{OUT} = G \cdot n^2 \cdot S_{IN} \quad (7.6)$$

However, the noise sources at the antenna inputs are generally white and uncorrelated with one another for any reasonable antenna separation⁴⁴. In addition, the noise generated in

each receiver path comes from physically different sources and hence are uncorrelated and dominantly white. Therefore, the output noise power is a *power summation* of uncorrelated noise sources

$$N_{OUT} = \sum_{i=1}^n G_i (N_{IN,i} + N_{RX,i}) = G \cdot n \cdot (N_{IN} + N_{RX}) \quad (7.7)$$

where the second equality is derived assuming equal noise power levels and gains for each receiver path. From (7.6) and (7.7) the output signal-to-noise ratio for n identical paths is

$$SNR_{OUT} = \frac{S_{OUT}}{N_{OUT}} = \frac{n \cdot S_{IN}}{N_{IN} + N_{RX}} \quad (7.8)$$

Compared to the result for the single-chain receiver (7.5), we conclude that the output signal-to-noise ratio of the phased-array multiple-antenna system is higher by the array size, n . Also, for negligible receiver noise ($N_{RX} \ll N_{IN}$), the input signal-to-noise ratio is improved by the array size, n , at the output.

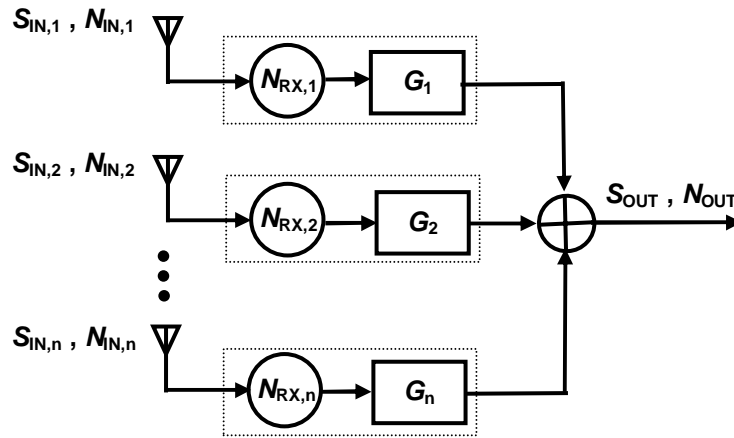


Figure 7.7: Schematic of a phased-array receiver used for SNR calculations

If the input noise sources, N_{IN} , were fully correlated, the output noise power would be

$$N_{OUT} = G \cdot (n^2 \cdot N_{IN} + n \cdot N_{RX}) \quad (7.9)$$

The output signal-to-noise ratio in this case is:

$$SNR_{out} = \frac{S_{OUT}}{N_{OUT}} = \frac{S_{IN}}{N_{IN} + \frac{N_{RX}}{n}} \quad (7.10)$$

which asymptotically reaches SNR_{in} for large n . The improvement in the output signal-to-noise ratio in this case is not as high as in the case of uncorrelated input noise sources. By comparing (7.4), (7.5), and (7.10) it can be seen that in the case of fully-correlated input noise sources, N_{IN} , the array reduces the effect of receiver noise, N_{RX} , making the output signal-to-ratio as good as the input for an infinite-size array.

7.1.2.1 Phase Shift vs. Time Delay

At this point, the difference between *phase shift* and the *time delay* in the signal, that has a subtle impact on the performance of phased-array systems, should be made clear. The arguments of the exponentials in the expression for electric and magnetic fields in (7.1), $\omega t \pm \mathbf{k} \cdot \mathbf{r}$, represent the total phase shift of the propagated wave. Therefore, signals with the same argument, $\omega t \pm \vec{k} \cdot \vec{r}$, undergo the same phase shift. In a phased-array system, for an in-phase addition of the signals at the outputs of all paths, the difference between the phases of input signals at different antenna elements is compensated within the receiver chains (Figure 7.6). In other words, in-phase signals are resulted if path difference and time delay compensate each other (*i.e.*, constant $\omega t \pm \mathbf{k} \cdot \mathbf{r}$ for different paths)⁴⁵. Therefore, in a phased-array system, one should ideally control the time delay for each receiver chain. For instance, a lossless dispersion-less transmission line can approximate an ideal time delay element over a wide range of frequencies. However, in a narrow-band communication system where the energy bearing signal is confined to a limited frequency, $\Delta\omega$, around a center frequency, ω_0 , where $\Delta\omega \ll \omega_0$, the angular frequency of the signal can be approximated with its center frequency. Note that for a single frequency, there is a one-to-one correspondence between signal phase shift and time delay. Therefore, a phase shifter around ω_0 provides an almost-constant time delay for a narrow window of frequencies. In general, the phase shifter block should behave like a delay element across the entire range of operation frequencies as much as possible to avoid signal distortion.

⁴⁵ Amplitude loss is ignored for closely spaced antenna elements in a LOS communication.

In the following section, multiple radio architectures for the implementation of phased-array systems are discussed.

7.2 Phased-Array Radio Architectures

Controlling the signal time delay (or phase shift for a narrow-band signal) in each path of a phased-array radio can be achieved by various methods involving multiple trade-offs in the performance of phased-array systems.

7.2.1 Phase Shifting and Signal Combining in Signal Path

The most straightforward method of adjusting the signal time delay, T_D , is by providing a variable phase shifter, ϕ , at the bandwidth of interest in each signal-path, as shown in Figure 7.8. These phase shifters should have a relatively low loss across the bandwidth of received signal so that they don't attenuate the received signal and degrade the overall signal-to-noise ratio. A variable low-loss and wide-band phase shifter is a challenging building block to implement in an integrated setting and is a source of active research [144]. By phase shifting and signal combining at RF , more radio blocks are shared resulting in reduced area and power consumption. Additionally, since the unwanted interference signals are cancelled after signal combining, the dynamic-range requirement of the following blocks is more relaxed allowing them to trade this with other system requirements such as power consumption. If amplitude control is needed, it can be achieved by variable-gain low-noise amplifiers before or after the phase shifters at RF .

Phase shifting and signal combining can also be performed after down-converting the received signals to an intermediate-frequency, IF . Due to the additional signal amplification at the RF stages, phase shifter loss will have a less deteriorating effect on receiver sensitivity in case it is performed at the IF stage. However, some of the aforementioned advantages, including a lower dynamic-range requirement for the RF mixer, become less effective. Moreover, the value of passive components (*e.g.*, inductors, capacitors) needed to provide a certain phase shift is inversely proportional to the carrier frequency. Since the value of integrated passive components is directly related to their physical size (*i.e.*, area), passive phase shifters at IF consume a larger area compared to the ones at RF .

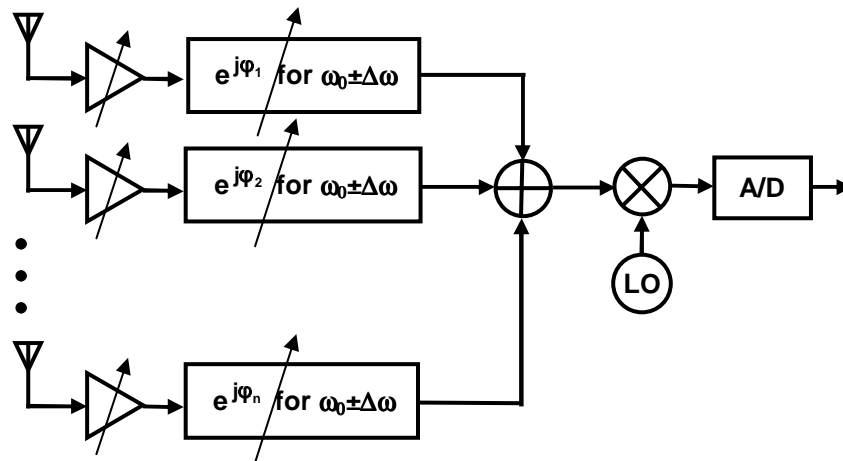


Figure 7.8: Phased-array receiver using signal-path (*RF* or *IF*) phase shifting

7.2.2 Phase Shifting in Local-Oscillator Path

As an alternative approach, one can indirectly vary the phase of the received signal by adjusting the phase of local-oscillator signal used to down-convert the signal to a lower frequency. This is due to the fact that the output phase of a multiplier (or mixer) is a linear combination of its input phases, *i.e.*,

$$\begin{aligned} V_{out}(t) &= \cos(\omega_{rf}t + \phi_{rf}) \times \cos(\omega_{lo}t + \phi_{lo}) \\ &= \frac{1}{2} \cos[(\omega_{rf} + \omega_{lo})t + (\phi_{rf} + \phi_{lo})] + \frac{1}{2} \cos[(\omega_{rf} - \omega_{lo})t + (\phi_{rf} - \phi_{lo})] \end{aligned} \quad (7.11)$$

Figure 7.9 shows a simplified phase-array receiver that uses *LO* phase shifting. Phase shifting at the *LO* port is advantageous in that the phase shifter loss does not directly deteriorate the receiver sensitivity. Additionally, the nonlinearity and loss of active phase shifters such as phase-interpolating implementations (*e.g.*, [145]) can be more easily tolerated in the *LO* path compared to the signal path. However, since the undesired interferences are only rejected after the combining step at the *IF*, *RF* amplifiers and mixers need to have a higher dynamic range than the ones in the signal-path phase shifting scheme of subsection 7.2.1. The increased number of building blocks might also increase the chip area and power consumption of the receiver. The control of signal amplitude can be made possible more easily with *IF* variable-gain amplifiers (VGA).

Note that since the frequency of the local oscillator is fixed, as mentioned in subsection 7.1.2.1 the exact path delay can be maintained for only a single *RF* frequency. In other words, LO phase shifting is not an efficient solution for wide-band *RF* signals.

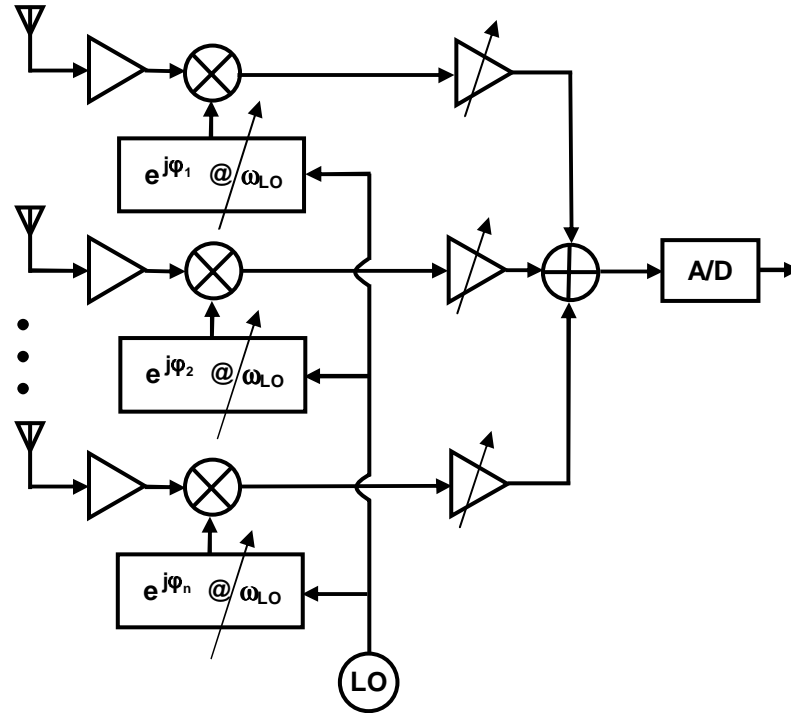


Figure 7.9: Phased-array receiver using LO phase shifting

7.2.3 Digital Array Implementation

The delay and amplitude of the received signal can be adjusted at the baseband using a digital processor (Figure 7.10). Digital array architecture is very flexible and can be adapted for other multiple antenna systems that were previously mentioned. Despite its versatility, baseband phased-array architecture uses a larger number of components compared to the previous two systems, resulting in a larger area and more power consumption. At the same time, since the interference signals are not cancelled before baseband processing, all the circuit blocks, including the power-hungry analog-to-digital converters, need to have a large dynamic range to accommodate all the incoming signals without distortion. Above all,

handling and processing a large amount of data coming from multiple parallel receivers is not inexpensive even for today's advanced digital technology.

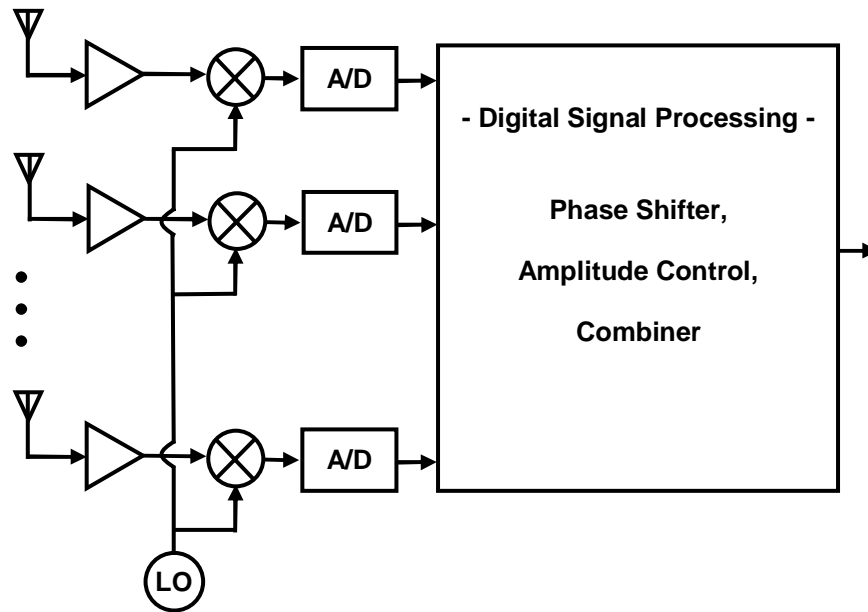


Figure 7.10: Phased-array receiver using baseband signal processing (digital array)

For instance, imagine a digital array of 8 receivers where each has a 6 bit analog-to-digital converter that samples the signal with a 10 MHz channel bandwidth at twice the Nyquist rate⁴⁶. These numbers are on the low end of the acceptable range for this system. Nevertheless, the baseband data-rate of the whole system can be calculated as

$$\text{Baseband Data-Rate} = 8^{RX} \times 2^{I\&Q} \times 20MS/s \times 6bits = 1.92Gb/s \quad (7.12)$$

As a comparison, the fastest way to send the data into a personal computer using today's PCI standard is $32bits \times 33MHz = 1.056Gb/s$. This rate is almost halved when notebook computers are used (*e.g.*, IEEE1394 standard supports 400Mb/s). Alternatively, a very powerful digital signal processing (DSP) core can be used to process this huge data, but it is going to be bulky, power-hungry, and expensive in today's technology.

⁴⁶ These numbers are typical of today's WLAN single-antenna receivers.

In short, unless faster and more efficient digital data processing becomes available at a lower price, digital implementations still seems to be a more expensive solution for multiple-antenna systems.

7.3 A 24 GHz Phased-Array Radio

To exploit the advantages of phased arrays, a multiple antenna phased-array radio system has been designed and its receiver has been fabricated.

First, we will discuss the choice of operation frequency for this implementation. One of the drawbacks of multiple-antenna systems compared to single-antenna ones is the excessive chip area and footprint used by many circuit blocks and antenna elements. Roughly speaking, the size of antennas and their spacing is proportional to the wavelength and hence inversely proportional to the carrier frequency. Additionally, a large portion of area used by *RF* integrated circuits is dedicated to passive components whose size and area scale down with frequency. In other words, moving to higher frequencies helps in designing more compact multiple-antenna systems. Moreover, higher frequencies will have more available bandwidth resulting in a higher system capacity. In multi-path fading environments (Figure 7.1 (b)), the received signal comprises of multiple time delayed copies of the transmitted signal. Therefore, the channel impulse response consists of a series of pulses. *Delay spread* quantifies the total time that the received signal has a significant energy due to the multi-path reflections [147]. Indoor channel measurements [146] show that for a constant bandwidth the average delay-spread at higher frequencies is smaller, pointing to the possibility of higher data-rate communication at higher carrier frequencies.

However, operating at higher frequencies poses several challenges from various perspectives: system, propagation, antenna, and circuit. Assuming constant antenna gains, the free-space attenuation of a propagated signal is proportional to the square of carrier frequency [3], indicating higher *path-loss* at higher frequencies. Also, the transmissibility of most materials is lower at higher frequencies, resulting in a higher signal loss caused by obstructing the line-of-sight (LOS) communication. Indoor channel measurements in a typical office building indicate a significantly higher path-loss between the floors at higher

frequencies [146]. Although antennas at higher frequencies are smaller, due to antenna theorem the total collected power at the receiving antennas also reduces with the increase of frequency [147]. Furthermore, active devices have less gain at higher frequencies. Issues such as unwanted coupling, signal loss in substrate, as well as modeling and simulation at these frequencies add to the challenge of higher frequency designs.

Considering all these points, while trying to take a substantial leap in the design of ultra-high-frequency radio systems, the ISM band at 24 GHz with 250 MHz available bandwidth was chosen for the implementation of phased-array transceiver.

In the next subsections, the architecture and implementation of this radio will be discussed.

7.3.1 Receiver Architecture

Our transceiver employs an *LO* phase shifting architecture for several principal reasons. Phase shifting and signal processing at baseband (*i.e.*, digital arrays) was eliminated due to the much larger chip area, power consumption, and the high demand on the baseband digital interface, particularly for the high data-rates of interest.

Variable phase shifters at 24 GHz radio-frequency will have a relatively higher loss due to the substrate loss, loss in passive components (especially inductors and varactors) and their limited self-resonance frequency. This loss in the signal path deteriorates the receiver's overall sensitivity and can be minimized by providing more gain at the low-noise amplifier preceding them. More importantly, the phase shifter's loss usually changes significantly with its phase shift that necessitates the use of *RF* variable-gain amplifiers with fine resolution to compensate these variations.

In comparison, the loss in the *LO* phase shifting networks can be easily compensated by high gain amplifiers (*e.g.*, limiters) without the need for any amplitude tuning. The reason for this is that many *RF* mixer implementations (*e.g.*, Gilbert-type) perform better when driven to switch with a large amplitude at the *LO* port making their gain independent of the *LO* amplitude. Also, generating multiple phases of an *LO* signal can be achieved in ways other than using phase shifters. Different methods for generating *LO* multiple phases will be discussed in subsection 7.3.2.3.

The aforementioned considerations led to the design of phase-array radio that uses different phases at the LO path. The block-diagram schematic of the 24 GHz phased-array receiver consisting of 8 paths is shown in Figure 7.11. The receiver uses a two-step downconversion architecture with an IF of about 5 GHz for three main reasons. Firstly, compared to single downconversion schemes such as homodyne, a heterodyne-type receiver achieves more selectivity and gain-control at multiple stages (refer to Chapter 2). Secondly, by choosing 5 GHz for IF frequency it will be possible to use the receiver as a *dual-mode* system. If the environment propagation properties at 24 GHz are acceptable, the system operates in the normal mode of high-data rate transmission. If high-data rate is not required, the receiver can bypass the 24 GHz front-end and operate at the existing 5 GHz wireless LAN frequencies discussed in Chapter 5 in a low-power mode. In the second scenario, IF amplifier and image-reject mixer act as the front-end LNA and RF mixer for the 5 GHz frequency band. Additionally, with the mentioned frequency planning, both LO frequencies can be generated in one synthesizer loop with the use of a divide-by-four block as shown in the lower part of Figure 7.11.

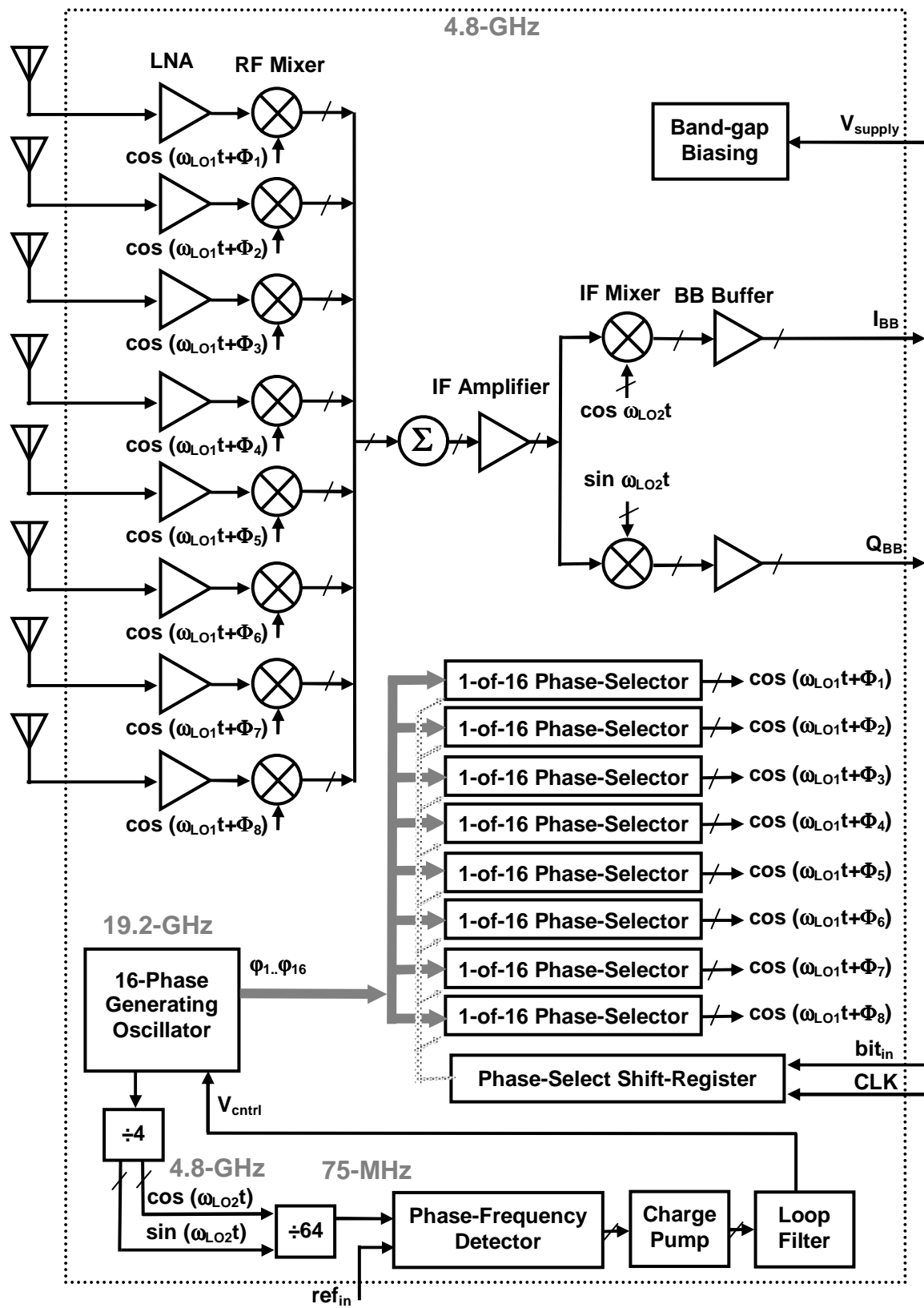


Figure 7.11: Block-diagram schematic of the 24 GHz phased-array receiver

A single oscillator core generates 16 discrete phases (*i.e.*, 4-bit resolution) that are used to control the phase of each path. A set of 8 phase-selectors (*i.e.*, analog phase multiplexer) provide the appropriate phase of LO to the corresponding RF mixer for each path, *independently*. In other words, the LO phase for each path is controlled irrespective of the phase of the other paths. The phase-selection data is serially loaded to an on-chip shift-register using a computer interface. In Figure 7.12, we show that using discrete LO phases does not sacrifice the beam-forming accuracy by a substantial amount. In fact, in the worst case the signal loss is less than 1dB in this 4-bit phase shifting scheme.

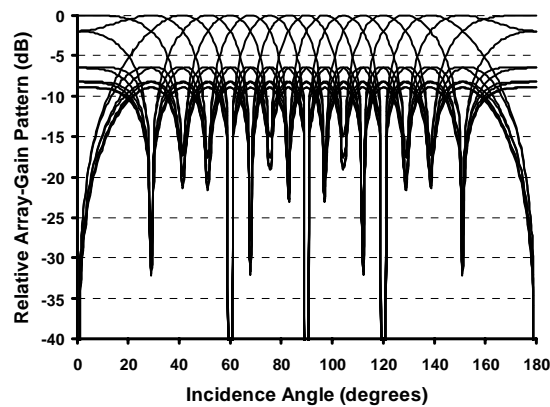


Figure 7.12: Relative gain of the array with 4-bit discrete phase shifting

The image-frequency of the first downconversion at 14.4 GHz is attenuated by the narrow-band transfer function on the front-end (*i.e.*, antenna and LNA). Since communication schemes around the image-frequency band are mainly low-power satellite services, no image-rejection architecture is used at the RF stage. The final down-conversion to baseband or very low-IF is done by a pair of quadrature mixers. The divide-by-four block that is used to generate the second LO will naturally produce in-phase and quadrature-phase signals to drive these mixers.

7.3.2 Receiver Building Blocks

The phased-array receiver has been designed and fabricated in a SiGe BiCMOS process with the maximum cut-off frequency (f_t) of 90 GHz for bipolar devices and the minimum channel length of 0.18 μm for the CMOS transistors. The process offers five metal layers where the top two layers are thicker and are used for on-chip routing of the high-frequency signals and for implementing on-chip spiral inductors.

In the following section, details of each of the building blocks will be discussed.

7.3.2.1 RF Front-End⁴⁷

Each RF front-end consists of a 2-stage LNA and a Gilbert-type mixer (Figure 7.13). The outputs of all 8 mixers are combined in the current domain and terminated with a tuned load at the IF frequency. The front-end has been designed to have about 20dB of gain and 5dB of noise-figure at 24 GHz. More information on the design of front-end can be found in [148].

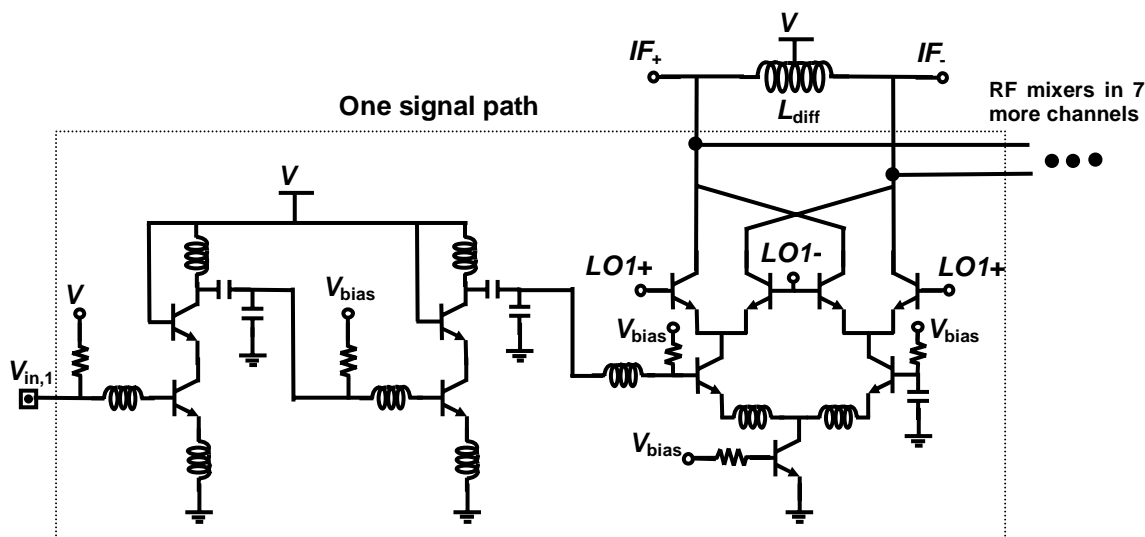


Figure 7.13: Schematic of the 24 GHz front-end consisting of a 2-stage LNA and Gilbert-type mixers in each channel

⁴⁷ The design of the signal path namely the 24GHz front-end, IF amplifier and mixer, as well as baseband buffers, has been done entirely by Xiang Guan from Caltech. These blocks are mentioned in this thesis merely to document the complete receiver design.

7.3.2.2 IF Circuitry⁴⁷

The *IF* stage consists of a tuned low-noise amplifier at an *IF* frequency of 4.8 GHz followed by a pair of in-phase and quadrature-phase double-balanced Gilbert-type mixer as shown in Figure 7.11 and Figure 7.14. The *IF* amplifier and mixer provide a combined gain of around 13dB and are followed by baseband differential-pair buffers as shown in Figure 7.11.

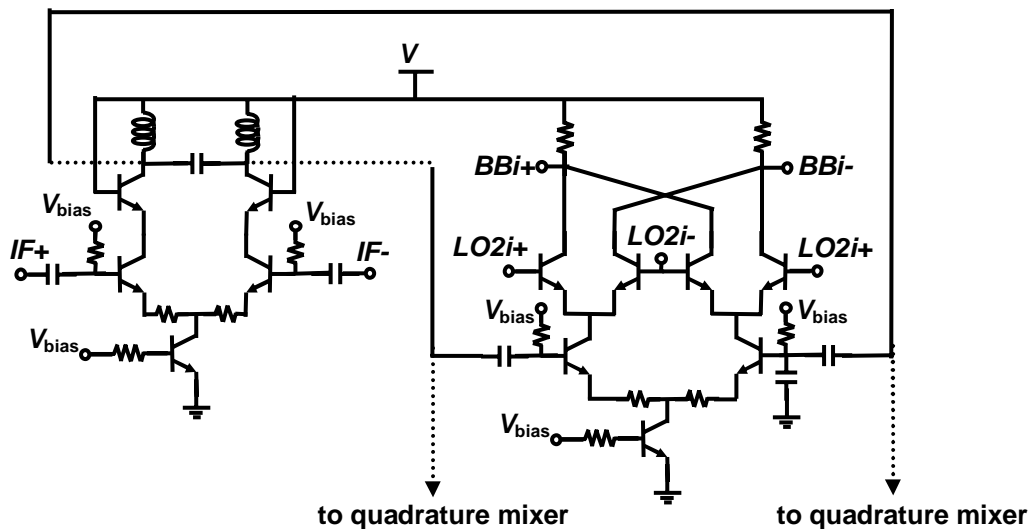


Figure 7.14: Schematic of the 4.8 GHz *IF* stage consisting of *IF* amplifiers and double-balanced Gilbert-type mixers

7.3.2.3 Generating Multiple Phases of Local Oscillator

At least two distinct methods to create various phases of a local-oscillator signal can be envisioned. In the first method, only one phase is generated in the oscillator core (two phases considering differential signals). Phase shifters, phase-interpolators, or similar blocks follow the oscillator in order to generate multiple phases of its output signal in a continuous or discrete fashion [145],[156]. These blocks can be narrow-band around the local-oscillator frequency and their loss is usually not a major concern in the local-oscillator path. In the second scheme, multiple phases are generated inside the oscillator core. Usually, this method results in discrete phases with a minimum resolution of $2\pi/N$, where N

is an integer number. A few of the common techniques that have been used to generate multiple phases of a narrow-band local-oscillator signal are described below.

I. Phase Shifting with All-Pass Functions

A common class of wide-band phase shifter design is based on the difference in the phase of two all-pass functions. The same principle can be used to create a narrow-band phase shifter with a low-sensitivity to component values. We will use the simple case of first-order all-pass functions to show the abovementioned scheme.

The transfer-function of a first-order all-pass filter can be generally represented as

$$H_{AP}(s) = \frac{s - \omega_0}{s + \omega_0} \quad (7.13)$$

As its name implies, an all-pass function, such as the one shown in (7.13), has a unity magnitude at all frequencies. The phase of the first-order transfer function in (7.13) at the angular frequency, ω is given by

$$\angle H_{AP}(j\omega) = -2 \tan^{-1}(\omega/\omega_0) \quad (7.14)$$

Therefore, the first-order all-pass function is capable of providing the desired phase shift at any given frequency without disturbing the signal amplitude. However, the value of phase shift is very sensitive to the variations in ω_0 . A combination of familiar first-order low-pass and high-pass RC filters forms a first-order all-pass function suitable for varying the phase of a narrow-band input signal by any arbitrary value given by (7.14), where $\omega_0=1/RC$. The circuit with its phase transfer function is shown in Figure 7.15.

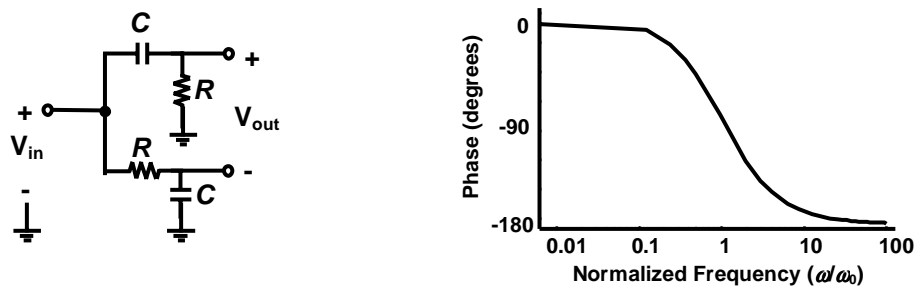


Figure 7.15: A first-order passive all-pass filter and its phase transfer-function

Note the subtle difference in the well-known passive RC polyphase filter [155] and the configuration in Figure 7.15. In the latter, the output is taken as a difference voltage of the low-pass and high-pass filter outputs, whereas in the former, the output voltage is defined between each individual output port and ground⁴⁸.

The somewhat steep slope of the phase transfer function for phase values other than 0° or 180° shows the sensitivity of the design to the variations in ω . A less sensitive design is achieved by subtracting two such all-pass functions. If the pole/zero frequencies of first-order all-pass functions are ω_1 and ω_2 , phase variations around the geometrical mean of the two, $\omega_0 = \sqrt{\omega_1\omega_2}$, is zero (lower curve in Figure 7.16). This general broadband phase shifting concept and the results for first-order all-pass functions are graphically depicted in Figure 7.16.

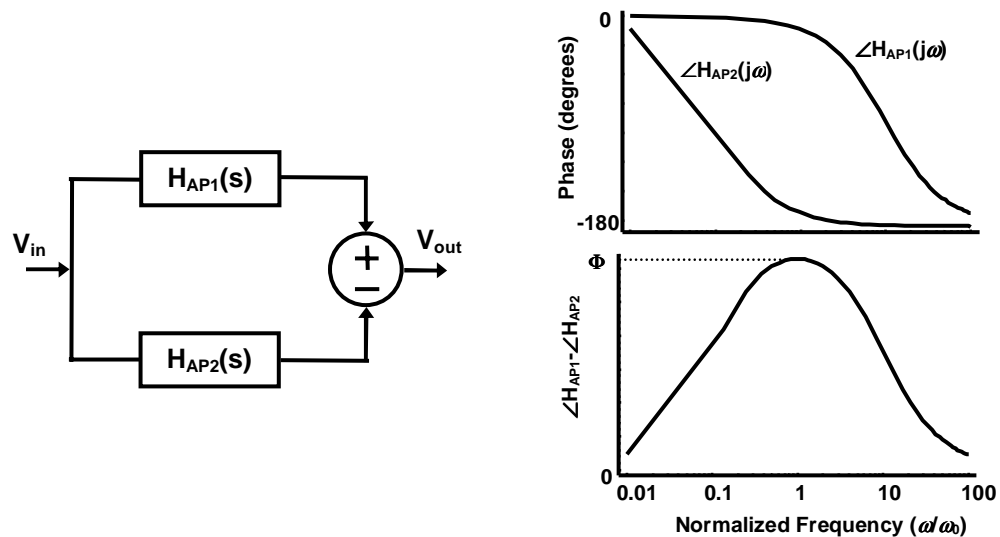


Figure 7.16: Broadband phase shifting using all-pass functions

Passive RC implementation of a first-order all-pass function has been used to generate multiple-phases of a local oscillator in the intermediate-frequency (IF) stage of an adaptive antenna receiver [156]. In high-frequency implementations, the unwanted parasitic components of passive components that construct the all-pass filter (*e.g.*, R and C in Figure

⁴⁸ A passive RC polyphase structure provides a constant phase shift equal to 90° between the output ports at all frequencies with the same amplitude at only $\omega_0=1/RC$.

7.15) might affect the all-pass transfer function substantially and should be considered with cautious in the design process.

II. Narrow-band Phase Interpolation

Phase interpolation has been used to generate multiple phases of a digital clock in high-speed signaling circuits [157], [158]. The output of a phase interpolator is a weighted sum of two out-of-phase periodic waveforms at its input. The phase of this signal can be varied by controlling the weight of signal paths. The block-diagram schematic of a generic phase interpolator and a vector diagrams for sinusoid input signals that are 90° out-of-phase are shown in Figure 7.17.

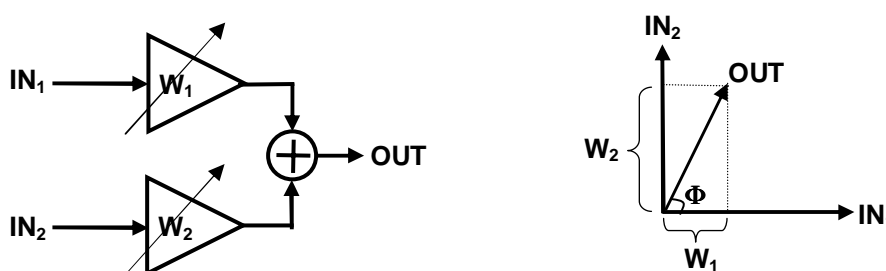


Figure 7.17: A generic phase-interpolator and a vector-diagram for sinusoid input signals

In theory, the input signals can have any arbitrary relative phase difference, except 0° and 180° . In most practical cases, a value of 45° or 90° is considered. An analog phase shifter based on interpolation for the local-oscillator of an adaptive antenna application has been proposed and implemented [145]. As can be seen in Figure 7.17, by varying signal-path weights, the amplitude of the interpolator's output changes as well. However, for the local-oscillator signal, this amplitude can be clamped to any desired value in a later stage. Finally, it is worth noting that the variations and inaccuracies in the relative phase of input signals of a phase-interpolator directly affect the output phase as well.

III. Multiple Phase Generation Using Coupled Oscillators

By coupling an array of similar oscillators using proper networks, their output frequency can be synchronized while a predetermined phase shift between adjacent elements is maintained [159],[161] (Figure 7.18). The coupling can be through passive components

such as transmission lines and discrete components [159], active elements [160], or even through magnetic coupling in the air [161]. The entire array of coupled oscillators can also be synchronized to a frequency- and phase-controlled source (*e.g.*, generated within a phased-locked loop) using an injection locking mechanism [159]. Instead, for electrically tunable oscillators such as voltage-controlled oscillators, a common frequency control signal can be applied to adjust the frequencies of oscillators at once [160].

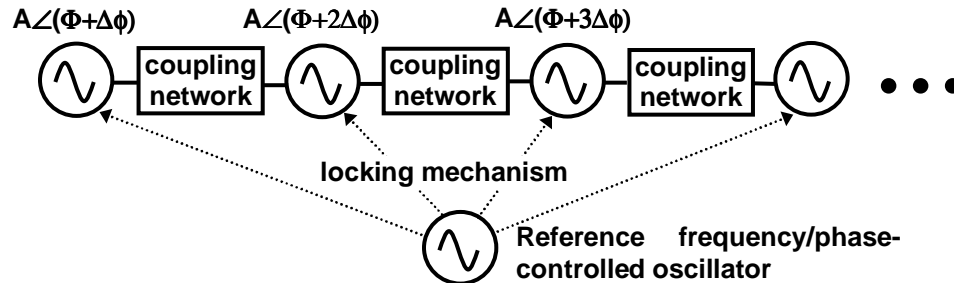


Figure 7.18: An array of coupled oscillators for multiple phase generation

IV. Multi-Phase Oscillators

Instead of utilizing a coupled network of oscillators, a single oscillator core can be used to generate multiple phases of a single frequency. Most of these techniques rely on extracting phases from equidistance nodes of a uniform closed oscillator loop. A phase shift of 360° is maintained across the loop in order to maintain a stable oscillation. Two specific implementations of multi-phase oscillators are shown in Figure 7.19. A closed loop of delay elements (*e.g.*, an inverter) with a loop-gain greater than one is the well-known ring-oscillator that is capable of generating multiple phases [169] (Figure 7.19(a)). Alternatively, the required delay can be achieved by using passive elements. Figure 7.19(b) shows a traveling wave oscillator where the necessary phase shift is accomplished by a transmission line driven by active elements that maintain a steady oscillation [176]. Due to the usage of more active components, the power consumption at the core of multi-phase oscillators is usually higher than the single-phase versions. However, in order to generate multiple phases from a single-phase oscillator, extra power is utilized in the following stages, such as the filter and phase-interpolators.

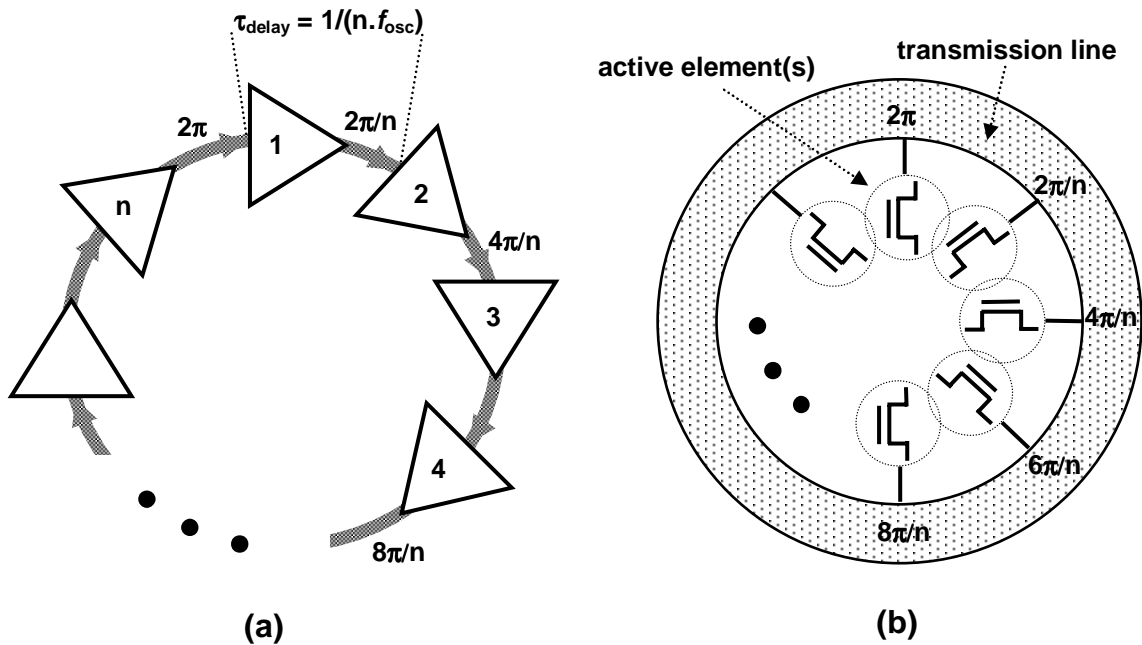


Figure 7.19: Multi-phase oscillators in ring configuration (a) using delay elements (b) traveling wave oscillator with a transmission line

7.3.2.4 A 19 GHz Multi-Phase Voltage Controlled Oscillator

In our design, a ring connection of 8 fully differential CMOS amplifiers forms the 19 GHz voltage-controlled oscillator capable of generating 16 phases (Figure 7.20) [162]. By flipping one of the connections, the number of amplifying stages is cut into half in a fully-differential structure (top left connection of Figure 7.20).

If no inductors at the amplifier outputs were used (*e.g.*, differential pair with resistive load, or CMOS inverters), each amplifier should have operated at a speed very close to the maximum operating frequency of transistors in the process and reliability could be sacrificed. To better observe this, imagine that each amplifier could be modeled with a single pole system

$$H(s) = \frac{A_0}{1 + \frac{s}{s_0}} \quad , \quad s_0 = j\omega_0 \quad (7.15)$$

Each amplifier could produce a phase shift equal to $\tan^{-1}(\omega/\omega_0)$. In the case of a 22.5° phase shift for each amplifier at 19 GHz, the pole should be at least at 46 GHz. Since the gain of each stage should be more than one to guarantee oscillation start-up, the unity-gain frequency of each amplifier ($\approx A_0 \times \omega_0$) approaches the device cut-off frequency.

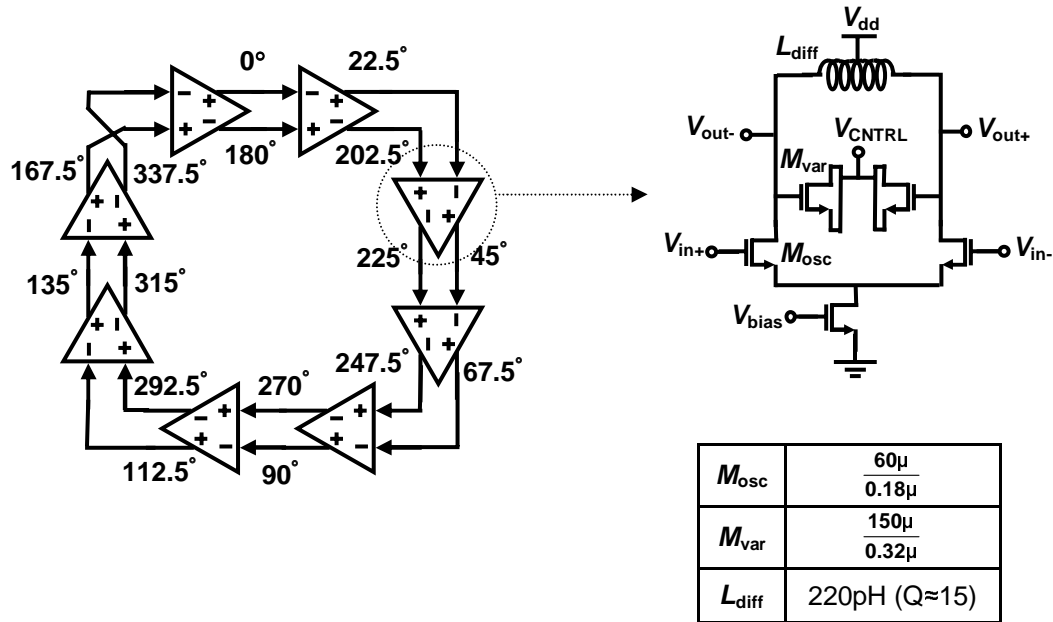


Figure 7.20: Schematic of the 19 GHz VCO that generates 16 phases of LO

However, inductors can generate the necessary phase shift for each amplifier in the following fashion. At the oscillation frequency, ω_{osc} , the equivalent parallel RLC load causes a phase shift of

$$\frac{\pi}{2} - \tan^{-1} \frac{L\omega_{osc}}{R(1 - LC\omega_{osc}^2)} \quad (7.16)$$

In case of a 22.5° phase shift for each stage, we should have

$$LC = \frac{1}{\omega_{osc}^2} \left(1 - \frac{1}{Q \times \tan \frac{3\pi}{8}} \right) \quad (7.17)$$

where Q is the load quality factor and is equal to $R/L \cdot \omega_{osc}$. For the $Q \approx 15$ at 19 GHz in this process, $LC \approx 0.97/\omega_{osc}^2$ or $\omega_{osc} \approx 0.99/\sqrt{LC}$. In other words, each amplifier is almost tuned at the oscillation frequency. Each of the designed amplifier stages draws less than 3.2mA from a 2.5V supply resulting in a total power-consumption of 63mW for the oscillator.

The center frequency can be tuned by changing the control voltage of differential MOS varactors. In order to make the high-frequency oscillator insensitive to loading, all the 8 differential outputs are buffered prior to connection to other circuit blocks (Figure 7.21). Each emitter-follower and the differential-pair draw about 1mA and 1.9mA from a 2.5V supply that result in about 9.8mW of power-consumption for each buffer.

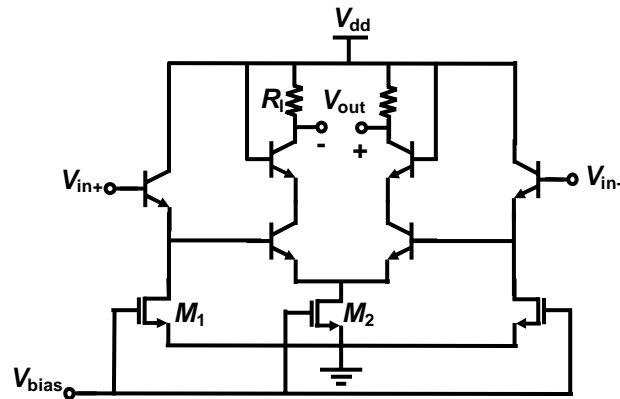


Figure 7.21: Buffers after the oscillator core

7.3.2.5 Phase-Selection Circuitry

As previously mentioned, each receiver path has independent access to all 16 phases of the local oscillator. In order to minimize the complexity of the phase-selection circuitry, the appropriate phase of the local oscillator for each path is selected in two steps. Initially, an array of 8 differential pairs with switchable current sources and a shared tuned load are used to select one of the 8 output pairs of oscillator (Figure 7.22). A dummy array with complementary switching signals is used to maintain a constant load and prevent relative changes in phases while switching. In the next step, another pair of cross-couple differential pairs selects the sign-bit resulting in complete access to all LO 16 phases. The

abovementioned cascaded configuration reduces the necessary number of phase selectors (*i.e.*, differential pairs in our case) from 2^4 to 2^3+2 for each path. The cross-coupled differential pairs at the output of each stage partially cancel the loss associated with the inductors and transistors' outputs and hence increase the LO amplitude driving RF mixers.

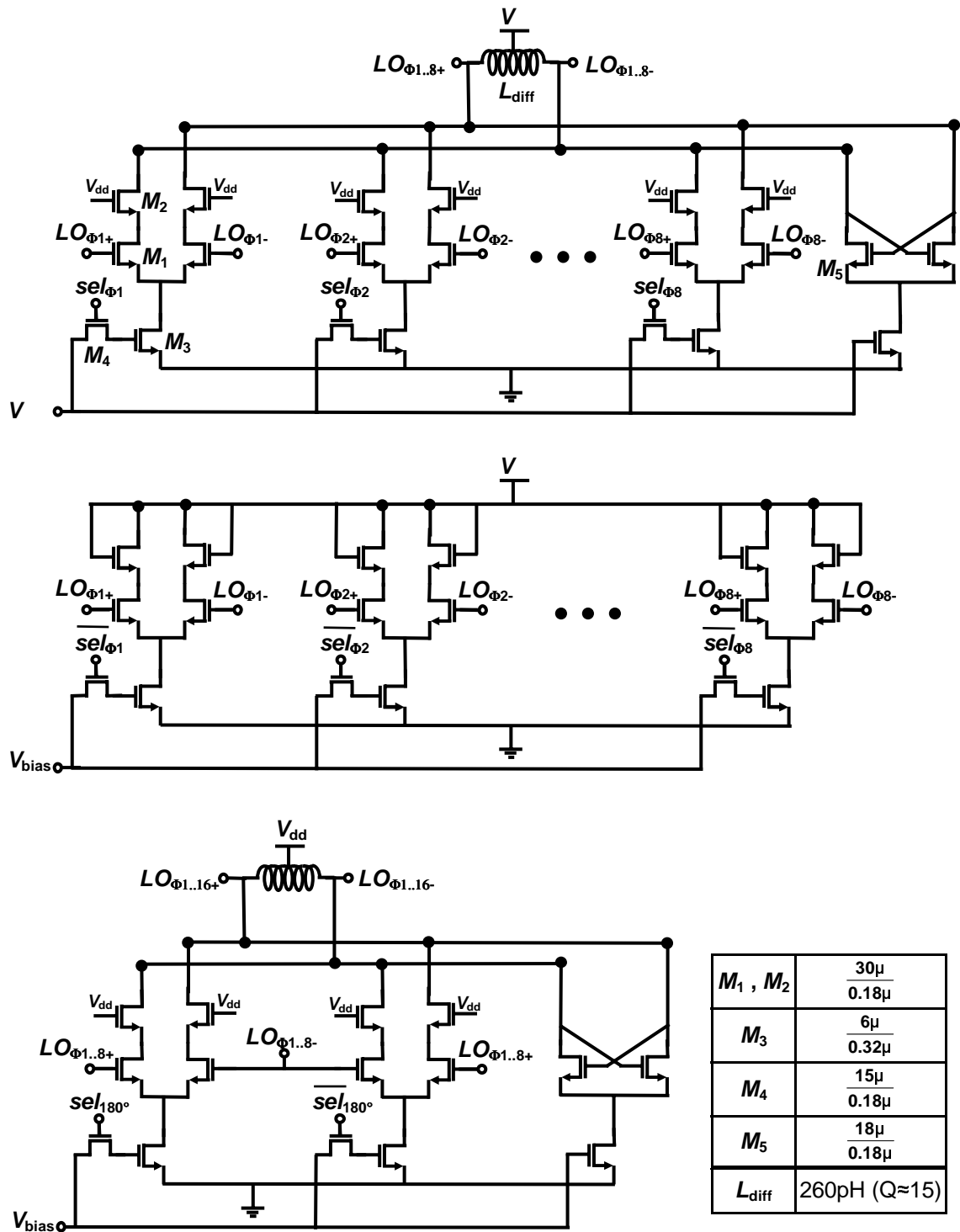


Figure 7.22: Schematic of LO phase selection circuitry for each path (biasing not shown). (a) selecting one of 8 oscillator output pairs; (b) dummy array to maintain constant loading for all phases; (c) sign selector

7.3.2.6 LO Phase-Distribution Network

The 16 generated phases of the voltage-controlled oscillator have to be fed into all the 8 phase-selection circuitries of Figure 7.11 in the most symmetric manner possible. In particular, the phase delay of the traces connecting these blocks should be equal for all local oscillator phases. Usually, small mismatches in delivering the LO phases to different receiver paths deteriorates the side-lobe attenuation significantly. The array response of the 8-path multiple-antenna system with a random LO phase mismatch of $\pm 2.5^\circ$ between the 8 paths is plotted versus the ideal case (*i.e.*, without phase mismatch) for comparison in Figure 7.23. As can be seen, this small mismatch can substantially deteriorate the nulls in the gain pattern. Note that based on electromagnetic simulations, the wavelength of a 19 GHz signal in typical micro-strip line in our utilized silicon technology is about $6000\mu\text{m}$, and hence a $\pm 2.5^\circ$ phase difference corresponds to the length difference of $\pm 40\mu\text{m}$.

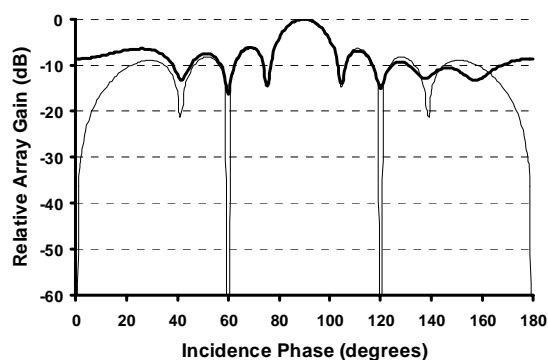


Figure 7.23: Array response with $\pm 2.5^\circ$ of mismatch in LO phase distribution (thick line) compared to the ideal case (thin line) for 8-path receiver

A symmetric tree structure for all 16 phases has been used to transfer the local-oscillator signal to the phase selection circuitry of each path with a minimal mismatch between the paths (Figure 7.24). The top two thicker metal layers in the process were used in constructing the signal distribution tree for a lower loss in LO signal. The process restrictions on the minimum width and spacing of these metal layers resulted in a relatively large size for the LO phase distribution network.

The LO phase distribution lines transform the input impedance of the phase selection circuitry to a new impedance at the LO buffer output node in Figure 7.21. This transformed impedance should be made equal to the complex conjugate of the output impedance of the LO buffer to achieve the maximum power transfer and hence the largest LO amplitude at the input of phase-selection circuitry. Under conjugate match condition and neglecting the loss in distribution lines, the theoretical maximum achievable differential signal swing at the input of each phase selection circuitry is

$$V_{diff} = \frac{1}{2\sqrt{n}} \cdot i_{tail} \cdot \sqrt{R_{out}R_{in}} \quad (7.18)$$

where i_{bias} and R_{out} are the tail current and output resistance of the differential-pair buffer in Figure 7.21, respectively, R_{in} is the input resistance of each phase-selector and $n=8$ is the number of phase selectors that are connected to a single LO buffer. In our implementation, with $R_{out} \approx 280\Omega$, $R_{in} \approx 600\Omega$, and $I_{tail} \approx 1.9\text{mA}$, the maximum swing based on (7.18) is about 140mV. Due to the inaccuracies in prediction and modeling of LO distribution lines in addition to their insignificant loss at 19 GHz, we expect the amplitude to be smaller in practice. However, the phase selection circuitry is designed to maintain the required LO amplitude across RF mixers.

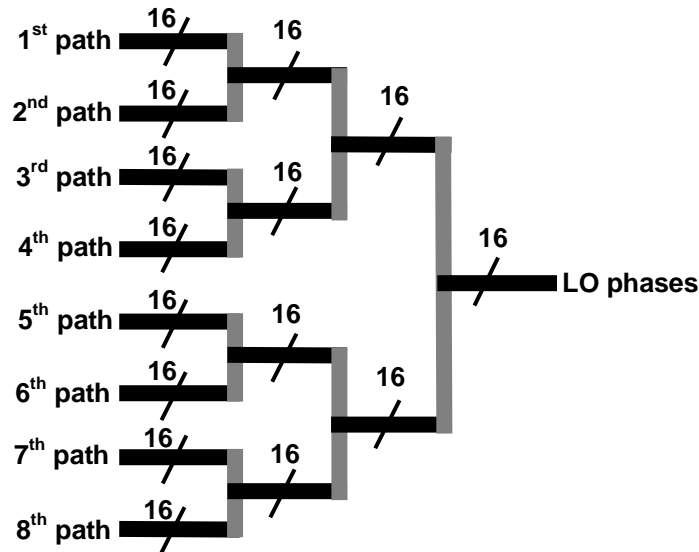


Figure 7.24: Tree structure used for a symmetric distribution of 16 LO phases

7.3.3 Measurement Results of the Implemented Receiver

The die micrograph of the fully integrated 24 GHz phased-array receiver is shown in Figure 7.25. The complete receiver occupies $3.3 \times 3.5 \text{ mm}^2$ of silicon area, of which about 5-10% is virtually unused. Special attention to a symmetric distribution of LO phases to each receiver path has resulted in a relatively large area being unused. The phase distribution network is made up of binary tree structures and takes up significant portion of the chip area by itself. The effect of these long lines at 19 GHz has been included in the design process. However, due to the lack of sufficient time before the fabrication deadline, optimum line structures for on-chip signal transmissions on silicon as well as coupling effects of close-by lines were not investigated.

Except for receiver inputs (8 pads), differential in-phase and quadrature-phase baseband outputs (4 pads), and PLL reference (1 pad), all the other pads are either ground or biasing/control voltage pads, hence making a truly fully integrated receiver.

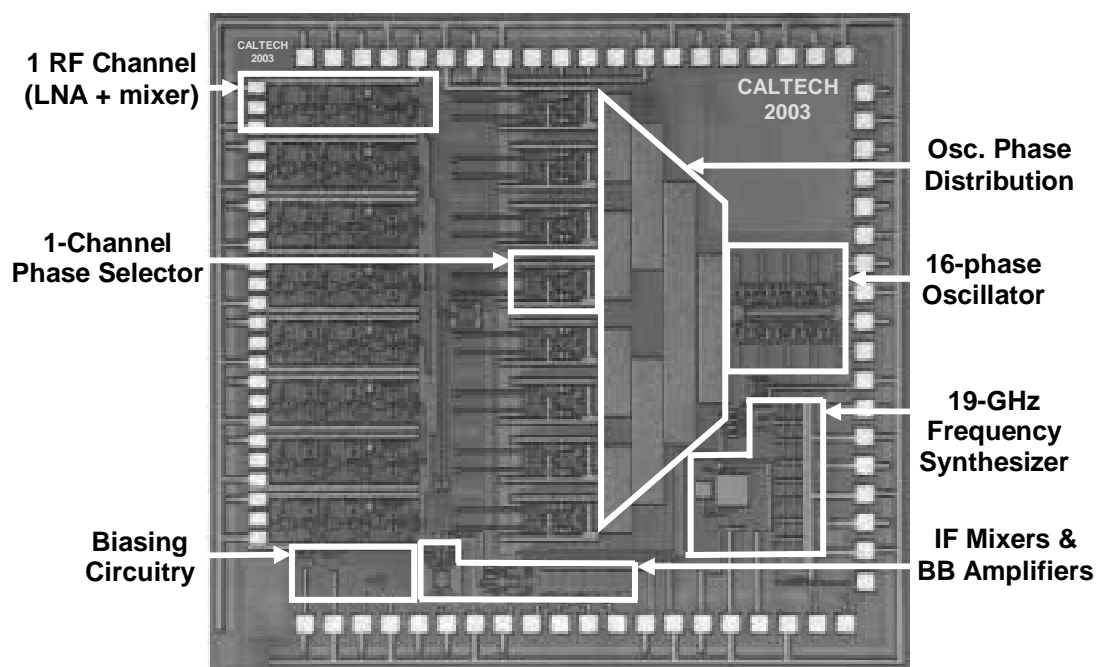


Figure 7.25: Die micrograph of the 24 GHz fully integrated phased-array receiver

An on-chip phased-locked loop (PLL) is designed to lock the 19 GHz LO signal to a 75 MHz reference signal source. Unfortunately, the input to one of the dividers in the chain

does not have a large enough amplitude and the PLL does not lock reliably. However, we can still adjust the frequency of VCO by changing the control voltage across varactors (a separate pad). In order to not disturb the symmetry of VCO output phases, none of them are connected to any pad for measurements. Nevertheless, we can verify the VCO performance by picking up the high-frequency signal via a loop antenna placed on top of the chip.

The frequency of the VCO can be varied from 18.8 GHz to about 21 GHz (Figure 7.26). The slope of this transfer characteristic is about 2.1 GHz/V at 19.2 GHz and reaches a maximum of 2.67 GHz/V close to 19.6 GHz.

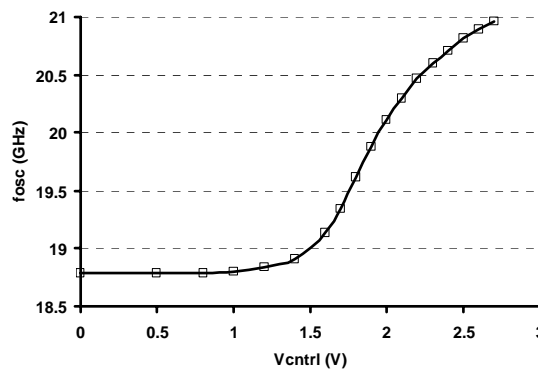


Figure 7.26: Oscillation frequency vs. varactors' control voltage

The output spectrum and the phase-noise of the VCO at 18.70 GHz is shown in Figure 7.27. The VCO achieves a phase-noise of -103dBc/Hz at 1 MHz offset from the carrier. The measurement at higher offset frequencies is limited by the thermal noise floor (-107.5dBc/Hz) of the spectrum analyzer used to measure the phase-noise. A variation of about 15dB is observed in the oscillator phase-noise with changes in the center frequency. The large variation can be attributed to two issues. A large tuning range and hence a large gain for the VCO results in an increase in phase-noise due to the common-mode noise from the control line [162]. Also, the quality factor of varactors varies as their value changes, and therefore the effective parallel resistance of the tank changes with the center frequency alterations. Consequently, the oscillator amplitude changes as it is designed to operate in the current limited region [112] in order to preserve power consumption. Increasing the VCO bias current results in a lower phase-noise variation that proves this hypothesis.

Reducing the unnecessarily large tuning-range by decreasing the size of varactors further lowers the phase-noise variations.

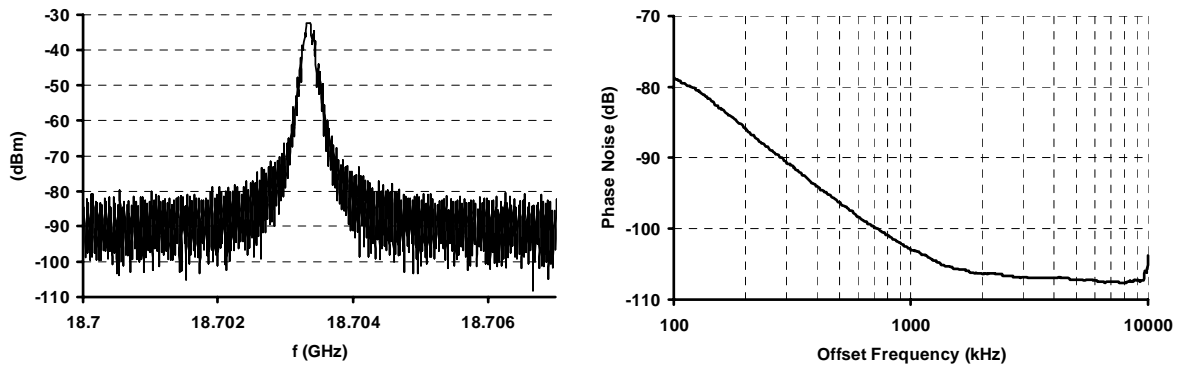


Figure 7.27: Oscillator output spectrum and phase-noise at 18.70 GHz

To compare the performance of this 8-phase oscillator to that of recently published oscillators on a silicon technology ([162]-[176]), the figure of merit defined in [112] has been used (Figure 7.28). The power-frequency-normalized (PFN) figure of merit is defined to normalize the performance of oscillators by taking the phase-noise and power-consumption into account

$$PFN = 10 \log \left[\frac{kT}{P_{\text{sup}}} \cdot \left(\frac{f_{\text{osc}}}{f_{\text{off}}} \right)^2 \right] - L\{f_{\text{off}}\} \quad (7.19)$$

In equation (7.19), k is the Boltzman constant, T is the absolute temperature and P_{sup} is the oscillator power dissipation. Also, the oscillator phase-noise $L\{f_{\text{off}}\}$ is measured at an offset frequency, f_{off} , from the oscillation frequency, f_{osc} .

As observed in Figure 7.28, the performance of the implemented 8-phase oscillator is comparable to the best results of other multi-phase versions ([162]-[169]) that generate fewer number of phases. The larger PFN of some of the single-phase oscillators is due to the fact that multi-phase oscillators use more active elements and thus their power consumption is larger.

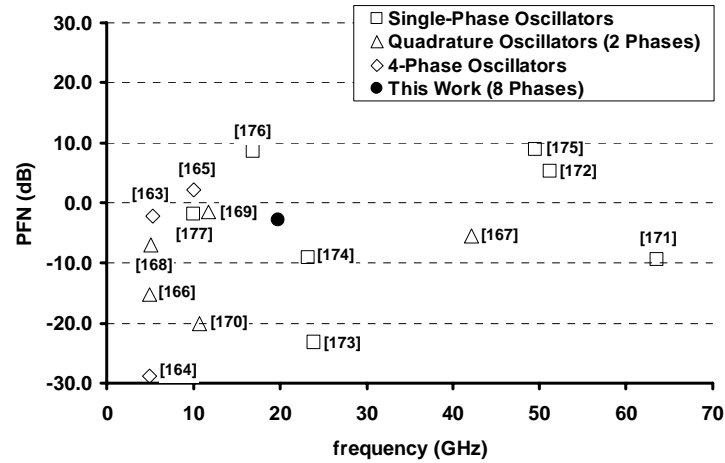


Figure 7.28: PFN of various oscillators

Receiver testing has been conducted in two steps. First, the performance of a single-chain 24 GHz receiver has been characterized. Hence, the RF signal is only fed into one of the input pads while others are simply left open. Second, the behavior of the complete array has to be measured. Ideally, all the input paths have to be connected to on-board patch antennas [152] and the reception pattern of the array is measured. However, in order to separate the effect of antenna array from the receiver, phase shifters in the input path are used to emulate the phase difference of signals at each path. Since we only had access to 4 high-frequency phase shifters at the time of measurement, array measurements have been performed with signal being fed to only four of the receiver paths. The setup used for array measurements is shown in Figure 7.29.

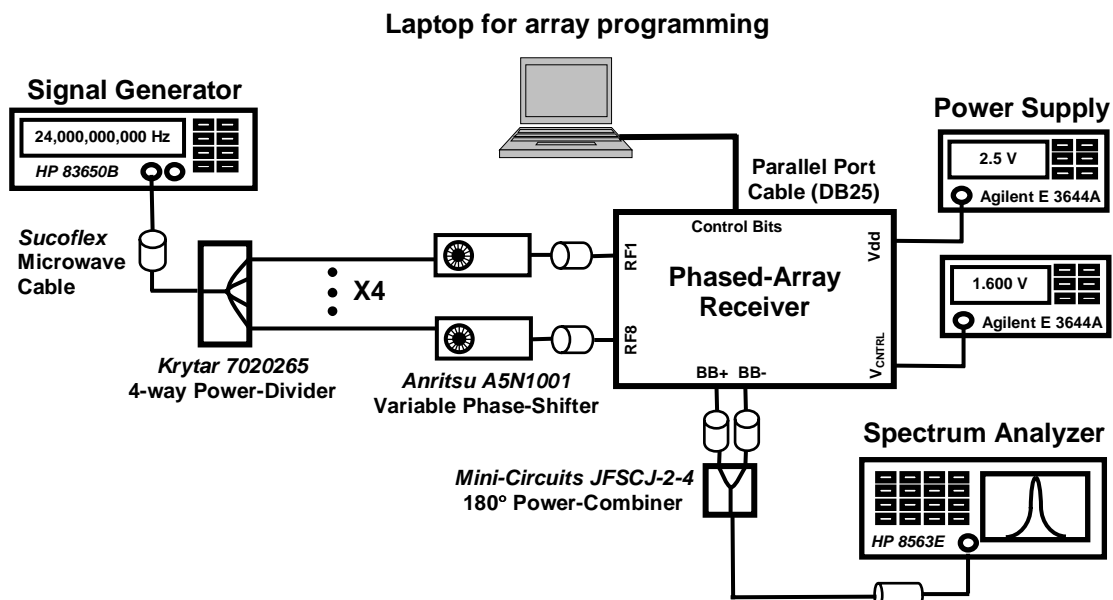


Figure 7.29: Measurement setup for 4-channel array characterization

For all measurements, the silicon chip has been mounted on a gold-plated brass substrate to provide a good grounding. A high-frequency board by Rogers Corp (duroid 5880) surrounds the chip and is used to connect the input, bias and control signal lines using wirebonds (Figure 7.30). Special attention has been paid to minimize the length of wirebonds at RF input and ground lines. The estimated inductance value of less than 0.6 nH for these wirebonds has been considered in the design of input matching circuitry. All signal and bias lines are fed with standard SMA connectors attached to the brass membrane. The input return-loss of the receiver including an input SMA connector, an input transmission line on duroid board and a wirebond is shown in Figure 7.31. The input has a satisfactory match especially in the 21 GHz-23 GHz frequency range.

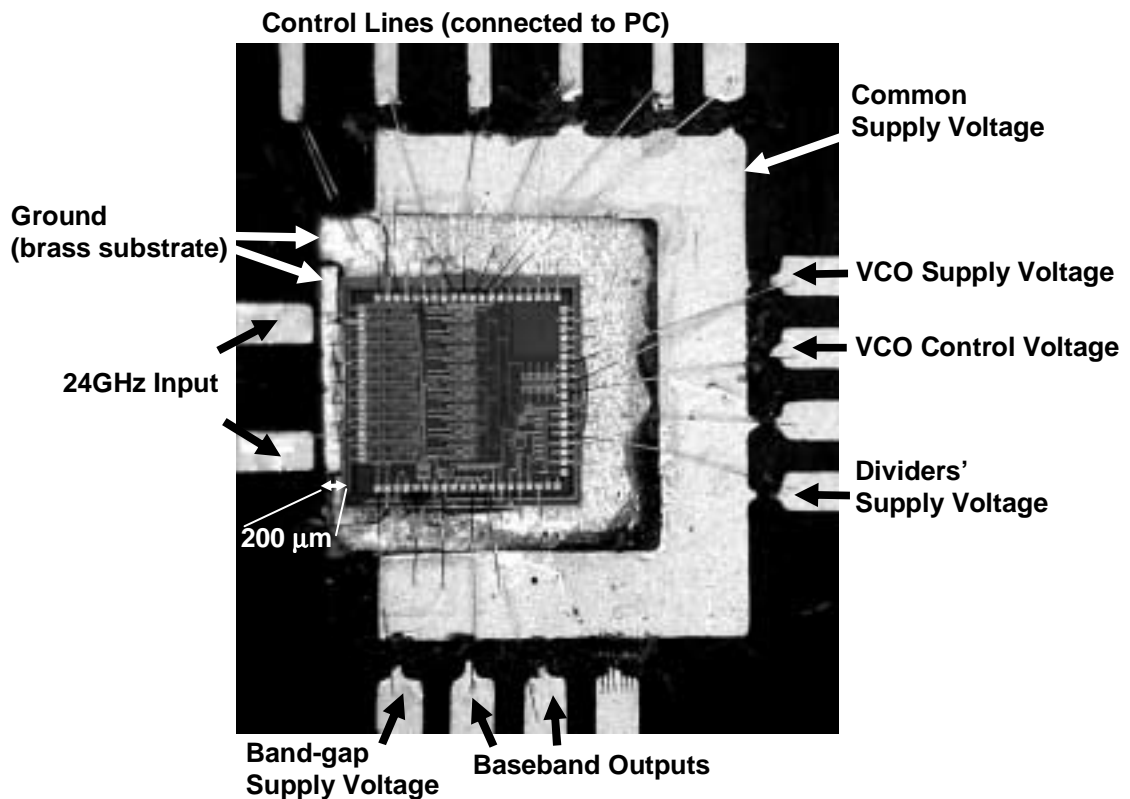


Figure 7.30: Close-up of the measured chip mounted on a brass substrate

The transfer function of each receiver path has been characterized by varying the input and LO frequency (Figure 7.32). The latter has been achieved by changing the control-voltage of the VCO. Measurement results reveal that *RF* front-end and *IF*-stage maximum-gain frequencies occur at about 23 GHz and 4.4 GHz instead of the designed values of 24 GHz and 4.8 GHz, respectively. The 4% discrepancy in the *RF* center frequency (in both gain and input return-loss) can be attributed to inaccuracies in predicting the spiral inductor values and layout/PCB parasitics. The signal at the image frequency is attenuated by about 35dB that seems to be sufficient, considering that no strong broadcaster exists within that band.

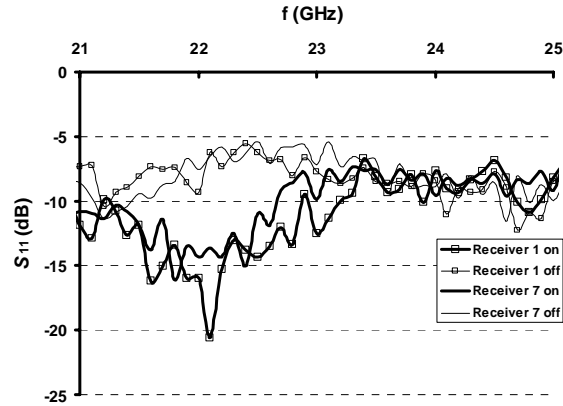


Figure 7.31: Input return-loss of the receiver

Multiple factors have been identified in explaining the 10dB lower-than-expected maximum gain for the receiver. The first is the loss in input connectors, transmission lines, and their respective transitions at 24 GHz. The second factor is the lower quality factor of inductors than what was expected from simulations. This fact has also been confirmed by other structures (such as oscillators) that were fabricated in the same process. The third is that the effect of loss in the *IF* combining lines proves to be more than what was anticipated. Finally, more measurements revealed that the phase-selector output providing the 19 GHz oscillator signal to the *LO* port of *RF* mixers is slightly off-tuned. This in turn causes a drop in the *LO* amplitude and a corresponding reduced gain for *RF* mixers that cannot switch completely with a lower *LO* drive. The combined effect of all the mentioned factors can be included in post-simulations to reproduce the receiver's measured transfer function.

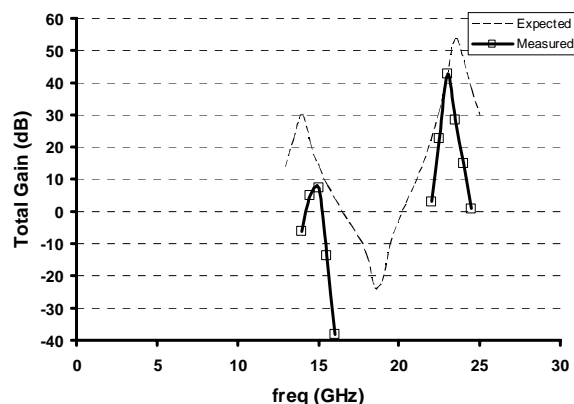


Figure 7.32: Receiver small-signal transfer function for the main and image signals.

In order to illustrate the receiver's large-signal handling, the output power of the receiver for a constant frequency is measured as a function of a varying input power (Figure 7.33). The input referred 1dB compression point of the receiver is about -27 dBm, at 15dBm of output power at 23 GHz.

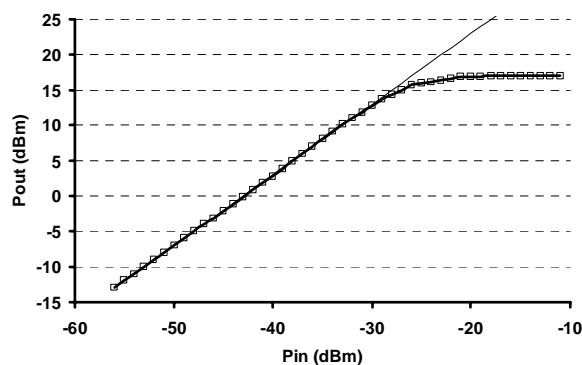


Figure 7.33: Large-signal response of the receiver at 23 GHz input frequency

A standard two-tone test was also performed for two *RF* inputs with the same power separated at 23 GHz by 5 MHz. A typical output spectrum of such a test is shown in Figure 7.34. The output power of the main signals and the ones caused by intermodulation are plotted as a function of the input signal level in Figure 7.34. Although in a system dominated by third-order nonlinearity, one expects a slope equal to 3dB/dB for third-order

intermodulation gain curve, the line is closer to 2.5dB/dB in this receiver. Higher nonlinear terms might be responsible for this difference. Extrapolated lines will meet at an output level of about 15.5dB.

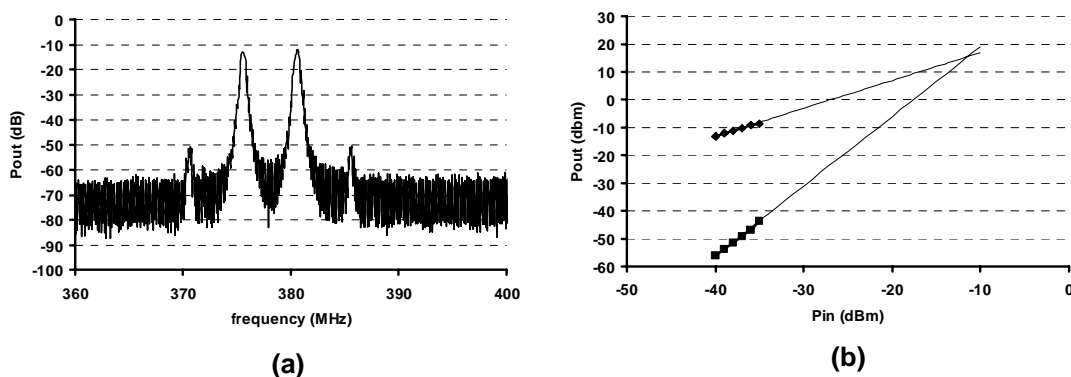


Figure 7.34: Intermodulation test of the receiver (a) Typical output spectrum when two large-signal input tones are applied (b) Results of two-tone test

Array measurements have been performed using the setup of Figure 7.29 where the RF input is fed to the first and seventh receiver paths using a power-divider and two adjustable phase shifters. Unfortunately, an oversight in the design of digital shift-registers prohibited access to all 16 phases, simultaneously. Receiver pattern measurements at 8 different angles with only two operating paths are shown in Figure 7.35. The difference between the peak and the null is 10-20dB in all cases. This value is mostly limited by the mismatch in different paths and can be significantly improved with a gain control block in each receiver path for future implementations. In any event, using all 8-paths is expected to significantly improve this number as well as make the beam-width narrower (Figure 7.36). Theoretical receiver patterns and the measurements at 3 different angles are shown in Figure 7.37 for a four-channel setup.

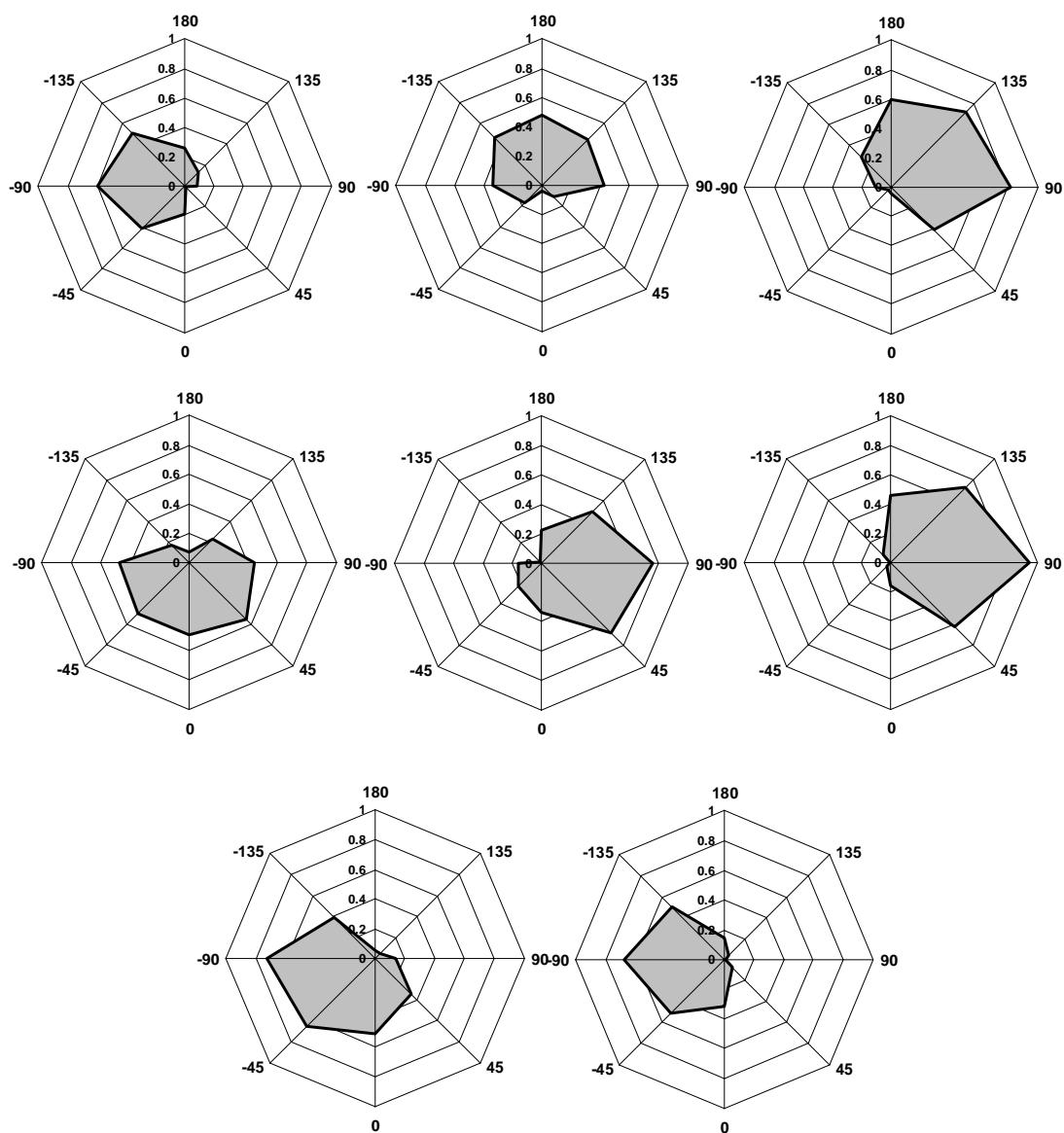


Figure 7.35: Received pattern measurements of the phased-array system with two operating paths

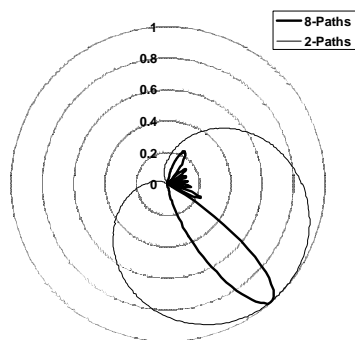


Figure 7.36: Simulated beam-width comparison of the 8-channel phased array with the case when only 2 paths are working

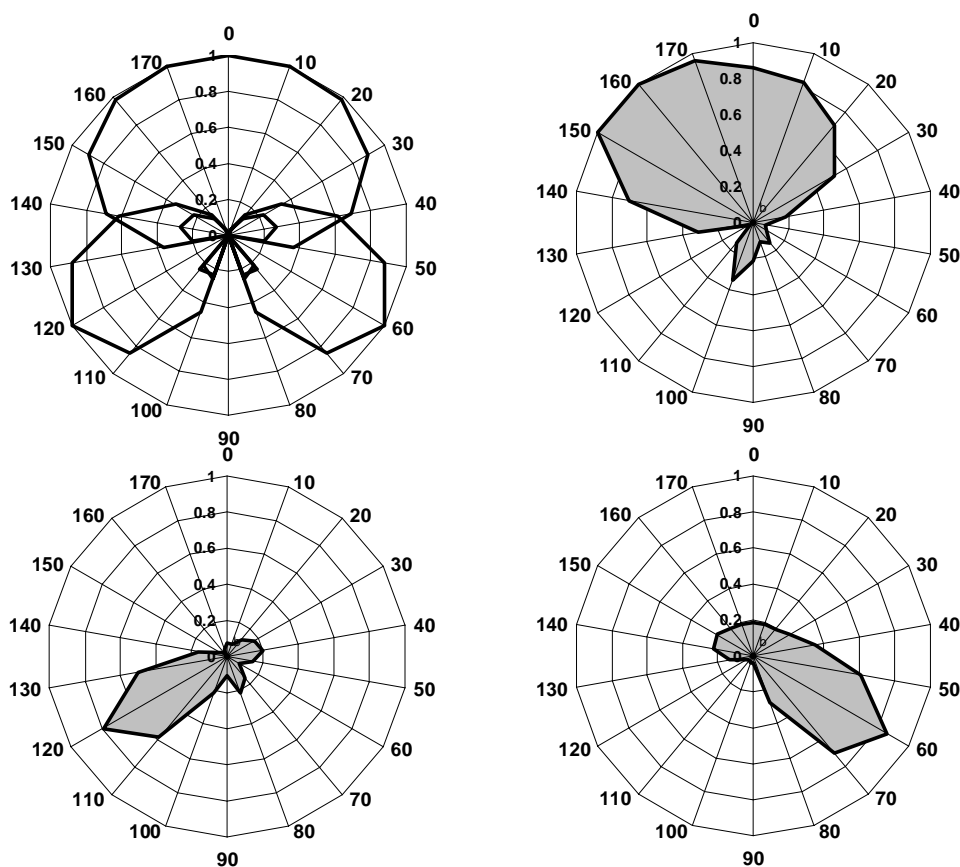


Figure 7.37: Received pattern measurements of the phased-array system with four operating paths compared with theory

A summary of the receiver's measured performance is presented in Table 7.1. Table 7.2 compares the recently published silicon-based receivers at around 24 GHz to the one discussed in this study⁴⁹.

⁴⁹ In the comparison table, the numbers for the signal path in this work are for one-channel only.

<i>Signal Path Performance (per path)</i>	
Peak Gain	43dB @ 23GHz
Noise-Figure	≈ 8.0dB
Input-Referred 1dB Compression Point	-27dBm @ 23GHz
Input-Referred 3 rd -Order Intercept Point	-11.5dBm (2 tones @ 23GHz, 23.005GHz)
On-chip Image Rejection	35dB
 <i>LO Path Performance</i>	
VCO tuning range	18.79GHz – 20.81GHz (10.2%)
K _{VCO}	max: 2.67 GHz/V , @19.2GHz: 2.1GHz/V
VCO Phase-Noise	-103dBc/Hz @ 1MHz offset from 18.7GHz
 <i>Nominal Power Dissipation @ 2.5V</i>	
Each RF Front-end (LNA+RF Mixer)	31mW (≈12mA)
IF Amplifier and Mixers (x2)	15mW (≈6mA)
Baseband Amplifiers and Buffers (x2)	111mW (≈44mA)
16-Phase VCO + LO Buffers	147mW (≈59mA)
Divide-by-two (x2)	52mW (≈21mA)
Each Phase-Selector	30mW (≈12mA)
Biasing	92mW (≈37mA)
 <i>Complete Receiver Performance (8 paths)</i>	
Beam-Forming Resolution	22.5° (measured up to 45°)
Beam-Forming Peak-to-Null Ratio	15-20dB measured for only 2 paths
Power Dissipation @ 2.5V	909mW (≈364mA) 718mW (w/o biasing and baseband buffers)
 Supply Voltage	 2.5 V
 <i>Implementation</i>	
Technology	SiGe, 90GHz HBT, 0.18μm CMOS
Die Area	3.5mm x 3.3mm

Table 7.1: Summary of the measured performance of the 24 GHz phased-array receiver

	This Work ('03)	[13] ('03)	[12] ('02)
<i>Signal Path</i>			
Input Frequency	22.5GHz	23GHz	24GHz
Peak Gain	30dB	27.5dB	16.3dB
Noise-Figure	8dB	7.5dB	N/A
CP1dB	-20dBm	N/A	-32.3dBm
IIP3	N/A	-19.5	N/A
Power Consumption	58mW @ 2.5V	205mW @ 3.9V	204mW @ 3.6V
<i>LO Path</i>			
VCO Frequency	19.2 GHz	No On-Chip Oscillator	24GHz
VCO Tuning Range	10.2%	N/A	N/A
VCO Phase-Noise	-103dBc/Hz @ 1MHz	N/A	-83dBc/Hz @ 1MHz
Power Consumption	147mW @ 2.5V	N/A	266mW @ 3.6V
Technology	SiGe BiCMOS (5M) $W_{emitter}=0.2\mu\text{m}$ $L_{CMOS}=0.18\mu\text{m}$	SiGe BiCMOS (5M) $W_{emitter}=0.4\mu\text{m}$ $L_{CMOS}=0.25\mu\text{m}$	SiGe HBT $W_{emitter}=1.2\mu\text{m}$
Comments	- Fully Integrated - Phased-Array (x8) - Board Level	- External LO - Single Path - Wafer Level	- Single Path - Wafer Level

Table 7.2: Comparison of recently published silicon-based receivers around 24 GHz

7.4 Summary

The first fully integrated multiple-antenna receiver targeting the 24 GHz ISM band using silicon technology is presented. The phased-array technology employed results in higher immunity to unwanted interference and therefore achieves a superior overall system capacity in a shared environment. The phased-array radio at 24 GHz is a cheap solution for high data-rate WLAN as well as for fixed wireless broadband access applications. The

receiver can be made compatible with the existing lower data-rate WLAN standards (dual-mode radio).

Chapter 8

Conclusion

This thesis presented a study of multi-band, multi-mode and multiple-antenna radio systems. The contributions of our study include the development of original concepts and new theoretical findings together with practical implications. As a result, integrated wireless devices with more functionality and versatility have been devised.

8.1 Summary

We have presented a unique view on multi-mode and multi-band radio systems that can simultaneously function at multiple frequency bands. These radios offer a higher data-rate, robustness, and improvement, in addition to the added functionality, in the performance of wireless systems. Our comprehensive treatment included the definition of such novel radios, formulation of their singular characteristics, proposition for transceiver architectures, and invention of circuit blocks.

Various transceiver architectures for this new class of *concurrent multi-band radios* were proposed. In order to verify the practicality of the theoretical findings, we presented the results for an integrated concurrent dual-band receiver operating at 2.4 GHz and 5.2 GHz frequency bands for wireless networking applications. Meticulous frequency-planning results in a high level of integration and a low power design for the concurrent receiver. Several new circuit concepts including the concurrent multi-band low-noise amplifier were demonstrated in this design. A general class of these concurrent multi-band amplifiers was investigated. Numerous implementations of integrated concurrent dual-band and triple-band amplifiers validated our theoretical predictions.

We also offered a theoretical treatment of nonlinear oscillators with multi-band resonator structures. It was shown that given certain nonlinearities these oscillators can generate multi-frequency outputs. The phase-noise of such negative-resistance oscillators with general resonator structure was addressed. By providing a link between the stored and dissipated energies of a network and its associated circuit parameters, useful interpretations of resonator quality factor were derived. With the aid of this analysis and the previously developed phase-noise models, dependencies of phase-noise on the resonator structure were derived. Inspired from our theoretical findings, enhanced resonators with a higher quality factor that can provide a superior oscillator phase-noise were found.

Finally, in order to enhance the performance of wireless systems by exploiting the spatial properties of the electromagnetic wave, multiple-antenna radios in phased-array configuration were investigated. The phased-array technology results in higher immunity to unwanted interference and therefore achieves a superior overall system capacity in a shared environment. The first fully integrated multiple-antenna receiver targeting the 24 GHz ISM band using silicon technology was presented. The phased-array radio at 24 GHz is a cheap solution for high data-rate WLAN, as well as for fixed wireless broadband access applications.

8.2 Recommendations for Future Work

Several radio architectures for concurrent multi-band systems were proposed that need to be further explored for implementations. The multi-band subsampling radio and digital implementations of concurrent receivers are in particular interesting areas for future investigations. The design and implementation of concurrent multi-band transmitters is another open area of research. Important issues such as cross-talk in these systems have to be systematically addressed and verified experimentally.

Concurrent and non-concurrent multi-band power-amplifiers are an open field of research that deserve further study. The issues of efficiency and linearity of these amplifiers in the concurrent operation should be studied theoretically. The analysis for a concurrent amplifier in a large-signal operation region should include general nonlinear time-varying

methods. Possibilities for the compensation of multi-band cross-talk and nonlinearity might include methods such as pre-distortion of signal or modifications in the modulating scheme.

There are still several remaining issues in the context of multi-band oscillators that needs to be addressed in the future. The phase-noise formulation of multi-band oscillators is still an open research topic. Also the behavior of asynchronous oscillator in frequency-locking loop(s) is another open aspect for later investigations. The application of simultaneous multi-frequency oscillations in a multi-band system has to be explored furthermore and verified experimentally.

The design and implementation of multiple-antenna systems at ultra high frequencies might be a significant topic for future research. The well-developed methods of microwave engineering at such frequencies do not readily apply to the silicon implementations, where the conductive substrate is inherently different from compound semiconductor substrates. Investigation of efficient on-chip signal transmission at high frequencies seems to be one of the priorities in this regard. The powerful signal-processing capabilities of silicon technologies can be utilized in adjusting the unpredictable behavior at these frequencies, such as center frequency variations and component mismatch due to process variations. Various architectures for integrated phased-array implementations of radio transceivers should be explored further. The signal-path phase shifting is among the potential low-power solutions for high bandwidth modulations that highly depends on efficient and wide-band phase shifter design.

In conclusion, our study has opened up numerous directions for future research in the area of multi-band, multi-mode and multiple-antenna integrated radio systems.

Appendix A

General Small-Signal Expressions for a Common-Source Amplifier

General expressions for the input-impedance and gain for an amplifier in a common-source configuration are given here.

Figure A.1 is the equivalent small-signal model for the circuit in Figure 4.3 where the bulk is ac-grounded. To simplify this equivalent model, we define $Z'_s = Z_s \parallel Z_{sb}$ and $Z'_L = Z_L \parallel Z_{db}$, where Z_{sb} , Z_{db} are the source-bulk and drain-bulk impedances.

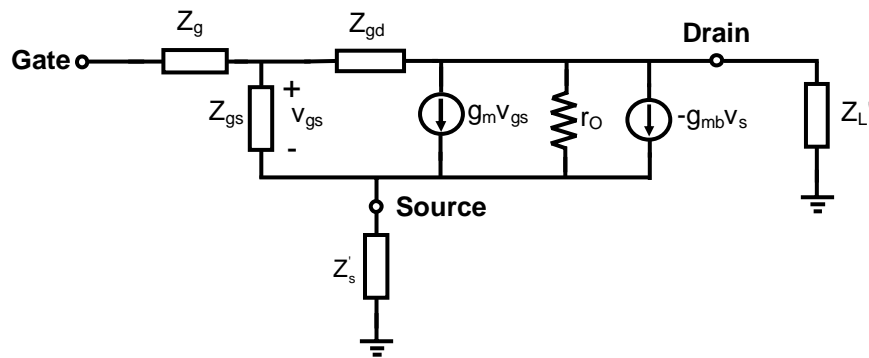


Figure A.1: Equivalent small-signal model for the generic amplifier of Figure 4.3

The transistor's output resistor, r_o , can be neglected, because it is relatively large compared to relatively small impedances in an RF circuit. Then, the small-signal input impedance and the voltage gain of this circuit are given by

$$Z_{in} = Z_g + (Z'_L + Z_{gd}) \cdot \frac{Z_{gs} + Z'_s(1 + g_m Z_{gs})}{Z_{gs} + [Z'_s(1 + g_{mb} Z'_L) + Z'_L] \cdot (1 + g_m Z_{gs}) + Z_{gd}} \quad (\text{A.1})$$

$$A_V = \frac{Z_{in} - Z_g}{Z_{in}} \cdot (Z'_L \parallel Z_{gd}) \cdot \left[\frac{1}{Z_{gd}} - \frac{g_m Z_{gs} - g_{mb} Z'_s}{Z_{gs} + Z'_s [1 + (g_m + g_{mb}) Z_{gs}]} \right] \quad (\text{A.2})$$

The input admittance can also be written as the parallel combination of equivalent admittances that gives more intuition in the design of input matching circuitry.

$$Y_{in} = \frac{1}{Z_g} \parallel \left\{ \begin{array}{l} \frac{1}{Z_{gs} + Z'_s(1 + g_m Z_{gs})} + \frac{1}{Z'_L + Z_{gd}} + \frac{g_{mb}}{1 + \frac{Z_{gd}}{Z'_L}} \\ + \frac{1}{1 + \frac{Z_{gd}}{Z'_L}} \cdot (g_m - g_{mb}) \cdot \frac{Z_{gs}}{Z_{gs} + Z'_s(1 + g_m Z_{gs})} \end{array} \right\} \quad (\text{A.3})$$

Appendix B

Noise Source Transformations

Adding a noiseless⁵⁰ 1-port network with an impedance Z_1 in series with the input of a given noisy 2-port network (Figure B.2 a) modifies its input referred equivalent current and voltage sources in the following way

$$\begin{aligned} i'_n &= i_n \\ e'_n &= e_n + Z_1 \cdot i_n \end{aligned} \quad (\text{B.1})$$

Similarly, adding a noiseless 1-port network with an admittance Y_1 in parallel with the input of a given noisy 2-port network (Figure B.2 b) modifies its input referred equivalent current and voltage sources as follows

$$\begin{aligned} i'_n &= i_n + Y_2 \cdot e_n \\ e'_n &= e_n \end{aligned} \quad (\text{B.2})$$

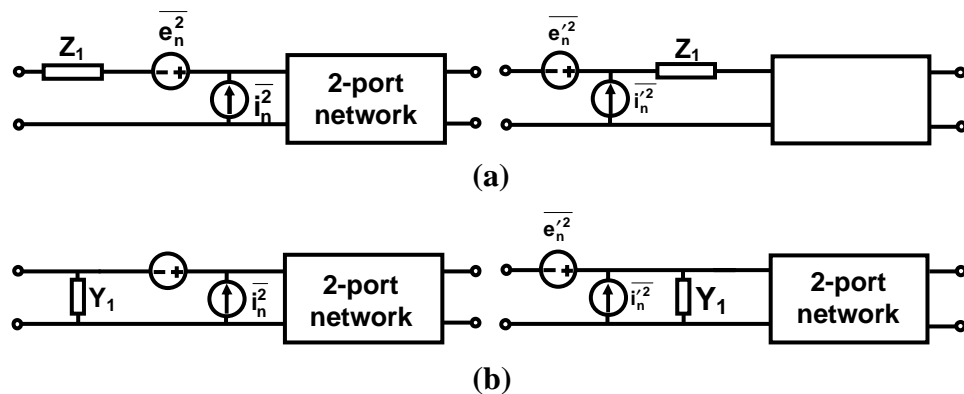


Figure B.2: Illustration of noise source transformation in (a) series (b) parallel cases

⁵⁰ In the case of a noisy Z_1 , its equivalent voltage noise source will be simply added to e_n .

Appendix C

Nonlinear Differential Equation of a Fourth-Order System with Multiple Sources of Loss

As it was mentioned in the footnote 28, ohmic loss of inductors, loss in the semiconductor substrate, and finite output resistance of the active device contribute to the resistive part of the dual-resonance tank of Figure 6.3. In this appendix, we will form the nonlinear differential equation of the same oscillator with multiple sources of loss shown in Figure C.3.

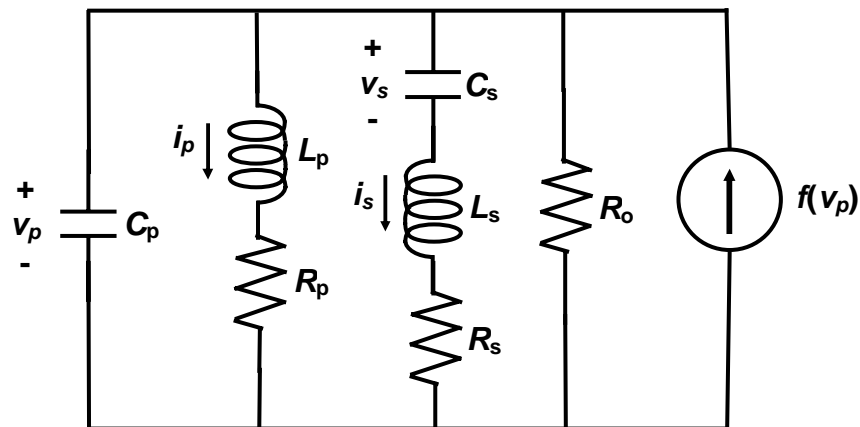


Figure C.3: A second-order oscillator model with multiple sources of loss

Once again, since the dual-band resonance load has four independent energy storing elements, a fourth-order system is resulted. Similar to the derivations in Chapter 6, by defining normalized inductor currents and capacitor voltages as independent state variables, we will have the following nonlinear matrix equation

$$\dot{\mathbf{X}} = \begin{bmatrix} -\frac{1}{\tau_p} & \omega_p & 0 & 0 \\ -\omega_p & 0 & -\omega_c & 0 \\ 0 & \omega_c & -\frac{1}{\tau_s} & -\omega_s \\ 0 & 0 & \omega_s & 0 \end{bmatrix} \mathbf{X} + \begin{bmatrix} 0 \\ \frac{1}{\sqrt{C_p}} f_i\left(\frac{x_2}{\sqrt{C_p}}\right) \\ 0 \\ 0 \end{bmatrix} \quad (\text{C.1})$$

where

$$\mathbf{X} = \left[\sqrt{L_p} i_p \quad \sqrt{C_p} v_p \quad \sqrt{L_s} i_s \quad \sqrt{C_s} v_s \right]^T \quad (\text{C.2})$$

and where ω_p , ω_s , ω_c and f_i are as before, time constants τ_p and τ_s are defined with

$$\tau_p = \frac{L_p}{R_p} \quad , \quad \tau_s = \frac{L_s}{R_s} \quad (\text{C.3})$$

Similar to the derivations in subsection 6.1.3, the characteristic equation of the Jacobean matrix of the zero solution of (C.1), can be written as

$$|\mathbf{J} - \lambda \mathbf{I}| = \lambda^4 + \left(\frac{1}{\tau_p} + \frac{1}{\tau_s} - \frac{1}{\tau_M} \right) \lambda^3 + \left(\omega_p^2 + \omega_s^2 + \omega_c^2 + \frac{1}{\tau_s \tau_p} - \frac{1}{\tau_M} \left(\frac{1}{\tau_p} + \frac{1}{\tau_s} \right) \right) \lambda^2 + \left(\frac{\omega_p^2}{\tau_s} + \frac{\omega_s^2 + \omega_c^2}{\tau_p} - \frac{1}{\tau_M} \left(\omega_s^2 + \frac{1}{\tau_p \tau_s} \right) \right) \lambda + \left(\omega_p^2 \omega_s^2 - \frac{\omega_s^2}{\tau_p \tau_M} \right) \quad (\text{C.4})$$

where

$$\tau_M = \frac{g_m - 1/R_o}{C_p} \quad (\text{C.5})$$

Applying the Ruth-Hurwitz method to the characteristic equation of (C.4) requires more algebraic manipulation than the case of equation (6.13). The oscillator start-up condition is found to be

$$g_m - \frac{1}{R_o} > C_p \left(\frac{1}{\tau_p} + \frac{1}{\tau_s} \right) \quad (\text{C.6})$$

The condition of (C.6) simplifies to the familiar one, *i.e.* $g_m R_o > 1$, when inductive losses zero ($\tau_p, \tau_s \rightarrow \infty$). In a resonator, the value of capacitors is typically orders of magnitude smaller than the inductors and with any reasonable amount of inductor loss, the right-hand-side of (C.6) should have a comparable or lower effect compared to $1/R_o$.

The general nonlinear differential equation in one of the state variables of (C.1) will look like

$$x^{(4)} + \left(\frac{1}{\tau_p} + \frac{1}{\tau_s} \right) x^{(3)} + \left(\omega_p^2 + \omega_s^2 + \omega_c^2 + \frac{1}{\tau_s \tau_p} \right) x^{(2)} + \left(\frac{\omega_p^2}{\tau_s} + \frac{\omega_s^2 + \omega_c^2}{\tau_p} \right) x^{(1)} + (\omega_p^2 \omega_s^2) x = \text{nonlinear terms} \quad (\text{C.7})$$

The linearized differential equation will then be

$$\begin{aligned} x^{(4)} + \left(\frac{1}{\tau_p} + \frac{1}{\tau_s} - \frac{1}{\tau_M} \right) x^{(3)} + \left(\omega_p^2 + \omega_s^2 + \omega_c^2 + \frac{1}{\tau_s \tau_p} - \frac{1}{\tau_M} \left(\frac{1}{\tau_p} + \frac{1}{\tau_s} \right) \right) x^{(2)} \\ + \left(\frac{\omega_p^2}{\tau_s} + \frac{\omega_s^2 + \omega_c^2}{\tau_p} - \frac{1}{\tau_M} \left(\omega_s^2 + \frac{1}{\tau_p \tau_s} \right) \right) x^{(1)} + \left(\omega_p^2 \omega_s^2 - \frac{\omega_s^2}{\tau_p \tau_M} \right) x = 0 \end{aligned} \quad (\text{C.8})$$

As we can note from (C.8), the presence of τ_p and τ_s changes the resonant frequencies from the ones given by (6.25).

Using expression (6.14), different modes of oscillation including conditions for simultaneous oscillation can be derived in a similar way to Chapter 6.

Appendix D

Possibility of Simultaneous Oscillations with a Fifth-Order Nonlinearity Expansion

In this appendix, we show the possibility of stable simultaneous oscillations for the system in Figure 6.4. In the case where the nonlinear function, g , in expression (6.14) is expanded up to a fifth power, assuming that high order derivatives of a_1 and a_2 are negligible (slowly varying amplitudes in transient) results in the following set of equations

$$\begin{cases} \dot{a}_1 = \beta_1 \left[k_1 a_1 + k_3 \left(\frac{3}{4} a_1^3 + \frac{3}{2} a_1 a_2^2 \right) + k_5 \left(\frac{5}{8} a_1^5 + \frac{15}{4} a_1^2 a_2^2 + \frac{15}{8} a_1 a_2^4 \right) \right] \\ \dot{a}_2 = \beta_2 \left[k_1 a_2 + k_3 \left(\frac{3}{4} a_2^3 + \frac{3}{2} a_2 a_1^2 \right) + k_5 \left(\frac{5}{8} a_2^5 + \frac{15}{4} a_2^2 a_1^2 + \frac{15}{8} a_2 a_1^4 \right) \right] \end{cases} \quad (\text{D.1})$$

where positive constants β_1 and β_2 are defined as

$$\beta_i = \frac{(\omega_i^2 - \omega_s^2)}{2[2\omega_i^2 - (\omega_p^2 + \omega_s^2 + \omega_c^2)]}, \quad i=1,2 \quad (\text{D.2})$$

The steady-state solutions for the amplitudes of two modes are found by setting $\dot{a}_1 = \dot{a}_2 = 0$ in (D.1)

$$\begin{cases} a_1 = 0 \\ a_2 = 0 \end{cases}, \begin{cases} a_1 = 0 \\ \left(\frac{5}{8} k_5 \right) a_2^4 + \left(\frac{3}{4} k_3 \right) a_2^2 + k_1 = 0 \end{cases}, \begin{cases} \left(\frac{5}{8} k_5 \right) a_1^4 + \left(\frac{3}{4} k_3 \right) a_1^2 + k_1 = 0 \\ a_2 = 0 \end{cases}, \begin{cases} \left(\frac{25}{4} k_5 \right) a_1^4 + \left(\frac{9}{4} k_3 \right) a_1^2 + k_1 = 0 \\ \left(\frac{25}{4} k_5 \right) a_2^4 + \left(\frac{9}{4} k_3 \right) a_2^2 + k_1 = 0 \end{cases} \quad (\text{D.3})$$

To check the stability of each of the steady-state solutions in (D.3), we form the Jacobean matrix of the equations in (D.1)

$$J = \begin{bmatrix} \beta_1 \left[k_1 + k_3 \left(\frac{9}{4} a_1^2 + \frac{3}{2} a_2^2 \right) + k_5 \left(\frac{25}{8} a_1^4 + \frac{45}{4} a_1^2 a_2^2 + \frac{15}{8} a_2^4 \right) \right] & \beta_1 \left[k_3 (3a_1 a_2) + k_5 \left(\frac{15}{2} a_1^3 a_2 + \frac{15}{2} a_1 a_2^3 \right) \right] \\ \beta_2 \left[k_3 (3a_1 a_2) + k_5 \left(\frac{15}{2} a_2^3 a_1 + \frac{15}{2} a_2 a_1^3 \right) \right] & \beta_2 \left[k_1 + k_3 \left(\frac{9}{4} a_2^2 + \frac{3}{2} a_1^2 \right) + k_5 \left(\frac{25}{8} a_2^4 + \frac{45}{4} a_1^2 a_2^2 + \frac{15}{8} a_1^4 \right) \right] \end{bmatrix} \quad (\text{D.4})$$

Now, we'll find the roots of the characteristic equation of the Jacobean matrix for each set of solutions in (D.3). In the case of zero amplitude for both modes

$$\begin{cases} a_1 = 0 \\ a_2 = 0 \end{cases} \Rightarrow |J - \lambda I| = \begin{vmatrix} \beta_1 k_1 - \lambda & 0 \\ 0 & \beta_2 k_1 - \lambda \end{vmatrix} \quad (\text{D.5})$$

The roots in this case, $\lambda_i = \beta_i k_1$, have positive sign for $k_1 > 0$ showing that the case where both amplitudes are zero (*i.e.*, no oscillation) is unstable. Note that based on expression (6.17), $k_1 > 0$ states the oscillator start-up condition $g_m R_p > 1$.

For the case, where only one of the amplitudes is zero, the other amplitude can be derived by solving the quadratic equation as a function of square of the amplitude in (D.3). Two cases should be considered depending on the sign of k_5 . For positive values of k_5 , the amplitudes are given by

$$\begin{cases} a_1 = 0 \\ a_2 = \sqrt{\frac{-3k_3 \pm \sqrt{9k_3^2 - 40k_1 k_5}}{5k_5}} \end{cases} \quad (\text{D.6})$$

where the following conditions should also hold for real amplitude values

$$\begin{cases} k_3 < 0 \\ k_5 < 0 \\ 9k_3^2 - 40k_1 k_5 > 0 \end{cases} \quad (\text{D.7})$$

For a negative k_5 , only the solution with the negative sign in (D.6) is valid for real amplitude values. The amplitudes in this case are

$$\begin{cases} k_3 < 0 \\ k_5 < 0 \end{cases}, \begin{cases} a_1 = 0 \\ a_2 = \sqrt{\frac{-3k_3 - \sqrt{9k_3^2 - 40k_1 k_5}}{5k_5}} \end{cases} \quad (\text{D.8})$$

The characteristic equation in both cases is

$$|J - \lambda I| = \begin{vmatrix} \left(-\beta_1 \sqrt{9k_3^2 - 40k_1k_5} \times \frac{a_2^2}{4}\right) - \lambda & 0 \\ 0 & \left(-\beta_2 \sqrt{9k_3^2 - 40k_1k_5} \times \frac{a_2^2}{2}\right) - \lambda \end{vmatrix} \quad (\text{D.9})$$

As can be seen from (D.9), both roots have a negative sign that shows stable oscillation at frequency ω_1 , in this case. Clearly, the same result is valid for oscillation at the other frequency, ω_2 .

If none of the amplitudes is zero (*i.e.*, simultaneous oscillation case), the amplitudes can be calculated by solving the quadratic equation in (D.3) as a function of the square of amplitudes resulting in

$$\begin{cases} a_1 = \sqrt{\frac{-9k_3 \pm \sqrt{81k_3^2 - 400k_1k_5}}{50k_5}} \\ a_2 = \sqrt{\frac{-9k_3 \pm \sqrt{81k_3^2 - 400k_1k_5}}{50k_5}} \end{cases} \quad (\text{D.10})$$

where the following conditions should hold for real amplitude values

$$\begin{cases} k_3 < 0 \\ k_5 > 0 \\ 81k_3^2 - 400k_1k_5 > 0 \end{cases} \quad (\text{D.11})$$

The characteristic equation in this case is given by

$$|J - \lambda I| = \begin{vmatrix} \beta_1 \frac{189k_3^2 - 800k_1k_5 \pm 21k_3\sqrt{81k_3^2 - 400k_1k_5}}{500k_5} - \lambda & \beta_1 \frac{6(9k_3^2 - 50k_1k_5 \pm k_3\sqrt{81k_3^2 - 400k_1k_5})}{125k_5} \\ \beta_2 \frac{6(9k_3^2 - 50k_1k_5 \pm k_3\sqrt{81k_3^2 - 400k_1k_5})}{125k_5} & \left(\beta_2 \frac{189k_3^2 - 800k_1k_5 \pm 21k_3\sqrt{81k_3^2 - 400k_1k_5}}{500k_5}\right) - \lambda \end{vmatrix} = \lambda^2 + d_1\lambda + d_2 \quad (\text{D.12})$$

For a stable simultaneous oscillation, both of the roots of the characteristic equation in (D.12) should have negative real sign. The necessary and sufficient condition for roots with negative real sign in the quadratic equation of (D.12) is to have $d_1 < 0$ and $d_2 > 0$. The conditions for simultaneous oscillation then can be simplified to

$$\begin{cases} k_3 < 0 \\ k_5 > 0 \\ \frac{9}{80}k_3^2 < k_1k_5 < \frac{81}{400}k_3^2 \end{cases} \quad (\text{D.13})$$

The stable oscillation amplitudes are then given by

$$a_1 = a_2 = \sqrt{\frac{-9k_3 - \sqrt{81k_3^2 - 400k_1k_5}}{50k_5}} \quad (\text{D.14})$$

As an example, let's consider the case where the nonlinear function is realized with a cross-coupled differential pair using bipolar junction transistors. As we showed in Chapter 6, the Taylor expansion of the nonlinear function can be written as (6.20). If only the terms up to a fifth power are considered, conditions (D.13) can be written as

$$\frac{32}{29} < g_m R_p < \frac{160}{133} \quad (\text{D.15})$$

And the amplitudes of simultaneous oscillations for the voltage across resonator, V_p , are given by

$$0.387 V_{th} < |V_p| < 0.671 V_{th} \quad (\text{D.16})$$

From (D.15) it is clear that the bias range for a stable simultaneous oscillation is very limited in this example. Also based on (D.16), the amplitudes of simultaneous oscillations are very small. These facts make the observation of simultaneous oscillations difficult.

It is reminded that the analysis here was merely intended to show the possibility of stable simultaneous oscillations when higher-orders, fifth-order in this case, are present in the power series expansion of the nonlinear function in the oscillator core. In practice, the nonlinear functions are more complicated than the ones in (6.18) and (6.20) and most likely include significant power at higher-order power terms. In any event, simultaneous oscillations are bias dependent (*e.g.*, (D.15)) and can be more-or-less easily observed in simulation by changing the bias conditions of the circuit.

Appendix E

Explicit Phase-Noise Derivation of a Fourth-Order Resonator Based on [110]

Let's follow the steps in [110] in detail to derive the phase-noise expression of a fourth-order system, such as the one shown in Figure 6.6, when the oscillator is generating only one of its two resonance frequencies.

As a first step, we'll derive the transfer function of the injected impulse current magnitude to the excess phase in the output oscillating voltage at different times for a dual-resonance load. It has been shown in [110] that this normalized and periodic transfer function, called *impulse sensitivity function* (ISF represented with Γ hereafter) directly affects the phase-noise expression of oscillators. Consider the dual-resonance load of Figure 6.6 in parallel with a source to model the injected noise current (Figure E.4).

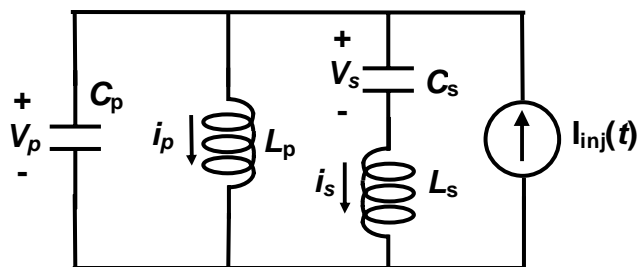


Figure E.4: Simplified model used to calculate ISF of an oscillator with a fourth-order resonator in Figure 6.6

Given arbitrary initial conditions for capacitor voltages and inductor currents, the output will have the general form of

$$V_p(t) = a_1 \cos(\omega_1 t + \phi_1) + a_2 \cos(\omega_2 t + \phi_2) \quad (\text{E.1})$$

where ω_1 and ω_2 are the two resonant modes of the circuit. Suppose the initial conditions are set such that only one of the resonant modes is excited

$$V_p(t) = a_1 \cos(\omega_1 t + \phi_1) \quad (\text{E.2})$$

Now imagine at $t=t_0$ the current source injects a charge q_{inj} into the tank. This sudden charge has to go to the parallel capacitor, C_p , completely causing its voltage to step up by q_{inj}/C_p .⁵¹ Now with the new initial condition, the voltage across the resonator can have both resonant frequencies simultaneously, *i.e.*,

$$t > t_0 : V_p(t) = b_1 \cos(\omega_1 t + \theta_1) + b_2 \cos(\omega_2 t + \theta_2) \quad (\text{E.3})$$

The current through C_p is simply the scaled derivative of its voltage, *i.e.*,

$$I_{C_p}(t) = \begin{cases} -C_p \omega_1 a_1 \sin(\omega_1 t + \phi_1) & t < t_0 \\ -C_p \omega_1 b_1 \sin(\omega_1 t + \theta_1) - C_p \omega_2 b_2 \sin(\omega_2 t + \theta_2) & t > t_0 \end{cases} \quad (\text{E.4})$$

Since the current through inductors doesn't change at $t=t_0$ and because of KCL, the current through C_p does not change at $t=t_0$ either.

Similarly for the voltage across C_s (*i.e.*, V_s), we can derive

$$V_s(t) = \begin{cases} \frac{\omega_s^2}{\omega_s^2 - \omega_1^2} a_1 \cos(\omega_1 t + \phi_1) & t < t_0 \\ \frac{\omega_s^2}{\omega_s^2 - \omega_1^2} b_1 \cos(\omega_1 t + \theta_1) + \frac{\omega_s^2}{\omega_s^2 - \omega_2^2} b_2 \cos(\omega_2 t + \theta_2) & t > t_0 \end{cases} \quad (\text{E.5})$$

And for the current through L_s and C_s

⁵¹ Any sudden charge into inductors will result a delta-function-type jump in their voltage.

$$I_s(t) = \begin{cases} -C_s \omega_1 \frac{\omega_s^2}{\omega_s^2 - \omega_1^2} a_1 \sin(\omega_1 t + \phi_1) & t < t_0 \\ -C_s \omega_1 \frac{\omega_s^2}{\omega_s^2 - \omega_1^2} b_1 \sin(\omega_1 t + \theta_1) - C_s \omega_2 \frac{\omega_s^2}{\omega_s^2 - \omega_2^2} b_2 \sin(\omega_2 t + \theta_2) & t > t_0 \end{cases} \quad (\text{E.6})$$

By evaluating (E.2)-(E.6) at $t=t_0$ we'll get two sets of solution for the amplitude and phase of oscillation in (E.3)

$$b_2 = 0, \quad \begin{cases} b_1 \cos(\omega_1 t_0 + \theta_1) = a_1 \cos(\omega_1 t_0 + \phi_1) + \frac{q_{inj}}{C_p} \\ b_1 \sin(\omega_1 t_0 + \theta_1) = a_1 \sin(\omega_1 t_0 + \phi_1) \end{cases} \quad (\text{E.7})$$

$$\omega_2 t_0 + \theta_2 = 0, \quad \begin{cases} b_1 \cos(\omega_1 t_0 + \theta_1) = a_1 \cos(\omega_1 t_0 + \phi_1) + \frac{q_{inj}}{C_p} \left(\frac{\omega_1^2 - \omega_s^2}{\omega_1^2 - \omega_2^2} \right) \\ b_1 \sin(\omega_1 t_0 + \theta_1) = a_1 \sin(\omega_1 t_0 + \phi_1) \end{cases}$$

The first solution in (E.7) is similar to the solution for an oscillator with single resonance tank such as the one analyzed in [110]. The second one, which is the solution for a dual resonance mode, essentially has the same form with a subtle difference: *the effect of injected current into the solution gets scaled by a factor less than one*. We call this factor, *ISF improvement factor*. It should not come as a surprise that the same result would be obtained by using the general expression of (6.31) and (6.32).

It is noteworthy that from (E.7) and as mentioned in [110], excess phase varies linearly with q_{inj} for small injected noise currents and ISF has a sinusoid form for relatively high quality factor *LC* oscillators, *i.e.*, $\Gamma \approx q_{inj} \cdot \sin(\alpha)$ where α is the injected current angle.

ISF derived from a Spice-type simulation for an oscillator with a fourth-order resonator and with a second-order resonator, both oscillating at the same frequency, is plotted in Figure E.5. Simulations show an ISF improvement factor within less than 5% of the predicted value using the direct expression in (E.7).

The complete phase-noise expression of an electrical oscillator at offset $\Delta\omega$ from center frequency in the $1/f^2$ region as given by [110] is

$$L = 10 \cdot \log \left(\frac{1}{2 \cdot \Delta \omega^2} \cdot \frac{1}{q_{\max}^2} \cdot \sum_n \frac{\overline{i_n^2}}{\Delta f} \cdot \Gamma_{rms,n}^2 \right) \quad (\text{E.8})$$

where the sum is over multiple sources of noise and q_{\max} is the maximum charge swing over the parallel tank capacitor in an LC oscillator.

Assuming a given negative resistance structure and its generated noise (*e.g.*, a fixed crossed-coupled pair with a given tail current source), the phase-noise according to (E.8) not only depends on the ISF, but also on the oscillation amplitude or the resonator maximum charge swing. If all the inductors have a quality factor, Q_{ind} ,⁵² the effective tank parallel resistance for the fourth-order resonator at the oscillation frequency ω_0 can be approximated as

$$R_{p,dual} = \frac{1}{R_{Lp}^{-1} + R_{Ls}^{-1}} = \frac{Q_{ind}}{C_{p,dual} \omega_0} \cdot \left| \frac{\omega_0^2 - \omega_s^2}{\omega_1^2 - \omega_2^2} \right| \quad (\text{E.9})$$

Remember that the same quantity for a second-order resonator would be

$$R_{p,sngle} = \frac{Q_{ind}}{C_{p,sngle} \omega_0} \quad (\text{E.10})$$

The ratio of overall tank resistances in the single- and dual-resonance loads is

$$\frac{R_{p,dual}}{R_{p,sngle}} = \frac{C_{p,sngle}}{C_{p,dual}} \cdot \left| \frac{\omega_0^2 - \omega_s^2}{\omega_1^2 - \omega_2^2} \right| \quad (\text{E.11})$$

Interestingly, this ratio is the very same *ISF improvement factor* that appeared in the injected current to phase expression of (E.7).

Now, to have the same oscillation amplitude in both oscillators biased in the current limited region and since $V_{\text{swing}} \propto I_{\text{ss}} \cdot R_p$

$$\frac{q_{\max,dual}}{q_{\max,sngle}} = \frac{C_{p,dual}}{C_{p,sngle}} = \left| \frac{\omega_0^2 - \omega_s^2}{\omega_1^2 - \omega_2^2} \right| \quad (\text{E.12})$$

⁵² For simplicity, we assume that the quality factor of optimized inductors with different values is more or less the same for a given process at a fixed frequency.

Due to the sinusoid waveform of ISF and from (E.7)

$$\frac{\Gamma_{rms,dual}^2}{\Gamma_{rms,sngle}^2} = \left| \frac{\omega_0^2 - \omega_s^2}{\omega_1^2 - \omega_2^2} \right|^2 \quad (\text{E.13})$$

Plugging (E.12) and (E.13) into the phase-noise expression of (E.7) would then give

$$L_{dual} = L_{sngle} \quad (\text{in } 1/f^2 \text{ region}) \quad (\text{E.14})$$

In other words, in the current limited region the improvement gained in ISF for a dual-resonant tank will get cancelled by the decrease in tank's equivalent parallel resistance.

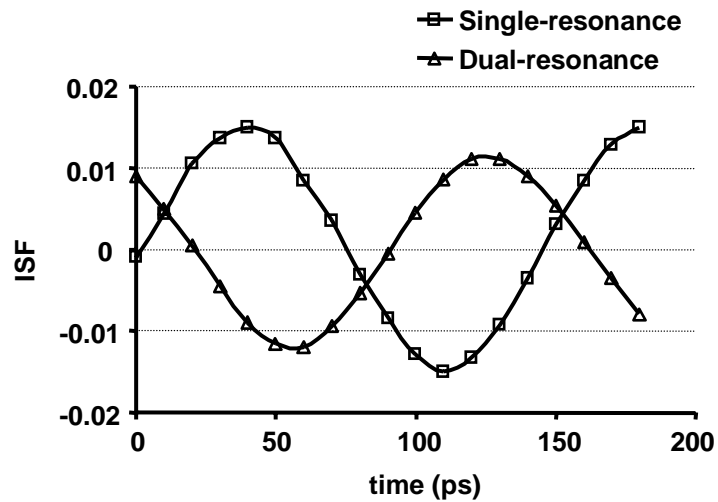


Figure E.5: Simplified model used to calculate ISF of an oscillator with a fourth-order resonator in Figure 6.6

The lengthy derivation presented here, agrees with our findings for a general resonator in this subsection 6.2.2 and only serves as one particular example of a resonator with an order higher than two.

Bibliography

- [1] G. Moore, "No Exponential Is Forever: But "Forever" Can Be Delayed," in *IEEE Int. Solid-State Circuits Conf. Dig. Tech. Papers*, February 2003, pp. 20-23.
- [2] C. Shannon, "A Mathematical Theory of Communication," *The Bell System Technical Journal*, vol. 27, pp. 379-423, 623-656, July-October 1948.
- [3] T. Rappaport, *Wireless Communications: Principles and Practice*, Prentice Hall, 1996.
- [4] FCC 02-48, "Revision of Part 15 of the Commission's Rules Regarding Ultra-Wideband Transmission Systems," released April 2002.
- [5] S. Dow, B. Ballweber, L. Chou, D. Eickbusch, J. Irwin, G. Kurtzman, P. Manapragada, D Moeller, J. Paramesh, G. Black, R. Wollscheid, and K. Johnson, "A Dual-Band Direct-Conversion/VLIF Transceiver for 50GSM/GSM/DCS/PCS," in *IEEE Int. Solid-State Circuits Conf. Dig. Tech. Papers*, February 2002, pp. 230-231.
- [6] V. Aparin, P. Gazzerro, J. Zhou, B. Sun, S. Szabo, E. Zeisel, T. Segoria, S. Ciccarelli, C. Persico, C. Narathong, and R. Sridhara, "A Highly-Integrated Tri-Band/Quad-Mode SiGe BiCMOS RF-to-Baseband Receiver for Wireless CDMA/WCDMA/AMPS Applications with GPS Capability," in *IEEE Int. Solid-State Circuits Conf. Dig. Tech. Papers*, February 2002, pp. 234-235.
- [7] R. Hartley, "Modulation System," U.S. Patent 1,666,206, April 1928.
- [8] D. K. Weaver, "A Third Method of Generation and Detection of Single-Sideband Signals," *Proc. IRE*, vol. 44, pp. 1703-1705, December 1956.
- [9] S. Wu and B. Razavi, "A 900 MHz/1.8 GHz CMOS Receiver for Dual Band Applications", *IEEE J. Solid-State Circuits*, vol. 33, no. 12, pp. 2178-2185, December 1998.
- [10] M. Reddy, D. Yates, C. Lee, G. Taskov, P. Mudge, T. Robinson, L. Li, B. Agarwal, and S. Hwang, "Highly Integrated, Dual Band/Tri-Mode SiGe BiCMOS Transmitter IC for CDMA Wireless Applications," in *IEEE Radio Frequency Integrated Circuits Symp. Dig. Papers*, June 2002, pp. 35-38.
- [11] B. Klepser, M. Punzenberger, T. Rühlicke, and M. Zannoth, "5 GHz and 2.4 GHz Dual-Band RF-Transceiver for WLAN 802.11a/b/g Applications," in *IEEE Radio Frequency Integrated Circuits Symp. Dig. Papers*, June 2003, pp. 37-40.

- [12] B. Wilkins, "Polaris Total RadioTM, A Highly Integrated RF Solution for GSM/GPRS and Edge," in *IEEE Radio Frequency Integrated Circuits Symp. Dig. Papers*, June 2003, pp. 383-386.
- [13] H. Darabi, J. Chiu, S. Khorram, H. Kim, Z. Zhou, E. Lin, S. Jiang, K. Evans, E. Chien, B. Ibrahim, E. Geronaga, L. Tran, and R. Rofougaran, "A Dual Mode 802.11b/Bluetooth Radio in 0.35 μm CMOS," in *IEEE Int. Solid-State Circuits Conf. Dig. Tech. Papers*, February 2003, pp. 86-87.
- [14] K. Grad, K. Barnett, J. Dunworth, T. Segoria, B. Walker, J. Zhou, D. Maldonado, A. See, and C. Persico, "Direct Conversion Dual-Band SiGe BiCMOS Transmitter and Receive PLL IC for CDMA/WCDMA/AMPS/GPS Applications," in *IEEE Int. Solid-State Circuits Conf. Dig. Tech. Papers*, February 2003, pp. 272-273.
- [15] A. Molnar, R. Magoon, G. Hatcher, J. Zachan, W. Rhee, M. Damgaard, W. Domino, and N. Vakilian, "A Single-Chip Quad-Band (850/900/1800/1900 MHz) Direct-Conversion GSM/GPRS RF Transceiver with Integrated VCOs and Fractional-N Synthesizer," in *IEEE Int. Solid-State Circuits Conf. Dig. Tech. Papers*, February 2002, pp. 232-233.
- [16] L. Der and B. Razavi, "A 2 GHz CMOS Image-Reject Receiver with Sign-Sign LMA Calibration," in *IEEE Int. Solid-State Circuits Conf. Dig. Tech. Papers*, February 2001, pp. 294-295.
- [17] A. Abidi, "Direct-Conversion Radio Transceivers for Digital Communications," *IEEE J. Solid-State Circuits*, vol. 30, no. 12, pp. 1399-1410, December 1995.
- [18] B. Razavi, "Design Considerations for Direct-Conversion Receivers," *IEEE Trans. Circuits and Systems II*, vol. 44, no. 6, pp. 428-435, June 1997.
- [19] <http://www.fcc.gov/911/enhanced/>
- [20] R. J. Hasler, "Adding GPS to CDMA Mobile-Telephone Handsets," *Microwave and RF*, pp. 69-78, March 2001.
- [21] C. E. Shannon, "Communications in the Presence of Noise," *Proc. IRE*, vol. 37, pp. 10-21, January 1949.
- [22] A. Kohlenberg, "Exact Interpolation of Band-Limited Functions," *J. Appl. Physics*, vol. 24, pp. 1432-1436, 1953.
- [23] A. Parssinen, R. Magoon, S. Long, and V. Porra, "A 2 GHz Subharmonic Sampler for Signal Downconversion," *IEEE Trans. Microwave Theory Tech.*, vol. 45, no. 12, pp. 2344-51, December 1997.
- [24] D. Shen, H. Chien-Meen, B. Lusignan, and B. Wooley, "A 900 MHz RF Front-End with Integrated Discrete-Time Filtering," *IEEE J. Solid-State Circuits*, vol. 31, no. 12, pp. 1945-54, December 1996.
- [25] M. Beaty and M. Dodson, "The Distribution of Sampling Rates for Signals with Equally Wide Equally Spaces Spectral Bands," *SIAM J. Appl. Math.*, vol. 53, no. 3, pp. 893-906, June 1993.

- [26] H. Hashemi and A. Hajimiri, "Concurrent Multiband Low-Noise Amplifiers-Theory, Design, and Applications," *IEEE Trans. Microwave Theory Tech.*, vol. 50, no. 1, pp. 288-301, January 2002.
- [27] J. Engberg, *Noise Theory of Linear and Nonlinear Circuits*, John Wiley & Sons, August 1995.
- [28] D. M. Pozar and S. M. Duffy, "A Dual-Band Circularly Polarized Aperture-Coupled Stacked Microstrip Antenna for Global Positioning Satellite," *IEEE Tran. Antennas Propagation*, vol. 45, pp. 1618-1625, November 1997.
- [29] Zi D. Liu, P. S. Hall, and D. Wake, "Dual-Frequency Planar Inverted-F Antenna," *IEEE Tran. Antennas Propagation*, vol. 45, no.10, pp. 1451-1458, October 1997.
- [30] L. Zaid, G. Kossiavas, J. Dauvignac, J. Cazajous, and A. Papiermik, "Dual-Frequency and Broad-Band Antennas with Stacked Quarter Wavelength Elements," *IEEE Tran. Antennas Propagation*, vol. 47, no. 4, April 1999.
- [31] H. Miyake, S. Kitazawa, T. Ishizaki, T. Yamada, and Y. Nagatomi, "A Miniaturized Monolithic Dual Band Filter Using Ceramic Lamination Technique for Dual Mode Portable Telephones," in *IEEE MTT-S Int. Microwave Symp. Dig.*, June 1997, pp. 789-792.
- [32] A. Nagayama, M. Nishibe, T. Inaoka, and N. Mineshima, "Low-Insertion-Loss DP3T MMIC Switch for Dual-Band Cellular Phones," *IEEE J. Solid-State Circuits*, vol. 34, pp.1051-1055, August 1999.
- [33] A. de Graauw, C. Copetti, and W. Weekamp, "A new thin film passive integration technology for miniaturisation of mobile phone front end modules: integration of a dual-band power amplifier, switch and diplexer for GSM," in *IEEE MTT-S Int. Microwave Symp. Dig.*, June 2000, vol. 3, pp. 1925-8.
- [34] D. Weaver, "A Third Method of Generation and Detection of Single-Sideband Signals," *Proc. IRE*, vol. 44, pp. 1703-5, December 1956.
- [35] J. Archer, J. Granlund, R. Mauzy, "A Broad-Band VHF Mixer Exhibiting High Image Rejection Over a Multidecade Baseband Frequency Range," *IEEE J. Solid-State Circuits*, vol. SC-16, no. 4, pp. 385-92, August 1981.
- [36] J. Rudell, J-J Ou, T. Cho, G. Chien, F. Brianti, J. Weldon, and P. Gray, "A 1.9 GHz Wide-Band IF Double Conversion CMOS Receiver for Cordless Telephone Applications," *IEEE J. Solid-State Circuits*, vol. 32, no. 12, pp. 2071-2088, December 1997.
- [37] R. Meyer, and A. Wong, "Blocking and Desensitization in RF Amplifiers," *IEEE J. Solid-State Circuits*, vol. 30, no. 8, pp. 944-946, August 1995.
- [38] P. Wambach and W. Sansen, *Distortion Analysis of Analog Integrated Circuits*, Kluwer Academic Publishers, 1998.
- [39] D. Leeson, "A Simple Model of Feedback Oscillator Noise Spectrum," *Proc. IEEE*, vol. 54, pp. 329-330, February 1966.
- [40] Atheros AR5002AP-2X Dualband Concurrent Chipset, <http://www.atheros.com>.

- [41] J. Tham, M. Margrait, B. Pregardier, C. Hull, R. Magoon, and F. Carr, "A 2.7V 900-MHz Dual-Band Transceiver IC for Digital Wireless Communication," *IEEE J. Solid-State Circuits*, vol. 34, no. 3, pp. 286-291, March 1999.
- [42] J. Imbornone, J. Mourant, and T. Tewksbury, "Fully Differential Dual-Band Image Reject Receiver in SiGe BiCMOS," in *IEEE Radio Frequency Integrated Circuits Symp. Dig. Papers*, June 2000, pp. 147-150.
- [43] W. Titus, R. Croughwell, C. Schiller, and L. DeVito, "A Si BJT Dual-Band Receiver IC for DAB," in *IEEE MTT-S Int. Microwave Symp. Dig.*, June 1998, vol. 1, pp. 345-348.
- [44] R. J. Hasler, "Adding GPS to CDMA Mobile-Telephone Handsets," *Microwave and RF*, pp. 69-78, March 2001.
- [45] H. Hashemi and A. Hajimiri, "Concurrent Dual-Band CMOS Low Noise Amplifiers and Receiver Architectures," in *VLSI Circuits Symp. Dig. Tech. Papers*, June 2001, pp. 247-250.
- [46] H. T. Friis, "Noise Figure of Radio Receivers," *Proc. IRE*, pp. 419-422, July 1944.
- [47] R. Engelbrecht and K. Kurokawa, "A Wide-Band Low-Noise L-band Balanced Transistor Amplifier," *Proc. IEEE*, vol. 53, pp. 237-247, March 1965.
- [48] C. Leitchi, "Microwave Field-Effect Transistors," *IEEE Trans. Microwave Theory Tech.*, vol. MTT-24, pp. 279-300, June 1976.
- [49] Y. Mimino, M. Hirata, K. Nakamura, K. Sakamoto, Y. Aoki, and S. Kuroda, "High Gain-Density K-Band P-HEMT LNA MMIC for LMDS and Satellite Communication," in *IEEE MTT-S Int. Microwave Symp. Dig.*, June 2000, pp. 17-20.
- [50] P. Marsh, S. Chu, S. Lardizabel, R. Leoni, S. Kang, R. Wohlert, A. Bowlby, W. Hoke, R. McTaggart, P. Lemonias, P. McIntosh, and T. Kazior, "Low Noise Metamorphic HEMT Devices and Amplifiers on GaAs Substrates," in *IEEE MTT-S Int. Microwave Symp. Dig.*, June 1999, vol. 1, pp. 105-108.
- [51] H. Dodo, Y. Amamiya, T. Niwa, M. Mamada, S. Tanaka, and H. Shimawaki, "Microwave Low-Noise GaAs HBTs," *IEEE Microwave Millimeter-Wave Monolithic Circuits Symp. Dig.*, vol. 2, pp. 693-696, 1998.
- [52] D. Greenberg, D. Ahlgren, G. Freeman, S. Subbanna, V. Radisic, D. Harvey, C. Webster, and L. Larson, "HBT Low-Noise Performance in a 0.18 μ m SiGe BICMOS Technology," in *IEEE MTT-S Int. Microwave Symp. Dig.*, June 2000, vol. 1, pp. 9-12.
- [53] F. Reif, *Fundamentals of Statistical and Thermal Physics*, Mc-Graw Hill, 1985.
- [54] D. Ham and A. Hajimiri, "Concepts and Methods in Optimization of Integrated LC VCOs", *IEEE J. Solid-State Circuits*, vol. 36, no. 6, pp. 896-909, June 2001.
- [55] R. G. Meyer, and W. D. Mack, "A 1 GHz BiCMOS RF Front-End IC.," *IEEE J. Solid-State Circuits*, vol. 29, pp. 350-5, March 1994.
- [56] A. Rofougaran, G. Chang, J. Rael, J. Chang, M. Rofougaran, P. Chang, M. Djafari, J. Min, E. Roth, A. Abidi, and H. Samueli, "A Single-chip 900 MHz Spread-

- Spectrum Wireless Transceiver in 1- μm CMOS--Part II: Receiver Design," *IEEE J. Solid-State Circuits*, vol. 33, no. 4, pp. 535-547, April 1998.
- [57] D. Shaeffer, A. Shahani, S. Mohan, H. Samavati, H. Rategh, M. del Mar Hershenson, Xu Min, C. Yue, DJ Eddleman, T. Lee, "A 115-mW, 0.5- μm CMOS GPS Receiver with Wide Dynamic-Range Active Filters," *IEEE J. Solid-State Circuits*, vol. 33, no. 12, pp. 2219-31, December 1998.
- [58] P. Leroux, J. Janssens, and M. Steyaert, "A 0.8dB NF ESD-Protected 9mW CMOS LNA," in *IEEE Int. Solid-State Circuits Conf. Dig. Tech. Papers*, February 2001, pp. 410-411.
- [59] A. Karanicolas, "A 2.7 V 900 MHz CMOS LNA and Mixer," in *IEEE Int. Solid-State Circuits Conf. Dig. Tech. Papers*, February 1996, pp.50-51.
- [60] A. Rofougaran, J. Y-C Chang, M. Rofougaran, and A. A. Abidi, "A 1 GHz CMOS RF Front-End IC for a Direct-Conversion Wireless Receiver," *IEEE J. Solid-State Circuits*, vol. 31, pp. 880-889, July 1996.
- [61] D. Shaeffer and T. H. Lee, "A 1.5-V, 1.5 GHz CMOS Low Noise Amplifier," *IEEE J. Solid-State Circuits*, vol. 32, pp. 745-59, May 1997.
- [62] R. Lehmann and D. Heston, "X-Band Monolithic Series Feedback LNA," *IEEE Trans. Microwave Theory Tech.*, vol. MTT-33, pp. 1560-1566, December 1985.
- [63] A. Abidi, G. Pottie, and W. Kaiser, "Power-Conscious Design of Wireless Circuits and Systems," *Proc. IEEE*, vol. 88, pp. 1528-1545, Oct. 2000.
- [64] M. Strutt and A. Van der Ziel, "Suppression of Spontaneous Fluctuations in Amplifiers and Receivers for Electrical Communication and for Measurement Devices," *Physica*, vol. IX, no. 6, pp. 513-527, June 1942.
- [65] L. Besser, "Stability Considerations of Low-Noise Transistor Amplifiers With Simultaneous Noise and Power Match," in *IEEE MTT-S Int. Microwave Symp. Dig.*, June 1975, pp. 327-329.
- [66] H. Haus and R. Adler, "Optimum Noise Performance of Linear Amplifiers," *Proc. IRE*, pp. 1517-1533, August 1958.
- [67] H. Fukui, "Available Power Gain, Noise Figure and Noise Measure of Two-Ports and Their Graphical Representation," *IEEE Trans. Circuits Theory*, vol. CT-13, pp. 137-142, June 1966.
- [68] R. Tucker, "Low-Noise Design of Microwave Transistor Amplifiers," *IEEE Trans. Microwave Theory Tech.*, vol. MTT-23, pp. 697-700, August 1975.
- [69] J. Engberg, *Noise Theory of Linear and Nonlinear Circuits*, John Wiley & Sons, Aug. 1995.
- [70] K. Fong, "Dual-Band High-Linearity Variable-Gain Low-Noise Amplifiers for Wireless Applications," in *IEEE Int. Solid-State Circuits Conf. Dig. Tech. Papers*, February 1999, pp. 224-225.

- [71] J. Ryyanen, K. Kivekas, J. Jussila, A. Parssinen, K. Halonen, "A Dual-Band RF Front-End for WCDMA and GSM Applications," in *Proc. IEEE Custom Integrated Circuits Conf.*, May 2000, pp. 175-178.
- [72] R. Magoon, I. Koullias, L. Steigerwald, W. Domino, N. Vakilian, E. Ngompe, M. Damgaard, K. Lewis, and A. Molnar, "A Triple-Band 900/1800/1900 MHz Low-Power Image-Reject Front-End for GSM," in *IEEE Int. Solid-State Circuits Conf. Dig. Tech. Papers*, February 2001, pp. 408-409.
- [73] J. Janssens, J. Crols, and M. Steyaert, "A 10 mW inductorless, broadband CMOS low noise amplifier for 900 MHz wireless communications," in *Proc. IEEE Custom Integrated Circuits Conf.*, May 1998, pp. 75-78.
- [74] David M. Pozar, *Microwave Engineering*, John Wiley and Sons, Inc., 2nd edition, 1998.
- [75] "IRE Standards on Electron Tubes: Definition of Terms, 1957," 57 IRE 7.S2, *Proc. IRE*, vol. 45, pp. 983-1010, July 1957.
- [76] A. Bellomo, "Gain and Noise Considerations in RF Feedback Amplifier," *IEEE J. Solid-State Circuits*, vol. 3, pp. 290-294, September 1968.
- [77] A. van der Ziel, *Noise*, Prentice-Hall, New York, 1954.
- [78] H. Rothe and W. Dahlke, "Theory of Noisy Fourpoles," *Proc. of the IEEE*, pp. 811-818, June 1956.
- [79] A. van der Ziel, *Noise in Solid State Devices and Circuits*, John Wiley & Sons, New York, 1986.
- [80] A. Abidi, "High-Frequency Noise Measurement on FET's with Small Dimensions," *IEEE Tran. Electron Devices*, vol. ED-33, pp. 1801-1805, Nov. 1986.
- [81] R. Jindal, "Hot-Electron Effects on Channel Thermal Noise in Fine-Line NMOS Field-Effect Transistors," *IEEE Tran. Electron Devices*, vol. ED-33, no. 9, pp.1395-1397, Sept. 1986.
- [82] A. Hajimiri, S. Limotyrakis, and T. H. Lee, "Jitter and Phase Noise in Ring Oscillators," *IEEE J. Solid-State Circuits*, vol. 34, pp. 790-804, June 1999.
- [83] J. Colvin, K. O., "Effects of Substrate Resistance on LNA Performance and Bondpad Structure for Reducing the Effects in a Silicon Bipolar Technology," *IEEE J. Solid-State Circuits*, vol. 34, pp. 1139-1344, September 1999.
- [84] H Tsui and J. Lau, "SPICE Simulation and Tradeoffs of CMOS LNA Performance with Source-Degeneration Inductor," *IEEE Tran. CAS-II*, vol. 47, pp. 62-65, January 2000.
- [85] J. Janssens and M. Steyaert, "Optimum MOS Power Matching by Exploiting non-Quasistatic Effect," *Electronics Letters*, vol. 35, no. 8, pp. 672-673, April 1999.
- [86] J. Greene, "Noisemanship-The Art of measuring Noise Figures Nearly Independent of Device Performance," *Proc. IRE*, pp. 1223-1224, July 1961.
- [87] H. Samavati, H. Rategh, and T. Lee, "A 5 GHz CMOS Wireless LAN Receiver Front End," *IEEE J. Solid-State Circuits*, vol. 35, no. 5, pp. 765-772, May 2000.

- [88] D. Shaeffer, "The Design and Implementation of Low-Power CMOS Radio Receivers," *Ph.D. dissertation*, Stanford University, December 1998.
- [89] B. Choi, Y. Lee, C. Park, and K. Yoon, "Super Low Noise Amplifier with Minimum Input Matching Network," *Electronics Letters*, vol. 36, no. 19, pp. 1627-1629, September 2000.
- [90] K. Kobayashi, A. Oki, L. Tran, and D. Streit, "Ultra-Low Power dc Power GaAs HBT S- and C-band Low Noise Amplifiers for Portable Wireless Applications," *IEEE Trans. Microwave Theory Tech.*, vol. 43, pp. 3055-3061, December 1995.
- [91] F. Ellinger, "A 5.2 GHz Variable Gain LNA MMIC For Adaptive Antenna Combining," in *IEEE MTT-S Int. Microwave Symp. Dig.*, June 1999, vol. 3, pp. 501-504.
- [92] U. Erben, H. Schumacher, A. Schuppen, and J. Arndt, "Application of SiGe Heterojunction Bipolar Transistors in 5.8 and 10 GHz Low-Noise Amplifiers," *Electronics Letters*, vol. 34, no. 15, pp. 1498-1500, July 1998.
- [93] F. Behbahani, J. Leete, Y. Kishigami, A. Roithmeier, K. Hoshino, and A. Abidi, "A 2.4 GHz Low-IF Receiver for Wideband WLAN in 6 μm CMOS-Architecture and Front-End," *IEEE J. Solid-State Circuits*, vol. 35, no. 12, pp. 1908-1916, December 2000.
- [94] T Liu and E. Westerwick, "5 GHz CMOS Radio Transceiver Front-End Chipset," *IEEE J. Solid-State Circuits*, vol. 35, no. 12, pp. 1927-1933, December 2000.
- [95] K. Yamamoto, T. Shimura, T. Asada, T. Okuda, K. Mori, K. Choumei, S. Suzuki, T. Miura, S. Fujimoto, R. Hattori, H. Nakano, K. Hosogi, J. Otsuji, A. Inoue, K. Yajima, T. Ogata, Y. Mijazaki, and M. Yamanouchi, "A 3.2 V Operation Single-Chip AlGaAs/GaAs HBT MMIC Power Amplifier for GSM900/1800 dual-band applications," in *IEEE MTT-S Int. Microwave Symp. Dig.*, June 1999, vol. 4, pp. 1397-1400.
- [96] A. Adar, J. DeMoura, H. Balshem, and J. Lott, "A High Efficiency Single Chain GaAs MESFET MMIC Dual Band Power Amplifier for GSM/DCS Handsets," in *IEEE GaAs IC Symp. Dig. Tech. Papers*, pp. 69-72, November 1998.
- [97] F. Raab, "Electronically Tunable Class-E Power Amplifier," in *IEEE MTT-S Int. Microwave Symp. Dig.*, May 2001, vol. 3, pp. 1513-1516.
- [98] F. Bohn, S. Kee, and A. Hajimiri, "Demonstration of a Switchless Class E/ F_{odd} Dual-Band Power Amplifier," in *IEEE MTT-S Int. Microwave Symp. Dig.*, June 2002, vol. 3, pp. 1631-1634.
- [99] D. Pozar, *Microwave and RF Wireless Systems*, John Wiley and Sons, 2000.
- [100] J. Crols and M. Steyaert, *CMOS Wireless Transceiver Design*, Kluwer Academic Publishers, 1997.
- [101] A. Zolfaghari, A. Chen, and B. Razavi, "A 2.4 GHz 34mW CMOS Transceiver for Frequency-Hopping and Direct-Sequence Applications," in *IEEE Int. Solid-State Circuits Conf. Dig. Tech. Papers*, February 2001, pp. 418-419.

- [102] B. Razavi, *RF Microelectronics*, Prentice Hall, 1998.
- [103] R. Betancourt, S. Verma, and T. Lee, "1 GHz and 2.8 GHz CMOS Injection-Locked Ring Oscillator Prescalers," in *VLSI Circuits Symp. Dig. Tech. Papers*, June 2001, pp. 47-50.
- [104] W. Chen and C. Kuo, "18 GHz and 7 GHz Superharmonic Injection Locked Dividers in 0.25 μm CMOS Technology," in *Proc. Eur. Solid-State Circuits Conf.*, September 2002, pp. 89-92.
- [105] H. Rategh and T. Lee, "Superharmonic Injection-Locked Frequency Dividers," *IEEE J. Solid-State Circuits*, vol. 34, no. 6, pp. 813-821, June 1999.
- [106] H. Wu and A. Hajimiri, "A 19 GHz 0.5-mW 0.35 μm CMOS Frequency Divider with Shunt-Peaking Locking-Range Enhancement," in *IEEE Int. Solid-State Circuits Conf. Dig. Tech. Papers*, February 2001, pp. 412-413.
- [107] A. Rofougaran, J. Chang, M. Rofougaran, and A. Abidi, "A 1 GHz CMOS RF Front-End IC for a Direct-Conversion Wireless Receiver," *IEEE Journal of Solid-State Circuits*, vol. 31, no. 7, pp. 880-889, July 1996.
- [108] H. T. Friis, "Noise Figure of Radio Receivers," *Proc. IRE*, pp. 419-422, July 1944.
- [109] M. Lax, "Classical Noise. V. Noise in Self-Sustained Oscillators," *Physical Review*, vol. 160, no. 2, pp. 290-307, August 1967.
- [110] A. Hajimiri and T. Lee, "A General Theory of Phase Noise in Electrical Oscillators," *IEEE J. Solid-State Circuits*, vol. 33, no. 2, pp. 179-194, February 1998.
- [111] A. Demir, A. Mehrotra, and J. Roychowdhury, "Phase Noise in Oscillators: A Unifying Theory and Numerical Methods for Characterization," *IEEE Trans. Circuits & Systems I*, vol. 47, no. 5, pp. 655-674, May 2000.
- [112] D. Ham, "Statistical Electronics – Noise Processes in Integrated Communication Systems", *Ph.D. Dissertation, California Institute of Technology*, May 2002.
- [113] Matt Straayer, Jose Cabanillas, and Gabriel Rebeiz, "A Low-Noise Transformer-Based 1.7 GHz CMOS VCO," in *IEEE Int. Solid-State Circuits Conf. Dig. Tech. Papers*, February 2002, pp. 287-287.
- [114] J. Craninckx and M. Steyaert, "Low-noise voltage-controlled oscillators using enhanced LC-tanks," *IEEE Trans. Circuits & Systems II*, vol. 42, no.12, pp.794-804, Dec. 1995.
- [115] L. Chua, C. Desoer, and E. Kuh, *Linear and Nonlinear Circuits*, McGraw-Hill, 1987.
- [116] S. Ramo, J. Whinnery, and T. Van Duzer, *Fields and Waves in Communication Electronics*, John Wiley and Sons, 3rd Edition, 1994.
- [117] K. Kurokawa, "Some Basic Characteristics of Broadband Negative Resistance Oscillator Circuits," *The Bell Systems Technical Journal*, pp. 1937-1955, July-August 1969.

- [118] B. Razavi, "A Study of Phase-Noise in CMOS Oscillators," *IEEE Journal of Solid-State Circuits*, vol. 31, no. 3, pp. 331-343, March 1996.
- [119] R. Foster, "A Reactance Theorem", *Bell Syst. Tech. J.*, vol 3, pp. 259-267, April 1924.
- [120] Wolfram Research, *Mathematica 4*, version 4.1.0.0, 1988-2000.
- [121] B. van der Pol, "On Oscillation Hystheresis in a Triode Generator with Two Degrees of Freedom," *Philosophical Magazine*, vol. 43, pp. 700-719, 1922.
- [122] J. S. Schaffner, "Simultaneous Oscillation in Oscillators," *IRE Tran. Circuit Theory*, vol. 1, no. 2, pp. 218-, June 1954.
- [123] M. I. Disman and W. A. Edson, "Simultaneous Asynchronous Oscillations in Class-C Oscillators," *Proc. IRE*, pp. 895-903, 1958.
- [124] C. Hayashi and M. Kuramitsu, "Self-Excited Oscillations in a System with Two Degrees of Freedom," *Memo. Faculty of Engineering, Kyoto University*, vol. 36, pp. 87-104, 1974.
- [125] T. Endo and S. Mori, "Mode Analysis of a Multimode Ladder Oscillator," *IEEE Tran. Circuits Syst.*, vol. CAS-23, pp. 100-113, February 1976.
- [126] S. Datardina and D Linkens, "Multimode Oscillations in Mutually Coupled van der Pol Type Oscillators with Fifth-Power Nonlinear Characteristic," *IEEE Tran. Circuits Syst.*, vol. CAS-25, no. 5, pp. 308-315, May 1978.
- [127] L. Chua and T. Endo, "Multimode Oscillator Analysis via Integral Manifolds, Part I: Non-Resonant Case," *International Journal of Circuit Theory and Applications*, vol. 16, pp. 25-58, 1988.
- [128] L. Chua and T. Endo, "Multimode Oscillator Analysis via Integral Manifolds, Part II: Resonant Case," *International Journal of Circuit Theory and Applications*, vol. 16, pp. 59-92, 1988.
- [129] Y. Iida and M. Morita, "Experimental Observation of Simultaneous Asynchronous Oscillation in an Oscillator Containing an Idler Circuit and Two Resonators," *Tran. IECE Japan*, vol. E 67, no. 7, 371-372, July 1984.
- [130] J. H. Ham and F. West, "A Touch-Tone Caller for Station Sets," pp 17-24, 1968.
- [131] J. Hale, *Oscillations in Nonlinear Systems*, Dover Publications Inc., 1992. (originally published by McGraw-Hill in 1963)
- [132] B. Razavi, *RF Microelectronics*, Prentice Hall, 1998.
- [133] S. Yim and K. O, "Demonstration of a Switched Resonator Concept in a Dual-Band Monolithic CMOS LC-Tuned VCO," in *Proc. IEEE Custom Integrated Circuits Conf.*, May 2001, pp. 205-208.
- [134] S. Wiggins, *Introduction to Applied Nonlinear Dynamics and Chaos*, Springer-Verlag Inc, New York, 1997.
- [135] J. Kraus, *Antennas*, McGraw Hill, Inc., second edition, 1988.
- [136] L. Khan, "Ratio Squarer," *Proc. IRE*, vol. 42, pp. 1074, November 1954.

- [137] C. Xiao, "Rayleigh Channel Fading Simulator: Problems and Solutions", *BCWS slides, Dept. of Electrical & Computer Engineering, University of Missouri-Columbia*.
- [138] A. Paulraj and T. Kailath, "On Beamforming in Presence of Multipath," *IEEE Int. Conf. Acoustics, Speech, and Signal Processing*, vol. 10, pp. 564-567, April 1985.
- [139] Alamouti, "A Simple Transmit Diversity Technique for Wireless Communications," *IEEE J. on Select. Area in Communications*, vol. 16, no. 8, pp. 1451-1458, October 1998.
- [140] E. Telatar, "Capacity of Multi-Antenna Channels," *Bell Labs Technical Memo*, June 1995.
- [141] V. Tarokh, N. Seshadari, and A. Calderbank, "Space-Time Codes for High Data Rate Wireless Communication: Performance Criterion and Code Construction," *IEEE Trans. Information Theory*, vol. 44, no. 2, pp. 744-765, March 1998.
- [142] D. Parker and D. Zimmermann, "Phased Arrays-Part I: Theory and Architectures," *IEEE Trans. Microwave Theory Tech.*, vol. 50, no. 3, pp. 678-687, March 2002.
- [143] D. Chapman, "Partial Adaptivity for the Large Array," *IEEE Trans. Antennas and Propagation*, vol. 24, no. 5, pp. 685-696, September 1976.
- [144] D. Parker and D. Zimmermann, "Phased Arrays-Part II: Implementations, Applications, and Future Trends," *IEEE Trans. Microwave Theory Tech.*, vol. 50, no. 3, pp. 688-698, March 2002.
- [145] M. Chua and K. Martin, "1 GHz Programmable Analog Phase Shifter for Adaptive Antennas," in *Proc. IEEE Custom Integrated Circuits Conf.*, May 1998, pp. 11-14.
- [146] D. Lu and D. Rutledge, "Investigation of Indoor Radio Channel from 2.4 GHz to 24 GHz," in *IEEE AP-S Int. Symp. Dig. Papers*, June 2003, pp. 134-137.
- [147] D. Rutledge, *The Electronics of Radio*, Cambridge University Press, 1999.
- [148] H. Hashemi, X. Guan, and A. Hajimiri, "A 24 GHz 8-Channel Phased-Array Receiver on Silicon," to be submitted to *IEEE Int. Solid-State Circuits Conf. 2004*.
- [149] E. Sonmez, A. Trasser, K.-B. Schad, P. Abele, and H. Schumacher, "A Single-Chip 24 GHz Receiver Front-End Using a Commercially Available SiGe HBT Foundry Process," in *IEEE Radio Frequency Integrated Circuits Symp. Dig. Papers*, June 2002, pp. 159-162.
- [150] Y. Li, M. Bao, M. Ferndahl, and A. Cathelin, "23 GHz Front-End Circuits in SiGe BiCMOS Technology," in *IEEE Radio Frequency Integrated Circuits Symp. Dig. Papers*, June 2003, pp. 99-102.
- [151] X. Guan and A. Hajimiri, "A 24 GHz CMOS Front-End," in *Proc. Eur. Solid-State Circuits Conf.*, September 2002, pp. 155-158.
- [152] D. Lu, D. Rutledge, M. Kovacevic, and J. Hacker, "A 24 GHz Patch Array with a Power Amplifier/Low-Noise Amplifier MMIC," *Int. J. Infrared & Millimeter Waves*, vol. 23, no. 5, pp. 693-704, May 2002.

- [153] I. Molina-Fernandez, E. Marquez-Segura, M. Fernandez-Navarro, T. Martin-Guerrero, C. Camacho-Penalosa, and N. Van Dijk, "Low-Cost 24 GHz Transceiver for Unlicensed Operation," *Electronics Letters*, vol. 38, no.10, pp. 458-459, May 2002.
- [154] C. Rheinfelder, S. Lindenmeier, J. Luy, C. Willner, and A. Schuppen, "A Sensor System Based on SiGe MMICs for 24 GHz Automotive Applications," in *IEEE MTT-S Int. Microwave Symp. Dig.*, May 2001, vol. 3, pp. 2239-2242.
- [155] J. Crols and M. Steyaert, *CMOS Wireless Transceiver Design*, Kluwer Academic Publishers, 1997.
- [156] T. Yakafumi, H. Tanimoto, S. Obayashi, and Y. Suzuki, "A Si 2 GHz 5-bit LO-phase-shifting Downconverter for Adaptive Antenna," in *VLSI Circuits Symp. Dig. Tech. Papers*, June 2000, pp. 66-67.
- [157] M. Horowitz, Chih-Kong Ken Yang, and Stefanos Sidiropoulos, "High-Speed Electrical Signaling: Overview and Limitations," *IEEE Micro*, vol. 18, no. 1, pp. 21-24, January-February 1998.
- [158] S. Sidiropoulos, "High-Performance Inter-Chip Signaling", *Ph.D. Dissertation, Stanford University*, 1998.
- [159] K. Stephan, "Inter-Injection-Locked Oscillators for Power Combining and Phased Arrays," *IEEE Trans. Microwave Theory Tech.*, vol. MTT-34, no. 10, pp. 1017-1025, October 1986.
- [160] A. Rofougaran, J Rael, M. Rofougaran, and A. Abidi, "A 900 MHz CMOS LC-Oscillator with Quadrature Outputs," in *IEEE Int. Solid-State Circuits Conf. Dig. Tech. Papers*, February 1996, pp. 392-393.
- [161] P. Liao and R. York, "A New Phase-Shifterless Beam-Scanning Technique Using Arrays of Coupled Oscillators," *IEEE Trans. Microwave Theory Tech.*, vol. 41, no. 10, pp. 1810-1815, October 1993.
- [162] J. Savoj and B Razavi, "A 10-Gb/s CMOS Clock and Data Recovery Circuit with a Half-Rate Binary Phase-Frequency Detector," *IEEE J. Solid-State Circuits*, vol. 38, no. 1, pp. 13-21, January 2003.
- [163] A. Rezayee and K. Martin, "A 10-Gb/s Clock Recovery Circuit with Linear Phase Detector and Coupled Two-Stage Ring Oscillator," *European Solid-State Circuits Conference Digest of Technical Papers*, pp. 419-422, Florence, September 2002.
- [164] J. Lee and B. Razavi, "A 40GB/s Clock and Data Recovery Circuit in 0.18 μ m CMOS Technology," in *IEEE Int. Solid-State Circuits Conf. Dig. Tech. Papers*, February 2003, pp. 242-243.
- [165] J. Rogers and J. Long, "A 10Gb/s CDR/DEMUX with LC Delay Line VCO in 0.18 μ m CMOS," in *IEEE Int. Solid-State Circuits Conf. Dig. Tech. Papers*, February 2002, pp. 254-255.
- [166] D. Shaeffer and S Kudszuz, "Microstrip Coupled VCOs for 40 GHz and 43 GHz OC-768 Optical Transmission," *European Solid-State Circuits Conference Digest of Technical Papers*, pp. 535.538, Florence, September 2002.

- [167] P. van de Ven, J. van der Tang, D. Kasperkovitz, and A. van Roermund, "An Optimally Coupled 5 GHz Quadrature LC Oscillator," in *VLSI Circuits Symp. Dig. Tech. Papers*, June 2001, pp. 115-118.
- [168] A Coban, K. Ahmed, and C. Chang, "A Highly-Tunable 12 GHz Quadrature LC-VCO in SiGe BiCMOS Process," in *VLSI Circuits Symp. Dig. Tech. Papers*, June 2001, pp. 119-120.
- [169] Johan D. van der Tang, Dieter Kasperkovitz, and Arthur van Roermund, "A 9.8-11.5 GHz Quadrature Ring Oscillator for Optical Receivers," *IEEE J. Solid-State Circuits*, pp. 438-442, vol. 37, no. 3, March 2002.
- [170] W. Winkler, J. Borngraber, B. Heinemann, and P. Weger, "60 GHz and 76 GHz Oscillators in 0.25 μ m SiGe:C BiCMOS," in *IEEE Int. Solid-State Circuits Conf. Dig. Tech. Papers*, February 2003, pp. 454-455.
- [171] M. Tiebout, H. Wohlmuth, and W. Simburger, "A 1V Fully-Integrated 51 GHz VCO in 0.12 μ m CMOS," in *IEEE Int. Solid-State Circuits Conf. Dig. Tech. Papers*, February 2002, pp. 300-301.
- [172] N. Saniei, H. Djahanshahi, and A. Salama, "25 GHz Inductorless VCO in a 45 GHz SiGe Technology," in *IEEE Radio Frequency Integrated Circuits Symp. Dig. Papers*, June 2003, pp. 269-272.
- [173] M. Danesh, F. Gruson, P. Abele, and H. Schumacher, "Differential VCO and Frequency Tripler using SiGe HBTs for the 24 GHz ISM Band," in *IEEE Radio Frequency Integrated Circuits Symp. Dig. Papers*, June 2003, pp. 277-280.
- [174] H. Wong, "A 50 GHz VCO in 0.25 μ m CMOS," in *IEEE Int. Solid-State Circuits Conf. Dig. Tech. Papers*, February 2001, pp. 372-373.
- [175] C. De Ranter and M. Steyaert, "A 0.25 μ m CMOS 17 GHz VCO," in *IEEE Int. Solid-State Circuits Conf. Dig. Tech. Papers*, February 2001, pp. 370-371.
- [176] H. Wu, and A. Hajimiri, "Silicon-Based Distributed Voltage-Controlled Oscillators," *IEEE J. Solid-State Circuits*, vol. 36, no. 3, pp. 493-502, March 2001.